Thermodynamic analysis of chemical interactions of the Zr-Cr-O and U-Cr-O systems at high temperatures for the evaluation of ATF (Accident Tolerant Fuel) under accidental conditions

Jinjiang Cui

Thèse

Soutenue publiquement le 13 Novembre 2023 à

L'Université de Lille

Par

Jinjiang CUI

En vue d'obtenir le grade de

Docteur de l'Université de Lille

Filière : Chimie théorique, physique, analytique

Ecole doctorale : Sciences de la Matière, du Rayonnement et de l'Environnement

Approche thermodynamique des interactions chimiques dans les systèmes Zr-Cr-O et U-Cr-O à hautes températures pour l'évaluation des combustibles ATF (Accident Tolerant Fuel) en conditions accidentelles

Rapporteurs	M. Alexander PISCH	Directeur de recherche CNRS, SIMaP, Grenoble INP-UGA
	M. Nicolas DAVID	Maître de conférences, IJL, Université de Lorraine
Examinateurs	Mme. Christine GUENEAU	Directrice de Recherche CEA
	Mme. Charlotte BECQUART	Professeure, UMET, Université de Lille
Directeur de thèse	M. Olivier TOUGAIT	Professeur, UCCS, Université de Lille
Co-encadrant de thèse	M. Pierre BENIGNI	Ingénieur de recherche CNRS, IM2NP, Aix-Marseille Université
Invité	M. Marc BARRACHIN	Ingénieur IRSN
Invitée	Mme. Evelyne FISCHER	Ingénieure, Grenoble INP

Thèse réalisée à l'unité de catalyse et chimie du solide UMR 8181 et à L'IM2NP UMR 7334
dirigée par M. Olivier Tougait, et M. Florent Louis
Présidente du jury de soutenance par Mme. Charlotte Becquart

Thesis

Public defense at 13 November 2023 at

Lille University

by

Jinjiang CUI

To obtain the title of

Doctor of Lille University

Sector: Theoretical, physical, analytical chemistry

Doctoral school: Matter, Radiation and Environmental Sciences

Thermodynamic approach to chemical interactions in Zr-Cr-O and U-Cr-O systems at high temperatures for the evaluation of ATF (Accident Tolerant Fuel) fuels under accident conditions

Rapporteurs	M. Alexander PISCH	Chargé de recherche CNRS, SIMaP, Grenoble INP-UGA
	M. Nicolas DAVID	Maître de conférences, IJL, Université de Lorraine
Examiners	Mme. Christine GUENEAU	Directrice de Recherche CEA
	Mme. Charlotte BECQUART	Professeure, UMET, Université de Lille
Supervisor	M. Olivier TOUGAIT	Professeur, UCCS, Université de Lille
Co-supervisor	M. Pierre BENIGNI	Ingénieur de recherche CNRS, IM2NP, Aix-Marseille Université
Guests	M. Marc BARRACHIN	Ingénieur IRSN
	Mme. Evelyne FISCHER	Ingénieure, Grenoble INP

Thesis carried out at the catalysis and solid chemistry unit UMR 8181 and at IM2NP UMR 7334
directed by M.Olivier Tougait and M. Florent Louis
President of the defense by Mme. Charlotte Becquart

Acknowledgement

This thesis has been accomplished thanks to the help of many people in many different aspects and domains. Without their help, the results in this document could never be achieved.

I would first express my gratitude to my director of thesis, M. Olivier TOUGAIT, who provided me the precious opportunity and support during the whole three years of my thesis. The many things he taught me during these three years would not only be useful for the academic study, but also for my life after the Ph.D.

I would like to express same gratitude to M. Pierre BENIGNI and M. Marc BARRACHIN, the supervisors of the thesis, for their constant help during the whole thesis work, and also when I was in Marseille and Cadarache. They unquestionable nurtured my passion to the science and research, and encouraged me to embark on the path of research.

Then I would like to express my gratitude the co-director of this thesis, M. Florent LOUIS, for all his help on the first year of the Ph.D. and concern all along the thesis.

I would like to express my gratitude to M. Roland DUCHER and Mme. Evelyne FISHER, for their great help and kindness of this work in part DFT and CALPHAD modeling. Their patience careful guidance and meticulous assistance undoubtedly was essential for this thesis.

I would like to express my gratitude to M. Alexander PISCH and M. Nicolas DAVID for their participants as rapporteurs of the jury of defense. I would like to express my gratitude to Mme. Christine GUENEAU and Mme. Charlotte BECQUART for their participants as members of jury of defense, and also their patience and kindness following the two CSI in the first two years of the thesis.

I'd like to express my appreciation to people who assisted various analysis or courses of this thesis: M. Georges MIKAELIAN, M. Matthieu TOUZIN, M. Philippe DEVAUX, Mme. Severine BELLAYER, Mme. Claire MINAUD, Mme. Andrea CAMPOS.

I'd like to thank all the Ph.D., post-doc, engineering and internship students around with me during these three years. They not only helped me with my academic work, but also my quotidian life in France, especially when it was difficult in the beginning. It was really a pleasure to work with them.

I'd like to thank all the UCCS laboratory and members of Chevreul.

Thanks to IRSN and CNRS-NEEDS for funding this thesis.

All the challenges, gains and happiness I've got for these three years would be a treasure of my life. Thanks for all the people I've met all along the journey.

Jinjiang CUI

Table of Contents

Acronyms and symbols

Acronyms:

ATF	Accident tolerant fuel
BSE	Back Scattered Electrons
CALPHAD	Calculation of phase diagram
CTBTO	Comprehensive Nuclear-Test-Ban Treaty Organization
DFT	Density Functional Theory
DSC	Differential Scanning Calorimetry
DTA	Differential Thermal Analysis
EBSD	Electron Back Scatter Diffraction
ECCS	Emergency cooling system
EDS	Energy Dispersive Spectroscopy
EPMA	Electron Probe Micro Analysis
GGA	Generalized Gradient Approximation
INES	International Nuclear Event Scale
LDA	Local Density Approximation
LOCA	Loss of coolant
LWR	Light water reactor
PCI	Pellet-cladding interaction
PPMS	Physical Property Measurement System
SE	Secondary Electrons
SEM	Scanning Electron Microscope
SGTE	Scientific Group Thermodata Europe
VASP	Vienna Ab initio simulation package
WDS	Wavelength Dispersive Spectroscopy
XRD	X-Ray Diffraction

Main symbols:

H	Enthalpy
C_p	Heat capacity
S	Entropy
G	Energy of Gibbs
X	Composition
T	Temperature
θ_E	Einstein temperature
Sol	Solubility
ΔH_0^{298}	Increment of enthalpy from 0K to 298K
$\Delta_f H$	Enthalpy of formation
$\Delta_f S$	Entropy of formation
$\Delta_{\mathrm{ds}}\overline{H}_i^{\infty}$	Partial drop solution enthalpy of i at infinite dilution
$\Delta_{\mathrm{mix}}\overline{H}_i^{\infty}$	Partial mixing enthalpy of i at infinite dilution

Introduction

Introduction

Since the 1950s, the light water reactor (LWR) has been developed and has become the most common commercial nuclear reactor, accounting for over 80% of global nuclear reactors now [1].

The potential risks of LWR for the public have gained attention after the Three Mile Island Unit 2 (TMI-2) accident in the United States and have been highlighted recently after the Fukushima Daichi accident [2]. Especially, the impact of the Fukushima Daichi accident renewed the worldwide drive to improve nuclear fuel technology in order to enhance again the safety of the reactor.

In this framework, the nuclear industries accelerated research programs to develop new fuel systems, referred to as an Accident Tolerant Fuel (ATF). The primary objective is to enhance the performance of fuel safety responses under design basis accident conditions and potentially under severe accident ones in order to increase the reaction time margin so the available response time for operators; this objective can be reached by reducing the fuel cladding deformation extent, the heating rate and hydrogen production from high-temperature steam oxidation; or by enhancing fission product retention to reduce severe consequences on the cladding integrity.

The introduction of a new fuel type requires extensive testing and evaluation procedures. Typically, this entire process can take between 10-15 years, from an initial conception to a fully commercial product. Consequently, the ATF conceptions under development are usually categorized into two distinct trajectories: near-term and longer-term, based on their anticipated timeline to full-core deployment. Near-term concepts are expected for integration into the existing LWRs and anticipated for commercially viable full-core deployment by the mid-2020s. Longer-term concepts remain in the stage of ongoing development and testing and are forecasted for future reactors.

In the context of the near-term ATF cladding concepts, coating a protective layer onto cladding emerges as a promising approach with the potential to improve oxidation resistance while maintaining minimum effects on the fuel performance under normal operation conditions [3], [4]. Notably, current studies concentrate mostly on chromium materials, such as metallic Cr, CrAl, or CrN. In France, Framatome has developed since early 2000, a Cr coating (~ 20 to 30 microns) onto its M5® cladding making this concept the preferred choice for reactor implementation in the near future.

In addition to this development in cladding, ongoing research is also conducted to enhance the retention of fission gases in the fuel itself. These efforts involve the addition of dopants into UO_2 ceramic fuel pellets to promote optimized microstructure with larger grains in comparison with standard fuel. This grain morphology exhibits improved efficacy in confining gaseous fission products, consequently reducing the internal pressure accumulation within the fuel rod before hypothetical accident conditions. It also offers notable advantages in limiting the phenomena of cladding ballooning and rupture, thereby contributing to a reduction in fuel rod fragmentation and spreading materials. Framatome has developed a UO_2 fuel containing chromium oxide (Cr_2O_3) with a maximum dopant concentration below 1500 ppm.

Until now, much efforts have been dedicated to the ATF fuel systems in design basis conditions while a little has been done to anticipate the behavior of these systems in severe accident conditions, i.e. when part of the fuel element is liquid. In this framework, this thesis aims investigate the Zr-Cr-O and U-Cr-O systems at high temperatures in order to provide some information on the behavior on these new fuel systems in these conditions. More precisely it aims to measure the thermodynamic properties of intermediate phases and to assess the high-temperature phase equilibria in the Zr-Cr and Zr-Cr-O systems on the one hand, and U-Cr and U-Cr-O on the other hand. Equilibrium studies in the systems at the highest 1700°C and thermodynamic properties like enthalpy of formation and heat capacity are planned to be measured. Based on an optimization of the binary systems, the assessments of the ternary systems would be re-evaluated. A better description of system Zr-Cr-O in 1200°C to 1700°C is aimed.

These new results will serve for new CALPHAD[1] optimizations which will be integrated into the NUCLEA[2] thermodynamic database. The results will provide initial elemental requirements to define the failure criteria for ATF fuel elements in the ASTEC[3] code simulations.

[1] The CALPHAD method is a reliable tool to develop thermodynamic databases for non-ideal systems with a large number of chemical elements.
[2] The NUCLEA database was initially developed by THERMODATA/INPG/CNRS with the CALPHAD method and supported by IRSN for more than 20 years. To date, it contains 18 elements: Ag-Al-B-Ba-C-Ca-Cr-Fe-In-La-Mg-Ni-O-Ru-Si-Sr-U-Zr. These elements covered the field of the key components in a reactor core under normal and accidental conditions. The elements H and Ar are also included in the gaseous phase. This database is continuously developed by SIMAP (University of Grenoble) with IRSN support.
[3] The severe accident integral code ASTEC, since almost 30 years by IRSN simulates the behaviour of a whole nuclear power plant under severe accident conditions, including severe accident management by engineering systems and procedures. Since 2004, the ASTEC code is progressively becoming the reference European severe accident integral code through in particular the intensification of research activities carried out in the frame of the SARNET European network of excellence.

This Ph.D. thesis includes 6 chapters:

Chapter I: An introduction of context, a review of nuclear accidents of LWRs, developed conceptions of accident tolerant fuel, and the study objective of this thesis

Chapter II: The experimental techniques and calculation/modeling methods employed

The next three chapters present the main results of this thesis work:

Chapter III: The results of the Zr-Cr binary system

Chapter IV: The results of the Zr-Cr-O ternary system

Chapter V: The results of the U-Cr binary system and the U-Cr-O ternary system

The general conclusions of this thesis are presented in **Chapter VI**.

Reference

[1] T. Murakami, 'A historical review and analysis on the selection of nuclear reactor types and implications to development programs for advanced reactors; A Japanese study', *Energy Reports*, vol. 7, pp. 3428–3436, Nov. 2021, doi: 10.1016/j.egyr.2021.05.049.

[2] B. R. Sehgal, 'Perspectives on LWR severe accidents and public risks', *Nuclear Engineering and Design*, vol. 354, p. 110253, Dec. 2019, doi: 10.1016/j.nucengdes.2019.110253.

[3] E. Kashkarov, B. Afornu, D. Sidelev, M. Krinitcyn, V. Gouws, and A. Lider, 'Recent Advances in Protective Coatings for Accident Tolerant Zr-Based Fuel Claddings', *Coatings*, vol. 11, no. 5, p. 557, May 2021, doi: 10.3390/coatings11050557.

[4] C. Tang, M. Stueber, H. J. Seifert, and M. Steinbrueck, 'Protective coatings on zirconium-based alloys as accident-tolerant fuel (ATF) claddings', *Corrosion Reviews*, vol. 35, no. 3, pp. 141–165, Aug. 2017, doi: 10.1515/corrrev-2017-0010.

Chapter I

Context and study objective

Chapter I. Context and study objective

I.1 Introduction

Light water reactor (LWR) uses light water as its coolant and neutron moderator. LWR has been developed since the 1950s and became the most common type of commercial nuclear reactor after the 1970s. Today, LWR makes up more than 80% of global nuclear reactors [1].

In the early years, severe accidents (involving core partial melting) were not considered to be highly probable although they were continuously studied. The potential risks of LWR for the public gained attention after the Three Mile Island Unit 2 (TMI-2) accident in the United States in 1979 and have been highlighted recently after the Fukushima Daichi accident in 2011 [2]. Even if no shortcomings in the nuclear fuel design were identified, the impact of the Fukushima Daichi accident renewed the worldwide drive to improve nuclear fuel technology that should enhance the safety of the reactor.

At Fukushima Daichi, following the tsunami, the failure of the safety systems at the three operational units under the earthquake caused reactor overheating, leading to severe accidents. The conditions in reactors caused extreme hydrogen production in some reactor buildings, then exploded and caused leaks of radioactive gas and materials. The generation of hydrogen was mainly caused by the oxidation of fuel rod claddings.

At Fukushima Daichi, as in most of the LWRs, the cladding of the fuel rods is made of Zr-based alloys. At normal operation temperatures, the zirconium cladding reacts with water resulting in the formation of a solid oxide layer on the cladding outer surface. This corrosive phenomenon is strongly accelerated at high temperatures (from 1500°C), e.g., if the fuel assemblies are no longer covered by liquid water and are insufficiently cooled.

In this framework, the nuclear industry initiated, and accelerated research programs aimed to develop a new generation of fuel systems to increase its performance safety response under severe accidents. Accident Tolerant Fuel (ATF) is a term used to describe these new conceptions. The purpose may be achieved by increasing the response time margin so the operators have available time for a backup solution; or by reducing the fuel cladding deformation extent, the rate of heat and hydrogen production from high-temperature steam oxidation; or by enhancing fission product retention thus reducing severe accident consequences. A short-term material approach is a protective coating on the outer surface of Zr alloys to slow down the hydrolysis and Zr oxidation reactions. The most studied layer deposited

at present are metallic-based chromium films, such as elemental Cr, CrAl, or CrN. In France, the Cr coating (~ 20 to 30 microns) is the preferred option in the industry. In addition to these developments of the new types of claddings, research is also conducted to improve the fission gas retention, by developing optimized fuel microstructure, with enlarged fuel grain size, while maintaining high pellet density. This coarser grain structure is thought to provide a better intragranular gas retention capability, which would reduce the internal pressure of the rod before the accident. The fuel pellets fabrication process thus integrates new additives and doping materials, such as chromium oxide or alumina. Framatome has developed an advanced UO_2 fuel containing chromium oxide (Cr_2O_3) with a maximum dopant concentration below 1500 ppm.

In the following sections, we are going to review the two most important accidents of LWR in history and describe stepwise events up to the core melting. We will not describe the core melt accident that happened at Chernobyl, in one of the four RBMK reactors that are water-cooled reactors, however, they are moderated differently from Boiling Water Reactors (i.e. BWR as those in Fukushima Daichi) or Pressurized Water Reactors (i.e. PWR as in TMI-2), by graphite.

In the second part, we will come back to more details on the ATF conceptions and in particular on the conceptions retained today by French nuclear industries.

In the final section, we will present the objectives of this Ph.D. thesis.

I.1.1 Three Mile Island (TMI) accident

The so-called TMI-2 accident was the first severe accident recorded in a commercial nuclear reactor of PWR type. This partial core-melt accident occurred at the Three Mile Island 2 reactor (TMI-2) near Harrisburg Pennsylvania on 28 March 1979, classified as a level 5 accident on the International Nuclear Event Scale (INES) of IAEA (See Figure I-1). The accident was caused by a design-based problem of the early conception of the reactor [3].

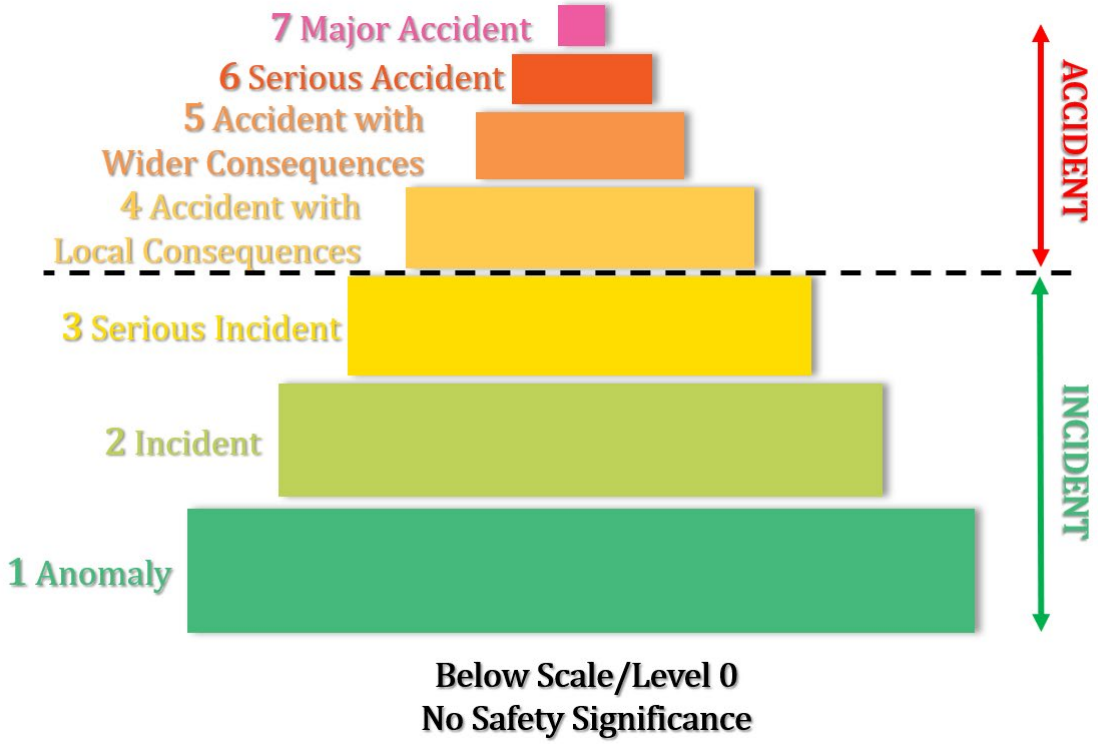

Figure I-1 The international nuclear and radiological event scale

The accident started with a loss of feeding water of a steam generator on the secondary side for 10-15 minutes. The dry-out of the steam generator significantly reduced the heat transfer efficiency of the core and increased the reactor pressure. The turbine was automatically tripped by this accident. The pilot-operated relief valve (PORV) was opened to discharge the pressure in the vessel but then blocked when it should be closed. This led to a loss of coolant and started the Emergency Core Cooling System (ECCS), generating a huge amount of steam. The steam flow then blocked the water in the pressurizer. The operator was misguided by the indication of a pressurizer, and manually shut down the pumps and closed the ECCS injection in a misjudgment. But the PORV was kept open.

The failure of equipment and faulty operations together caused a considerable amount of coolant loss from the vessel. With no addition of water, the core was almost fully exposed after a boil-off of water in the vessel, which was approximately 130 minutes after the first failure of the steam generator.

The decay heat raised the cladding temperature in the situation of the absence of coolant and caused a very exothermic zirconium-stream reaction. Nearly 50% of the core was melted down and flowed to the bottom of the vessel. (See Figure I-2)

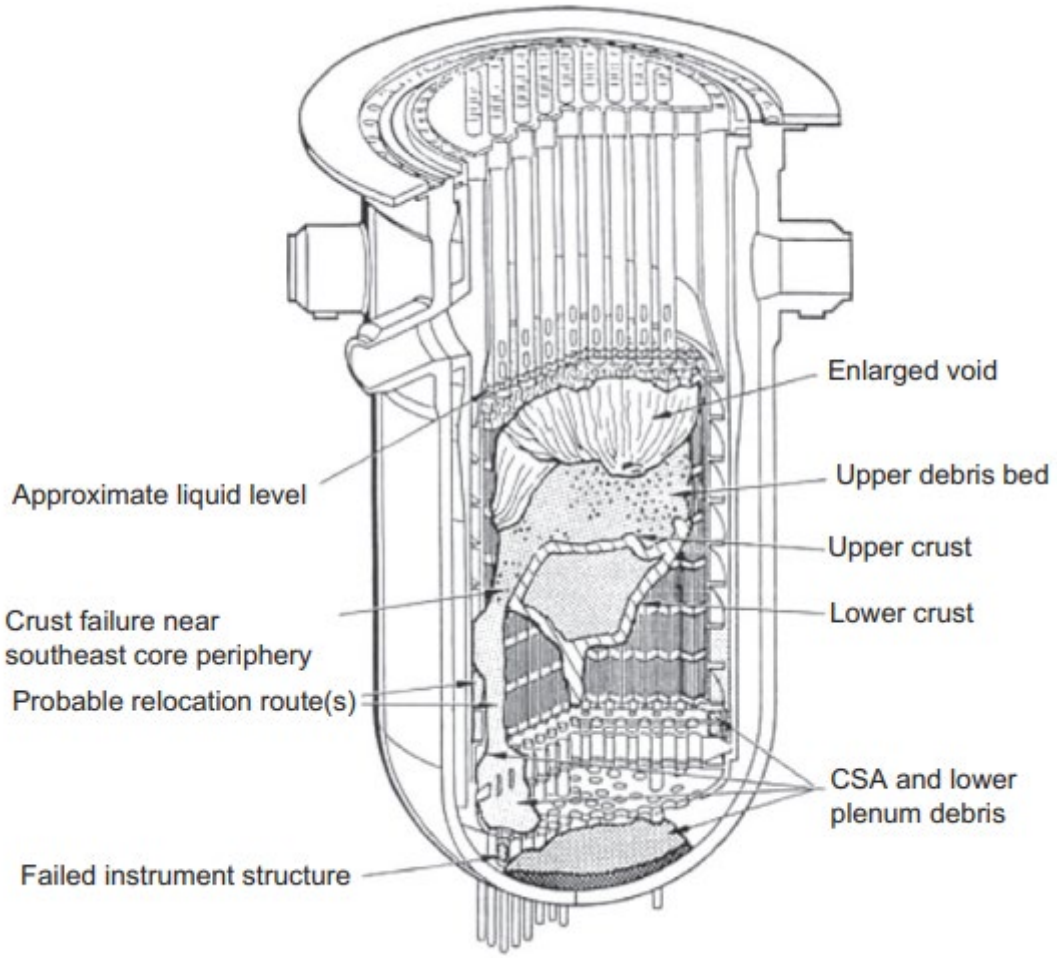

Figure I-2 Hypothesized core damage configuration at 226 minutes [3]

The further melting was stopped after the operators restarted the pumps and the vessel was refilled with water. The debris bed was formed with molten fuel and fragments. The debris reheated molten materials and flowed down to the lower head. It cooled down after hours. The temperature of the core decreased at last after 6 days, by a natural flow circulated between the steam generator and the core.

During the accident, a large amount of radioactive materials was released in the confinement and even in the auxiliary building. Nevertheless, about 0.01% of fission product was only released into the environment, like ^{131}I, ^{137}Cs, and ^{90}Sr.

Luckily the TMI-2 accident did not cause injuries or deaths. The nuclear station was caught in complete paralysis. During these days, at least 200k residents nearby were evicted. No resident around or operator was affected by radiation. This was mainly attributed to the automatic safety facilities and the three protection barriers concept in the nuclear station. From this accident, the whole focus of the LWR safety research shifted beyond design-based accidents. (i.e. severe accidents) even though the LOCA experiments and research did not terminate. It led to numerous safety improvements to France's nuclear power plants: plant operation and instrumentation, containment of radioactive substances, implementation of emergency plans, etc.

I.1.2 Fukushima accident

The Fukushima Daichi accident was one of the only two nuclear accidents classified as a level 7 with the Chernobyl one on the International Nuclear Event Scale (INES) in history. It occurred on 11 Mars 2011 at the Fukushima Daichi nuclear power station. An earthquake of Richter magnitude equal to 9.0 and a tsunami wave triggered by this earthquake successively hit the plant. On detecting the earthquake, all the BWR reactors were automatically shut down in the first moment by control rod insertion. Because of these shutdowns and other electrical grid supply problems, the reactors' electricity supply failed, and their emergency diesel generators automatically started. Critically, these were required to provide electrical power to the pumps that circulated coolant through the reactors' cores. The giant tsunami wave with a height of 14 meters crossed over the 10-meter embankment of the Fukushima plant, caused a loss of external power supply of reactors 1 to 4 in the power plant and also flooded the emergency diesel generator. The earthquake felled the outside poles of the electricity of the plant and cut off the power transmission of the off-site power supply. In this situation, the emergency cooling system (ECCS) and water circuit pumps were disabled.

The resulting loss of reactor core cooling led to the increase of temperature of the cores because of the decay heat. A possible applied action at that moment was to conduct freshwater or seawater by fire engines through the fire protection (FP) line [4]. But the action was not employed eventually.

After a boil-off of the coolant in the vessel, the fuels in Units 1 to 3 were exposed to high-temperature steam. The claddings were melted and the radioactive materials in the fuel rods were released. Thereby Unit 1 was out of water supply for 14h and Unit 2 or Unit 3 for 6-7h

[2]. The cores were then progressively melted down, relocated to the lower head of the vessel and interacted with the vessel. It led to the vessel rupture in the three units and the interaction between the melted core and the concrete of the containment.

The violent zirconium-steam reaction at high temperatures (>1500°C) caused a substantial amount of hydrogen production and contributed to cause an increase of the pressure of the vessel. Some of the produced hydrogen went out to the reactor buildings. Some venting attempts were made but unsuccessful in reducing enough the inner pressure and the hydrogen concentration.

At last, explosions occurred one after another in Units 1,3 and 4 of the plants and destroyed the upper structures of the reactor buildings. About 9 billion Bq of radioactive materials were released into the environment, making it one of the most terrible nuclear disasters in history. A report from CTBTO (Comprehensive Nuclear-Test-Ban Treaty Organization) [5] shows that the radioactive materials released could be found all over the world.

Another main effect of the disaster was the pollution of the Pacific Ocean. The report of IRSN in 2011 showed that about 27 PBq ^{137}Cs isotopes were released into the ocean from March to July 2011, which could be the largest release of man-made radioactive materials into the ocean ever observed.

Since the accident, new water has been pumped in to cool fuel debris in the reactors. At the same time, ground and rainwater have leaked in, creating more radioactive wastewater that now needs to be stored and treated. On 24 August 2023, the Japanese government started to evacuate the wastewater (containing mainly tritium) in the ocean, which will continue for 30 years in the future.

In France, lessons have been learned from this accident. Complementary safety assessments carried out on all French nuclear installations in the year following the Fukushima Daiichi accident have led to the definition of a "hardcore" concept, made up of a limited number of equipment able to cope with extreme accidental conditions.

I.1.3 Material interactions during a severe accident

The reactor core is a high-energy density structure. In a light water reactor, the energy density is often 50 to 75 MW/m^3, and the thermal power can reach 3000MW [6]. Once the cooling system is disabled, the temperature of the core will rise rapidly and can reach the melting

temperature of the UO_2 fuel (2850°C). A comprehensive review of the interactions at high temperatures between materials inside the core and melted core (or corium) formation has been recently published by Barrachin *et al.* [7]. A schema providing the material interaction in a core as a function of temperature during an LWR severe accident is shown in Figure I-3.

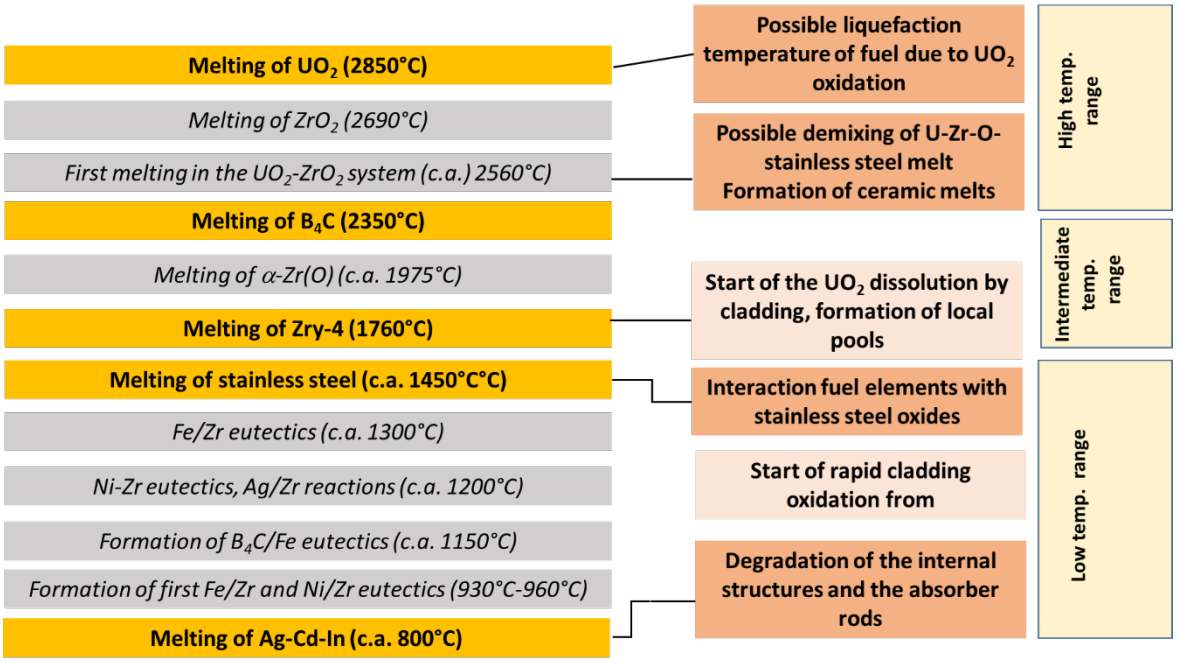

Figure I-3 LWR severe accident-relevant melting and chemical interaction temperatures which result in the formation of the liquid phase [7].

According to this scheme and the current understanding of core behavior in accidental conditions [8], [9], a typical sequence of a severe accident can be roughly distinguished into four main temperature regimes:

1. Regime I, 800°C-1450°C. In this regime, the absorber rods melt and eutectic reactions start to occur between some metallic components of the core (zircaloy guide tube, stainless steel cladding, absorber rods). The lowest melting temperature is related to the melting temperature (800°C) of the Ag-Cd-In alloy of the absorber rods devoted to the power control of the reactor but the degradation of the core only starts when the absorber rod cladding (stainless steel) interacts with the zircaloy guide tube with eutectic melt formation (from 930°C).
2. Regime II, 1450°C-2300°C. In this regime, the main degradation of the core becomes the melting of fuel resulting from its interaction with Zircaloy cladding. Even if only pools may be formed locally in the core, the degradation is already significant.

3. Regime III, above 2300°C. A large molten pool formed due to a partial/full relocation of fuel rod materials towards the lower plenum of the vessel. The corium composition can be variable from compositions located in the metallic-oxidic part of the U-O-Zr-steel system to fully oxidic.
4. Regime IV. The vessel possibly fails, and melting core debris is released into the reactor cavity pit. The molten materials then interact with concrete and the melt composition changes progressively, including more and more oxides from concrete. Concrete species (SiO_2) and combustible gases are released.

To understand and simulate the physically occurring phenomena in the core in severe accident conditions, the previous description shows that it is necessary to characterize a system with a large number of chemical elements. The assessment and modeling should cover not only the individual materials of core structures but also the interactions within and with surrounding materials in a large temperature interval.

This difficult task is ongoing in IRSN with the support of the NUCLEA thermodynamic database [10] developed with the help of the CALPHAD method.

I.1.4 Thermodynamic modeling of interactions between core materials at high temperatures: the NUCLEA database

At the end of the 1980s, the development of a modern thermodynamic database had become necessary to perform precise calculations in severe accident conditions. The CALPHAD method developed at that moment was a possible approach to increase the reliability and the applicability of thermodynamic databases for non-ideal systems with a large number of chemical elements by ensuring the consistency of experimental data.

The NUCLEA database has been initially developed by THERMODATA/INPG/CNRS and supported by IRSN for more than 20 years. With this database, it is possible to make calculations of thermodynamic properties and phase equilibria in a chemical system containing 18 elements: Ag-Al-B-Ba-C-Ca-Cr-Fe-In-La-Mg-Ni-O-Ru-Si-Sr-U-Zr. These elements cover the field of the key components in a reactor core under accidental conditions, including the fuel rods as (UO_2, Zr), the control rods as (B, C, In, Ag), the fission products (which are important for the calculation of the decay heat) as (Ru, La, Ba, Sr), the stainless-steel structures as (Fe, Ni, Cr) and the concrete as (Al_2O_3, CaO, SiO_2, MgO). The elements H and Ar are also included in the gaseous phase.

This large database continues to be developed by SIMAP (University of Grenoble) with IRSN support (by integrating new elements, Pu, Cs, Mo, and Ce and by modeling more ternary systems) and to be validated on simulated corium tests.

I.2 Accident tolerant fuel conceptions

I.2.1 Introduction, the context of ATF, international and French directions

New types of fuel have been proposed by the nuclear industry since the Fukushima Daichi accident. In the United States and Europe in particular, manufacturers are developing fuel elements known as ATF (Accident Tolerant Fuel), which are more robust in terms of safety, as well as having other interesting properties in normal operation (e.g. reduced fuel cycle costs). The aim is to achieve better behavior in the event of an accident, particularly in terms of degradation under loss of coolant (LOCA) conditions, hydrogen production and the release of fission products. These new concepts can be grouped into two categories which it is important to distinguish, one acting on the properties of the cladding and the other on those of the fuel.

For the cladding, zirconium alloys have been chosen as the cladding material of UO_2 fuel since the 1950s. Zircaloy-4 was preferred because of its excellent corrosion and irradiation resistance, low thermal neutron absorption cross-section and good ductility. However, in the Fukushima-Daichi accident in 2011, the violent oxidation reaction of zirconium occurred in high-temperature steam conditions and ended with an explosion of released hydrogen gas. This underlined the impact of hydrogen production in an LWR core melt accident and the necessity to improve the corrosion resistance of cladding in such conditions.

Objectives of the new concepts are mainly to increase the corrosion resistance of cladding in LOCA accident conditions, then to reduce hydrogen release and finally to increase the safety time margin for operators to regain control of the reactor [11], [12] before entering in severe accident conditions. Improved cladding concepts should be able to tolerate longer time in LOCA conditions than current Zircaloy, and maintain the same or improved performance in normal operating conditions.

For fuel, the main objective of the new concepts is to improve the capacity to retain more efficiently the fission gases inside the UO_2 grains. It can be done by enlarging the grain fuel structure by introducing dopants at the fabrication stage. This coarser grain structure is thought to provide a better intragranular gas retention capability, which would reduce the internal

pressure of the rod before the accident. This is beneficial in reducing ballooning and bursting of the cladding. A reduced amount of fission gas at the grain boundaries could reduce the fuel fragmentation and dispersal in case of rod burst since fuel fragmentation is likely generated by an overpressure of the intergranular gas bubbles.

The introduction of a new fuel system requires extensive testing and evaluation. Typically, this entire process can take between 10-15 years, from concept to a fully commercial product. For that reason, ATF concepts under development are usually categorized as near-term or longer-term, based on their anticipated timeline to full-core deployment. Near-term concepts are expected to be implemented in the existing LWRs. These near-term concepts are expected to be commercially viable for full-core deployment by the mid-2020s. Longer-term concepts are still being developed and tested.

For the near-term ATF cladding concepts, deposition of the protecting layer on Zircaloy cladding quickly appears as a reasonable solution that can significantly improve the oxidation resistance in accident conditions without a significant impact on the fuel performance in normal conditions. This developing direction has been for now a good short-term solution for ATF fuels [13], [14].

Till now, extensive studies on Zircaloy-based claddings with different coating materials have been investigated by many researchers around the world. A recent article by Yang *et al.* [12] reviewed the works including MAX phase coatings, carbide coatings, nitride coatings, pure metal coatings and alloy coatings.

The method of chromium coating on zirconium cladding was initially developed by CEA and EDF in a French Joint Nuclear R&D Program. Framatome developed a production line using the physical vapor deposition method to coat a full-length cladding [15].

For the fuel new concepts, Framatome proposes UO_2 fuel containing chromium oxide (Cr_2O_3) with a maximum dopant concentration of approximately 1500 ppm. Doped UO_2 fuel is manufactured with the same specifications and enrichment as UO_2 with burnable neutron absorbers. Light water reactor cores fueled with doped UO_2 fuel have the same neutron spectrum as those with UO_2 fuel, due to the low level of additive. Cr_2O_3-doped fuels have been irradiated for a long time in many countries worldwide and comprehensive databases are available. They are commercially available.

The collaboration between Framatome, EDF and CEA has succeeded in the delivery and insertion of the first complete fuel assembly comprised of 100% Cr_2O_3 enhanced pellets and chromium-coated rods in a nuclear power plant in the United States in 2021. In 2023, Framatome signed with EDF to test the ATF technology in an operating nuclear power plant in France [16].

I.2.2 Cr-coated Zircaloy-based cladding and Cr_2O_3-doped UO_2 fuel

The chromium coating on zirconium alloys is the most advanced and mature solution in developed coating materials of ATF [15]. Typically layer with a thickness of about 15 to 20 µm is deposited on the surface of the Zircaloy substrate. The method has been developed by many institutions, with different elaboration processes. For example, Framatome developed a physical vapor deposition technique that forms an un-porous and dense layer at the surface of M5® (Zr-based alloy with ~ 1 % wt Nb and traces of Fe) without modifying the microstructure of the substrate, as shown below in Figure I-4.

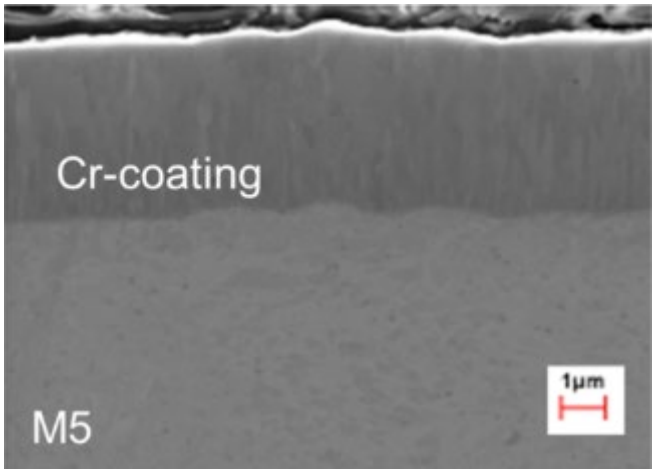

Figure I-4 Microstructure of Cr-coated M5 cladding fabricated by Framatome with physical vapor deposition technique [15]

The numerous advantages and excellent properties of chromium coating were summarized by Yang *et al.* [12]. The oxidation resistance and both physical and chemical properties were highlighted by many researchers [17]-[22].

As for near-term ATF cladding, incremental conceptions of advanced fuel have been developed. A range of oxide additives was studied in combining with UO_2 powder during the fabrication of the fuel to modify the microstructure of the fuel pellets, such as oxides of Cr, Al, Nb, Mg

and Ti [23]–[28]. Among these additives, the most studied was Cr_2O_3, or a mixture of Cr_2O_3-Al_2O_3, which is known to enhance grain growth during sintering [23]. The major interest regarding the fuel rod is to increase the pellet-cladding interaction (PCI) margin by enhancing the fuel viscoelastic behavior. At the same time, larger grains also benefit the retention of fission gas [29]. A comparison of pure UO_2 pellets and Areva/Framatome's doping sample is shown in Figure I-5. It illustrates the bigger grain size after doping. In practice, Bourgeois *et al.* [25] reported a maximum of 70 μm of grain size at the solubility limit, and further enhancement can be obtained by additional dopant mass at higher temperatures than eutectic temperature of 1925K for the 50 at % Cr composition (Cr-Cr_2O_3). The effect of dopant on the heat capacity of the fuel is found negligible [23]. Based on parametric studies, chromium content is specified at an optimum value of 0.16 wt% corresponding to the solubility limit in UO_2 at the applicable sintering conditions [30]–[32].

Other effects of Cr_2O_3 additives in the UO_2 fuel pellets were reported: effect on heat capacity [23], fracture strength [33], pellet radial crack [34], corrosion resistance [35], grain size [36], and rigidity [24].

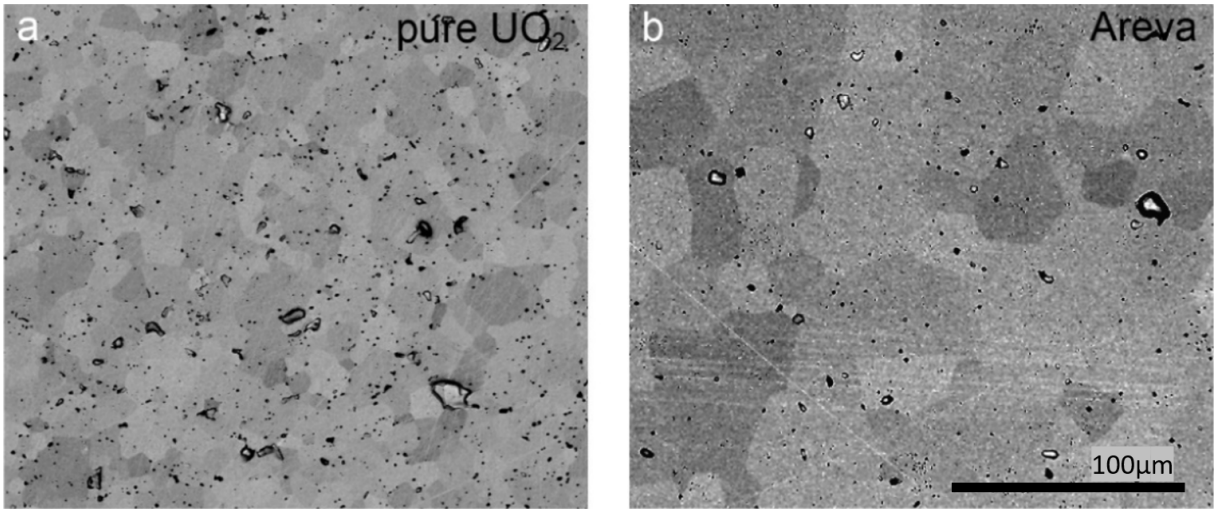

Figure I-5 BSE images of sintered pellets. a) pure UO_2 sintered at 1700°C and oxygen potential -420kJ/mol for 10h; b) Cr-doped UO_2 sample, sintering conditions unknown [36]. The two photos are at the same scale.

The more recent studies of the Cr_2O_3 doping in UO_2 will be discussed in detail in Chapter V.

I.2.3 The motivation for the present Ph.D. work

To increase reactor safety margins in the future, numerous fuel concepts are currently under development in the frame of accident-tolerant fuel systems (or ATF). The strategy implemented by designers aims, in an accident situation, to provide fuel that is better at 'retaining' fission products than the uranium dioxide (UO_2) currently used, and a cladding material that is more resistant to oxidation in environments rich in steam at temperatures at least below 1200°C. Under severe accident conditions, these improvements should likely lead, at least in the first times of the accident sequence, to a reduction in the heat generated by the cladding oxidation reaction and a corresponding reduction in the amount of hydrogen produced. Even if these new fuel concepts are expected to significantly slow down the oxidation kinetics, the long-term absence of core cooling will lead to a core meltdown. At this stage, there is very little experimental data to characterize the behavior of these new so-called ATF materials in severe accident conditions and their impact on accident progression. The assessment of the behavior of such materials is planned to be performed with the ASTEC system code used at IRSN for nuclear reactor safety evaluations. One of the objectives of the thesis is to characterize the melting margins of these “new” materials and in particular of the cladding which is the first containment barrier regarding the fission product release. The option currently being studied in France in the short term would be a UO_2 type fuel (possibly doped or not with chromium oxide) with a zirconium alloy cladding (M5 type) covered with a chromium coating.

In this framework, the thesis aims to establish the high-temperature phase equilibria in the Zr-Cr and Zr-Cr-O systems, and U-Cr and U-Cr-O on the one hand. Equilibrium data about mutual solubilities, and invariant reactions (eutectic points, eutectoid points…) are essential for further CALPHAD modeling. Thermodynamic data like enthalpy of formation or heat capacity would be useful to establish a description of the Gibbs energy of phases. Predictable experimental difficulties are to prevent oxidation of samples/avoid significant vaporization of Cr or Cr_2O_3 after high-temperature annealing; a challenge will be also to elaborate the binary and ternary stoichiometric phases, that will require adequate preparing methods and proper annealing durations/temperatures.

Once these data have been established, they will be considered in conjunction with past publications to perform CALPHAD modeling which will be integrated into the NUCLEA thermodynamic database. They will finally provide the initial elements needed to define the failure criteria for ATF fuel elements in the ASTEC simulations.

I.3 Objective and methodology of the study

The state of the art on the thermodynamics of these systems will show that they have been little studied (except Zr-Cr). For the Zr-Cr binary phase diagram, for which an intermetallic compound $ZrCr_2$ exists, numerous studies are available, but they often disagree, particularly on liquidus temperatures. The experimental data available on the Zr-Cr-O ternary system in the metal-oxide part are much more limited. Only Rhee and Hoch [37] presented three experimental isothermal cross sections at 1200°C, 1500°C and 1700°C with the existence of a ternary compound of stoichiometry Zr_3Cr_3O for which no thermodynamic data are available. The U-Cr binary system has no intermetallic compounds. It is characterized by a eutectic at 870°C with a composition close to U-19Cr (in % at.). In the ternary system, three ternary compounds $UCrO_4$, UCr_2O_6 and CrU_3O_{10-x} were identified. Concerning chromium solubility in uranium oxides, only that in UO_2 is reported, of the order of 0.1% wt.%. For the U-Cr-O ternary system, we have only the isothermal section at 1273 K reported by Yamanaka *et al.* [38], which does not mention the presence of ternary compounds and which is probably incorrectly represented, given the known existence of these compounds. The objective of the work planned in this thesis will be to reduce the experimental uncertainties on the Zr-Cr-O and U-Cr-O systems in terms of phase equilibria at high temperatures as well as thermodynamic data and to fill the identified lacks. This can be divided into the following tasks:

1. For the Zr-Cr binary phase diagram, the experiments will aim to measure the eutectic temperature and eutectic composition, as well as the liquidus temperatures in the zirconium-rich zone. For the Zr-Cr-O ternary phase diagram, the first task will be to confirm the sections established by Rhee and Hoch and establish the solubility of oxygen in liquid Zr-Cr alloys (if possible).
2. For the systems U-Cr and U-Cr-O, the work aims to review literature results and to make a preliminary study of the complex system U-Cr-O.
3. An important part of this work will be also devoted to the determination of thermodynamic data of the compounds identified in the different systems like the $ZrCr_2$ polymorphs, $Zr_3Cr_3O_x$ and $UCrO_4$. An important part of this work will consist of elaborating on the purest samples possible, identifying stable polymorphs in the Zr-Cr system, and determining lattice parameters, atom positions and possible solubility domains. After that, measurements of thermodynamic properties will be applied to these prepared pure samples: enthalpy of formation $\Delta_f H$ at room temperature and specific heat capacity C_p in a temperature interval

as large as possible by coupling a semi-adiabatic method (from 1.8K-300K) and relaxation method (from 298K-1063K).

4. The CALPHAD modeling for the systems Zr-Cr, U-Cr and ternary system Zr-Cr-O will be performed using Thermo-calc software. The modeling of Zr-Cr and U-Cr systems is supposed to be realized with experimental data obtained in this work as well as past experimental experiments. The Zr-Cr-O system will involve the Zr-O and Cr-O systems already modelled in the NUCLEA database. DFT calculations will be also accomplished for 2 main purposes: a) as validation support of the structural data and enthalpy of formation obtained in this work, and comparing with the simulation results in literature; b) to obtain reference values & initial values for the CALPHAD modeling, for some compounds for which experimental data are too difficult or impossible to collect, e.g. enthalpy of formation of metastable end-members of Laves phases in Zr-Cr binary system.

I.4 Reference

[1] T. Murakami, 'A historical review and analysis on the selection of nuclear reactor types and implications to development programs for advanced reactors; A Japanese study', *Energy Reports*, vol. 7, pp. 3428–3436, Nov. 2021, doi: 10.1016/j.egyr.2021.05.049.

[2] B. R. Sehgal, 'Perspectives on LWR severe accidents and public risks', *Nuclear Engineering and Design*, vol. 354, p. 110253, Dec. 2019, doi: 10.1016/j.nucengdes.2019.110253.

[3] B. R. Sehgal, 'Light Water Reactor Safety', in *Nuclear Safety in Light Water Reactors*, Elsevier, 2012, pp. 1–88. doi: 10.1016/B978-0-12-388446-6.00001-0.

[4] Tokyo Electric Power Company, 'Fukushima Nuclear Accident Analysis Report', Tokyo Electric Power Company, Jun. 2012.

[5] 'Fukushima-related measurements by the CTBTO', *CTBTO*. https://www.ctbto.org/news-and-events/news/fukushima-related-measurements-ctbto

[6] S. J. Zinkle and G. S. Was, 'Materials challenges in nuclear energy', *Acta Materialia*, vol. 61, no. 3, pp. 735–758, Feb. 2013, doi: 10.1016/j.actamat.2012.11.004.

[7] M. Barrachin, 'Corium Experimental Thermodynamics: A Review and Some Perspectives', *Thermo*, vol. 1, no. 2, pp. 179–204, Aug. 2021, doi: 10.3390/thermo1020013.

[8] Mignanelli, M.-A., Mason, P.-K., and Turland, B.-D, 'Melt Stratification for In-Vessel and Ex-Vessel Events', Commission of the European Communities, Luxembourg, Final Summary Report STRATIEX(00)-P008, 2000.

[9] P. Hofmann, 'Current knowledge on core degradation phenomena, a review', *Journal of Nuclear Materials*, vol. 270, no. 1–2, pp. 194–211, Apr. 1999, doi: 10.1016/S0022-3115(98)00899-X.

[10] E. Fischer, 'NUCLEA Thermodynamic Database for Corium, and Mephista Thermodynamic Database for Fuel Applications'. Institut de Radioprotection et Sûreté Nucléaire, St Paul lez Durance, France, 2021.

[11] K. A. Terrani, 'Accident tolerant fuel cladding development: Promise, status, and challenges', *Journal of Nuclear Materials*, vol. 501, pp. 13–30, Apr. 2018, doi: 10.1016/j.jnucmat.2017.12.043.

[12] J. Yang *et al.*, 'Review on chromium coated zirconium alloy accident tolerant fuel cladding', *Journal of Alloys and Compounds*, vol. 895, p. 162450, Feb. 2022, doi: 10.1016/j.jallcom.2021.162450.
[13] E. Kashkarov, B. Afornu, D. Sidelev, M. Krinitcyn, V. Gouws, and A. Lider, 'Recent Advances in Protective Coatings for Accident Tolerant Zr-Based Fuel Claddings', *Coatings*, vol. 11, no. 5, p. 557, May 2021, doi: 10.3390/coatings11050557.
[14] C. Tang, M. Stueber, H. J. Seifert, and M. Steinbrueck, 'Protective coatings on zirconium-based alloys as accident-tolerant fuel (ATF) claddings', *Corrosion Reviews*, vol. 35, no. 3, pp. 141–165, Aug. 2017, doi: 10.1515/corrrev-2017-0010.
[15] J. Bischoff *et al.*, 'AREVA NP's enhanced accident-tolerant fuel developments: Focus on Cr-coated M5 cladding', *Nuclear Engineering and Technology*, vol. 50, no. 2, pp. 223–228, Mar. 2018, doi: 10.1016/j.net.2017.12.004.
[16] Framatome, 'Framatome, EDF sign agreement to test Protect enhanced accident tolerant fuel in French reactor'. https://www.framatome.com/medias/framatome-and-edf-sign-agreement-to-test-protect-enhanced-accident-tolerant-fuel-in-french-reactor/?lang=en
[17] J.-C. Brachet *et al.*, 'Early studies on Cr-Coated Zircaloy-4 as enhanced accident tolerant nuclear fuel claddings for light water reactors', *Journal of Nuclear Materials*, vol. 517, pp. 268–285, Apr. 2019, doi: 10.1016/j.jnucmat.2019.02.018.
[18] M. Steinbrück, N. Vér, and M. Große, 'Oxidation of Advanced Zirconium Cladding Alloys in Steam at Temperatures in the Range of 600–1200 °C', *Oxid Met*, vol. 76, no. 3–4, pp. 215–232, Oct. 2011, doi: 10.1007/s11085-011-9249-3.
[19] H.-G. Kim, I.-H. Kim, Y.-I. Jung, D.-J. Park, J.-Y. Park, and Y.-H. Koo, 'Adhesion property and high-temperature oxidation behavior of Cr-coated Zircaloy-4 cladding tube prepared by 3D laser coating', *Journal of Nuclear Materials*, vol. 465, pp. 531–539, Oct. 2015, doi: 10.1016/j.jnucmat.2015.06.030.
[20] F. Qi *et al.*, 'Pellet-cladding mechanical interaction analysis of Cr-coated Zircaloy cladding', *Nuclear Engineering and Design*, vol. 367, p. 110792, Oct. 2020, doi: 10.1016/j.nucengdes.2020.110792.
[21] D. Arias and J. P. Abriata, 'The Cr−Zr (Chromium-Zirconium) system', *Bulletin of Alloy Phase Diagrams*, vol. 7, no. 3, pp. 237–244, Jun. 1986, doi: 10.1007/BF02868997.
[22] R. V. Umretiya, B. Elward, D. Lee, M. Anderson, R. B. Rebak, and J. V. Rojas, 'Mechanical and chemical properties of PVD and cold spray Cr-coatings on Zircaloy-4', *Journal of Nuclear Materials*, vol. 541, p. 152420, Dec. 2020, doi: 10.1016/j.jnucmat.2020.152420.
[23] J. Arborelius *et al.*, 'Advanced Doped UO_2 Pellets in LWR Applications', *Journal of Nuclear Science and Technology*, vol. 43, no. 9, pp. 967–976, Sep. 2006, doi: 10.1080/18811248.2006.9711184.
[24] J. C. Killeen, 'Fission gas release and swelling in UO_2 doped with Cr_2O_3', *Journal of Nuclear Materials*, vol. 88, no. 2–3, pp. 177–184, Feb. 1980, doi: 10.1016/0022-3115(80)90272-X.
[25] L. Bourgeois, Ph. Dehaudt, C. Lemaignan, and A. Hammou, 'Factors governing microstructure development of Cr_2O_3-doped UO_2 during sintering', *Journal of Nuclear Materials*, vol. 297, no. 3, pp. 313–326, Sep. 2001, doi: 10.1016/S0022-3115(01)00626-2.
[26] H. Assmann, W. Dörr, G. Gradel, G. Maier, and M. Peehs, 'Doping UO_2 with niobia — Beneficial or not?', *Journal of Nuclear Materials*, vol. 98, no. 1–2, pp. 216–220, May 1981, doi: 10.1016/0022-3115(81)90401-3.
[27] T. Fujino, T. Shiratori, N. Sato, K. Fukuda, K. Yamada, and H. Serizawa, 'Post-irradiation examination of high burnup Mg doped UO_2 in comparison with undoped UO_2, Mg–Nb

doped UO_2 and Ti doped UO_2', *Journal of Nuclear Materials*, vol. 297, no. 2, pp. 176–205, Aug. 2001, doi: 10.1016/S0022-3115(01)00609-2.

[28] J. B. Ainscough, F. Rigby, and S. C. Osborn, 'The effect of titania on grain growth and densification of sintered UO_2', *Journal of Nuclear Materials*, vol. 52, no. 2, pp. 191–203, Oct. 1974, doi: 10.1016/0022-3115(74)90167-6.

[29] M. H. A. Piro *et al.*, 'Pellet-Clad Interaction Behavior in Zirconium Alloy Fuel Cladding', in *Comprehensive Nuclear Materials*, Elsevier, 2020, pp. 248–306. doi: 10.1016/B978-0-12-803581-8.09799-X.

[30] Ch. Riglet-Martial *et al.*, 'Thermodynamics of chromium in UO_2 fuel: A solubility model', *Journal of Nuclear Materials*, vol. 447, no. 1–3, pp. 63–72, Apr. 2014, doi: 10.1016/j.jnucmat.2013.12.021.

[31] T. Cardinaels *et al.*, 'Chromia doped UO_2 fuel: Investigation of the lattice parameter', *Journal of Nuclear Materials*, vol. 424, no. 1–3, pp. 252–260, May 2012, doi: 10.1016/j.jnucmat.2012.02.025.

[32] A. Leenaers, L. de Tollenaere, C. Delafoy, and S. Van den Berghe, 'On the solubility of chromium sesquioxide in uranium dioxide fuel', *Journal of Nuclear Materials*, vol. 317, no. 1, pp. 62–68, Apr. 2003, doi: 10.1016/S0022-3115(02)01693-8.

[33] M. Oguma, 'Microstructure Effects on Fracture Strength of UO_2 Fuel Pellets', *Journal of Nuclear Science and Technology*, vol. 19, no. 12, pp. 1005–1014, Dec. 1982, doi: 10.1080/18811248.1982.9734249.

[34] C. Delafoy and P. Dewes, 'AREVA NP's new UO_2 fuel development and qualification for LWRs applications', Top fuel 2006 International Meeting, Salamanca, Spain, Nucler fuel:Addressing the future, Oct. 2006.

[35] K. Backman, L. Hallstadius, and G. Roennberg, 'Westinghouse Advanced Doped Pellet - Characteristics and Irradiation Behaviour', International Atomic Energy Agency (IAEA), 1011–4289, 2010. [Online]. Available: http://inis.iaea.org/search/search.aspx?orig_q=RN:42094971

[36] P. Kegler *et al.*, 'Chromium Doped UO_2-Based Ceramics: Synthesis and Characterization of Model Materials for Modern Nuclear Fuels', *Materials*, vol. 14, no. 20, p. 6160, Oct. 2021, doi: 10.3390/ma14206160.

[37] S. K. Rhee and M. Hoch, 'The system chromium-zirconium-oxygen at 1200, 1500, and 1700°C', *Trans. AIME*, vol. 230, no. 7, pp. 1687–1690, Dec. 1964.

[38] S. Yamanaka, J. Shimizu, and M. Miyake, 'Thermodynamic study of the compatibility of oxide fuel with metals', *Journal of Nuclear Materials*, vol. 201, pp. 27–34, May 1993, doi: 10.1016/0022-3115(93)90156-S.

Chapter II

Experimental techniques and calculation/modeling methods

Chapter II. Experimental techniques and calculation/modeling methods

II.1 Samples elaboration: synthesis and thermal treatment

II.1.1 Raw materials and main procedures

The raw materials used for the preparation of the samples in the different chemical systems are listed in Table II-1. Zr-Cr samples were synthesized from Zr sponge of van Arkel grade and chromium chunks. Zr-Cr-O ternary samples were made from Zr sponges, Cr chunks, ZrO_2 powder and Cr_2O_3 chunks. U-Cr-O ternary samples were synthesized from natural U shavings, Cr chunks, Cr_2O_3 chunks and U_3O_8 powder.

Table II-1 Raw materials and purities

Material	Supplier	Form	Purity / wt.%	Lot	Purity Check
Zr	Lab stock	Sponge	>99.99		
Cr	Alpha Aesar	Granules -4+7 mesh	>99.999	N08F024	O<222 ppm* N<22 ppm S<11 ppm
Al	Alfa Aesar	Rods	99.95	N27E009	99.99*
ZrO_2	Fisher Scientific	Nano-powder	>99%	1602443	
Cr_2O_3	Alfa Aesar	3-6mm Fused lump	99.60%	M14F020	K<132 ppm Ca<96 ppm Na<46 ppm
U	Lab stock	Shavings			
U_3O_8	Lab stock	Powder			
W	Plansee	Sheet	>99.97	0093913374	Fe<30µg/g; Mo<100 µg/g
Ar	Air Liquide	Gas	≥ 99.9999 (vol.)	231-147-0(EC)	ALPHAGAZ 2* CO_2 < 100 PPB; CO < 100 PPB; Total CnHm< 100 PPB; O_2 < 100 PPB; H_2O < 500 PPB; H_2 < 100 PPB

* According to the lot chemical analysis, the supplier's data

Three different procedures were applied for the preparation of the samples:

1) By melting the raw materials in an arc furnace under argon and then annealing the resulting ingots in a resistance furnace up to 1700°C.
2) By grinding the raw materials in an agate mortar. A pellet is then prepared from the powder mixture in an 8 mm die under a press and annealed in a resistance furnace.
3) By combining 1) and 2). In the two ternary systems, Zr-Cr-O and U-Cr-O, a combined procedure was used to obtain a homogeneous mixing of metal and oxide materials. The procedure begins by grinding and mixing the oxides in an agate mortar and preparing a pellet. The pellet and weighed metals are melted together in an arc furnace. The ingot is crushed and mixed again in the agate mortar to improve its homogeneity. A new pellet is prepared with the resulting powder and annealed in a resistance furnace. This procedure avoids the potential risk of a significant loss of mass due to the dispersion of the powders in the arc furnace and ensures that the samples are as homogeneous as possible.

II.1.2 Arc melting furnace and resistance annealing furnace

The arc melting furnace used is an Edmund Bühler GmbH MAM-1 model, equipped with a water-cooled copper hearth put under a high-purity argon atmosphere (Table II-1). The arc furnace is designed for the rapid melting of samples from up to 20 g and 3500°C. It is ideally suited to melting samples of 300-500 mg, the typical masses adopted for our samples. With such masses, it is possible to carry out characterizations with several techniques while maintaining good homogeneity.

Before melting, the raw materials are carefully weighed using a balance with an accuracy of ± 10^{-3} g accuracy and then placed in the crucible cavity of the copper hearth.

In our experience, up to 3 samples can be prepared simultaneously in the same sequence. A Ti-Zr bead with a mass of around 500 mg is settled beside acting as an oxygen getter. After reinstalling the copper hearth and tightening the fixing screws. The air in the furnace chamber is evacuated by a high vacuum pump for 5 minutes and then the chamber is filled with high-purity Argon. This procedure is repeated 3 times (Table II-1). The final argon pressure is adjusted to 0.7-0.8 bar to ensure a tight seal in the furnace chamber. Once the furnace's electric power is switched on, an arc is created between the electrode and the copper hearth. The

position of the electrode tip can be controlled manually using the handle at the top of the furnace. The power of the arc can be controlled by a potentiometer.

The Ti-Zr bead is melted first to consume the amount of residual oxygen in the chamber before the raw materials are melted. During the elaboration process, the raw materials are completely melted by the arc in a few seconds and take on a spherical shape due to the surface tension. After the cut off of the arc, the molten liquid sphere cools and solidifies within 2 to 3 seconds due to heat exchange with the water-cooled copper hearth of the furnace. This cooling can be considered as quenching.

The chamber is then backfilled with Ar to atmospheric pressure and disassembled. The samples are turned over for the next melting operation to ensure their microstructural homogeneity. The whole procedure is repeated at least 3 times for a given sample. Once the operation is complete, the masses of these samples are carefully reweighed to assess the potential mass loss. The mass loss is typically 1-3 mg, as about 0.33% by weight of the samples, often due to the vaporization of Cr.

A cylindrical Eraly resistance furnace, installed in a horizontal position and having a maximum temperature of 1200°C, is used for low-temperature annealing (T < 1000°C). The temperature is controlled with an Eraly West Pro 16 regulator. The main body of the furnace is a quartz heating tube wrapped in resistance coils and heat isolation materials. For short annealing, the samples are placed in alumina or tantalum crucibles, which are moved through the quartz tube using an alumina boat. As required, the tube is flushed with high-purity Ar (Table II-1) to achieve an oxygen-free environment or by a stream of air to maintain oxidizing conditions. The gas flow rate is set in the range of 3-6 L/h. The furnace is not equipped with a cooling system. In most cases, the annealed samples are therefore cooled by conduction and natural convection, which can take from 4 to 6 hours.

When long-term annealing (> 7 days) is required, the samples are first wrapped in W-foil (Table II-1) and then sealed in a quartz tube under Ar. The quartz tube is then placed in a similar Eraly furnace, but installed vertically. This vertical position allows the samples sealed in the quartz tubes to be quenched in cold water at the end of the annealing process

High-temperature annealing (>1000°C) is performed using a Nabertherm, RHTH 120/150/18 resistance furnace. This furnace equipped with a digital temperature controller can heat up to 1700°C with a maximum heating rate of 5°C/min. The furnace muffle is an alumina tube with a gas inlet and outlet water-cooled flanges through which a high purity argon flow (Table II-1)

of 200 L/h is maintained to ensure an inert atmosphere during annealing. The samples are placed in tantalum crucibles with a graphitized surface, which is then placed in an alumina boat and the whole assembly is positioned in the alumina muffle tube of the furnace.

Depending on the annealing target temperatures, heating can take from 3 to 6 hours. Once reached, the annealing temperature is maintained for a period varying between 10 minutes and 48 hours. Samples cannot be quenched with this furnace and the natural cooling of the sample inside the furnace after annealing usually takes between 6 and 10 hours depending on the annealing temperature reached.

Samples are carefully weighed before and after annealing. On some occasions, thin oxidation layers were found on the surface of annealed samples, however, no significant mass change was detected and no significant oxidation was found in subsequent SEM and XRD studies.

II.1.3 Preparation of pellets

The preparation of pellets is used for two main purposes in this study.

1) In the preparation of ternary samples, arc melting of a mixture of several oxide powders, like ZrO_2, Cr_2O_3, or UO_2, is often needed. Mixing and then pelletizing the powders reduces the risk of dispersion of the powders during the arc melting operation and also favors the simultaneous melting of the different phases, oxides, or metals, present.
2) In the preparation of pure ternary compounds, such as Zr_3Cr_3O or $UCrO_4$, as-cast samples are crushed and ground to a fine powder and then pelletized. This protocol ensures mechanical homogenization of the sample and reduces its grain size before subsequent annealing. Compared to an as-cast sample, it is estimated that this mechanical homogenization step reduces the annealing time required by a factor of 10. This also has the benefit of limiting the risk of strong oxidation of the samples inherent in long annealing at high temperatures.

The pellets are prepared by filling an 8 mm die (Eurolab) made of high-strength steel with 200-500 mg of fully ground powder mixture. Two high-strength steel spacers having a mirror-like surface are used to clip the powder. The die is placed under a press that exerts a pressure of 2 to 4 bars on the plunger. The pellet should be pressed for at least 5 minutes and then carefully removed from the mold. Based on the pressure used during preparation, the compaction of the pellet is visually estimated to be about 50%.

II.2 Sample Analysis: XRD, SEM, EPMA

II.2.1 XRD

X-ray diffraction (XRD) is used for phase identification in almost all the samples in this study. The diffractometer is a Bruker D8 ADVANCE model equipped with a PSD (Position Sensitive Detector, Vantec 1 type), an Anton Parr HTK1200N chamber and a θ-θ Bragg-Brentano geometry in a θ–2θ configuration using filtered Cu Kα radiation ($\lambda = 1.5406$Å). The diffraction patterns are recorded at ambient temperature under high purity Ar. Typical values for the scan parameters are as follows: [25° - 85°] 2θ angle range, 0.02° step size and 0.5 s count time. Rietveld patterns are scanned with [15° - 125°] 2θ angle range, 0.01° step size and 1 s count time. The FullProf software suite [1] is used for the Rietveld refinement and the selected reference crystallographic data for the different phases are listed in Table II-2. Most of the CIF files were downloaded from the ICSD database, except the lattice parameters of the Zr_3Cr_3O compound which were refined in this study. In the fitting process, the acceptance criterion is $\chi^2 < 10$ which guarantees an uncertainty < 1% at. on the phase fractions. The definition of the χ^2 factor is given on page 42 of the pdf file of the Fullprof User's Guide [2].

Two different protocols were adopted to prepare the samples for the XRD experiments:

1) For non-radioactive samples, a glass sample holder is used. The samples are ground with an agate mortar and pestle under ethanol to a fine powder. After thorough mixing, the powder is placed on the sample holder with a plastic dropper and then naturally air-dried to vaporize the remaining ethanol.
2) For radioactive samples, a plastic sample holder (provided by Bruker, diameter ∅25mm) with coverage of Kapton film (thickness 7.5 μm, provided by Elemental Scientific Instruments France, code TF-475) is used. The sample undergoes a similar milling procedure. A glass disc with a frosted top surface is placed at the bottom of the sample holder. The mixture of powder and ethanol is homogeneously deposited on the glass disc using a dropper. Once the powder has dried and the ethanol has completely evaporated, the top surface of the powder bed is covered with a Kapton film to prevent the spread of radioactive material. A pre-test is performed to ensure that the film does not interfere with the measurement results.

Table II-2. Crystallographic data is used for phase identification in this work.

Structure Form	Structure Type	Space Group	Reference	Ref. ICSD
hcp-Zr	hcp#Mg	P 63/m m c	[3]	164572
bcc-Zr	bcc#W	I m -3 m	[4]	169452
bcc-Cr	bcc#W	I m -3 m	[5]	625717
$ZrCr_2$-C14	Laves(2H)#$MgZn_2$	P 63/m m c	[6]	100165
$ZrCr_2$-C15	Laves(cub)#$MgCu_2$	F d -3 m	[7]	102860
$ZrCr_2$-C36	Laves(4H)#$MgNi_2$	P 63/m m c	[8]	626949
Zr_3Cr_3O	$NiTi_2$	F d -3 m	This work	
ZrO_2 monoclinic	Baddeleyite	P 2_1/c	[9]	403483
ZrO_2 tetragonal	Fluorite#CaF_2	F m -3 m	[10]	36700
Zr_3O_{1-x}	FeF_3	R -3 c H	[11]	27023
Cr_2O_3	Corundum#Al_2O_3	R -3 c H	[12]	258428
UO_2	Fluorite#CaF_2	F m -3 m	[13]	35204
U_3O_8	U_3O_8	A m m 2	[14]	16559
U gamma	Bcc#W	I m -3 m	[15]	236070
U beta	Beta U	P 42/m n m	[16]	76490
U alpha	Alpha U	C m c m	[15]	236068
$UCrO_4$	$BiVO_4$	P b c n	[17]	15859
UCr_2O_6	Rosiaite#$PbSb_2O_6$	P -3 1 m	[18]	274

II.2.2 SEM

Almost all samples, except for a few low-compact pellets, were analyzed by SEM (Scanning Electron Microscopy) to confirm their overall composition, observe their microstructure and determine the compositions of the phases present.

Surface treatment of the samples before the metallographic examination is as follows. First, the samples are cut/ground into pieces. The selected pieces are then embedded in Epoxy or Bakelit resins.

The Epoxy resin is prepared according to the following protocol. The liquid resin and liquid hardener (both supplied by ESCIL, DBF/HY956) are mixed in a ratio of 4:1 and poured into

the mold (Ø 25mm or Ø 32mm) in which the samples have previously been suitably arranged. The mold is then placed under a fume hood for 24 hours to complete the curing of the resin.

The Bakelite resin requires a mounting press (Struers CitoPress-30) that can heat up to 150°C under 250 bar. The samples are embedded in a compacted powder charge of Bakelite (Struers, Polyfast phenolic hot mounting resin with carbon filler). About 20 mins are required for the heating and cooling cycle.

The pre-polish and polish procedures are performed using a Struers Tegramin-30 auto-polisher in automatic and/or manual mode as required. The surface of the sample is pre-polished with SiC abrasive papers (grades 320 to 4000 mesh) under water cooling. Before each change to a finer SiC paper, the surface is observed under the optical microscope to ensure that the polishing lines are uniform, indicating that polishing with the current SiC paper is complete.

Some tests are made with powder samples. The preparation is simple: carbon tape is used to paste a very small quantity (~1mg) of powder sample on a metallic bedding block. The powder should be well spread and compacted, to avoid potential splash of powder during vacuuming of the SEM chamber.

The final surface polishing is performed with diamond suspensions from 6 µm to ¼ µm (Struers DP-Suspension A). The embedded samples are cleaned after polishing in an ethanol ultrasonic bath for at least 20 minutes. Optical microscopy is used to check that no residue of the polishing suspension remains on the surface of the sample. Depending on the hardness of the samples, the polishing steps can last from 2h to 2h30 until a perfect mirror polish is obtained, suitable for SEM analysis.

Metallographic investigations are carried out on two Scanning Electron Microscopes (SEM): JEOL JSM-7800F LV or SEM Hitachi SU5000. The images are recorded in Secondary Electron (SE)/Back-Scattered Electron (BSE) modes and chemical composition is measured by Energy Dispersive X-ray Spectroscopy (EDS - Oxford Instruments SDD detector, AZTEC 80 mm² spectrometer) under high vacuum ($< 3 \times 10^{-3}$ mbar). The working distance is set between 3 and 10 mm. The accelerating voltage is set between 5 and 20 kV to improve topological or chemical contrast. The Hitachi microscope is also equipped with a symmetrical EBSD camera with a CMOS sensor operating at a working distance of 10 mm at an accelerating voltage of 20 kV.

To avoid the build-up of electronic charges during observation, particularly with epoxy resins, the surface of the resin pads is sputtered with carbon to maintain electrical conductivity. The resin pad is bonded to the metal sample holder with carbon tape for the same purpose.

II.2.3 EPMA

EPMA (Electron Probe Micro-Analysis) is carried out on a Cameca SX 100 instrument equipped with five Wavelength Dispersive Spectrometers (WDS). A probe current of 100 nA and an accelerating voltage of 10 kV are employed. The sample preparation procedure is the same as for SEM.

II.3 Thermal analysis and calorimetry

II.3.1 Step annealing method

Not having access to a thermal analyzer capable of reaching very high temperatures, a so-called step annealing method in a conventional furnace was used to measure eutectic and melting temperatures in this temperature range.

Square baskets of 10 mm square and 3 mm high were handcrafted using a high-purity W sheet (Table II-1). The samples were then placed in these baskets, which were then loaded together in an alumina boat. The W basket acts as a liner preventing chemical reactions between the samples and the alumina boat. Compared to the use of commercial W-crucibles, making W-baskets in the laboratory from W-sheets is considerably cheaper and allows for more experiments.

A schematic diagram of the step annealing method is shown in Figure II-1. The samples are subjected to a series of anneals at different temperatures starting with a rather low temperature and gradually increasing the annealing temperature by 10°C until the melting temperature. The shape of the samples is observed after annealing the cooled samples. When a sample is observed to have melted for the first time after reaching a certain temperature, its melting temperature is calculated by taking the average of this temperature (T) and the previous annealing temperature (T-10°C). The uncertainty in the measured value is estimated to be ±7°C.

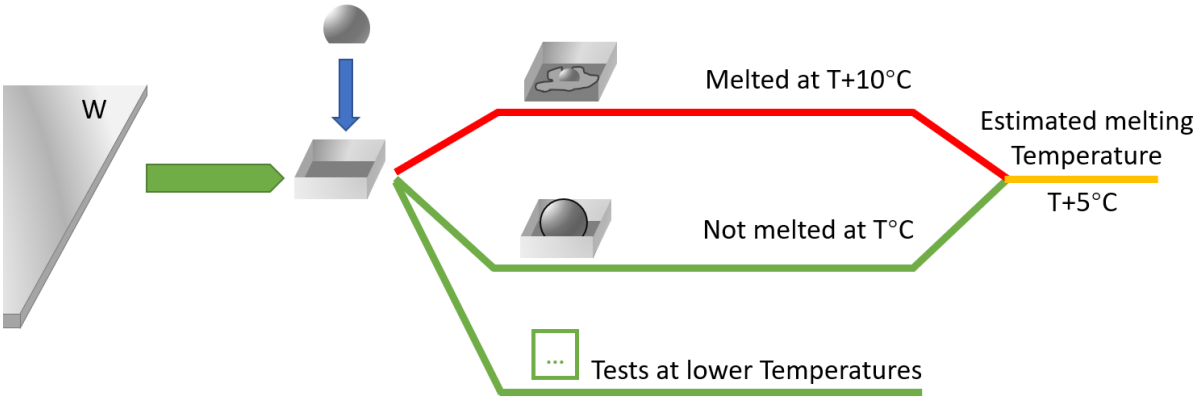

Figure II-1 Schematic view of the step annealing method

The melted samples are then examined by SEM and XRD.

II.3.2 Specific heat

PPMS (Physical Property Measurement System, GmbH Im Tiefen See 58 D-64293 Darmstadt of Quantum Design Company) is an instrument designed to measure the specific heat capacity, the magnetic susceptibility and the electrical/thermal transport properties in a fully automatic between 1.9 K and 400 K way under external magnetic field up to ±16 Tesla. In this work, PPMS was used to measure the heat capacity of $ZrCr_2$ C14/C15, Zr_3Cr_3O and $UCrO_4$ ternary phases from 1.9 K to room temperature.

For this measurement, the shape of the sample should be cubic with a side length of < 2 mm and a mass of around 10 mg. The bottom surface of the samples is pre-polished to ensure better thermal contact with the platform of the calorimetric sensor of the instrument. 40 measuring points are defined automatically with a denser distribution of measuring points at lower temperatures. The uncertainty of the measurements is estimated to be ± 5% from 2 to 300 K.

II.3.3 DTA/DSC

To determine the eutectic temperatures in the Zr-Cr system, DTA (Differential Thermal Analysis) was performed with a Linseis HDSC PT1600 instrument equipped with a type S (Pt/Rh) sensor. The masses of the samples were 300 mg. Before the measurements, each sample was annealed for 1 hour at 1000°C in a ZrO_2 crucible under an inert atmosphere. The sample in its ZrO_2 crucible was then placed on the sensor of the HDSC PT 1600. A piece of Zr-alloy

acting as an oxygen getter was also inserted in the gas inlet line. The chamber was evacuated and flushed with Helium 4.0 three times to ensure an oxygen-free atmosphere. A helium flow of 5 L/h is kept during the measurement. The heating rate is set at 5 K/min from ambient temperature to 1500°C.

A Differential Scanning Calorimeter (DSC), a DSC 111 instrument of the Setaram company, is used to measure the specific heat capacity above room temperature, from 300 K to 1063 K. Synthetic sapphire provided by the NBS-NIST [19] was used for heat flow calibration. Both the sample (Cr_2Zr C15 112.842 mg, Cr_2Zr C14 112.271 mg, Cr_3Zr_3O 275.84 mg) and calibration material (Al_2O_3 153.244 mg) were hermetically sealed in stainless steel crucibles in a glove box under argon. The measurements were performed using the so-called "step-scan" or "small temperature steps" method with the experimental protocol described in [20].

II.3.4 Isothermal calorimetry

The formation enthalpies of the $ZrCr_2$ Laves phases and the Zr_3Cr_3O ternary compound were measured by high-temperature drop-solution calorimetry. In this method, the formation enthalpy is calculated from the measurements of the drop-solution enthalpies of the elements and the compound in the solvent at infinite dilution.

As an example, for the $ZrCr_2$ Laves phase, $\Delta_{ds}\overline{H}_i^{\infty}$ with $i = Zr, Cr$ and $ZrCr_2$ are measured and the formation enthalpy is calculated according to Equation (II-1):

$$\Delta_f \boldsymbol{H}_{\boldsymbol{ZrCr_2}} = \Delta_{\boldsymbol{ds}}\overline{\boldsymbol{H}}_{\boldsymbol{Zr}}^{\boldsymbol{\infty}} + \mathbf{2}\Delta_{\boldsymbol{ds}}\overline{\boldsymbol{H}}_{\boldsymbol{Cr}}^{\boldsymbol{\infty}} - \Delta_{\boldsymbol{ds}}\overline{\boldsymbol{H}}_{\boldsymbol{ZrCr_2}}^{\boldsymbol{\infty}} \quad \text{(II-1)}$$

$\Delta_{ds}\overline{H}_{Zr}^{\infty}$ at 900°C was determined in previous studies [20] [21]. Hence, the present work was focused on the measurement of $\Delta_{ds}\overline{H}_{Cr}^{\infty}$, $\Delta_{ds}\overline{H}_{ZrCr_2}^{\infty}$ and $\Delta_{ds}\overline{H}_{Zr_3Cr_3O}^{\infty}$.

A Tian-Calvet high-temperature calorimeter is used at 900 ± 1°C. The solvent used is liquid aluminum (Alfa Aesar, 99.99 % see Table II-1). An alumina crucible is loaded with a typical mass of around 10 grams of Al. Then, this crucible is inserted in a vitreous silica tube with a piece of Ti having the shape of a tube section placed on top of the crucible and acting as an oxygen getter. The silica tube is connected to the sample distributor in a gas-tight way and the whole assembly is evacuated using a rotary pump and flushed three times with argon. At the beginning of an experiment, the silica tube containing the crucible and solvent is slowly introduced into the calorimeter and the Al load melts and heats up to the calorimeter temperature.

When thermal equilibrium is reached and a stable baseline is obtained, 4 aluminum pieces are successively dropped in the solvent for heat calibration. After this calibration step, 3 to 6 pieces of samples (of Cr, $ZrCr_2$, or Zr_3Cr_3O) are successively dropped. Between each drop, it is checked that the calorimetric signal returns to the baseline. During the whole experiment, which lasts around 10-12 hours, the analog calorimetric differential signal from the thermopiles is digitized by a Keithley 2182 Nanovoltmeter and recorded vs. time on a computer. Acquisition files are processed with a homemade Python program which allows performing numerical integration of the individual peaks after appropriate baseline subtraction. Masses of the crucible, solvent, Ti getter, calibration pieces and samples are all weighed with the precision balance having a ±0.02 mg uncertainty. At the end of an experiment and after cooling and solidification of the Al bath, the whole crucible assembly is visually inspected and weighed again. No trace of oxidation was observed as the bath surface has a bright metallic appearance and the mass balance is respected to within 0.1 mg. The mass gain of the Ti getter is a few tenths of mg.

The original data were recorded as scattered points of tension (μV), which can be transformed by a calibration procedure to the thermal flux (μW) as a function of time (s). The enthalpy of the drop solution was calculated with a Python program.

$$\Delta_{ds}\bar{H}_{298.1K}^{Texp} \times n = \int \phi dt = \int FU(t)dt \qquad \text{(II-2)}$$

where $\Delta_{ds}\bar{H}_{298.1K}^{Texp}$ is the enthalpy of the partial drop solution, n is the number of moles in the sample, ϕ is the thermal flux after subtraction of the interpolated baseline, t is the time, F is the calibration factor of the calorimeter and U is the measured voltage at the terminals of the differential flux meter.

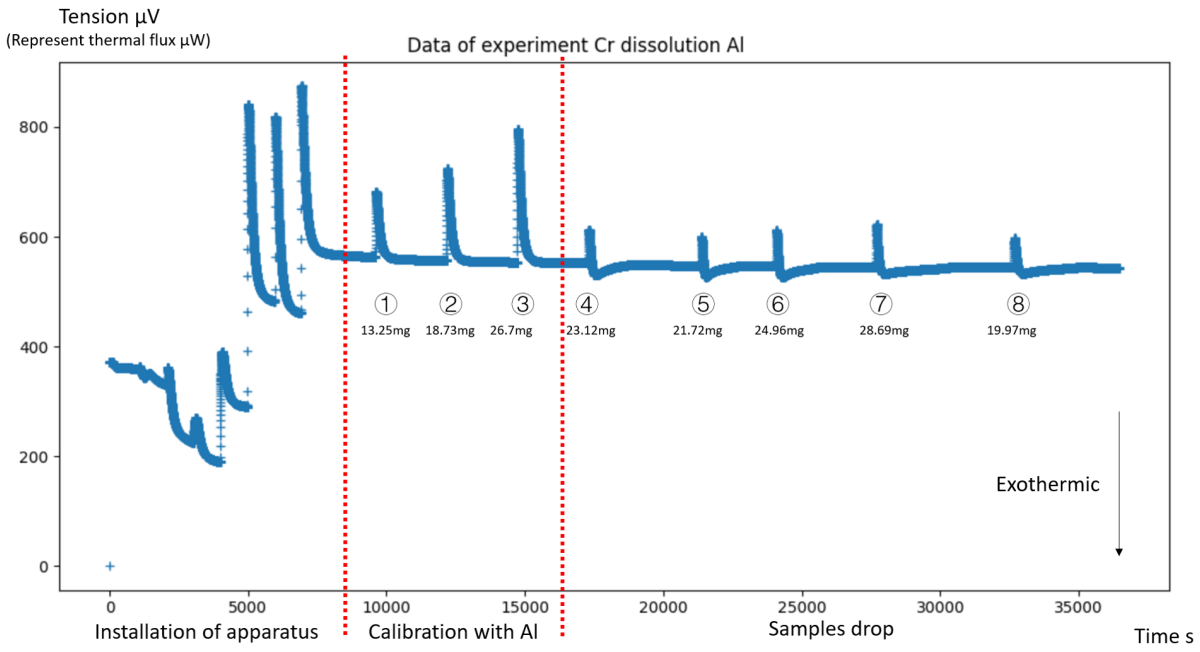

Figure II-2 Data of a drop solution experiment of Al (for calibration) and Cr chunks in solvent Al at 900°C

In Figure II-2, the data of a drop solution experiment is presented. The data is recorded since the beginning of the experiment (insertion of the silica tube into the calorimeter). The first 3 drops of pure Al chunks in Al solvent show endothermic peaks, that correspond to the heat increment of these chunks. The integrated enthalpy values are used to calibrate the sensitivity factor F of the calorimeter with their mass, following Equation (II-3).

$$\boldsymbol{F = \frac{\phi}{U} = \frac{\frac{m}{M}\int C_p dT}{\int U dt}} \qquad \text{(II-3)}$$

where m is the mass of Al chunk, M is the atomic mass of Al, C_p is the heat capacity of Al, U is the tension measured and T, t represent the temperature and time, respectively.

The calibration factor F in this study is around 1000 W/V.

Calorimetric peak areas were calculated using the Simpson integration method.

The ingots are cut longitudinally and, after polishing the surface, are observed by SEM to check the complete dissolution of the samples.

II.4 DFT calculations

The $ZrCr_2$ and Zr_3Cr_3O stoichiometric compounds were investigated by both calorimetry and DFT calculations. We had three main motivations for performing such calculations in addition to the experiments:

1) To determine the enthalpy of phase transitions between the various structures of the $ZrCr_2$ compound.
2) To fill the gap in data on metastable end-members in the Zr-Cr system that cannot be obtained experimentally and which are useful for the CALPHAD modeling.
3) To support our experimental calorimetry investigations for these two compounds.

II.4.1 General presentation on the DFT method

In our work, electronic structure calculations were performed using the DFT (Density Functional Theory) implemented in the VASP (Vienna Ab initio Simulation Package) software [23].

A DFT calculation consists of solving the Schrödinger equation given below:

$$\widehat{\boldsymbol{H}}\boldsymbol{\Psi} = \boldsymbol{E}\boldsymbol{\Psi} \tag{II-4}$$

where $\widehat{H}$ is the Hamiltonian operator, Ψ, the wave function of the system and E, the total energy of the system. In the case of a solid constituted by P electrons and Q nuclei, that has a mass M and a charge Z, we have for a non-relativistic Hamiltonian operator, the following expression:

$$\widehat{\boldsymbol{H}} = \widehat{\boldsymbol{T}}_{\boldsymbol{n}} + \widehat{\boldsymbol{T}}_{\boldsymbol{e}} + \widehat{\boldsymbol{V}}_{\boldsymbol{ee}} + \widehat{\boldsymbol{V}}_{\boldsymbol{nn}} + \widehat{\boldsymbol{V}}_{\boldsymbol{ne}} \tag{II-5}$$

where:

Physical quantity	Operator (atomic unit)
Kinetic energy of nuclei (*n*)	$\hat{T}_n = -\frac{1}{2M}\sum_{\alpha=1}^{Q}\nabla_\alpha^2$
Kinetic energy of electrons (*e*)	$\hat{T}_e = -\frac{1}{2}\sum_{i=1}^{P}\nabla_i^2$
Coulomb potential energy *n-n*	$\hat{V}_{nn} = \sum_{\alpha<\beta}^{Q}\frac{Z_\alpha Z_\beta}{\lvert\vec{R}_\alpha - \vec{R}_\beta\rvert}$

Physical quantity	Operator (atomic unit)
Coulomb potential energy *e-e*	$\hat{V}_{ee} = \sum_{i<j}^{P} \frac{1}{\left\|\vec{r}_i - \vec{r}_j\right\|}$
Coulomb potential energy *n-e*	$\hat{V}_{ne} = -\sum_{\alpha=1}^{Q} \sum_{i=1}^{P} \frac{Z_\alpha}{\left\|\vec{r}_i - \vec{R}_\beta\right\|}$

It is possible to find a solution to this equation for a simple system such as a hydrogen atom. However, this is not the case in the more complex situation where P electrons are interacting.

In many methods, the Hartree-Fock approximation is considered a starting point. The DFT is another way to proceed. It consists in determining the total energy of the system from the electron density. Even if this theory is exact from the point of view of the quantum physics principles, some approximations are required in the calculation.

II.4.2 Born-Oppenheimer approximation

The mass of the electron is considerably smaller than the masses of the nuclei. Nuclei can be then considered to be fixed compared to the much more mobile electrons. The Born-Oppenheimer approximation consists of decoupling the dynamics of nuclei and electrons. In this way, the $\hat{V}_{nn}$ term becomes a constant in the Hamiltonian, which can be written as:

$$\boldsymbol{\hat{H} = \hat{H}_{elec} + V_{nn}} \tag{II-6}$$

where V_{nn} is an additional constant.

In accepting the approximation, the wave function can be written as a product of an electronic wave function $\Psi_{elec}(\{\vec{r}\}, \{\vec{R}\})$ and a nuclear wave function $\Psi_{nucl}(\{\vec{R}\})$:

$$\boldsymbol{\Psi = \Psi_{nucl}(\{\vec{R}\}) \otimes \Psi_{elec}(\{\vec{r}\}, \{\vec{R}\})} \tag{II-7}$$

where $\{\vec{R}\}$ and $\{\vec{r}\}$ represent the position vectors of nuclei and electrons respectively.

In the same way, the total energy of the system can be written as a sum of the contributions of the nuclei and the electrons:

$$\boldsymbol{E = E_{nucl}(\{\vec{R}\}) + E_{elec}(\{\vec{R}\})} \tag{II-8}$$

The problem is therefore reduced to solving the Schrödinger equation with fixed nuclei and position vectors $\{\vec{R}\}$:

$$\widehat{\boldsymbol{H}}_{\boldsymbol{elec}}\boldsymbol{\Psi}_{\boldsymbol{elec}}\left(\{\vec{\boldsymbol{r}}\},\{\vec{\boldsymbol{R}}\}\right)=\boldsymbol{E}_{\boldsymbol{elec}}\{\vec{\boldsymbol{R}}\}\boldsymbol{\Psi}_{\boldsymbol{elec}}\left(\{\vec{\boldsymbol{r}}\},\{\vec{\boldsymbol{R}}\}\right) \quad \text{(II-9)}$$

where $\widehat{H}_{elec}$ is written as:

$$\widehat{\boldsymbol{H}}_{\boldsymbol{elec}}=\widehat{\boldsymbol{T}}_{\boldsymbol{e}}+\widehat{\boldsymbol{V}}_{\boldsymbol{ee}}+\widehat{\boldsymbol{V}}_{\boldsymbol{ne}}$$
$$=-\frac{\boldsymbol{1}}{\boldsymbol{2}}\sum_{\boldsymbol{i=1}}^{\boldsymbol{P}}\boldsymbol{\nabla}_{\boldsymbol{i}}^{\boldsymbol{2}}+\sum_{\boldsymbol{i<j}}^{\boldsymbol{P}}\frac{\boldsymbol{1}}{\left|\vec{\boldsymbol{r}}_{\boldsymbol{i}}-\vec{\boldsymbol{r}}_{\boldsymbol{j}}\right|}-\sum_{\boldsymbol{\alpha=1}}^{\boldsymbol{Q}}\sum_{\boldsymbol{i=1}}^{\boldsymbol{P}}\frac{\boldsymbol{Z}_{\boldsymbol{\alpha}}}{\left|\vec{\boldsymbol{r}}_{\boldsymbol{i}}-\vec{\boldsymbol{R}}_{\boldsymbol{\beta}}\right|} \quad \text{(II-10)}$$

with the same symbols as in section 3). These same symbols and notations will always be kept in the following.

The DFT method allows us to describe the system only based on its electron density ρ(x,y,z). Thus, it is not necessary to solve a system with 3P variables, but only to determine the electron density which is a function of only 3 variables.

II.4.3 From wave function to electronic density

II.4.3.1 Hohenberg-Kohn Theorem

The DFT method allows to write the total electronic energy of a system as a functional of the electronic density. The relation between the electronic density $\rho(\vec{r})$ and the wave function $\Psi_{elec}(\vec{r},\overrightarrow{r_2},\dots,\overrightarrow{r_P})$ is the following:

$$\boldsymbol{\rho}(\vec{\boldsymbol{r}})=\boldsymbol{P}\int|\boldsymbol{\Psi}_{\boldsymbol{elec}}(\vec{\boldsymbol{r}},\overrightarrow{\boldsymbol{r_2}},\dots,\overrightarrow{\boldsymbol{r_P}})|^{\boldsymbol{2}}\boldsymbol{d}\overrightarrow{\boldsymbol{r_2}}\dots\boldsymbol{d}\overrightarrow{\boldsymbol{r_P}} \quad \text{(II-11)}$$

The DFT was found empirically by [24], [25], and proven by [26] to be an exact theory that is based on the two following theorems.

Theorem 1 (potential-density uniqueness): For any system of interacting particles, subject to an external potential $V_{ext}(\vec{r})$, this potential is uniquely determined (and thus the Hamiltonian as well), to be within one additive constant, by the electronic density of the system in its ground state ρ_0. Thus, all properties of the system can be expressed from the knowledge of the density ρ_0.

Theorem 2 (variational principle): The total energy E is a unique functional of the electronic density $\rho(\vec{r})$ for a given external potential V_{ext}, as:

$$\boldsymbol{E}[\boldsymbol{\rho}(\vec{\boldsymbol{r}})]=\boldsymbol{T}[\boldsymbol{\rho}(\vec{\boldsymbol{r}})]+\boldsymbol{E}_{\boldsymbol{ee}}[\boldsymbol{\rho}(\vec{\boldsymbol{r}})]+\boldsymbol{V}_{\boldsymbol{ext}}[\boldsymbol{\rho}(\vec{\boldsymbol{r}})] \quad \text{(II-12)}$$

where $T[\rho(\vec{r})]$ is the kinetic energy of the electrons, $E_{ee}[\rho(\vec{r})]$ is the interaction energy between electrons and $V_{ext}[\rho(\vec{r})]$ is the interaction energy between nuclei and electrons. The functional reaches its minimum at the fundamental state of the electronic density $\rho_0(\vec{r})$:

$$\left[\frac{\partial \boldsymbol{E}[\boldsymbol{\rho}(\vec{\boldsymbol{r}})]}{\partial[\boldsymbol{\rho}(\vec{\boldsymbol{r}})]}\right]_{\boldsymbol{\rho}(\vec{\boldsymbol{r}})=\boldsymbol{\rho_0}(\vec{\boldsymbol{r}})} = \mathbf{0} \tag{II-13}$$

with a minimization constraint related to P, which is the total number of electrons in the system:

$$\boldsymbol{P} = \int \boldsymbol{\rho}(\vec{\boldsymbol{r}})\boldsymbol{dr} \tag{II-14}$$

The two theorems validated the initial approach of Thomas and Fermi and made the DFT, an exact theory for the fundamental state.

The expression (II-12) can be formally re-written as:

$$\begin{aligned}\boldsymbol{E}[\boldsymbol{\rho}(\vec{\boldsymbol{r}})] = \boldsymbol{T}[\boldsymbol{\rho}(\vec{\boldsymbol{r}})] + \boldsymbol{E_H}[\boldsymbol{\rho}(\vec{\boldsymbol{r}})] + \boldsymbol{V_{ne}}[\boldsymbol{\rho}(\vec{\boldsymbol{r}})] \\ + \boldsymbol{E_{ee}}[\boldsymbol{\rho}(\vec{\boldsymbol{r}})] - \boldsymbol{E_H}[\boldsymbol{\rho}(\vec{\boldsymbol{r}})]\end{aligned} \tag{II-15}$$

The first term is the kinetic energy of the system, the second one corresponds to Hartree energy which reflects the electron-electron coulombic repulsion, the third, the coulombic terms of interaction between electrons and nuclei and the difference between the fourth and fifth terms, an energy of quantum origin, which is the exchange and correlation energy (noted as $E_{XC}[\rho(\vec{r})]$, defined as:

$$\boldsymbol{E_{XC}}[\boldsymbol{\rho}(\vec{\boldsymbol{r}})] = \boldsymbol{E_{ee}}[\boldsymbol{\rho}(\vec{\boldsymbol{r}})] - \boldsymbol{E_H}[\boldsymbol{\rho}(\vec{\boldsymbol{r}})] \tag{II-16}$$

The functional $E[\rho(\vec{r})]$ is not accessible in particular because the expressions of $T[\rho(\vec{r})]$ and $E_{XC}[\rho(\vec{r})]$, are not known. The approach of Kohn and Sham detailed below, makes it possible to estimate $T[\rho(\vec{r})]$.

II.4.3.2 Kohn-Sham equation

The Kohn-Sham approximation consists of replacing the real system with a fictitious system composed of P particles not interacting with each other and submitted to an effective potential $\hat{v}_{KS}(\vec{r})$. This hypothetical system has the same ground-state electron density as the real system.

The non-interacting electrons which form the fictitious system can be described by single-electron functions ψ_i, so-called Kohn-Sham orbitals. The electron density of the fictitious system is written as follows.

$$\boldsymbol{\rho(\vec{r}) = \sum_{i=1}^{P} |\psi_i(\vec{r})|^2} \quad \text{(II-17)}$$

The Kohn-Sham formalism transforms the P-electron problem into a system of P single-electron equations and their eigenfunctions, the KS orbitals. These orbitals can be used to construct the electron density of the system which can be used, in turn, to calculate the total energy of the real system:

$$\boldsymbol{E_{KS}[\rho(\vec{r})] = T_{KS}[\rho(\vec{r})] + E_H[\rho(\vec{r})] + E_{ne}[\rho(\vec{r})] + E_{XC}[\rho(\vec{r})]} \quad \text{(II-18)}$$

where $T_{KS}[\rho(\vec{r})]$ is the kinetic energy of the fictitious system formed by P non-interacting electrons, $E_H[\rho(\vec{r})]$ is the Hartree energy, $E_{ne}[\rho(\vec{r})]$ is the coulomb interaction energy between electrons and nuclei and $E_{XC}[\rho(\vec{r})]$ is the energy of exchange and correlation.

The Hartree energy is written as:

$$\boldsymbol{E_H[\rho(\vec{r})] = \frac{1}{2} \int d\vec{r} \int d\vec{r'} \frac{\rho(\vec{r})\rho(\vec{r'})}{\left|\vec{r} - \vec{r'}\right|}} \quad \text{(II-19)}$$

The kinetic energy of the hypothetical system is written as:

$$\boldsymbol{T_{KS}[\rho(\vec{r})] = \frac{1}{2} \sum_{i=1}^{P} \int \psi_i^*(\vec{r}) \nabla^2 \psi_i(\vec{r}) d\vec{r}} \quad \text{(II-20)}$$

The solutions must respect the orthonormalization constraint:

$$\boldsymbol{\langle \psi_i | \psi_j \rangle = \delta_{ij}} \quad \text{(II-21)}$$

The minimization of the density functional $E_{KS}[\rho(\vec{r})]$ with respect to the ψ_i functions lead to the so-called Kohn-Sham equations:

$$\boldsymbol{\left[-\frac{1}{2}\nabla^2 + \hat{v}_{KS}(\vec{r})\right] \psi_i(\vec{r}) = \hat{H}_{KS}(\vec{r}) \psi_i(\vec{r}) = \varepsilon_i \psi_i(\vec{r})} \quad \text{(II-22)}$$

where $\hat{H}_{KS}(\vec{r})$ is the K-S monoelectronic Hamiltonian and $\hat{v}_{KS}$ is the effective potential seen by an electron and written as:

$$\boldsymbol{\hat{v}_{KS} = \hat{v}_{ne} + \hat{v}_H + \hat{v}_{XC}} \quad \text{(II-23)}$$

Where $\hat{v}_{ne}$ is the coulomb interactive potential between electrons and nuclei, $\hat{v}_H$ is the Hartree potential defined as:

$$\hat{v}_H(\vec{r}) = \int d\vec{r'} \frac{\rho(\vec{r'})}{\left|\vec{r} - \vec{r'}\right|} \quad \text{(II-24)}$$

and $\hat{v}_{XC}$ is the potential of exchange and correlation.

The terms constituting $\hat{H}_{KS}$ depend on the solution $\rho(\vec{r})$.Then the K-S equations must be solved by a self-consistent method. Their solutions provide the electron density and the energy of the system in its ground state. The $E_{XC}[\rho(\vec{r})]$ the term can be calculated by different approximations. The generalized gradient approximation (GGA) [27], [28] will be adopted in this study.

II.4.4 Complementary approximations

II.4.4.1 LDA and GGA functionals

The first approximation for calculating the energy of exchange and correlation is the Local Density Approximation (or LDA). This approximation is well suited to cases where the electron density varies little. The LDA functional can be written as:

$$E_{XC}^{LDA}[\rho(\vec{r})] = \int \rho(\vec{r}) \varepsilon_{XC}^{hom}[\rho(\vec{r})] d\vec{r} \quad \text{(II-25)}$$

where ε_{XC}^{hom} is the energy of exchange and correlation of a homogeneous electron gas that can be written as a sum of two terms:

$$\varepsilon_{XC}^{hom}[\rho(\vec{r})] = \varepsilon_X^{hom}[\rho(\vec{r})] + \varepsilon_C^{hom}[\rho(\vec{r})] \quad \text{(II-26)}$$

In a homogeneous electron gas, the energy of exchange ε_X^{hom} is exactly calculated:

$$\varepsilon_X^{hom}[\rho(\vec{r})] = \frac{3}{4} \sqrt[3]{\frac{3\rho(\vec{r})}{\pi}} \quad \text{(II-27)}$$

So,

$$E_X^{LDA} = -\frac{3}{4}\left(\frac{3}{\pi}\right)^{\frac{1}{3}} \int \rho(\vec{r})^{\frac{4}{3}} d\vec{r} \quad \text{(II-28)}$$

The analytical expression of the energy of correlation ε_C^{hom} is not known. It was first calculated by quantum Monte-Carlo method [29]. Subsequently, analytical expressions have been established [30], [31].

The GGA (Generalized Gradient Approximation) approximation corrects the LDA approximation in the case where $\rho(\vec{r})$ has large variations. Considering the effect of electron density heterogeneity, an additional dependence on $\nabla\rho(\vec{r})$ is introduced into the equation of ε_{XC}:

$$\boldsymbol{E_{XC}^{GGA}[\rho(\vec{r})] = \int \rho(\vec{r})\varepsilon_{XC}[\rho(\vec{r}), \nabla\rho(\vec{r})]d\vec{r}} \quad \text{(II-29)}$$

There are several versions of the GGA functional in the literature. The GGA approximation with Perdew, Burke and Ernzerhof correction (PBE) [32], [33], currently used in solid-state physics will be chosen in this work.

II.4.4.2 Pseudo potential

The pseudo-potential, or effective potential, is also an approximation introduced to simplify the calculation of a complex system. In a compound, the core electrons do not participate in the formation of the chemical bond, which involves only the valence electrons. Planar wave functions are suitable for valence electrons that delocalize from the core regions. For core electrons, strong bonds with nuclei restrict them to the vicinity of atomic sites, so their wave functions are difficult to describe with a plane wave basis. One way to overcome this difficulty is to treat core electrons as fixed and to use an effective potential or pseudo-potential, to evaluate their interaction with valence electrons.

There are several types of pseudopotentials. Norm-Conserving Pseudo-Potentials (NCPP) has good transferability, i.e. good efficiency in different chemical environments. These pseudo-potentials often have large cut-off energies. Another possibility is to use Ultra-Soft Pseudo-Potentials (USPP) [34], which do not conserve the norm but allow lower cut-off energy, thus accelerating the convergence of the calculations. The Projector Augmented Wave (PAW) method [35] will be used with the USPP in this study.

II.4.5 DFT parameters

DFT calculations are performed on the $ZrCr_2$ stoichiometric compound in the C14, C36 and C15 structures and for the metastable end-members $ZrZr_2$, $CrZr_2$ and $CrCr_2$ and on the ternary compound Zr_3Cr_3O.

Version 5.6 of the VASP (Vienna Ab initio Simulation Package) is used in these calculations. GGA-PBE (Perdew, Burke and Enzerof [32]) functional is employed with a USPP-PAW pseudo potential and a cut-off energy of 300 eV.

The choice of the cut-off energy was tested with a Monkhorst mesh $15 \times 15 \times 15$ for the Cr bcc phase (Figure II-3). Convergence is achieved for a cut-off energy above 250 eV.

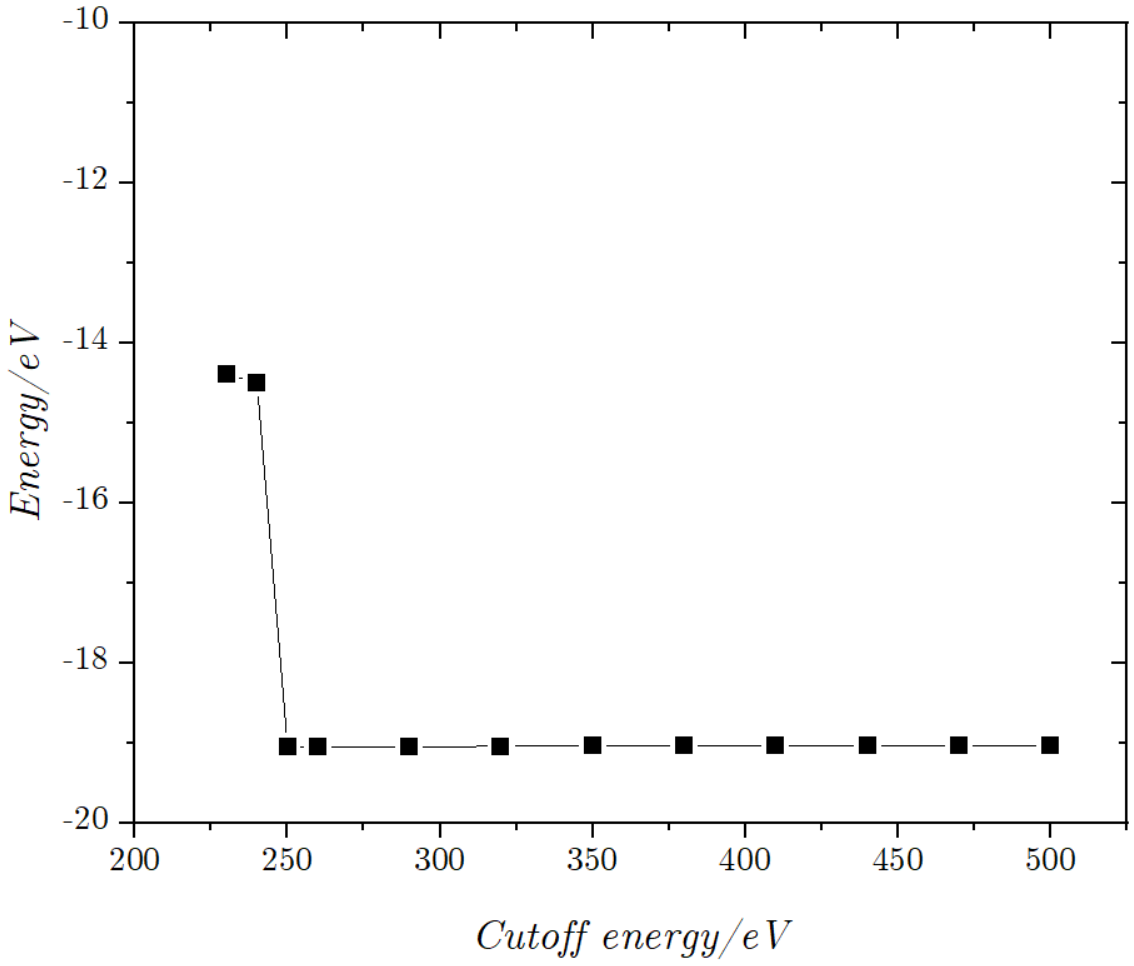

Figure II-3 Calculated energy as a function of the cut-off energy for Cr Bcc

For the cut-off energy, the convergence of the calculations is obtained from 10 k-points (i.e. meshing 10x10x10). Two calculations considering or not considering the spin polarization of the Cr bcc anti-ferromagnetic phase were realized. The energy convergence criterion is set to 10^{-6} eV. Energy convergence tests as a function of the number of k-points in the Brillouin zone are made for pure Zr hcp and Cr bcc structures and a cut-off energy of 300 eV, see Figure II-4.

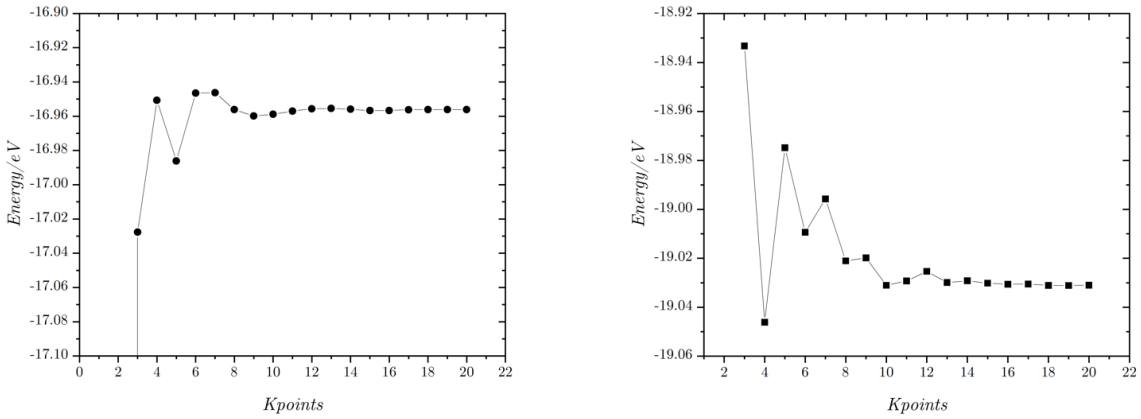

Figure II-4 Calculated energy as a function of the number of k-points. Left: Zr hcp structure, Gaussian type mesh. Right: Cr bcc structure, Monkhorst type mesh.

For oxygen, the calculation is established by modeling a single O_2 molecular in a ten times larger lattice. The cut-off energy was 300 eV and a simple Monkhorst mesh $1 \times 1 \times 1$ was set, as only one molecular exists in the lattice.

The parameters of calculations are listed in Table II-3. The C14 and C15 Laves phases were calculated with a Monkhorst mesh $10 \times 10 \times 10$ and a cut-off energy of 300 eV.

Meta-stable end-members Cr_2Cr, Zr_2Zr and Zr_2Cr in the C14 and C15 structures are calculated without considering magnetism, as Laves phases of $ZrCr_2$ are paramagnetic [36] at ambient temperatures. All calculations for the end members are initiated with the relaxed lattice parameters of $ZrCr_2$ in the C14 or C15 structures, and then fully relaxed to obtain the minimum energy. The choices in terms of functional and k-point mesh chosen for the Laves phases are used for the metastable end-members calculations.

For the Zr_3Cr_3O phase, the calculations were made with a Monkhorst mesh $12 \times 12 \times 12$ and a cut-off energy of 300 eV. The convergence tests of kpoints show no significant difference with kpoints denser than $5 \times 5 \times 5$.

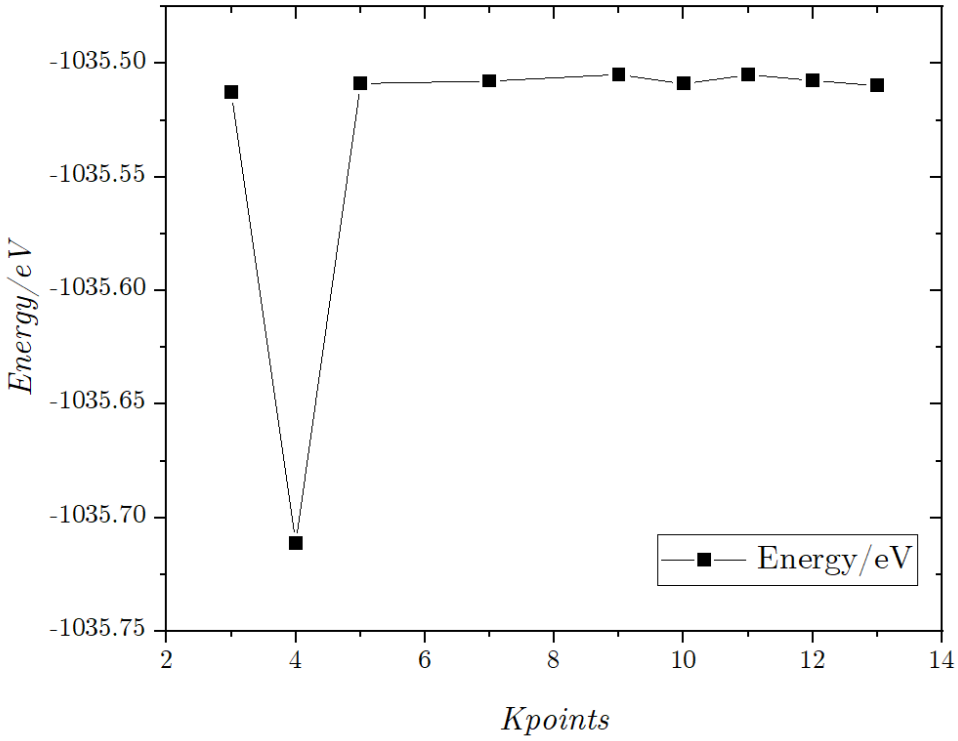

Figure II-5 Calculated energy as a function of the number of k-points for Zr_3Cr_3O

Table II-3 Parameters of simulations

Component	Kpoints	Cut-off energy/eV	Magnetism
Cr	10x10x10	300	None/antiferro
Zr	10x10x10	300	None
O_2	1x1x1	300	Para
$ZrCr_2$/$CrCr_2$/$CrZr_2$/$ZrZr_2$	10x10x10	300	None
Zr_3Cr_3O	12x12x12	300	None/antiferro

II.5 CALPHAD method

II.5.1 Equilibrium and state functions

According to the 2nd law, an isolated system reaches its equilibrium state when its entropy is maximal. The infinitesimal entropy change dS can be written as a function of the internal energy change dU of the system, the temperature T, the pressure p, the volume change dV, the chemical potential μ_i and the change dN_i of the number of moles of the component i:

$$\mathbf{d}S = \frac{1}{T}\mathbf{d}U - \frac{p}{T}\mathbf{d}V + \sum_{i=1}^{n}\frac{\mu_i}{T}dN_i \qquad \text{(II-30)}$$

However, this criterion is not very useful because it is not possible in practice to keep the internal energy, the volume and the quantity of components of the system constant at the same time.

More common is an open system that can exchange matter and energy with its environment. One or more intensive variables can be held constant (e.g. pressure or temperature) and equilibrium is then achieved by the exchange of matter and/or energy with its environment. In an open system, and using (II-30) the infinitesimal internal energy change is written as:

$$\mathbf{d}\boldsymbol{U} = \boldsymbol{T}\mathbf{d}\boldsymbol{S} - \boldsymbol{p}\mathbf{d}\boldsymbol{V} + \sum_{\boldsymbol{i=1}}^{\boldsymbol{n}} \boldsymbol{\mu_i} \boldsymbol{dN_i} \tag{II-31}$$

By Legendre transformation, it is possible to define a series of state functions that reach an extremum at an equilibrium state when their characteristic variables are held constants. The most used state functions are listed in Table II-4. Because the sign of some functions (like the Gibbs energy) is defined as an opposite to those of S, ψ, or ϕ, these functions will reach their minimum at equilibrium.

Table II-4 State functions that reach their extremum at equilibrium if the characteristic state variables are constant. Table from [37].

Name	Symbol or definition	Characteristic state variables		
Entropy	S	U	V	N_i
Massieu's function	$\psi = S - U/T$	$1/T$	V	N_i
Planck's function	$\phi = S - \frac{U}{T} - p\frac{V}{T}$	$1/T$	p/T	N_i
Internal energy	U	S	V	N_i
Enthalpy	$H = U + pV$	S	$-p$	N_i
Helmholtz free energy	$F = U - TS$	T	V	N_i
Gibbs energy	$G = U + pV - TS$	T	$-p$	N_i
Grand potential	$-pV = U - TS - \sum_I \mu_i N_i$	T	V	μ_i
Gibbs-Duhem equation	$0 = U + pV - TS - \sum_i \mu_i N_i$	T	p	μ_i

The most commonly used state function in this table is the Gibbs energy G which reaches its minimum under isothermal and isobaric conditions if the quantities of all components are constant. All state functions defined only with intensive variables, such as the Gibbs-Duhem

equation, are always zero. In practice, at least one extensive variable is needed to define the size of the system.

II.5.2 The CALPHAD method

Phase diagrams play a crucial role in materials research. They are of great use in the design of new materials and manufacturing processes as well as in the optimization of material properties and process operation. The CALPHAD (CALculation of PHAse Diagrams) method was born in the 1960s [38] but took off in the 1970s [39] with the development of computers.

The method is based on the global minimization of the Gibbs energy in a multi-component, multi-phase chemical system and can be applied to a simple binary system as well as to a system with a large number of chemical elements.

Each phase of the system is described by a Gibbs energy function which depends on the temperature, pressure and composition variables and a number of adjustable parameters. The values of these parameters are optimized numerically to fit an extensive dataset of calculated (e.g. by DFT), estimated or experimentally determined thermodynamic properties of individual phases and equilibria between the phases of the system. The principle of the method is shown in Figure II-6.

Dedicated CALPHAD software packages are needed to perform all the required numerical calculations and optimizations. Commercial software such as FactSage, MTDATA, PANDAT, MatCalc, JMatPro and Thermo-Calc, as well as open source code such as Open Calphad and PyCalphad are now available. The optimized thermodynamic description of the system, stored as a database file, makes it possible to calculate any thermodynamic properties that can be derived from the Gibbs energy, to determine the equilibrium state of the system under any conditions of temperature, pressure and composition and in particular to reproduce the phase diagram.

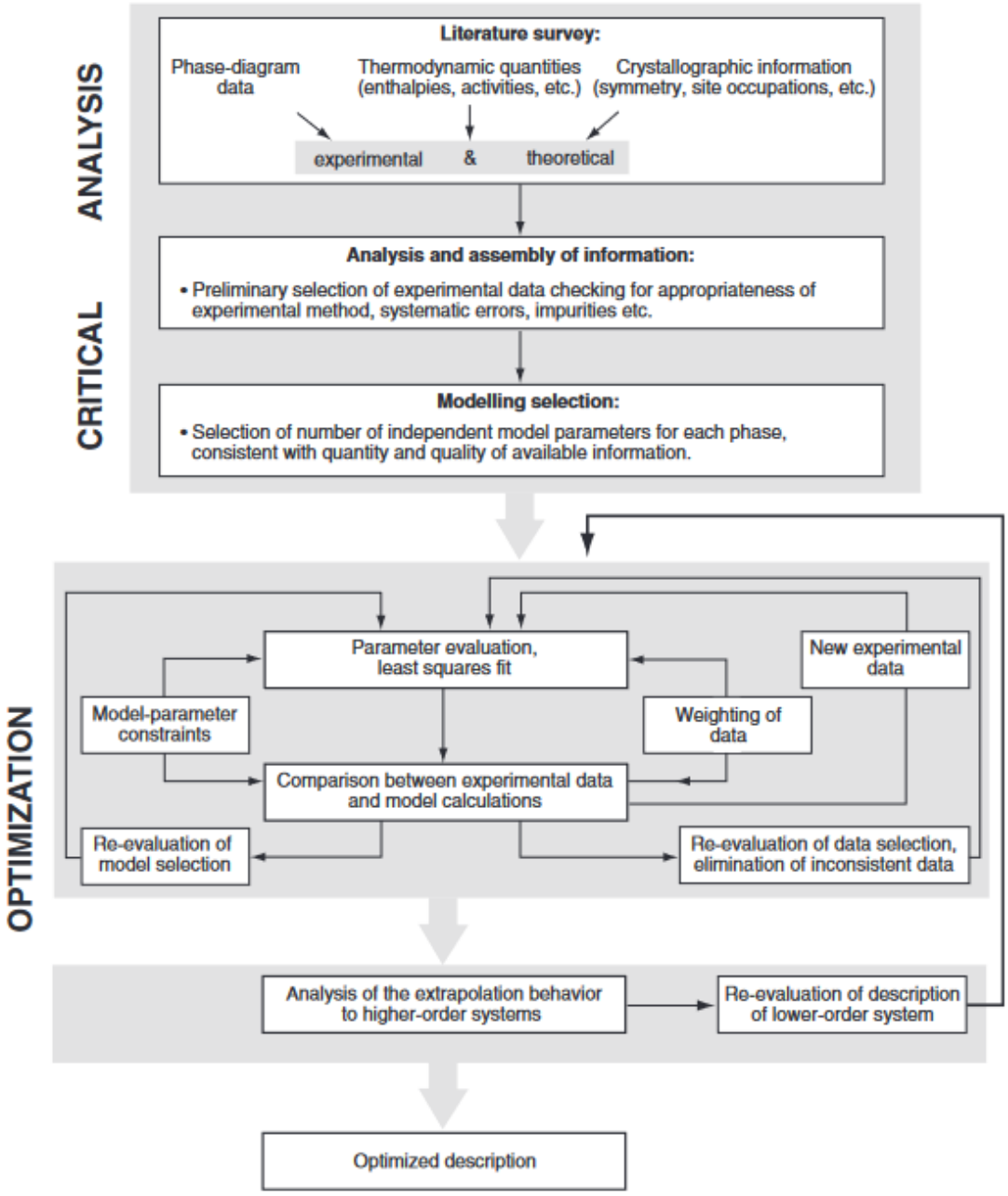

Figure II-6. Principle of the CALPHAD assessment method from Lukas et al. [37]

In this work, we used version 2022b of the Thermo-calc software for the CALPHAD assessment of the Zr-Cr and U-Cr binary systems and the Zr-Cr-O ternary system.

II.5.3 Gibbs energy models for the various types of phases

In this section, the Zr-Cr binary system is taken as an example. In this system, the phases to be modeled are the solutions phases (HCP_A3, BCC_A2 and liquid) and the stoichiometric different Laves phases (C14 and C15).

II.5.3.1 Pure elements - SGTE data

The Gibbs energies of the pure elements relative to the Standard Element Reference (SER) at 10^5 Pa and 298.15 K (denoted as $G - H_{SER}$) are taken from the SGTE data compiled by Dinsdale [40]. For an element *i* at temperature *T* in its phase α, it takes the following form:

$$^{\circ}\boldsymbol{G_i^{\alpha}(T)} - {}^{\circ}\boldsymbol{H_i^{SER}} = \boldsymbol{a + bT + cTln(T) + \sum dT^n} \quad \text{(II-32)}$$

where *a, b, c, d* are numerical coefficients and n has a set of integer values typically 2,3 and -1. The standard element reference state is defined as HCP_A3 for Zr and BCC_A2 for Cr at 298.15 K.

Analytical expressions for the other thermodynamic properties (Table II-5) can be obtained directly from (II-32) using classical thermodynamic relations.

Table II-5 Analytical expressions of important thermodynamic properties of the elements.

Thermodynamic quantity	**Expression**
Entropy *S*	$S = -\mathrm{b} - \mathrm{c} - \mathrm{cln}(T) - \sum dT^n$
Enthalpy *H*	$H = \mathrm{a} - \mathrm{c}T - \sum (n-1)dT^n$
Heat capacity C_p	$C_p = -c - \sum n(n-1)dT^{n-1}$

II.5.3.2 Models for solution phases

The HCP_A3, BCC_A2 and liquid solution phases, present in the Zr-Cr system, are defined as substitutional solutions.

For a given solution phase α, the total molar Gibbs energy is written as:

$$\boldsymbol{G_m^{\alpha}} = {}^{ref}\boldsymbol{G_m^{\alpha}} + {}^{id}\boldsymbol{G_m^{\alpha}} + {}^{ex}\boldsymbol{G_m^{\alpha}} \quad \text{(II-33)}$$

where the ${}^{ref}G_m^{\alpha}$ represents a contribution from the mechanical mixing of the pure elements:

$${}^{ref}\boldsymbol{G_m^{\alpha}} = \sum_{i=Zr,Cr} \boldsymbol{x_i}\left({}^{\circ}\boldsymbol{G_i^{\alpha}} - \mathbf{H_i^{SER}}\right) \quad \text{(II-34)}$$

with x_i being here the mole fraction of element $i(=\mathrm{Zr\ or\ Cr})$.

${}^{id}G_m^{\alpha}$ is the ideal entropy of mixing term, here we have:

$${}^{id}\boldsymbol{G_m^{\alpha}} = \sum_{i=Zr,Cr} \boldsymbol{RT(x_i ln x_i)} \quad \text{(II-35)}$$

R is the perfect gas constant and T is the temperature.

The excess term ${}^{ex}G_m^{\alpha}$ is written according to the Redlich-Kister polynomial description [41]:

$$ {}^{ex}\boldsymbol{G_m^{\alpha}} = \boldsymbol{x_{Cr}x_{Zr}}\sum_{\boldsymbol{i=0}}^{\boldsymbol{n}} {}^{\boldsymbol{i}}\boldsymbol{L_{Cr,Zr}^{\alpha}}(\boldsymbol{T})(\boldsymbol{x_{Cr}} - \boldsymbol{x_{Zr}})^{\boldsymbol{i}} \tag{II-36} $$

By restricting the polynomial expansion to the first three terms, it becomes:

$$ \begin{aligned} {}^{ex}\boldsymbol{G_m^{\alpha}} = \boldsymbol{x_{Cr}x_{Zr}}\big[&{}^{\boldsymbol{0}}\boldsymbol{L_{Cr,Zr}^{\alpha}}(\boldsymbol{T}) + {}^{\boldsymbol{1}}\boldsymbol{L_{Cr,Zr}^{\alpha}}(\boldsymbol{T})(\boldsymbol{x_{Cr}} - \boldsymbol{x_{Zr}})^{\boldsymbol{1}} \\ &+ {}^{\boldsymbol{2}}\boldsymbol{L_{Cr,Zr}^{\alpha}}(\boldsymbol{T})(\boldsymbol{x_{Cr}} - \boldsymbol{x_{Zr}})^{\boldsymbol{2}}\big] \end{aligned} \tag{II-37} $$

where ${}^{i}L_{Cr,Zr}^{\alpha}(T)$ are the parameters describing the interaction between Cr and Zr, parameters which are themselves written as a sum of an enthalpic and an entropic term according to:

$$ {}^{\boldsymbol{i}}\boldsymbol{L_{Cr,Zr}^{\alpha}}(\boldsymbol{T}) = \boldsymbol{a_i} + \boldsymbol{b_i T}, \qquad \boldsymbol{i = 0, 1, 2} \tag{II-38} $$

in which a_i, b_i are parameters whose values will be optimized.

II.5.3.3 Model for the intermetallic compounds

Only two C14 (hexagonal) and C15 (cubic) Laves phases of the $ZrCr_2$ compound will be introduced in our CALPHAD assessment of the Zr-Cr system. Both Laves phases are described with the same two-sublattice model as $(Cr, Zr)_2(Cr, Zr)$. This choice is governed by the fact that the description must be fully compatible with other already-assessed systems in the thermodynamic NUCLEA database developed at IRSN.

Similar to equation (II-33), the Gibbs free energy is written as a sum of the three ${}^{ref}G$, ${}^{id}G$ and ${}^{ex}G$ terms. Their new definitions are given below:

$$ \begin{aligned} {}^{\boldsymbol{ref}}\boldsymbol{G} = \boldsymbol{y'_{Zr}y''_{Zr}G_{Zr:Zr}} + \boldsymbol{y'_{Zr}y''_{Cr}G_{Zr:Cr}} + \boldsymbol{y'_{Cr}y''_{Zr}G_{Cr:Zr}} \\ + \boldsymbol{y'_{Cr}y''_{Cr}G_{Cr:Cr}} \end{aligned} \tag{II-39} $$

$$ {}^{\boldsymbol{id}}\boldsymbol{G} = \boldsymbol{RT}[\boldsymbol{2}(\boldsymbol{y'_{Zr}ln y'_{Zr}} + \boldsymbol{y'_{Cr}ln y'_{Cr}}) + (\boldsymbol{y''_{Zr}ln y''_{Zr}} + \boldsymbol{y''_{Cr}ln y''_{Cr}}) \tag{II-40} $$

$$ \begin{aligned} {}^{\boldsymbol{ex}}\boldsymbol{G} = \boldsymbol{y'_{Zr}y'_{Cr}}\big(\boldsymbol{y''_{Zr}L_{Zr,Cr:Zr}} + \boldsymbol{y''_{Cr}L_{Zr,Cr:Cr}}\big) + \boldsymbol{y''_{Zr}y''_{Cr}}(\boldsymbol{y'_{Zr}L_{Zr:Cr,Zr}} \\ + \boldsymbol{y'_{Cr}L_{Cr:Cr,Zr}}) \end{aligned} \tag{II-41} $$

where

- ✓ y_i' and y_i'' are the molar fractions of the element i in the first and the second sublattices respectively.

- ✓ $G_{\mathrm{A:B}}$ is the Gibbs free energy of the compound in which the first sublattice is only occupied by A atoms and the second sublattice by B atoms.
- ✓ The L quantities are the interaction parameters between Cr and Zr on the two sublattices. For example, $L_{Zr,Cr:Zr}$ represents the interaction between Cr and Zr on the 1st sublattice when the second sublattice is only occupied by Zr atoms.

The reference term (Equation II-35) involves 4 stoichiometric so-called end-members: Cr_2Zr, Zr_2Zr, Cr_2Cr and Zr_2Cr the last three being metastable.

For these three metastable end-members, the Gibbs free energy is described as:

$$\mathbf{G_{A:B}} = \Delta_f \boldsymbol{H}_{\boldsymbol{A_2B}}^{\boldsymbol{SER}} + \mathbf{2}\boldsymbol{G}_{\boldsymbol{A}}^{\boldsymbol{REF}} + \boldsymbol{G}_{\boldsymbol{B}}^{\boldsymbol{REF}} \quad \text{(II-42)}$$

where $\Delta_f H_{A_2B}^{SER}$ is the enthalpy of formation of the A_2B phase in SER conditions and G_A^{REF} and G_B^{REF} are the Gibbs energy of pure elements A and B taken from the SGTE data [40].

The enthalpy of formation of the A_2B phase will be calculated at 0 K by DFT, and its value at 298 K is calculated by a Born-Haber thermodynamic cycle using the Neumann-Kopp additivity rule to estimate the heat capacity of the compound.

For the stable Cr_2Zr phase, the parameters of the Gibbs energy (Equation (II-32)) will be optimized based on the measured formation enthalpy and heat capacity.

II.6 Reference

[1] J. Rodriguez-Carvajal, 'Recent Developments of the Program FULLPROF, in Newsletter of the Commission on Powder Diffraction (IUCr)', vol. 26, pp. 12–19, 2001.

[2] J. Rodríguez-Carvajal, 'AN INTRODUCTION TO THE PROGRAM', p. 139.

[3] T. Maimaitiyili *et al.*, 'Observation of the δ to ε Zr-hydride transition by in-situ synchrotron X-ray diffraction: Observation of the δ to ε Zr-hydride transition by in-situ synchrotron X-ray diffraction', *Crystal Research and Technology*, vol. 51, no. 11, pp. 663–670, Nov. 2016, doi: 10.1002/crat.201600234.

[4] X. Yang, N. Takeichi, K. Shida, H. Tanaka, N. Kuriyama, and T. Sakai, 'Novel Mg–Zr–A–H (A=Li, Na) hydrides synthesized by a high pressure technique and their hydrogen storage properties', *Journal of Alloys and Compounds*, vol. 509, no. 4, pp. 1211–1216, Jan. 2011, doi: 10.1016/j.jallcom.2010.09.187.

[5] Kugler, W.; Knorr, K.; Prandl, W., 'Roentgenbeugungsuntersuchungen an der magnetostriktiven Verzerrungswelle in Chrom: Amplitude und Temperaturabhaengigkeit', *Zeitschrift fuer Kristallographie (1983) 162, (*) Article ID * (p. 151-153)*.

[6] Suprunenko, P.A.; Markiv, V.Ya.; Tsvetkova, T.M., 'Magnetic and X-ray diffraction study of Laves phases in the ternary systems {Ti, Zr, Hf}-Cr-Al', *Russian Metallurgy (English Translation) (1984) 1984, (1) Article ID * (p. 207-210)*.

[7] Kornilov, I.I.; Budberg, P.B.; Shakhova, K.I.; Alisova, S.P., 'The equilibrium diagram of $TiCr_2$ - $ZrCr_2$', *Doklady Akademii Nauk SSSR (1965) 161, (6) Article ID * (p. 1378-1381)*.
[8] V. V. PetKov, S. B. Prima, L. A. Tretyachenko, and O. A. Kocherzhinskij, 'New data on the laves phases in Zr-Cr systems', 1973.
[9] H. Fukui, M. Fujimoto, Y. Akahama, A. Sano-Furukawa, and T. Hattori, 'Structure change of monoclinic ZrO_2 baddeleyite involving softenings of bulk modulus and atom vibrations', *Acta Crystallogr B Struct Sci Cryst Eng Mater*, vol. 75, no. 4, pp. 742–749, Aug. 2019, doi: 10.1107/S2052520619007923.
[10] S. Khalili and H. M. Chenari, 'Successful electrospinning fabrication of ZrO_2 nanofibers: A detailed physical – chemical characterization study', *Journal of Alloys and Compounds*, vol. 828, p. 154414, Jul. 2020, doi: 10.1016/j.jallcom.2020.154414.
[11] Dubertret, A.; Lehr, P., 'Description d'une surstructure Zr_3O_{1-X}', *Comptes Rendus des Seances de l'Academie des Sciences*, vol. Serie C: Sciences Chimiques, no. 267, pp. 820–822.
[12] N. O. Golosova *et al.*, 'Structural and magnetic properties of Cr_2O_3 at high pressure', *Journal of Alloys and Compounds*, vol. 722, pp. 593–598, Oct. 2017, doi: 10.1016/j.jallcom.2017.06.140.
[13] S. A. Barrett, A. J. Jacobson, B. C. Tofield, and B. E. F. Fender, 'The preparation and structure of barium uranium oxide $BaUO_{3+x}$ ', *Acta Crystallogr B Struct Sci*, vol. 38, no. 11, pp. 2775–2781, Nov. 1982, doi: 10.1107/S0567740882009935.
[14] B. O. Loopstra, 'Neutron diffraction investigation of U_3O_8', *Acta Cryst*, vol. 17, no. 6, pp. 651–654, Jun. 1964, doi: 10.1107/S0365110X6400158X.
[15] S. Chakraborty, G. Choudhuri, J. Banerjee, R. Agarwal, K. B. Khan, and A. Kumar, 'Micro-structural study and Rietveld analysis of fast reactor fuels: U–Mo fuels', *Journal of Nuclear Materials*, vol. 467, pp. 618–627, Dec. 2015, doi: 10.1016/j.jnucmat.2015.09.055.
[16] A. C. Lawson, C. E. Olsen, J. W. Richardson, M. H. Mueller, and G. H. Lander, 'Structure of β-uranium', *Acta Crystallogr B Struct Sci*, vol. 44, no. 2, pp. 89–96, Apr. 1988, doi: 10.1107/S0108768187009406.
[17] M. Bacmann, E. F. Lewy-Bertaut, and G. Bassi, 'Paramètres atomiques et structures magnétiques de $UCrO_4$', *bulmi*, vol. 88, no. 2, pp. 214–218, 1965, doi: 10.3406/bulmi.1965.5838.
[18] A. Collomb, J. J. Capponi, M. Gondrand, and J. C. Joubert, 'Synthese de quelques oxydes mixtes de type $A^{6+}B^{3+}O_6$ en milieu hydrothermal sous tres haute pression', p. 5.
[19] G. A. Uriano, 'National Bureau of Standards Certificate - Standard Reference Material 720 Synthetic Sapphire (a-Al2O3)', 1982.
[20] P. Benigni *et al.*, 'Measurement of the heat capacity of ZnSb by DSC between 300 and 673 K', *Calphad*, vol. 55, pp. 238–242, Dec. 2016, doi: 10.1016/j.calphad.2016.09.008.
[21] K. Gajavalli, M. Barrachin, P. Benigni, J. Rogez, G. Mikaelian, and E. Fischer, 'Determination of solution enthalpy of zirconium in liquid aluminum', *The Journal of Chemical Thermodynamics*, vol. 135, pp. 198–204, Aug. 2019, doi: 10.1016/j.jct.2019.03.037.
[22] A. Decreton *et al.*, 'Contribution to the description of the absorber rod behavior in severe accident conditions: An experimental investigation of the Ag–Zr phase diagram', *Journal of Nuclear Materials*, vol. 465, pp. 849–856, Oct. 2015, doi: 10.1016/j.jnucmat.2015.05.039.
[23] G. Kresse and D. Joubert, 'From ultrasoft pseudopotentials to the projector augmented-wave method', *Phys. Rev. B*, vol. 59, no. 3, pp. 1758–1775, Jan. 1999, doi: 10.1103/PhysRevB.59.1758.

[24] L. H. Thomas, 'The effect of the orbital velocity of the electrons in heavy atoms on their stopping of α-particles', *Math. Proc. Camb. Phil. Soc.*, vol. 23, no. 6, pp. 713–716, Apr. 1927, doi: 10.1017/S0305004100011221.
[25] E. Fermi, 'Eine statistische Methode zur Bestimmung einiger Eigenschaften des Atoms und ihre Anwendung auf die Theorie des periodischen Systems der Elemente', *Z. Physik*, vol. 48, no. 1–2, pp. 73–79, Jan. 1928, doi: 10.1007/BF01351576.
[26] P. Hohenberg and W. Kohn, 'Inhomogeneous Electron Gas', *Phys. Rev.*, vol. 136, no. 3B, pp. B864–B871, Nov. 1964, doi: 10.1103/PhysRev.136.B864.
[27] J. P. Perdew, 'Accurate Density Functional for the Energy: Real-Space Cutoff of the Gradient Expansion for the Exchange Hole', *Phys. Rev. Lett.*, vol. 55, no. 16, pp. 1665–1668, Oct. 1985, doi: 10.1103/PhysRevLett.55.1665.
[28] J. P. Perdew, 'Generalized gradient approximations for exchange and correlation: A look backward and forward', *Physica B: Condensed Matter*, vol. 172, no. 1–2, pp. 1–6, Jun. 1991, doi: 10.1016/0921-4526(91)90409-8.
[29] D. M. Ceperley and B. J. Alder, 'Ground State of the Electron Gas by a Stochastic Method', Phys. Rev. Lett., vol. 45, no. 7, pp. 566–569, Aug. 1980, doi: https://doi.org/10.1103/PhysRevLett.45.566.
[30] S. H. Vosko, L. Wilk, and M. Nusair, 'Accurate spin-dependent electron liquid correlation energies for local spin density calculations: a critical analysis', *Can. J. Phys.*, vol. 58, no. 8, pp. 1200–1211, Aug. 1980, doi: 10.1139/p80-159.
[31] J. P. Perdew and A. Zunger, 'Self-interaction correction to density-functional approximations for many-electron systems', *Phys. Rev. B*, vol. 23, no. 10, pp. 5048–5079, May 1981, doi: 10.1103/PhysRevB.23.5048.
[32] J. P. Perdew, K. Burke, and M. Ernzerhof, 'Generalized Gradient Approximation Made Simple', *Phys. Rev. Lett.*, vol. 77, no. 18, pp. 3865–3868, Oct. 1996, doi: 10.1103/PhysRevLett.77.3865.
[33] J. P. Perdew, M. Ernzerhof, and K. Burke, 'Rationale for mixing exact exchange with density functional approximations', *The Journal of Chemical Physics*, vol. 105, no. 22, pp. 9982–9985, Dec. 1996, doi: 10.1063/1.472933.
[34] D. Vanderbilt, 'Soft self-consistent pseudopotentials in a generalized eigenvalue formalism', *Phys. Rev. B*, vol. 41, no. 11, pp. 7892–7895, Apr. 1990, doi: 10.1103/PhysRevB.41.7892.
[35] P. E. Blöchl, 'Projector augmented-wave method', *Phys. Rev. B*, vol. 50, no. 24, pp. 17953–17979, Dec. 1994, doi: 10.1103/PhysRevB.50.17953.
[36] J. Pavlů, J. Vřešt'ál, and M. Šob, 'Stability of Laves phases in the Cr–Zr system', *Calphad*, vol. 33, no. 2, pp. 382–387, Jun. 2009, doi: 10.1016/j.calphad.2008.11.003.
[37] H. L. Lukas, S. G. Fries, and B. Sundman, *Computational thermodynamics: the CALPHAD method*. Cambridge ; New York: Cambridge University Press, 2007.
[38] L. Kaufman, 'The lattice stability of metals—I. Titanium and zirconium', *Acta Metallurgica*, vol. 7, no. 8, pp. 575–587, Aug. 1959, doi: 10.1016/0001-6160(59)90195-6.
[39] L. Kaufman and H. Bernstein, *Computer calculation of phase diagrams With special reference to refractory metals*. United States: Academic Press Inc, 1970. [Online]. Available: http://inis.iaea.org/search/search.aspx?orig_q=RN:02004171
[40] A. T. Dinsdale, 'SGTE DATA FOR PURE ELEMENTS', p. 109.
[41] O. Redlich and A. T. Kister, 'Algebraic Representation of Thermodynamic Properties and the Classification of Solutions', *Ind. Eng. Chem.*, vol. 40, no. 2, pp. 345–348, Feb. 1948, doi: 10.1021/ie50458a036.

Chapter III

Zr-Cr binary system

Chapter III. Zr-Cr binary system

III.1 Introduction

The binary Zr-Cr system is important to evaluate the degradation behavior of the Cr-coated cladding in severe accident conditions. In this chapter, we will present the results of our experimental and modeling work on this system. We were interested in the whole system, including the thermodynamic properties of the $ZrCr_2$ different Laves phases and the phase equilibria with the characterization of the invariant transformations. The obtained experimental data associated with DFT calculations will serve to develop a CALPHAD model of the system which will be presented at the end of this chapter and its extension to the Zr-Cr-O ternary system which will be discussed in the next chapter.

The first sub-section (III.2) is devoted to a discussion about the previous experimental studies on phase relations in the Zr-Cr system (III.2.1.1), the reported transformations between the $ZrCr_2$ Laves polymorphs and the thermodynamic studies (III.2.1.2), including DFT calculations and CALPHAD modeling works (III.2.3). Then, in sub-section III.2.4, the main objectives of our experimental work on the Cr-Zr binary system are presented.

The results will be presented and discussed in the different parts of sub-section III.3.

- ✓ Section III.3.1 focuses on the $ZrCr_2$ compound, with a discussion on the stabilities of the different Laves polymorphs, crystallographic structures, homogeneity domains and measurements of their thermodynamic properties in parallel with DFT calculations.
- ✓ Section III.3.2 is dedicated to the determination of the invariant equilibria in the system.

Section III.4 includes the thermodynamic modeling of the binary system by the CALPHAD method using our new results combined with selected results from the literature.

Section III.5 is devoted to the conclusion and some perspectives.

III.2 Literature review

III.2.1 Overview of the Zr-Cr system.

The first comprehensive assessment of the system was made by Arias and Abriata [1] in 1986 who drew the phase diagram shown as the background in Figure III-1. It includes the following phases: the liquid, the bcc terminal solid solutions, (Cr) and (βZr) with a maximum chromium solubility of approximately 8 at.% at 1332 °C, the hexagonal terminal solid solution, (αZr), which shows a maximum solubility of 0.49 at.% Cr at 836°C, the three Laves phases, $\gamma ZrCr_2$, $\alpha ZrCr_2$, and $\beta ZrCr_2$, with the C14 (hexagonal), C15 (cubic), and C36 (hexagonal) structures, respectively. This system has been the subject of many investigations, even recently. They are tentatively summarized in Figure III-1 where almost all the available experimental data obtained until now are superimposed on the Arias version of the phase diagram. The huge number of experimental data has led to different versions of the phase diagram over the years. After this initial version by Arias, first CALPHAD optimizations of this system were proposed by Zeng *et al.* [2] and Ansara *et al.* [3]. With the development of the *ab initio* calculations, it was possible to progressively integrate the missing thermodynamic data of the phases. New modelings were then reported by Pavlů *et al.* [4], Lu *et al.* [5], Yang *et al.* [6], and more recently Lafaye *et al.* [7]. In the following sections, we will discuss the remaining uncertainties according to our analysis and the experimental results.

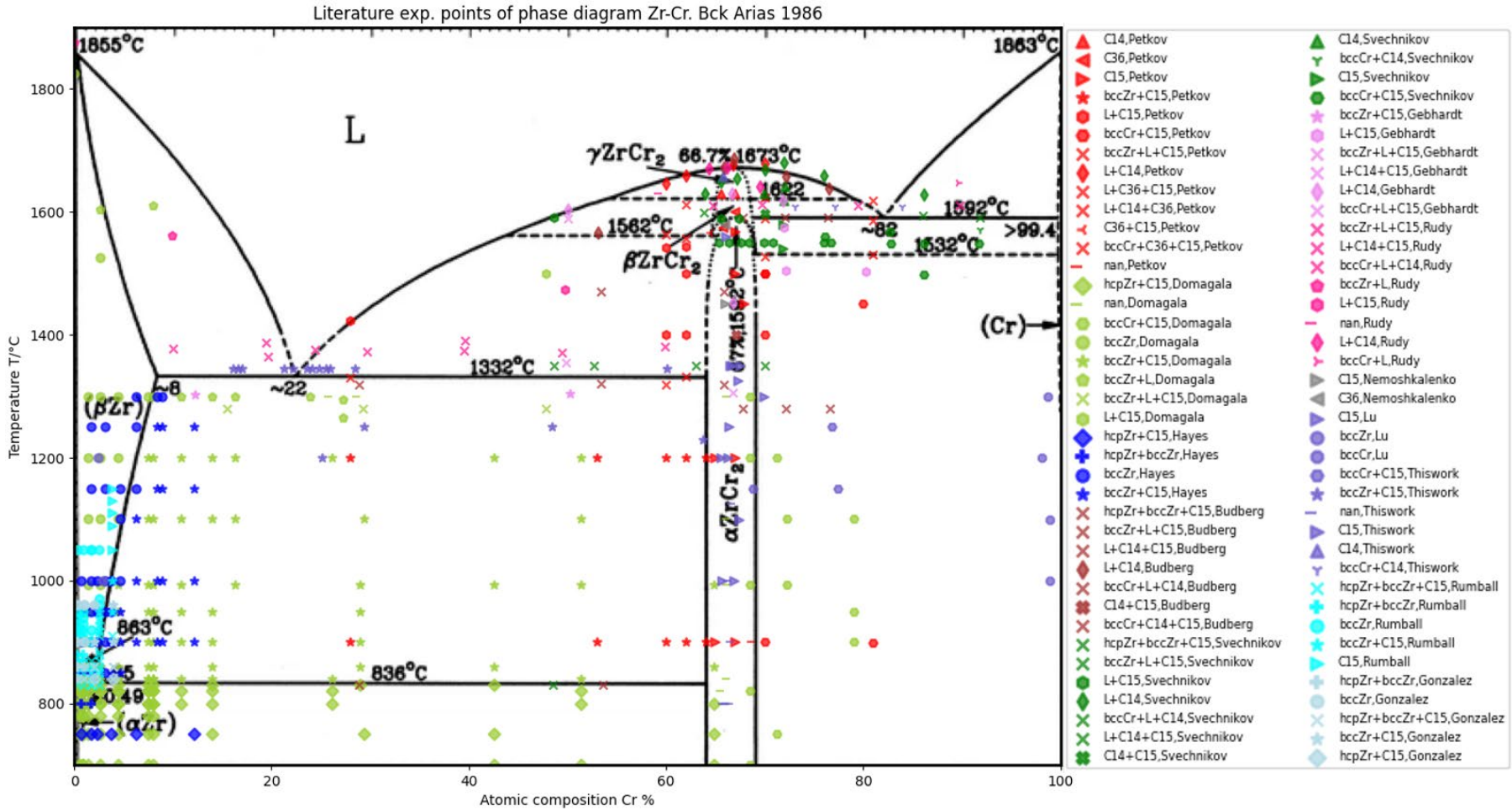

Figure III-1. Cr-Zr phase diagram from Arias and Abriata [1] (background) and experimental data points from literature. All points with the same color are from the same author; all points with the same symbol belong to the same single or two-phase domain. 'X' points correspond to three phases of equilibria. Nan = is not analyzable. '-' are the points nan, that were not announced in the publications.

III.2.1.1 Invariant reactions, mutual solubilities and phase diagram

The pure Zr *hcp* structure is stable at room temperature and transforms to the *bcc* structure at 863°C which is stable up to the Zr melting point.

On the Zr-rich side, the solid solution based on the *bcc* structure transforms by a eutectoid reaction $(\text{bcc Zr}) \rightleftharpoons (\text{hcp Zr}) + \text{ZrCr}_2(\text{C15})$ as reported by several authors [8]–[12]. These authors mostly agreed on the eutectoid temperature value of 830 ±10°C, and a eutectoid composition in Cr < 2% at., e.g. Domagala *et al.* [8] reported ~1% at. Cr, Hayes *et al.* [13] measured a composition of 1.8% at. Cr and Rumball and Elder [11] reported 1.22-1.65% at. Cr.

Two eutectic reactions were found in the Zr-Cr system:

- ✓ The Zr-rich eutectic reaction $\text{L} \rightleftharpoons \text{bcc Zr} + \text{ZrCr}_2\ (\text{C15})$ was first reported by Domagala *et al.* [8]. In this document, it is noted as E1. The temperature of E1 was found in the range between 1270°C [10] and 1370°C [14]. Most results agreed with a value of 1340±20°C (Table III-1). For the eutectic composition, a value of 28±1% at. Cr is usually reported by different authors, except for Petkov *et al.* [15] who indicated a value of 22% at Cr.
- ✓ The Cr-rich eutectic reaction $\text{L} \rightleftharpoons \text{bcc Cr} + \text{ZrCr}_2\ (\text{C15})$ was reported by Budberg *et al.* [9], and is noted as E2 in this document. The E2 eutectic temperature is in the range of 1590 to 1635°C and the E2 eutectic composition was commonly accepted as around 80±1% at. Cr (Table III-1).

Table III-1 Temperatures and compositions of eutectic points in the Zr-Cr system reported in the literature

Reference	T_{E1}/°C	X_{E1}/% *at.* Cr	T_{E2}/°C	X_{E2}/% *at.* Cr
Domagala [8]	1280±10	27.8	1635±15	80
Svechnikov [10]	1270	27.8	1590	80
Gebhardt [16]	1355	28		
Budberg [9]	1320±10		1580±10	80
Rudy [14]	1370±5 /1380	28		
Svechnikov [12]	1360		1590	80
Petkov [15]	1330	22	1590±10	82
Kanazawa [17]		28		79.5
Yang [6]*	1332	26	1590	81.2
Lu [5]*	1316	27.8	1561	82.4
Lafaye [7]*	1335	28.6	1580	80.4
Arias [1]*	1332	22	1592	82

* Assessed values in CALPHAD modeling.

The solubility of Cr in hcp Zr and bcc Zr was reported in [8], [13], [14], [16], [18].

- ✓ The solubility limit of Cr in hcp Zr is reached at the temperature of the eutectoid reaction $(\mathrm{bcc\ Zr}) \leftrightarrows (\mathrm{hcp\ Zr}) + \mathrm{ZrCr_2}\ (\mathrm{C15})$. It was determined as negligible [13], very limited [18] or <0.49% at. [8]. There is therefore a consensus on the low solubility of chromium in hcp zirconium.
- ✓ For bcc Zr, the solubility of Cr has its maximum at the temperature of the E1 eutectic reaction, $\mathrm{L} \leftrightarrows (\mathrm{bcc\ Zr}) + \mathrm{ZrCr_2}\ (\mathrm{C15})$. There was a common agreement [8], [13], [14], [16] about a value of around 8% Cr at.

Pure Cr is stable in the bcc structure from room temperature up to its melting point. A very weak or negligible solubility limit of Zr in bcc Cr was reported in [5], [8], [10], [12], [14], [18].

Data of these solubilities are listed in Table III-2.

Table III-2 Mutual solubilities in bcc Cr, hcp Zr and bcc Zr reported in the literature

Reference	$\mathbf{Sol_{Cr\rightarrow Zr\ hcp}}$ /% $\boldsymbol{at.}$ Cr	$\mathbf{Sol_{Cr\rightarrow Zr\ bcc}}$ /% $\boldsymbol{at.}$ Cr	$\mathbf{Sol_{Zr\rightarrow Cr^*}}$ /% $\boldsymbol{at.}$ Cr
Hayes [13]	Negligible	6.2	
Mcquillan [18]	Very limited		<1.5
Domagala [8]	<0.49	7.63	<1.73
Svechnikov [10]			Negligible
Gebhardt [16]		9.6	
Rudy [14]		8.6	Very weak
Svechnikov [12]			Negligible
Lu [5]			~2.4

* The max solubility of bcc Zr in bcc Cr

III.2.1.2 Intermetallic compound $ZrCr_2$ and phase stability

As far as it is known, the first studies on the $ZrCr_2$ stoichiometric compound were published by Laves and Wallbaum [19] and Wallbaum [20] that reported a new type of intermetallic stoichiometric compound, now known as Laves phases, formulated as AB_2 with typical structures. Later on, $ZrCr_2$ was determined as the only intermetallic compound in the Zr-Cr system [8], [13] and two Laves polymorphs were identified and labeled as C14 and C15. The various structures of the Laves phases are compared in Figure III-2, including the C36 structure whose existence will be discussed later. The C15 Laves phase of $ZrCr_2$ is a cubic phase with a prototype of $MgCu_2$ and a space group $Fd\bar{3}m$, and a lattice parameter a=7.215 Å whereas the

C14 Laves phase is a hexagonal phase with a prototype $MgZn_2$ and a space group $P6_3/mmc$, with the lattice parameters a=5.102 Å, c=8.273 Å.

Published data on the melting temperature of $ZrCr_2$ compound, transition temperatures of the polymorphs and extension of its stability domain are summarized in Table III-3. There are significant differences in these temperatures and compositions. This highlights the need for a new experimental determination of these transition temperatures of the $ZrCr_2$ compound.

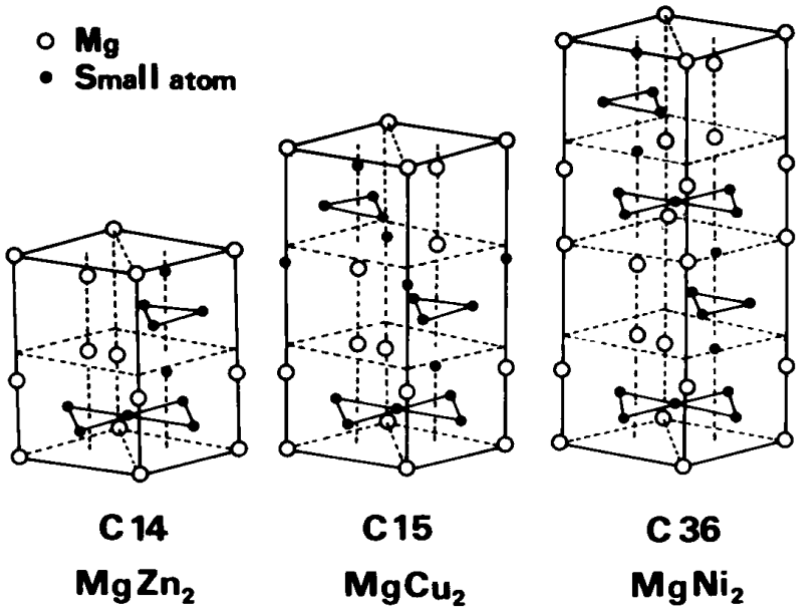

Figure III-2 Structures of the C14, C36, and C15 Laves phases in their prototypes. Figure from Kitano *et al.* [21]. Open circles: Mg atoms; full dots: small atoms as Zn, Cu or Ni.

Subsequent studies [9], [10], [12], [22]–[25] were focused on the stability of the Laves phases and the transition temperature between C14 and C15. Some authors [27], [28] considered the C14 phase to be more stable than the C15 at low temperatures (the data reported in these publications contrary to the accepted state of the art on the Zr-Cr system were reasonably not included in Table III-3). Some other publications [22], [23] stated that C15 was the most stable phase at low temperatures. The problem was discussed in detail by Shen and Paasche [24], who concluded that the misunderstanding was caused by sluggish transformation kinetics between C14 to C15 polymorphs.

Table III-3 Published data of $ZrCr_2$ compound: melting temperatures and transition temperatures of polymorphs

Reference	$T_{melting}/°C$	$T_{Trans}/°C$*	$Sol_{Laves}/\%\ at.\ Cr$	Method
Jordan [22]		Near $T_{melting}$		Exp
Domagala [8]	1700			Exp
Svechnikov [10]	1675			Exp
Alisova [23]		1480±10		Exp
Gebhardt [16]	1630			Exp
Budberg [9]	1675±10	1470±10 Zr side 1280±10 Cr side		Exp
Shen [24]		1550~1600		Exp
Gebhardt [25]		1590		Exp
Rudy [14]	1675±20			Exp
Svechnikov [12]	1680	1620		Exp
Petkov [15] [26]	1670±10	1590/1620	64-69	Exp
Kanazawa [17]			66~69	Exp
Yang [6]	1673		62.1~67.9	CALPHAD
Lu [5]	1697	1546/1621	64.3~67.2	Exp+CALPHAD
Lafaye [7]	1698	1517/1624	63.4~67.9	CALPHAD
Arias [1]	1673	1592/1622		Review

* A single temperature is the transition temperature of $C14 \rightleftharpoons C15$. Two temperatures with a slash correspond to the situation that C36 was reported in the publication: the temperature before the slash is the temperature of $C15 \rightleftharpoons C36$; the temperature after the slash is the temperature of $C36 \rightleftharpoons C14$.

Consequently, rapid cooling after melting does not allow enough time for the transition C14 → C15 to take place, and the C14 phase is retained in a metastable state at room temperature. It was concluded that the C15 phase was stable at low temperatures and the C14 phase at high temperatures. The transition temperature was considered to be between 1550 and 1600°C by Shen and Paasche [24]. The result was later accepted by other authors. However, a relatively important dispersion of the transition temperature ±50°C can be noticed.

The melting temperature of $ZrCr_2$ was also studied by many early researchers [8]–[10], [12], [14], [25], [26] and the published values are in the range 1630-1700°C.

Petkov *et al.* [15], [26] discovered a new $ZrCr_2$ Laves polymorph adopting the C36 form ($MgNi_2$ type, $P6_3/mmc$, a=5.102 Å, c=16.62Å) using powder XRD. The transition sequence between the three Laves phases of $ZrCr_2$ was established by Petkov et al. combining DTA and XRD results as $C14 \overset{1620℃}{\Longleftrightarrow} C36 \overset{1590℃}{\Longleftrightarrow} C15$. The transition temperature from C15 to C36 varied between 1530 and 1560°C from one side to the other side of the stability domain of $ZrCr_2$ with a maximum of 1590°C. at 66.7% at. Cr. The unit cell of the C36 phase compared to the unit

cell of the C14 phase, is only doubled in the c-axis direction because of a difference in the stacking of atomic layers. This was the reason that the C36 and C14 phases have similar XRD patterns. As a consequence, only diffraction peaks corresponding to the planes (1 0 5), (2 0 1), (1 0 7), and (2 0 3) (Figure III-3) having low intensity can be used to distinguish the C14 phase from the C36 one. In practice, this is often difficult because of multiple overlaps between peaks and background noise. To our knowledge, the Petkov's study is the main experimental support for the existence of the C36 phase in the Zr-Cr system. The C36 phase of $ZrCr_2$ is also reported in more recent publications [17], [29]. However, in some of them, the authors were not fully convinced about its existence because of the insignificant difference between the diffraction peaks of C14 and C36. Other researchers reported the C36 phase existence together with some other Laves structures with more complex stacking sequences noted as 6H, 8H, 12H, and 14H [30] (for complex structures stacked with 6/8/12/14 times of basic repeat layer structure of Laves phases).

The non-stoichiometric domain of $ZrCr_2$ was first reported by Svechnikov and Spektor [31], who indicated a narrow area of existence of the compound around its stoichiometric composition. Some more experimental data on the stability domains were published by other authors [9], [12], [17], [23], [32], [33] but the results were inconsistent. Recently, Lu *et al.* [5] made new experiments to determine the extension of the non-stoichiometry domain of $ZrCr_2$ at 1000°C (65.5% and 67.1% at. Cr, composition determined from his phase diagram), 1100°C (67.4% at. Cr), 1200°C (65.6% and 66.5% at. Cr), and 1300°C (70.0% at. Cr).

As a conclusion, the remaining uncertainties on the Zr-Cr system are depicted in Figure III-4 and listed below:

- ✓ Solubilities of the terminal bcc chromium and zirconium solution phases
- ✓ Characterization of the eutectic temperatures
- ✓ Existence of the different Laves phases and the transition temperature between the polymorphs of $ZrCr_2$ and the range of composition for this compound
- ✓ Melting temperature of $ZrCr_2$
- ✓ Liquidus line

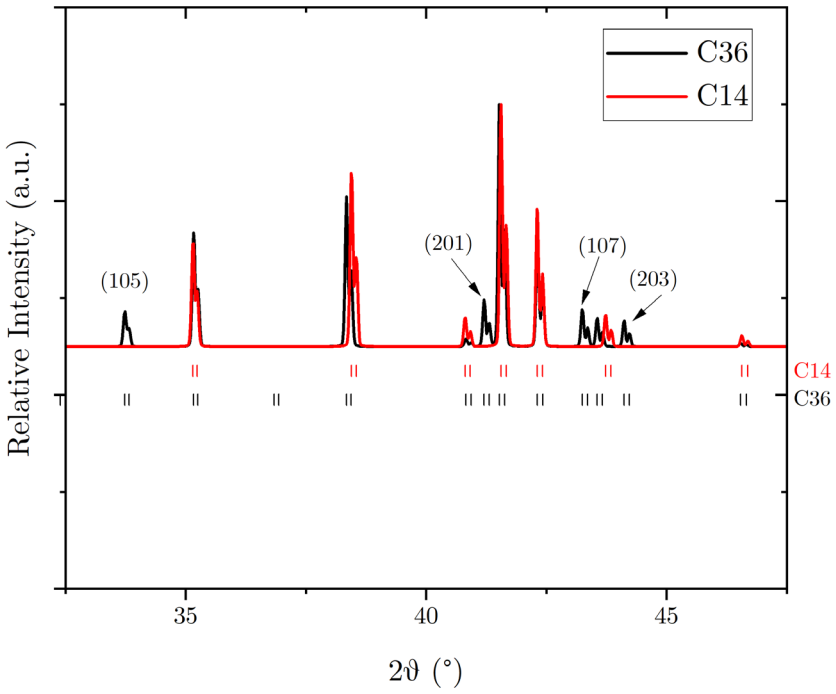

Figure III-3 Comparison of the diffraction patterns of Laves phases C14/C36 of $ZrCr_2$ in an interval 30~50°. The labeled peaks (105), (201), (107), and (203) are the peaks considered for identification of the C36 phase from C14. The crystallographic information used was detailed in Chapter II.

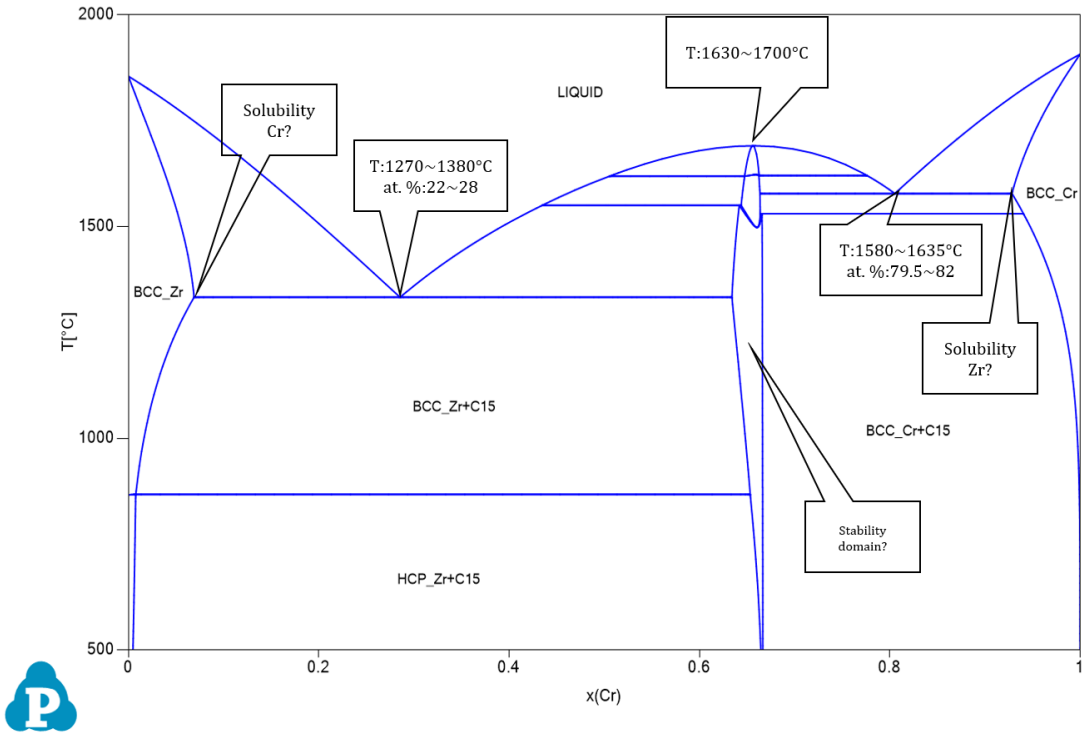

Figure III-4 Identified uncertainties in the Zr-Cr phase diagram. Background by Lafaye *et al.* [7].

III.2.1.3 Thermodynamic studies

There were very few experimental thermodynamic data for the Laves phases of the Zr-Cr system. Skripov and Mirmelstein [34] measured the specific heat capacity of $ZrCr_2$ C15 from 5.3K to 293K by adiabatic calorimetry. Recently, Samanta and Jain [35] determined the specific heat capacity of the same phase from 298K to 860K by DSC. Matsui [36] determined indirectly the enthalpy of the formation of $ZrCr_2$ C15 as -14.8±1.9 kJ/(mol. atom) from the measurement of the Cr vapor pressure over a $ZrCr_2$ sample by Knudsen effusion mass spectrometry. No other experimental studies were published on the thermodynamic properties of $ZrCr_2$. Heat capacity and standard enthalpy of formation will be measured again in this work by different methods, respectively relaxation calorimetry and solution calorimetry in liquid aluminum.

III.2.2 DFT results

Numerous DFT calculations have been performed on the Laves phases of $ZrCr_2$ to determine the enthalpy of formation of the different polymorphs (C14, C15, C36) at 0K. The published values are summarized in Table III-4.

The enthalpy of formation values of C14 vary from -3.66 kJ/mol [4] to -21.3 kJ/mol [37], of C15 from -7.3 kJ/mol [38] to -32.1 kJ/mol [39] and of C36 from -6.42 kJ/mol [4] to -25.58 kJ/mol [37]. The values show a wide dispersion and, for the C15 phase, are significantly less exothermic than the only experimental value. This highlights the need for a new experimental determination of the enthalpy of formation.

Table III-4 Calculated enthalpy of formation of Laves phases of $ZrCr_2$ in literature.

Author	Type	Enthalpy of formation/ $kJ.mol^{-1}$	Enthalpy of formation/ $kJ.mol^{-1}.atom^{-1}$	Approximations*
Chen [40]	C14	-9	-3	PAW-PW91
Pavlů [4]	C14	-3.66	-1.22	PAW-PBE
Lu [5]	C14	-9.06	-3.02	PAW-PW91
Sun [37]	C14	-21.3	-7.1	APW+lo*-PBE
Lafaye [7]	C14	-3.33	-1.11	PAW-PBE
Krčmar [41]	C15	-14.5	-4.8	USPP-PW91
Kellou [42]	C15	-21.1	-7.0	FP-LAPW-PBE
Chen [40]	C15	-14.5	-4.8	PAW-PW91
Yao [39]	C15	-32.1	-10.7	ScRLDA-PBE
Pavlů [4]	C15	-8.64	-2.88	PAW-PBE
AFLOW[43]	C15	-13.9	-4.6	PAW-PBE
OQMD [44]	C15	-10.4	-3.5	PAW-PBE
Sarhaddi[45]	C15	-15.6	-5.2	PWPP/USPP-PBE
Lu [5]	C15	-14	-4.7	PAW-PW91
Sun [37]	C15	-28.9	-9.63	APW +lo-PBE
Lafaye [7]	C15	-8.25	-2.75	PAW-PBE
Pavlů [4]	C36	-6.42	-2.14	PAW-PBE
Chen [40]	C36	-12.1	-4.03	PAW-PW91
Lu [5]	C36	-11.8	-3.94	PAW-PW91
Sun [37]	C36	-25.58	8.53	APW +lo-PBE

* Note as the electronic structure for core electrons-exchange and correlation functional.

III.2.3 CALPHAD assessment

Zeng *et al.* [2] performed the first CALPHAD assessment of the Cr-Zr system (Figure III-5). They mostly accepted the results of Petkov *et al.* [15], and then admitted that the three $ZrCr_2$ Laves polymorphs (C14, C15 and C36) were stable. An important difference between the Arias and Zeng versions is that the former phase diagram (Figure III-1) is manually drawn according to evaluated invariant temperatures and compositions, while the Zeng's one, with superimposed

experimental data, is made by the computer calculation method now called CALPHAD, which includes a description of the Gibbs energy of each phase in the system. Another visible difference is that Arias assumed the composition range did not depend on temperature up to 1332°C for $ZrCr_2$, whereas Zeng considered the temperature effect on the composition range. To achieve the overall consistency between all experimental points at high temperatures and the modeling, Zeng used a three-term Redlich-Kister polynomial, linearly dependent on temperature, for the description of the excess Gibbs energy of the liquid phase. For the Laves phases, a Wagner-Schottky model was used to describe the non-stoichiometric range (Table III-5).

Table III-5 Laves phase models in the various CALPHAD studies.

Author	Phase	Sublattice formula
Zeng [2]	C14	$(Cr,Zr)_6(Cr,Zr)_4Cr_2$
	C36	$(Cr,Zr)_6(Cr,Zr)_4Cr_2$
	C15	$(Cr,Zr)_2(Cr,Zr)_1$
Yang [6]	C14/Hexagonal phase	$(Cr,Fe,Zr)_2(Cr,Fe,Zr)_1$
	C15/Cubic phase	$(Cr,Fe,Zr)_2(Cr,Fe,Zr)_1$
Lu [5]	C14/C36/C15	$(Cr,Nb,Zr)_2(Cr, Nb,Zr)_1$
Lafaye [7]	C14	$(Cr,Nb,Sn,Zr)_4$ $(Cr,Nb,Sn,Zr)_2$ $(Cr,Nb,Sn,Zr)_6$
	C36	$(Cr,Nb,Sn,Zr)_4$ $(Cr,Nb,Sn,Zr)_4$ $(Cr,Nb,Sn,Zr)_{16}$
	C15	$(Cr,Nb,Sn,Zr)_2$ $(Cr,Nb,Sn,Zr)_1$

It must be stressed that no experimental thermodynamic data were available to support the Zeng's optimization.

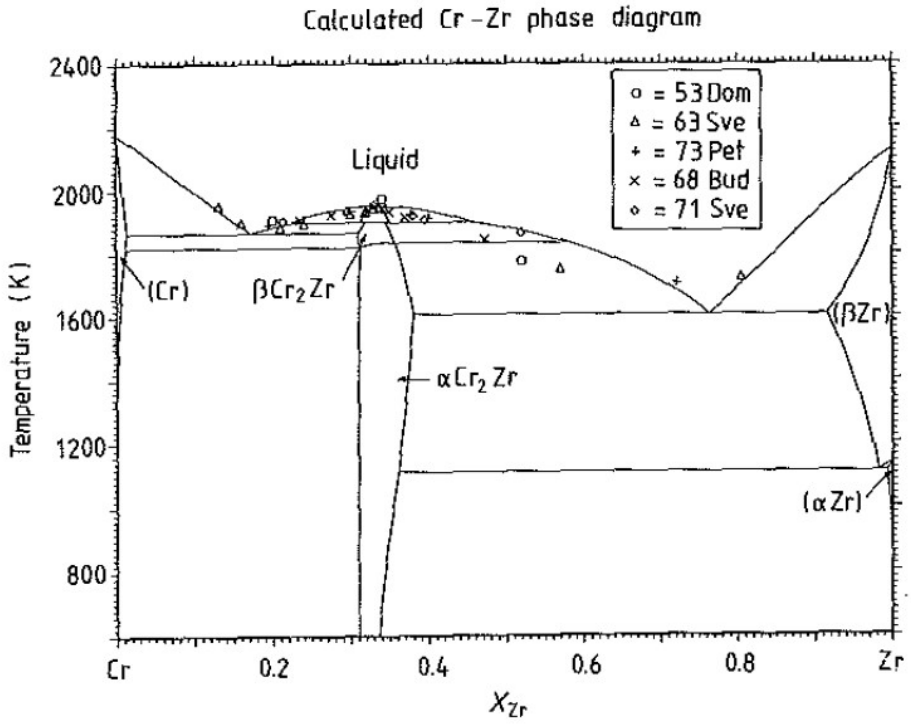

Figure III-5 Phase diagram optimized by Zeng *et al.* [2]

Subsequent CALPHAD assessments of the phase diagrams were published [4]–[7]. The three Laves phases are modeled in these optimizations, except the one of Yang *et al.* [6] (Figure III-6), who combined C14 and C36 in the same phase because of the great difficulty of separating experimentally these two phases. The DFT results of Pavlů *et al.* [4] for the enthalpies of formation of C14 and C15 were used in this assessment. They were less negative than Zeng's ones, and also allowed Yang to obtain a better modeling of the ternary system Zr-Fe-Cr.

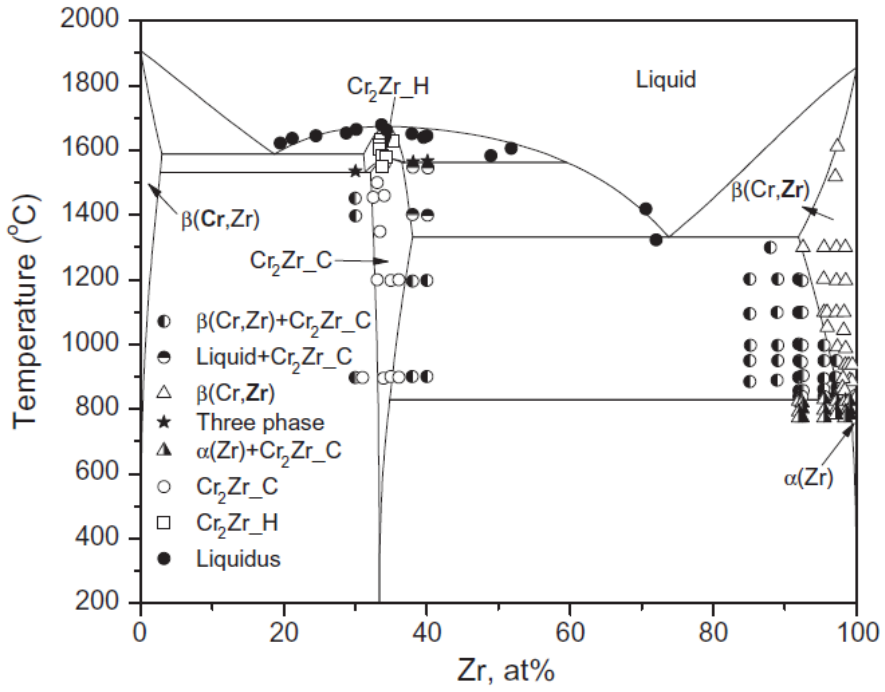

Figure III-6 Phase diagram published by Yang *et al.* [6]

The Laves phases were defined as a hexagonal phase and a cubic phase, both having an extension in the ternary system Zr-Fe-Cr (Table III-5).

Yang *et al.* [6] defined the Laves phases with two sublattices and allowed all 3 elements Cr, Fe, and Zr to exist in the sublattices. The definition was simpler compared to the Zeng's one and ensured compatibility with the extension into the ternary system.

Lu *et al.* [5] performed DFT calculations to determine the enthalpies of formation of the Laves phases. They were much more negative than in the study of Pavlů *et al.* [4]. The three Laves phases were modeled and SQS calculations were made to determine the mixing enthalpy of the *bcc* and *hcp* solution phases. The definition of the Laves phases was similar to the Yang's one. In this work, single-phase regions of *bcc* and C15 were less extensive in composition than in the previous modeling studies [2], [4] with an extension into the Zr-Nb-Cr system. (Table III-5)

Lafaye *et al.* [7] also made DFT calculations of the enthalpy of formation of the Laves phases and SQS calculations for mixing enthalpies of *bcc* and *hcp* solid solutions. The enthalpies of the formation of C14, C15 and C36 are consistent with the simulation results of Pavlů *et al.* [4]. The Zr-Cr modeling was included in the more complex model of the Zr-Nb-Sn-Cr quaternary

system. As a result, the definition of the Laves phases appears to be relatively complex (Table III-5).

A comparison of the phase diagrams of Lafaye *et al.* [7] and Lu *et al.* [5] is shown in Figure III-7. The authors used similar parameters for the definition of the Gibbs energies of phases. We can remark that the two modeled phase diagrams are in agreement, and also consistent with the experimental data. The main discrepancy is related to the Cr-rich side, where Lafaye calculates a higher solubility of zirconium in chromium.

A remark about these modeling is related to the calculated solubility of Zr in *bcc* Cr: respectively reported 2.8% at. [6], 2.4% at. [5], and 7% at. [7]. The values are all too high compared with the experimental value, which was usually considered to be negligible.

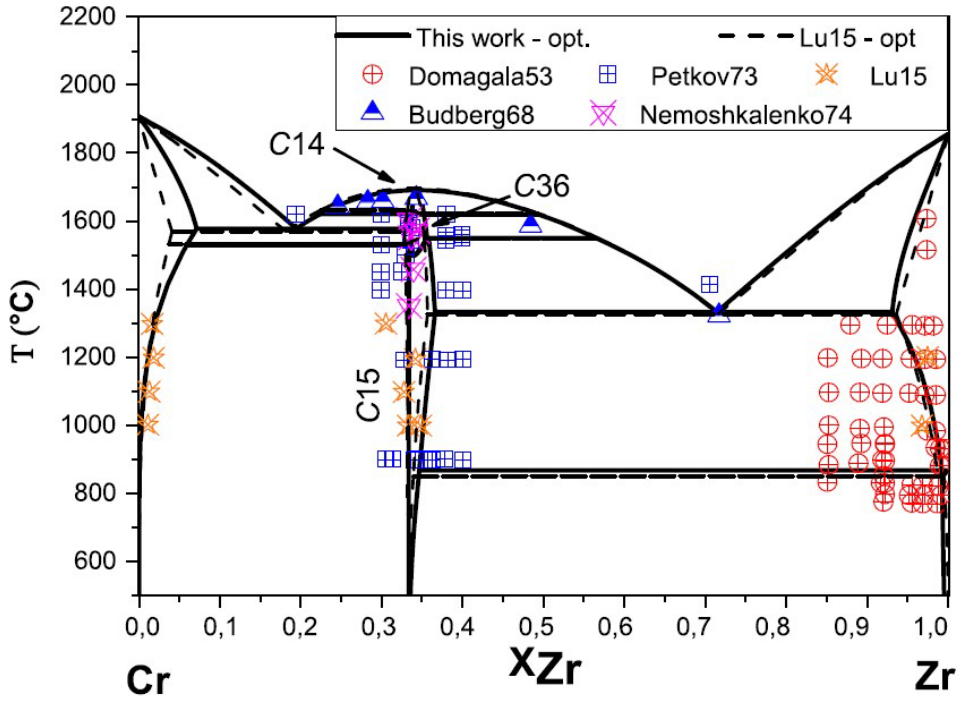

Figure III-7 Phase diagram of Zr-Cr system published by Lafaye *et al.* [7] with a comparison of Lu *et al.* [5]

Since few thermodynamic properties of Laves phases have been measured prior to our work, the authors used the Kopp-Neumann approximation to calculate the C_p in their CALPHAD models. However, a number of weaknesses in this approximation needs to be highlighted:

- ✓ For the C15 phase, it is difficult to determine which phase of Zr should be chosen in the calculation. An approximation combined with bcc Zr and bcc Cr is proper for phase C15, as all these phases adopt a cubic symmetry. But it makes just as much sense to combine Zr hcp and Cr bcc for the C15 polymorph since these phases are all stable at low temperatures.
- ✓ The difference of C_p between C14 and C15 phases can not be calculated by the Kopp-Neumann rule. In practice, the authors often take the same C_p for the different Laves phases [4], [7]. In this situation, an enthalpy or entropy of formation derived from experiments is required to correct the respective stability of phases.

In these CALPHAD modelings, the entropy of the $ZrCr_2$ phases was adjusted during optimization, but not based on experimental C_p data whereas some experimental data are available as previously reported in our bibliography review. Different entropy values can significantly alter the stability of $ZrCr_2$, especially at high temperatures. An experimental value of entropy (which can be calculated using experimental heat capacity data down to near 0K, and will be measured again in this work) is required to establish an accurate model of Gibbs energy.

III.2.4 Working plan

Based on the literature study, the following experimental and modeling works plans have been planned to solve the uncertainties of this system:

1. An experimental study on the $ZrCr_2$ intermetallic compound: to confirm the stable phases, their structures, the substitutional solubility domains and the melting/transition temperatures between $ZrCr_2$ polymorphs. For this purpose, samples will be prepared by arc furnace and annealed in a resistance furnace at pre-defined temperatures and times, then examined by XRD, DTA and SEM-SE, BSE, EDS, EBSD, and EPMA techniques. One of the main objectives of this study, if it can be achieved, will be to confirm or refute the existence of the C36 polymorph as a stable phase.
2. A study on invariant reactions and key points of the phase diagram: including the two eutectic points, the mutual solubility of the pure elements and the eutectoid phase transition on the Zr-rich side. The methods employed will be similar to those mentioned in 1. One of the main objectives of this study will be to reduce the uncertainties on the temperatures of the eutectic reactions.

3. An experimental study on the thermodynamic properties of $ZrCr_2$ including the determination of the enthalpy of formation by drop solution calorimetry and heat capacity measurements over a large temperature interval by combining the relaxation calorimetry (PPMS) from 1.8K to 298 K with DSC between 298 K to 1063K. These thermodynamic properties have been only measured once before and need to be independently confirmed.
4. Complementary DFT calculations with two main objectives: 1) to provide enthalpy of formation values to compare with literature DFT/experimental results, and to estimate the enthalpy of transition between the $ZrCr_2$ polymorphs; 2) to provide estimates of the enthalpies of formation of the metastable end-members of the Laves phase solid solutions for our subsequent CALPHAD optimization.
5. A new CALPHAD evaluation of the system to test the overall consistency of all the selected results, including the new results obtained in this work.

III.3 Experimental results and DFT calculations

III.3.1 Polymorphs, homogeneity domain and phase transitions of the $ZrCr_2$ Laves compounds

III.3.1.1 Polymorphs

The first objective of this study was to confirm the stabilities of the polymorphs of $ZrCr_2$. The samples were prepared by direct fusion of the metals and were heat-treated for a wide range of temperatures and for various dwell times (Table III-6). The chromium vaporization during the high-temperature thermal treatment was monitored by weighting each crucible with the sample before and after the annealing. The samples were examined by powder XRD and the resulting diffractograms were analyzed by the Rietveld method using the Fullprof software [46].

Table III-6 Annealed and as-cast samples of $ZrCr_2$: chromium compositions by EDS and phase contents by XRD

Treatment	EDS/at. %	XRD/at. %		
		C14	C15	χ^2
as-cast	65.5±0.1	100	0	
as-cast		99.67	0.33	
as-cast		100	0	
as-cast	66.81±0.35	100(1.37)	0	7.38
800°C-1.25h		100(0.92)	0	27.7
800°C-1h		99.59	0.41	
850°C-1h	67.74±0.64	100(2.93)	0	9.13
900°C-12h		99.97(0.01)	0.03(0.01)	12.9
1000°C-1h		98.02(0.00)	1.98(0.00)	26.0
1000°C-1h	67.41±0.24	100(2.07)	0	6.30
1125°C-1h		58.21(1.47)	41.79(0.96)	33.9
1125°C-1h	67.06±0.1	81.07(3.69)	18.93(1.75)	12.9
1250°C-1h		5.22(0.33)	94.78(0.32)	7.93
1300°C-1h	66.92±0.24	0	100(0.89)	5.74
1325°C-1h		0.29(0.00)	99.71(0.00)	16.4
1350°C-1h		4.4(0.29)	95.6(0.67)	5.69
1500°C		0.66(0.32)	99.34(1.48)	12.7
1560°C-0.5h		0	100	10.2
1710°C-10min		0	100(1.85)	14.92

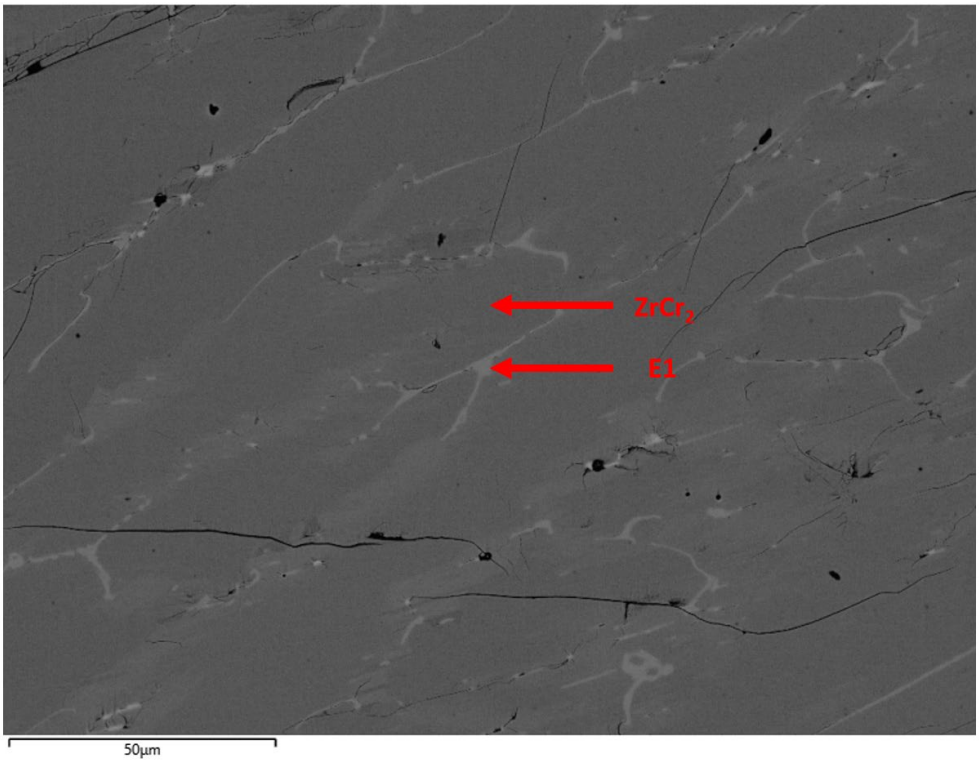

Figure III-8 The micrograph in BSE mode of an as-cast sample with 65.5% at. Cr

In Figure III-8, the surface composition contrast of an as-cast sample Zr33Cr67 is presented. The overall composition of the sample was measured as 65.5% at. Cr which is slightly lower than the target composition (67% at. Cr), probably as a result of Cr vaporization during the arc melting. The $ZrCr_2$ phase was crystallized as a primary phase during the cooling of the sample, occupying the majority of the section. The remaining liquid solidified as E1 eutectic at the intergranular zones. However, these white zones were too thin (typically with a width of around a few microns) to perform accurate composition measurements.

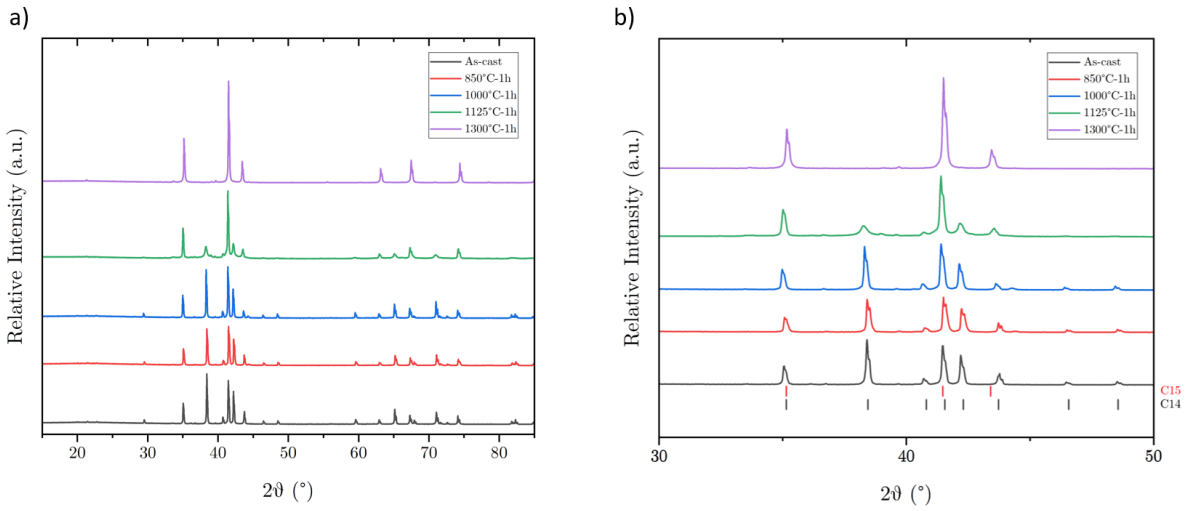

Figure III-9 XRD patterns of as-cast samples and samples annealed 1 h at 850, 1000, 1125 or 1300°C a) 15°-85° range; b) 30°-50° range, with Bragg peaks of C14/C15 Laves phases.

Figure III-9 illustrates the phase changes of the $ZrCr_2$ crystal structure according to the various annealing temperatures and dwells. The C14 hexagonal phase, which is the most stable polymorph of $ZrCr_2$ at high temperatures, is the only phase detected in the as-cast sample.

The samples annealed at 850°C and 1000°C for 1 hour also show the C14 crystalline form, which is in principle not stable at these annealing temperatures. As the transition between the Laves phases is sluggish, the samples were not able to transform to the C15 structure under the applied annealing conditions (temperature and time).

These samples also confirmed the existence of the C14 phase of $ZrCr_2$ in the high-temperature range, and C15 in the low-temperature one. These findings are in complete agreement with the previous studies [24].

The sample annealed (1125°C-1h) shows a two-phase mixture of C14 and C15, meaning that these samples were in the process of being converted from C14 to C15. The work of Petkov *et al.* [15] suggests the following phase transformations on cooling: C14→C36→C15 with the respective transition temperatures 1620°C and 1590°C. On this basis, a certain fraction of the C36 phase would be expected in these samples, particularly at the interfaces between C14 and C15. These samples were therefore carefully examined by XRD and SEM-EBSD.

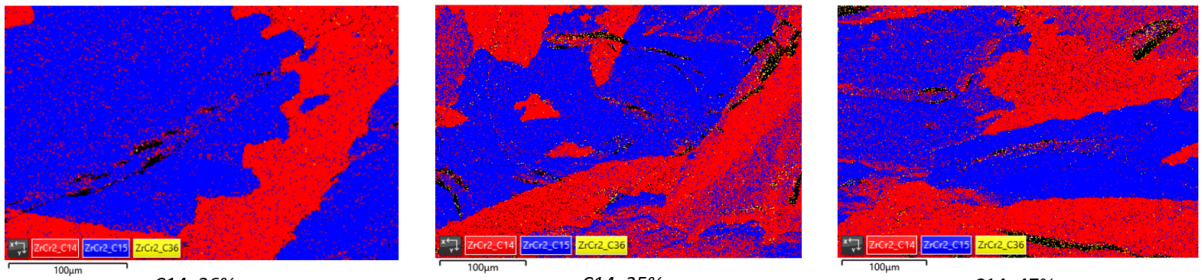

Figure III-10 EBSD maps of $ZrCr_2$ specimens annealed 1 h at 1125°C. C14: red zones, C15: blue zone, C36: yellow zone. The phase fraction of each polymorph detected is noted below each figure in % at.

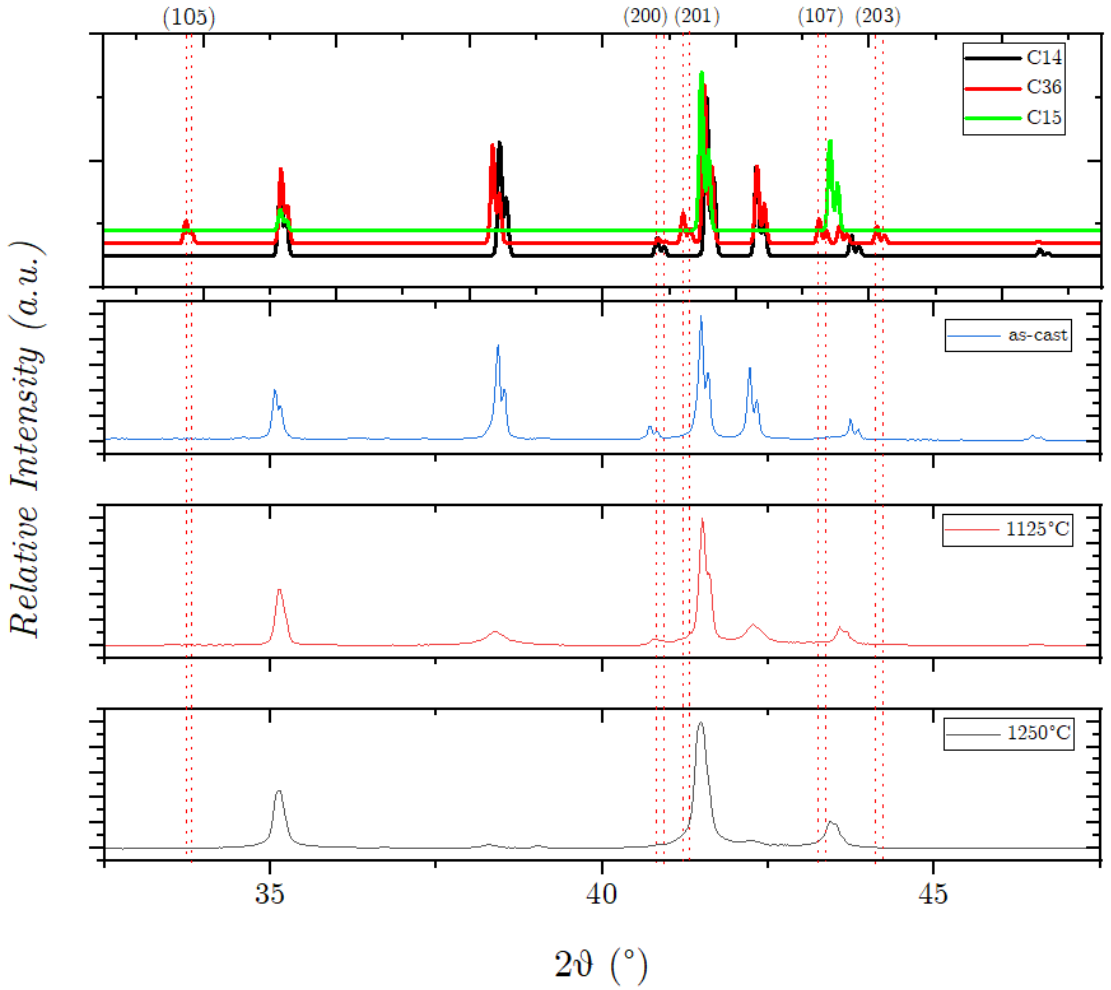

Figure III-11. 30°-50° range of XRD patterns of samples at the as-cast state or annealed 1h at 1125°C, or 1250°C. The top of the figure shows a comparison of the calculated diffraction peaks of the C14, C36 and C15 structures. Crystallographic parameters used in the calculations are detailed in Chapter II. The vertical red dotted lines and Miller indices show the diffraction peaks to identify C36 from C14.

The EBSD maps of Figure III-10 show large zones of the C14 and C15 phases whereas the C36 phase only represents a very small surface fraction. The surface fractions of the three phases

shown in Figure III-10 are: a) C14 36% at., C15 64% at., C36 0% at.; b) C14 35% at., C15 64% at., C36 1% at.; c) C14 47% at., C15 52% at., C36 1% at. In the figure, the spots of the C36 phase are barely visible. More importantly, no C36 phase zones were found at the interfaces between the C14 and C15 phases. This shows that the transformation between C14 and C15 can be direct.

XRD results shown in Figure III-11 are consistent with the EBSD results. The diffraction peaks of the planes (105), (201), (107) and (203) were used to distinguish the C36 phase from the C14. These peaks were not visible in the XRD patterns, which tends to confirm a transition between the C14 and C15 phases without the C36 one.

This finding is consistent with some earlier studies [8], [9], [12], [14], [16], [23], [24], in which the C14 and C15 structures were the only Laves phases unambiguously identified in the Zr-Cr binary system.

Nevertheless, our experiment does not unquestionably prove that C36 does not exist in the Zr-Cr system. At this stage, it is clear that C36 is not found in all our experimental results, and it does not affect the direct transition between C14 and C15. Considering the lack of experimental data on this phase in literature, it will be therefore decided not to take the C36 phase into account for our CALPHAD model. A similar choice was previously made by Yang *et al.* [6].

Crystallographic parameters of the two stable phases were determined by Rietveld refinement of $ZrCr_2$ samples that were 100% C14 or 100% C15. The sample used for C14 was an as-cast sample and the sample for C15 was annealed at 1500°C for 30 minutes. The Rietveld plots are shown in Figure III-12. To minimize the difference between the experimental and simulated diffraction patterns, the least–square minimization procedure was carried out by considering reliability factors such as the weighted/unweighted profile R-factor (R_{WP}/R_P), the expected R-factor (R_{EXP}) and the χ^2 (goodness of fit factor). All the refinements were obtained with χ^2 around or less than 10. The refined crystallographic lattice constants of these two phases are listed in Table III-7 with the values of the Rietveld refined parameters and also compared to the existing literature data.

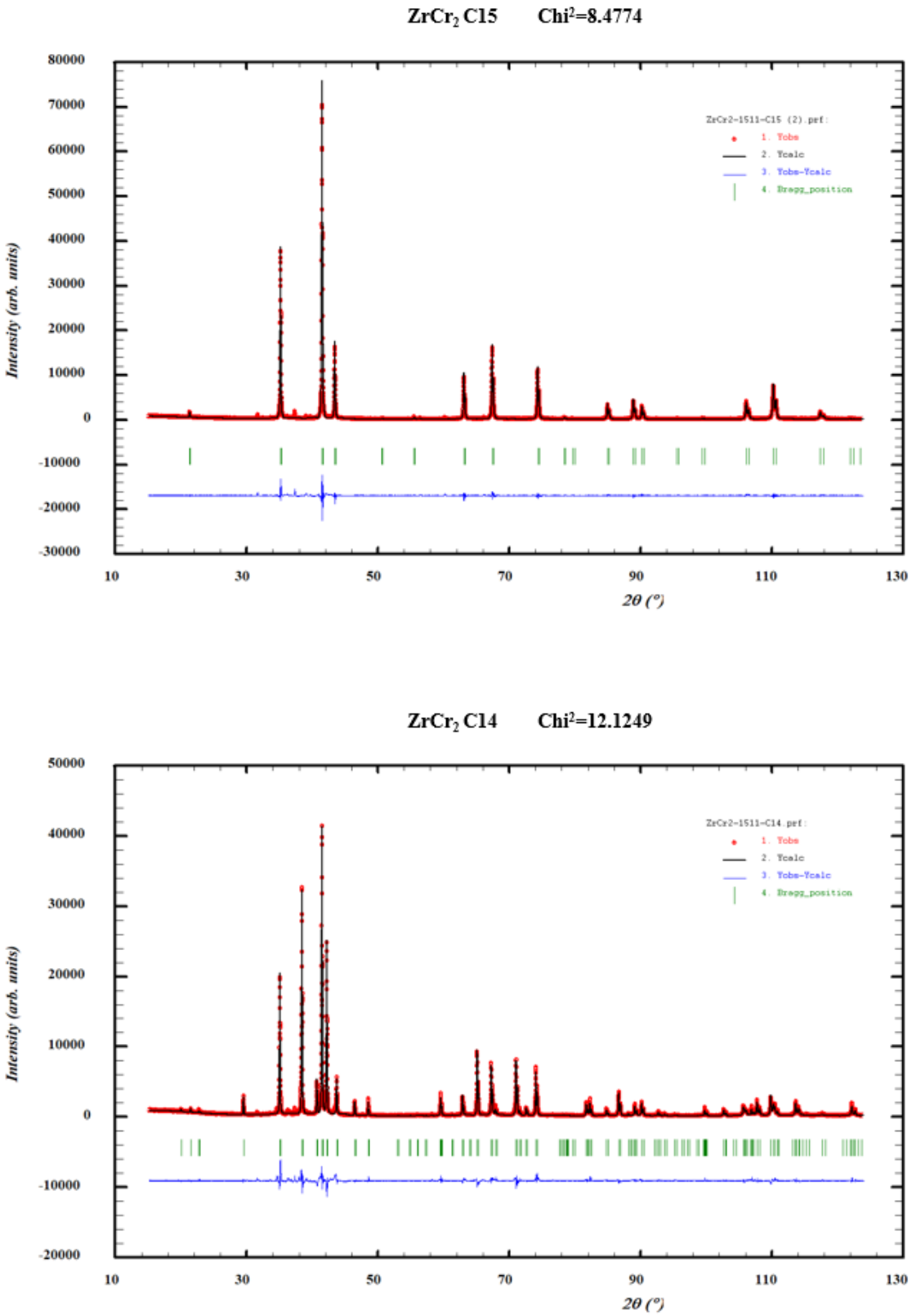

Figure III-12 Rietveld fitting of the XRD patterns of $ZrCr_2$ C15 (above) and C14 (below) $ZrCr_2$ polymorphs

Table III-7 Refined parameters of C14 and C15 $ZrCr_2$

Refined parameters	**$ZrCr_2$ C15**				**$ZrCr_2$ C14**			
Lattice parameters(Å)	a=7.211 (1)				a=b=5.114 (1) c=8.273 (1)			
Lattice parameters in literature (Å)*	a=7.215				a=b=5.102 c=8.273			
Unit cell volume(Å^3)	374.98				187.388			
Atomic positions (element x y z)	Cr	0	0	0	Cr1	0	0	0
					Cr2	0.829	0.661	0.250
	Zr	0.375	0.375	0.375				
					Zr	0.333	0.667	0.0587
R_p	6.47				9.74			
R_{wp}	8.44				13.9			
R_{exp}	3.48				3.98			
χ^2	5.89				12.1			

* C15 :[47] ; C14 :[48]

In the literature, some studies [17], [29] showed XRD patterns of $ZrCr_2$ samples containing unfitted peaks that do not correspond to the C14 or C15 structures. One possible explanation is that these samples could be slightly oxidized after annealing and form the Zr_3Cr_3O ternary phase as a side product, which has hardly been studied in the past. The characterization of this ternary phase will be presented in Chapter IV. Here, an XRD pattern of a slightly oxidized $ZrCr_2$ sample is shown in Figure III-13. The sample was annealed at 1560°C for 0.5 h and showed a nearly 100% C15 phase fraction. Some additional peaks are found which could not be fitted with the C14 phase. These peaks were finally identified to be representative of a small percentage of the Zr_3Cr_3O phase which has been characterized in our work on the Zr-Cr-O ternary system.

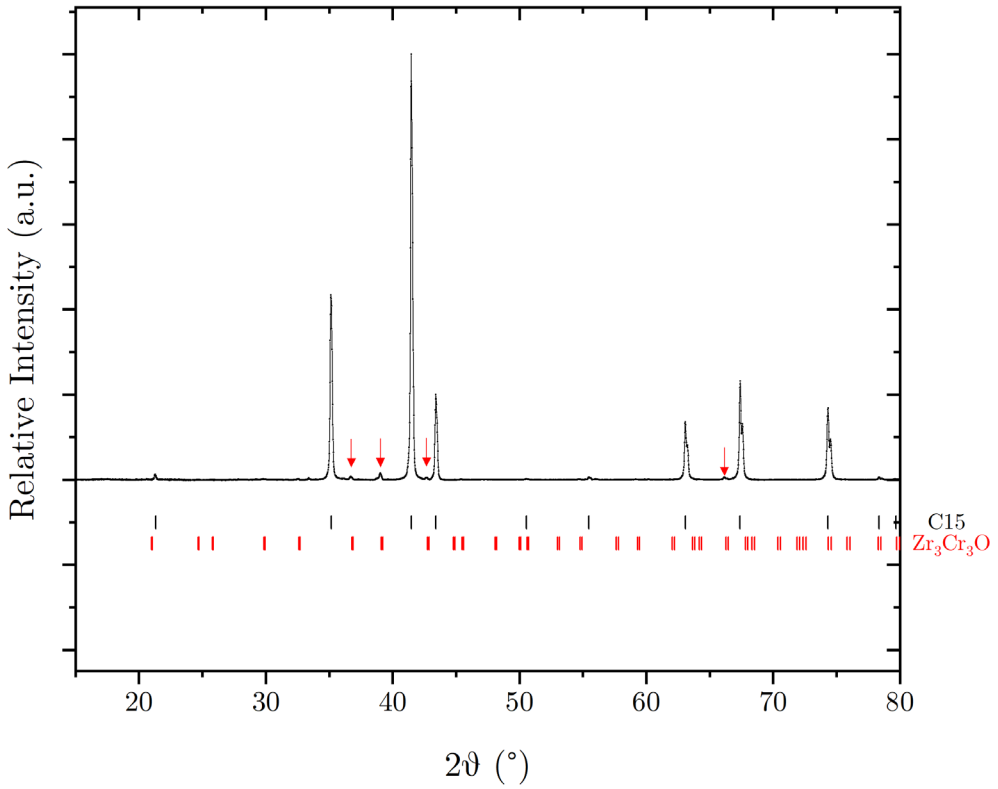

Figure III-13 XRD pattern of a $ZrCr_2$ sample annealed at 1560°C for 0.5 h (major phase C15) that is slightly oxidized (Zr_3Cr_3O). Red arrows point out the weak peaks indicating oxidation.

III.3.1.2 $ZrCr_2$ non-stoichiometry range

As presented in the literature review, the non-stoichiometry range of the $ZrCr_2$ phase is an important issue that was not fully resolved.

To measure the solubility limits on both sides of the $ZrCr_2$ compound, the first objective is to elaborate biphasic samples (Zr+$ZrCr_2$) or ($ZrCr_2$+Cr), that contain large zones of $ZrCr_2$ which should allow us to perform accurate composition measurement by SEM/EDS. The target compositions were selected so that $ZrCr_2$ was the primary phase that crystallized when the liquid cooled. On the Zr-rich side, sample compositions were chosen in the range between 28.5% and 64%. at. Cr whereas on the Cr-rich side, they were chosen between 68% to 80% at. Cr. To start, 8 as-cast samples on the Zr-rich side and 7 as-cast samples on the Cr-rich side were prepared and analyzed. The preparation conditions and the results of the analyses of these samples are listed in Table III-8. The annealing time of the samples was strictly controlled to avoid oxidation and loss of mass through the vaporization of Cr.

The compositions of as-cast samples and annealed samples at different temperatures from 1150 to 1300°C were measured by SEM-EDS. The as-cast samples conserved their phase content prevailing at solidus temperatures as a result of fast cooling. The lattice parameters of the phases were fitted by the Rietveld method. The compositions were calculated as an average of at least 12 compositions detected in different acquisition areas to reduce measure errors to ±0.1% mass.

Table III-8 Alloy compositions investigated on both sides of the $ZrCr_2$ compound. Results of SEM/EDS composition measurements and lattice parameter values of the C14 and C15 phases obtained by Rietveld refinement of the XRD patterns.

Sample composition in at %	**Treatment**	X_{Sample} **at.% Cr**	X_{ZrCr_2} **at.% Cr**	χ^2	**Lattice parameters (Å)**		
					C14: a=b	**C14: c**	**C15: a=b=c**
Zr75Cr25	as-cast	24.8	-				
Zr74Cr26	as-cast	25.5	-				
Zr74Cr26	1200°C-10h	25.1	63.7				
Zr70Cr30	as-cast	28.5	-				
Zr70Cr30	1300°C-10h	29.4	63.8				
Zr50Cr50	1150°C-2h	48.4	64.3				
Zr38Cr62	as-cast	60.1	64.4	10.9	5.115(1)	8.283(1)	
Zr35Cr65	1300°C-10h	63.7	65.0	8.2			7.213(1)
Zr30Cr70	as-cast			5.6019	5.103(1)	8.272(1)	
Zr29Cr71	as-cast	73.1	66.7				
Zr29Cr71	1150°C-2h	68.8	68.0	9.3132	5.102(2)	8.279(1)	7.206(1)
Zr22Cr78	as-cast	77.1	70.2	5.9828	5.104	8.298	
Zr20Cr80	1300°C-10h	76.8	68.9				
Zr22Cr78	1150°C-2h	77.4	70.5	8.91			7.192(1)
Zr13Cr87	as-cast	83.9	70.5				

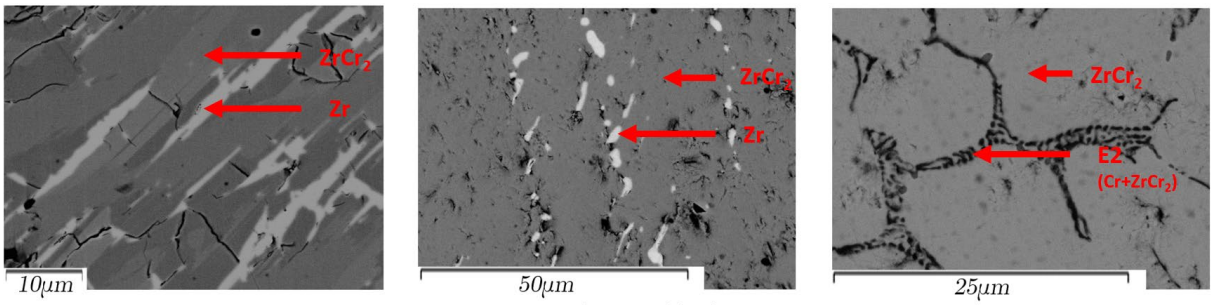

Zr38Cr62(60.1 at. %Cr) — *As cast*

Zr35Cr65(63.7 at. %Cr) — *Annealed 10 h at 1300°C*

Zr29Cr71(68.8 at. %Cr) — *Annealed 2 h at 1150°C*

Figure III-14 Micrographs of 3 samples. The images were captured by the SEM-BSE detector and the compositions between parentheses are determined by SEM-EDS at an accelerating voltage of 20 kV and a working distance of 10 mm.

The micrographs of 3 representative samples of Table III-8 are reported in Figure III-14. The sample Zr38Cr62 was an as-cast sample, whereas the other ones were annealed at different temperatures (1300°C for Zr35Cr65 and 1150°C for Zr29Cr71). The samples Zr38Cr62, and Zr35Cr65 are all biphasic with Zr and $ZrCr_2$ phases whereas $ZrCr_2$ and Cr phases are present in the Zr29Cr71 sample.

In the micrographs of the Zr38Cr62 and Zr35Cr65 samples, the bright zone abnormally stands for the nearly pure Zr but not E1 eutectic structure. The anomalies in measurements could be caused by the nature of this eutectic structure, which is difficult to identify at low magnification; or by a slight oxidation of the sample, which stabilized the Zr phase.

For the Zr29Cr71 sample, the dark zone is identified in a eutectic structure form between the primary $ZrCr_2$ dendrites.

Our experimental solubility limit points on both sides of the non-stoichiometric compound $ZrCr_2$ are superimposed on the phase diagram in Figure III-15. The extension of the stability domain of $ZrCr_2$ on the Zr-rich side is maximum at the eutectic temperature T_{E1}. In our work, the composition of the $ZrCr_2$ phase at T_{E1} can be assessed using the as-cast Zr38Cr62 sample. Our measurements gave 65±1% at. Cr and is in good agreement with the phase diagram modeled by Lu [6]. On the Cr-rich side, the non-stoichiometry of $ZrCr_2$ reaches its maximum value at the eutectic temperature T_{E2}. As shown in the following figure, we measured chromium contents up to 70.5% at. Cr in the $ZrCr_2$ phase. These results were in good agreement with [15], [17] (~69% at. for both), but much larger than values that can be estimated from the modeling of the system by Lu and by Lafaye (67.9% at.).

As already reported for the Laves phases of other systems (Nb-Cr, Zr-Co, Nb-Co, etc.) and according to Kanazawa *et al.* [17], the non-stoichiometry of $ZrCr_2$ on the Cr-rich side can be explained by the following geometrical argument. Since the diameter of the Cr atom is much smaller than that of the Zr atom, it is easier for the atom to occupy the Zr atom sublattice sites in the $ZrCr_2$ crystal than the reverse. This occupation leads to anti-site defects. On the Zr-rich side, the excess Zr atoms could only be introduced in the vacancies of the structure due to their relatively bigger size. This is the reason why the Laves phase in the Zr-Cr system should theoretically present higher stoichiometry deviation on the Cr-rich side than on the Zr-rich side.

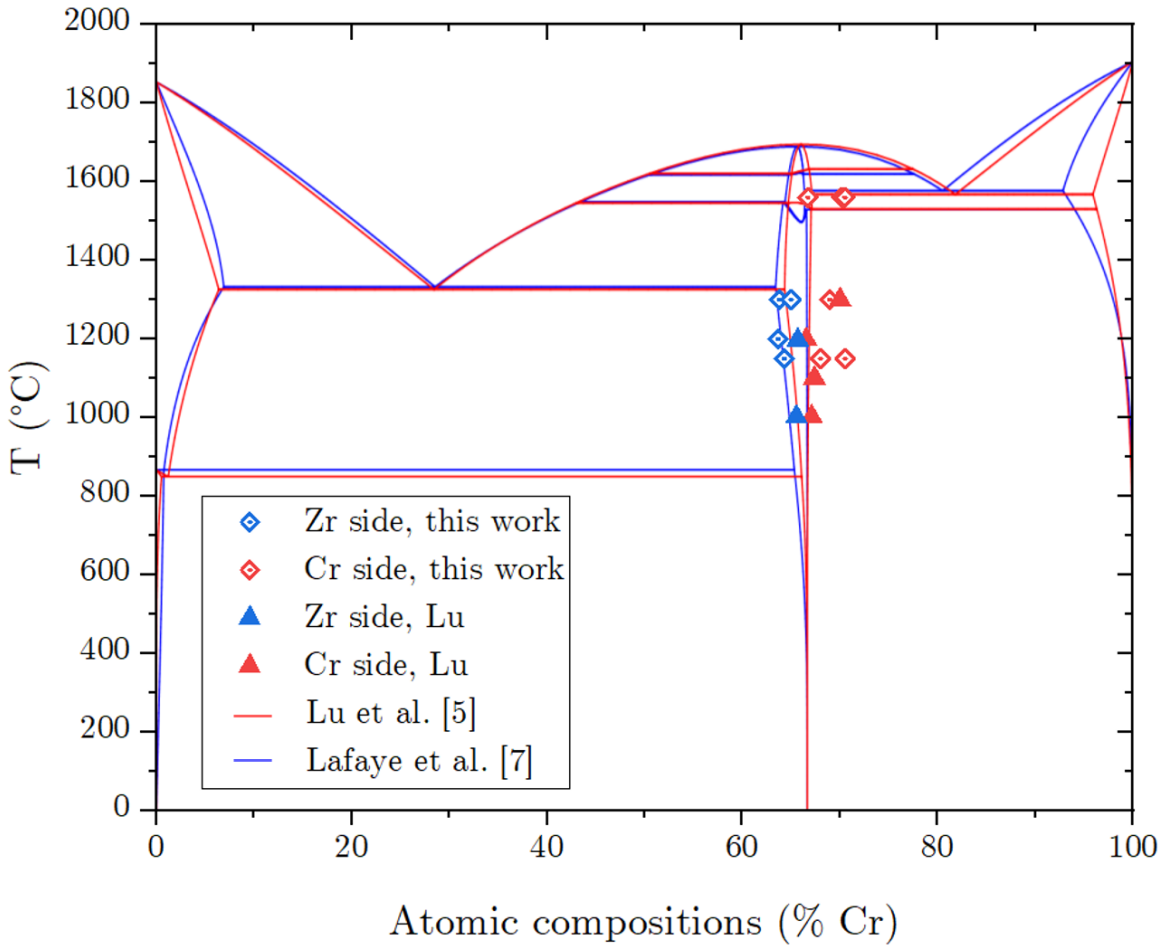

Figure III-15 Measurements of solubility limits on the Zr-rich (blue points) and Cr-rich (red points) sides of $ZrCr_2$ superimposed on the phase diagrams of Lafaye *et al.* [7] (blue lines) and Lu *et al.* [5] (red lines)

III.3.1.3 C14/C15 transition temperature and melting temperature of $ZrCr_2$

A step annealing method was used to determine the transition temperature between C14 and C15 and the melting temperature of $ZrCr_2$. The method has been detailed in Chapter II.

To measure the temperature of the transition between the C14 and C15 structures of $ZrCr_2$, a first annealing test was realized at 1600°C for 30 min, a temperature reported to be in the stability domain of the C36 phase [15]. The sample was then examined by XRD and 100% C15 $ZrCr_2$ was found, as shown in Figure III-16.

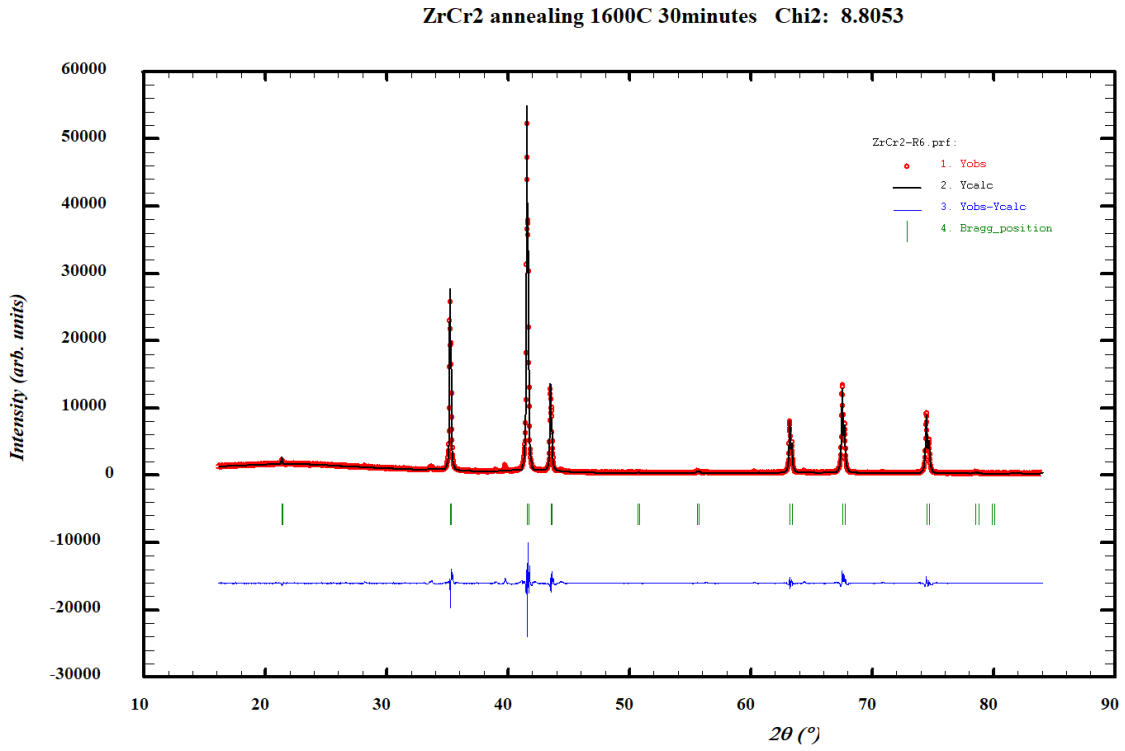

Figure III-16 XRD pattern of the $ZrCr_2$ sample annealed 30 min at 1600°C

The tests were repeated every 10°C from 1653°C to 1693°C (slightly lower than the highest melting temperature of $ZrCr_2$ reported in the literature [8]). The annealing times were reduced from 30 to 10 min as the temperature was increased from 1653°C to 1693°C to avoid significant sample oxidation and/or Cr vaporization. The samples were then examined by XRD.

During initial tests, samples annealed at 1703°C were accidentally oxidized after 10 minutes of annealing. This was also the highest annealing temperature achievable with our furnace. This is an additional reason to explain why the maximum temperature for the successive annealing tests was set at 1693°C.

Two major results were obtained with these experiments:

1. No trace of melting was observed at the upper annealing temperature considered in this work, i.e. at 1693°C. Our results indicate that the melting temperature of the $ZrCr_2$

compound should be higher than 1693±7°C, which is higher than most of the melting temperatures reported for $ZrCr_2$ in the literature [9], [12], [14]–[16], but is consistent with the result of Domagala *et al.* [8], who suggested a melting temperature of 1700°C. However, the accurate melting temperature of $ZrCr_2$ has not been obtained in this work.

2. All these samples were found monophasic with a pure C15 phase. Neither C14 nor C36 phase was found in these samples. All the XRD patterns on the different annealed samples (Figure III-17) were similar to the XRD pattern of the sample annealed at 1600°C for 30 min (Figure III-16). One possible explanation for this result is that our furnace which cools down slowly allows the complete C14 to C15 transformation.

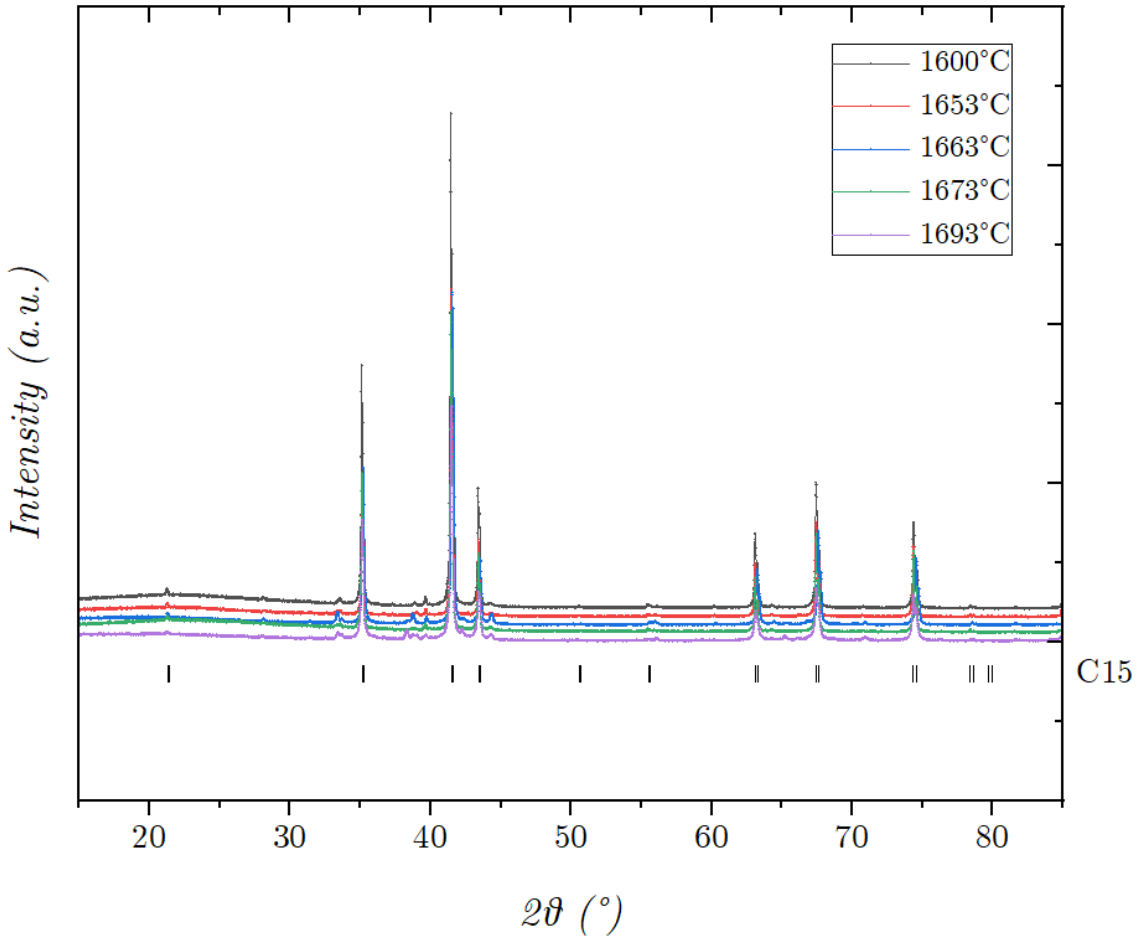

Figure III-17 XRD patterns of step annealing $ZrCr_2$ samples at different temperatures

III.3.2 Eutectic reactions

The composition and temperature of the eutectic point (E1) on the Zr-rich side of the Zr-Cr phase diagram were studied. The temperature of E1 was measured by DTA for two samples

with respective compositions Zr81Cr19 and Zr79Cr21. The DTA results are shown in Figure III-18, where two endothermic peaks were detected. The onset temperatures of peaks were chosen as the more accurate measured temperatures for the corresponding thermodynamic arrests, illustrated in Figure III-19. The temperatures were identified as the intersection point of the interpolated baseline with the "steepest" tangent line of the front peak, which refers to the tangent line that has the largest absolute slope of all the points on the front side of the peak.

The first peak is found at 852.2±0.4°C, which corresponds to the eutectoid reaction (bcc Zr) + $ZrCr_2$ C15 $\rightleftharpoons$ (hcp Zr).

$$T_{Zr,tr} = 852.2 \pm 0.4°C$$

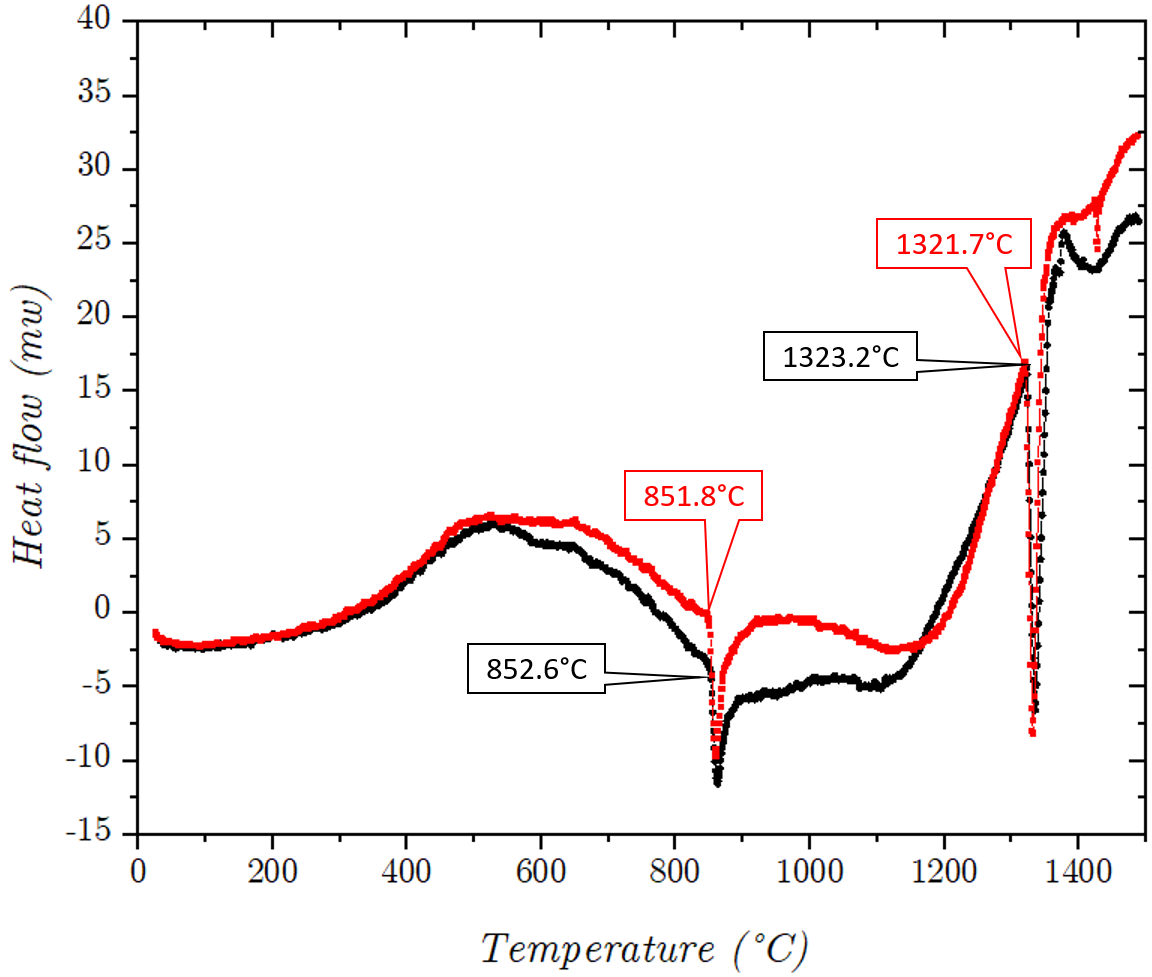

Figure III-18 DTA measurements on 2 compositions located on the Zr-rich side of the Zr-Cr system. Temperature scans are performed from 25°C to 1500°C with a heating rate of 5°C/min. Red line and labels: Zr81Cr19 (measured 21.3% at. Cr with EDS); black line and labels: Zr79Cr21 (measured 22.2% at. Cr with EDS).

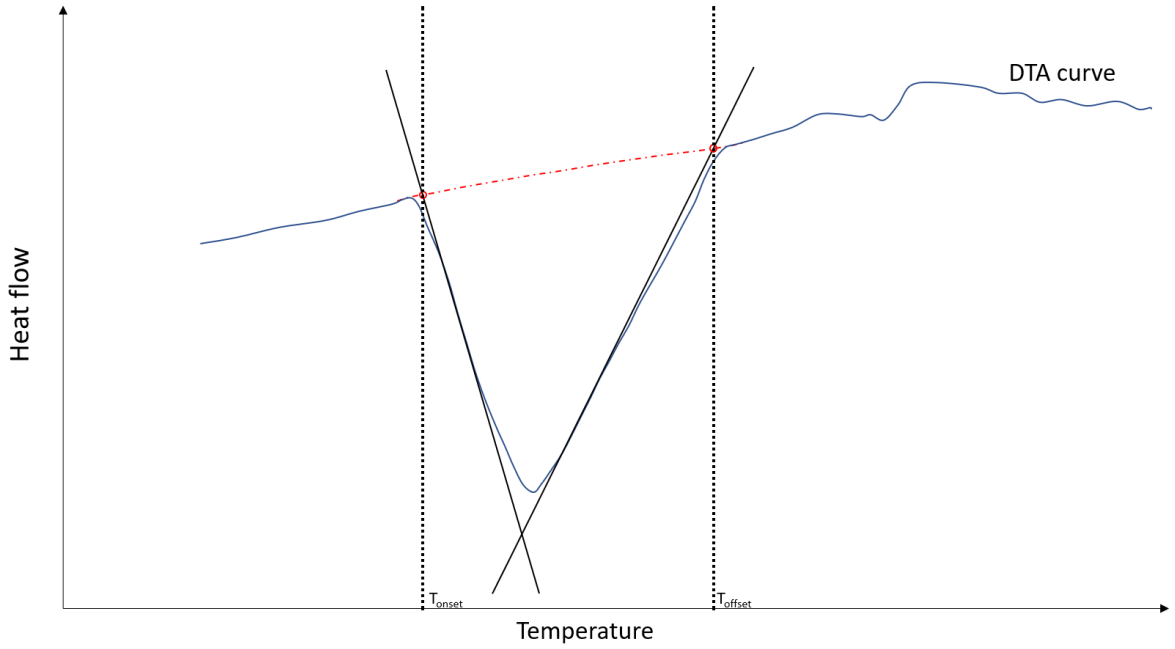

Figure III-19 Representative schema of the method for choosing the onset temperature. The red dotted line is a fitting of the baseline.

The second peak corresponds to the eutectic temperature of E1, which is 1322.4±0.7°C.

A summary of the values of the E1 eutectic temperature published in the literature is reported in Table III-9. Our results are in agreement with [9], [15] but lower than the data in [12], [14], [16].

Table III-9 Comparison of published experimental works on two eutectic points E1 and E2 in the Zr-Cr system and the results of this work

Reference	T_{E1}/°C	X_{E1}/% *at.* Cr	T_{E2}/°C	X_{E2}/% *at.* Cr
Domagala [8]	1280±10	27.8	1635±15	80
Svechnikov [10]	1270	27.8	1590	80
Gebhardt [16]	1355	28		
Budberg [9]	1320±10		1580±10	80
Rudy [14]	1370±5/1380	28		
Svechnikov [12]	1360		1590	80
Petkov [15]	1330	22	1590±10	82
Kanazawa [17]		28		79.5
This work	1322.4±0.7	27.2±0.1	1608±7	80±0.1

The eutectic point temperature (E2) on the Cr-rich side was measured using the same method as previously, i.e. a stepwise annealing test of 10°C from 1540°C to 1660°C. The sample was observed to melt at a temperature of between 1620°C and 1630°C.

To check the accuracy of the method, a temperature calibration was performed with Ti metal using the same annealing conditions. In our tests, Ti was observed to melt between 1680°C and 1690°C. The reported melting temperature of Ti is 1668°C (SGTE [49]). Therefore, our measurement overestimates the reference temperature by 17±5°C.

The eutectic temperature of E2 after calibration taking into account the rule of propagation of measure error becomes:

$$T_{E2} = 1608 \pm 7°C$$

This temperature can be evaluated as reasonably consistent with the measurements of [9], [12], [15], respectively $1580 \pm 10°C$ $1590 \pm 10°C$ and $1590 \pm 10°C$ when we consider the difficulties in achieving precise measurements at high-temperature.

The compositions of the two eutectic points were measured with multiple as-cast samples having different compositions near the eutectic points. The global compositions and the eutectic compositions were all confirmed by SEM-EDS.

Two BSE micrographs are presented:

- ✓ In Figure III-20-a), the sample Zr75Cr25 (with a global composition of 24.8% at. Cr) near E1 has a uniform appearance at the chosen zooming factor. The eutectic 2-phase structure was difficult to resolve.
- ✓ In Figure III-20-b), the sample Zr20Cr80 (with a global composition of 80% at. Cr) near E2 shows a clear eutectic structure.

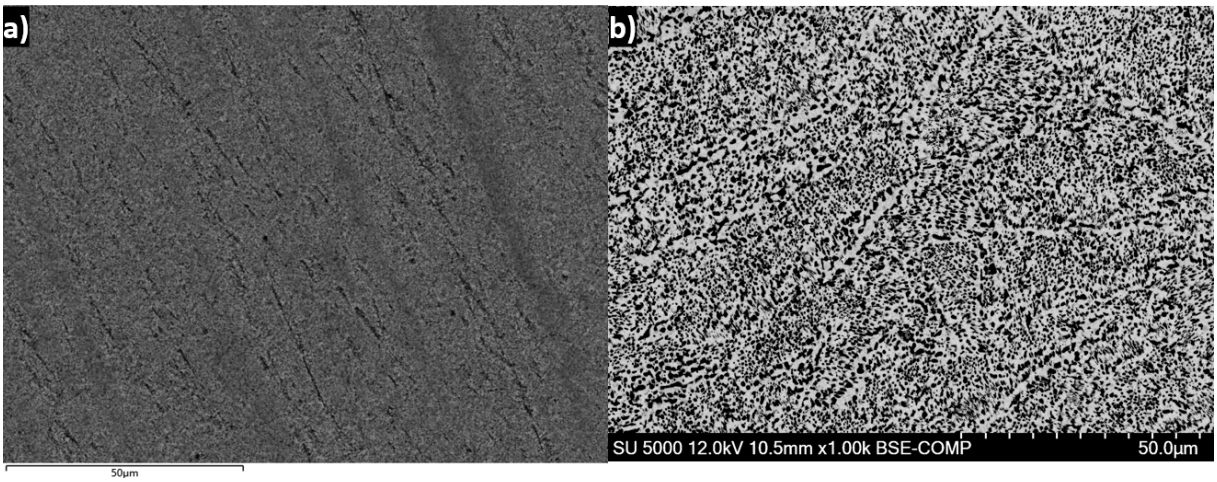

Figure III-20 SEM images in BSE mode a) 24.8% at. Cr; b) 80% at. Cr as-cast samples.

To discriminate the Zr and $ZrCr_2$ phases in the Zr75Cr25 sample, the eutectic microstructure was magnified by a factor of 10k~20k, as shown in Figure III-21. Though different compositions of Cr can be differentiated by a difference in brightness in the micrograph, we did not obtain a clear SEM image of the eutectic structure in this sample.

Compared to E1, the eutectic structure of E2 is easier to observe. Some EDS point measurements in the white and black areas (Figure III-20b) show a Cr/Zr ratio of approximately 2:1 and a practically pure Cr composition respectively, which confirms that the two phases in the eutectic structure are those expected. The eutectic composition was then determined by measuring an average composition in a large zone of homogeneous eutectic structure.

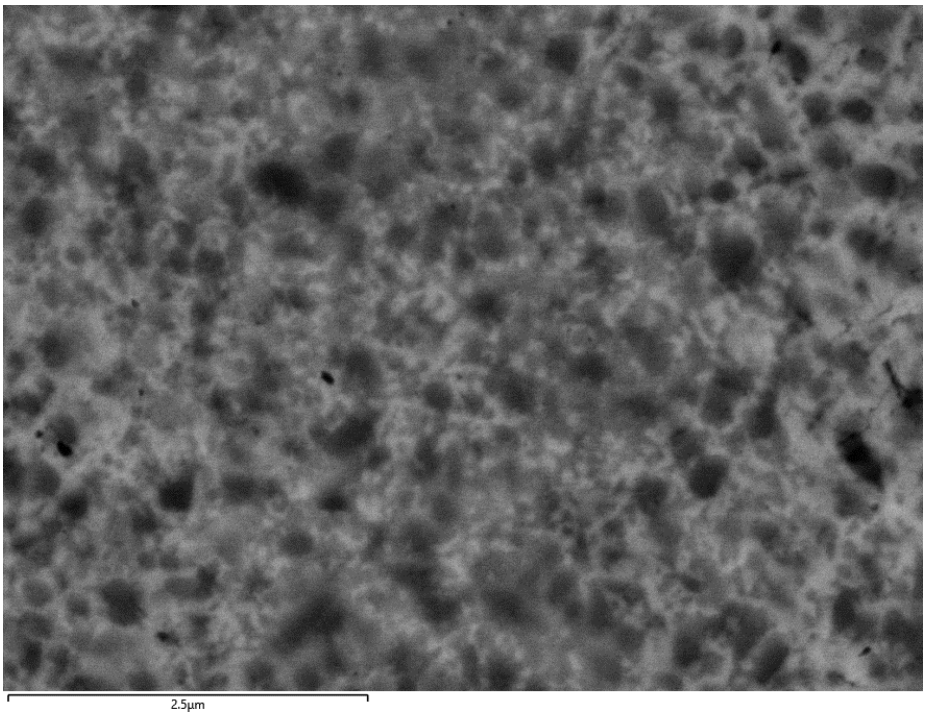

Figure III-21 SEM image in BSE mode of the as-cast sample Zr75Cr25 (24.8 %at. Cr by EDS). The color difference shows a mixing of two phases, whose compositions could not be accurately measured by EDS.

The maximum solubilities of Cr in bcc Zr and hcp Zr in bcc Cr are also measured by following the same method. The solubility of Cr in bcc Zr was measured with as-cast samples Zr75Cr25, the sample of Figure III-20 a). In some areas of this sample, bcc Zr was formed as a secondary phase with maximum solubility of Cr. The solubility of bcc Zr in bcc Cr was measured with sample Zr20Cr80, the sample of Figure III-20 b), and the eutectic structure was sparse enough to realize measurements. The values were then determined by taking the average of at least 30 measurements in different areas of different samples.

Finally, it was found for the eutectic compositions:

$$X_{E1} = 27.2 \pm 0.1\%\ at.\,\mathrm{Cr}$$

$$X_{E2} = 80 \pm 0.1\%\ at.\,\mathrm{Cr}$$

And for mutual solubilities at solid state:

$$\mathrm{Sol}_{\mathrm{Zr(Cr)}} = 7.1 \pm 0.1\%\ at.\,\mathrm{Cr}$$

$$\mathrm{Sol}_{\mathrm{Cr(Zr)}} = 0.5 \pm 0.1\%\ at.\,\mathrm{Zr}$$

The eutectic composition of E1 was reported by different authors. These values can be classified into two groups, [8], [16], [31] constituting the first group of authors who reported a value roughly around 26~28% whereas the second group [1], [15] proposed and agreed with a value of about 22% at. Cr. More recently Kanazawa *et al.* [17] found a value of 28% at. Cr. The result of our study is consistent with Kanazawa, and the values reported by the first group.

For E2, our value is consistent with the eutectic compositions reported in all publications [8], [9], [12], [31] around 80~82% at. Cr.

For the maximum solubility of Cr in bcc Zr, the value of 7.1% at. Cr, we found, is slightly lower than what was proposed in the literature [8], [13], [14], [18], [32] i.e. 8% at. Cr, but always in an acceptable uncertainty interval.

For the maximum solubility of Zr in bcc Cr, as reviewed, the authors agreed with a very weak solubility. However, higher values were reported in the results of recent modeling [5], [7]. Our measurement is consistent with early studies [8], [18] and corresponds to an accurate composition at the eutectic temperature E2. This value will be used for our CALPHAD modeling.

III.3.3 Thermodynamic properties of $ZrCr_2$

III.3.3.1 Enthalpy of formation

Enthalpy of formation of $ZrCr_2$ C14 and C15 phases was measured by drop solution method using a Tian-Calvet calorimeter in Al solvent at 900°C. The value of enthalpy of formation was calculated by a thermal cycle involving the enthalpy of drop solution of pure Zr, Cr and $ZrCr_2$ at infinite dilution. The details and experimental procedures are presented in Chapter II.

The experimental results are listed in Table III-10. The relation between the enthalpy of partial drop solution, $\Delta_{ds}\overline{H}_{298K}^{Texp}$,and the enthalpy of mixing, $\Delta_{mix}H_{Texp}$ is given by Equation (III-1).

$$\boldsymbol{\Delta_{mix}\overline{H}_{Texp} = \Delta_{ds}\overline{H}_{298K}^{T_{exp}} - \Delta H_{L,298K}^{T_{exp}}} \quad \text{(III-1)}$$

where T_{exp} is the experimental calorimeter temperature in K, $\Delta H_{L,298K}^{T_{exp}}$ is the enthalpy increment required to convert the sample from its crystalline state at room temperature to its liquid state at T_{exp}. This term is calculated with the SGTE database [49].

Table III-10 Drop solution experiment data of Cr and C14 or C15 of $ZrCr_2$ types. $\Delta_{ds}\overline{H}_{i,298K}^{Texp}$ is the enthalpy of partial drop solution and $\Delta_{mix}\overline{H}_{Cr,T_{exp}}$ is the enthalpy of mixing calculated at the calorimeter temperature T_{exp} = 900°C.

Sample Type	**Composition (at. ‰)***	$\Delta_{ds}\overline{H}_{i,298K}^{T_{exp}}$ **(kJ/mol)**	$\Delta_{mix}\overline{H}_{Cr,T_{exp}}$ **(kJ/mol)**
Cr	0.81	-16.48	-65.88
Cr	2.82	-20.94	-70.35
Cr	4.95	-14.22	-63.63
Cr	7.03	-18.53	-67.94
Cr	9.32	-18.36	-67.77
Cr	0.57	-19.57	-68.97
Cr	1.67	-17.75	-67.16
Cr	2.82	-20.13	-69.54
Cr	4.13	-18.96	-68.36
Cr	5.32	-17.39	-66.80
Cr	0.66	-21.23	-70.64
Cr	2.03	-16.60	-66.00
Cr	3.52	-19.94	-69.35
Cr	5.06	-22.28	-71.69
Cr	6.56	-17.45	-66.85
$ZrCr_2$ C15**	0.10	-162.35	
$ZrCr_2$ C15	0.29	-167.96	
$ZrCr_2$ C15	0.47	-178.77	
$ZrCr_2$ C15	0.68	-181.18	
$ZrCr_2$ C15	0.92	-184.03	
$ZrCr_2$ C15	0.09	-164.13	
$ZrCr_2$ C15	0.25	-183.63	
$ZrCr_2$ C15	0.48	-177.53	
$ZrCr_2$ C15	0.74	-194.21	
$ZrCr_2$ C15	0.93	-188.63	
$ZrCr_2$ C15	0.07	-159.50	
$ZrCr_2$ C15	0.28	-167.38	
$ZrCr_2$ C15	0.48	-189.67	
$ZrCr_2$ C15	0.68	-192.44	
$ZrCr_2$ C15	0.88	-191.07	
$ZrCr_2$ C14	0.07	-143.03	
$ZrCr_2$ C14	0.29	-171.69	
$ZrCr_2$ C14	0.50	-168.95	
$ZrCr_2$ C14	0.04	-146.49	
$ZrCr_2$ C14	0.15	-165.25	
$ZrCr_2$ C14	0.28	-167.75	
$ZrCr_2$ C14	0.39	-182.45	
$ZrCr_2$ C14	0.50	-187.62	

*Composition reached of sample in solvent after drops.

**Purity of $ZrCr_2$ samples was confirmed by XRD, all >97% at.

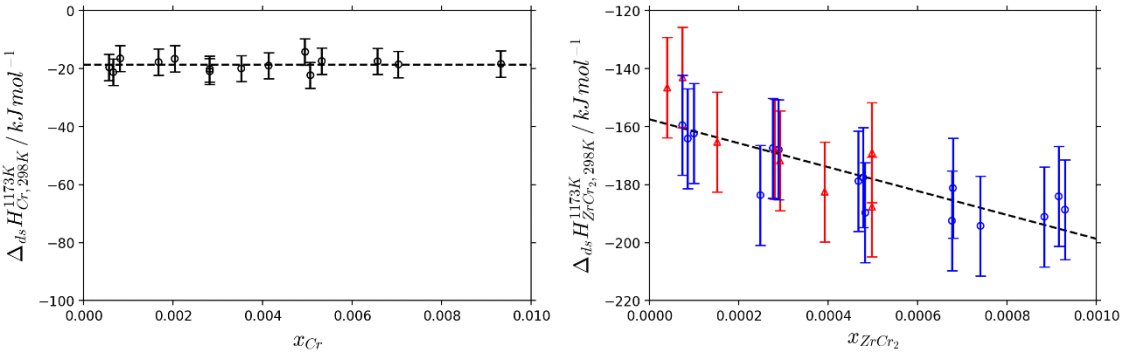

Figure III-22 Linear fitting of drop solution enthalpies for Cr and $ZrCr_2$. a) experimental data for Cr, where the dotted line shows the average value; b) experimental data for $ZrCr_2$ both for the C14 (red triangles) and C15 (blue circles) phases, where the black dashed line is the linear fitting of all the points.

The enthalpy of solution at infinite dilution can be calculated by a linear extrapolation of experimental data to zero solute composition, as in Figure III-22. In practice, the slope of the linear fitting of Cr data is not significantly different from zero, which indicates that in this case the enthalpy of solution at infinite dilution can be calculated with an average of all the values. The enthalpy of drop solution at infinite dilution of Cr in liquid Al at 900°C is then:

$$\Delta_{ds}\overline{H}^{\infty,1173K}_{Cr,298K} = -18.65 \pm 1.17 kJ/mol$$

The measured error was calculated with a 95% confidence interval of normal distribution. The same method is followed to evaluate other errors in this thesis.

The enthalpy of mixing at infinite dilution of Cr at 900°C/1173K is calculated as:

$$\Delta_{mix}\overline{H}^{\infty}_{Cr,1173K} = -68.1 \pm 10\ kJ/mol$$

Where the $\pm 10\ kJ/mol$ uncertainty is roughly estimated considering the large uncertainty on the pure chromium enthalpy of melting and that the experimental temperature is $\approx 1000\ K$ below the Cr melting point.

The data for Laves phases C14 and C15 (Figure III-22-right) do not display a significant difference. It is likely since the uncertainty of the measurement is rather large compared to the enthalpy of phase transition $C14 \rightleftharpoons C15$ (which will be discussed later). Therefore, we analyzed the data of the two phases together to obtain a value, which may be called a "representative" drop solution enthalpy of the $ZrCr_2$ compound at infinite dilution.

For this representative drop enthalpy of solution at infinite dilution of $ZrCr_2$ compound, we obtain:

$$\Delta_{ds}\bar{H}^{\infty,1173K}_{ZrCr_2,298K} = -157.5 \pm 6.5 \text{ kJ/mol}$$

A comparison of literature values of enthalpies of partial dissolution and partial mixing for chromium in liquid aluminum is presented in Table III-11, and plotted in Figure III-23, versus the experimental temperatures. The Cr drops were performed from ambient temperature, except for Maciąg and Rzyman [50] where the sample was dropped from 873K. Important experimental details related to Maciag's data are missing such as the composition of the samples and the quantity measured. Nevertheless, the results presented by the authors could be reasonably confirmed as enthalpies of drop dissolution regarding the whole article (in the article, the data was noted as the enthalpy of solution).

Table III-11 Comparison of literature values of the partial drop solution enthalpy $\Delta_{ds}\bar{H}^{\infty}_{Cr}$ and partial mixing enthalpy $\Delta_{mix}\bar{H}^{\infty}_{Cr,T_{exp}}$ of Cr at infinite dilution in liquid aluminum measured at different temperatures. T_{exp}. X^{max}_{Cr} the maximum Cr mole fraction reached in the binary Cr-Al liquid during the experiments. X^{sat}_{Cr} is the Cr mole fraction at saturation, i.e. the Cr mole fraction in the binary liquid in equilibrium with, depending on temperature, the $Al_{11}Cr_2$ or bcc phases, as calculated using the Cr-Al CALPHAD modeling of Murray [51].

References	T_{exp} **K**	X^{max}_{Cr}	X^{sat}_{Cr}	$\Delta_{ds}\bar{H}^{\infty}_{Cr}$ **kJ mol^{-1}**	$\Delta_{mix}\bar{H}^{\infty}_{Cr,T_{exp}}$ **kJ mol^{-1}**
Esin [52]	1830	0.55	0.568		-35.51
Kek [53]	1123	0.0164	0.0250	-27.5 ± 1.3*	-75.2 ± 10[#]
Sudavtsova [54]	1920	0.3	0.593		-32 ± 3
Zubkov [55]	1073	0.733	0.0138	-50.6 ± 0.83*	-75.9 ± 10[#]
Saltykov [56]	1723	0.3949	0.455		-33.1 ± 0.3
Maciag [50]	1123**	Not stated	0.0250	-70.8 ± 1.4[##]	-103.1 ± 10[#]
This work	1173	0.009	0.0441	-18.65 ± 1.17	-68.1 ± 10[#]

*reported uncertainty, [#]value and expanded uncertainty (95% confidence level) calculated/estimated by us, **drop is performed from 873 K, not room temperature, [##]reported standard deviation

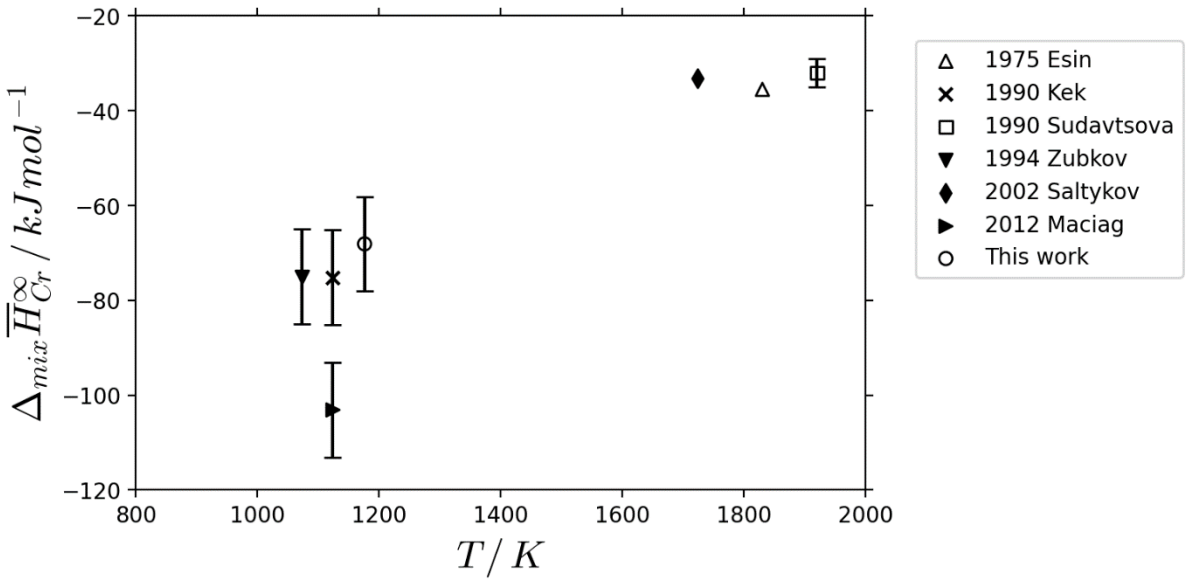

Figure III-23 Comparison of partial mixing enthalpies of Cr at infinite dilution in liquid aluminum vs. experimental temperatures.

Figure III-23 shows a variation of the partial enthalpy of mixing $\Delta_{mix}\overline{H}^{\infty}_{Cr,\,T_{exp}}$ with temperature showing good agreement of our value with the results of Kek *et al.* [53] and Zubkov [55] for the working temperature of 900 K along with reasonable linear extrapolation to higher temperatures [54] and [56]. So, it can be considered that the observed difference within these two groups of values can be interpreted as a dependency of the enthalpy of mixing versus temperature, this quantity decreasing progressively when temperature increases, and the system tends towards ideality.

Many publications have shown that zirconium or/and zirconium compounds are difficult to dissolve in any metallic solvent. To be sure of the completeness of the dissolution process, examinations were performed on the solidified Al ingot. SEM results are shown in Figure III-24 and Figure III-25 for Cr and $ZrCr_2$ respectively. Figure III-24 is stitched of BSE images displaying the entire vertical cross-section of the ingot. In the grey background (Al), a white needle-like phase (identified as Al_7Cr by SEM-EDS) is mainly present in the bottom of the ingot and gradually becomes sparser as we move away from the bottom. However, the peritectic melting temperature of Al_7Cr is lower than the calorimeter temperature (1173 K), we, therefore, assume that these crystals did not precipitate during the experiments but when the silica tube containing the crucible and bath was removed from the calorimeter, i.e. at the end of the experiment.

An image of an ingot resulting from the dissolution of $ZrCr_2$ in Al is shown in Figure III-25, Cr is found homogeneously distributed in the entire ingot with a low content (<0.4% at.) without precipitation; a white Zr-rich phase was found in the dark background (as Al). Both clusters and needle-like phases were found as $ZrAl_3$, which could indicate that a sample dropped was not fully dissolved based on the argument of Gajavalli *et al.* [57]. Differently, in the other ingot, no cluster of $ZrAl_3$ was found, indicating that the samples may be fully dissolved. The risk of clusters of $ZrAl_3$ hiding in the main body of the ingot and not appearing on the cross-section should be admitted, which could barely be completely excluded.

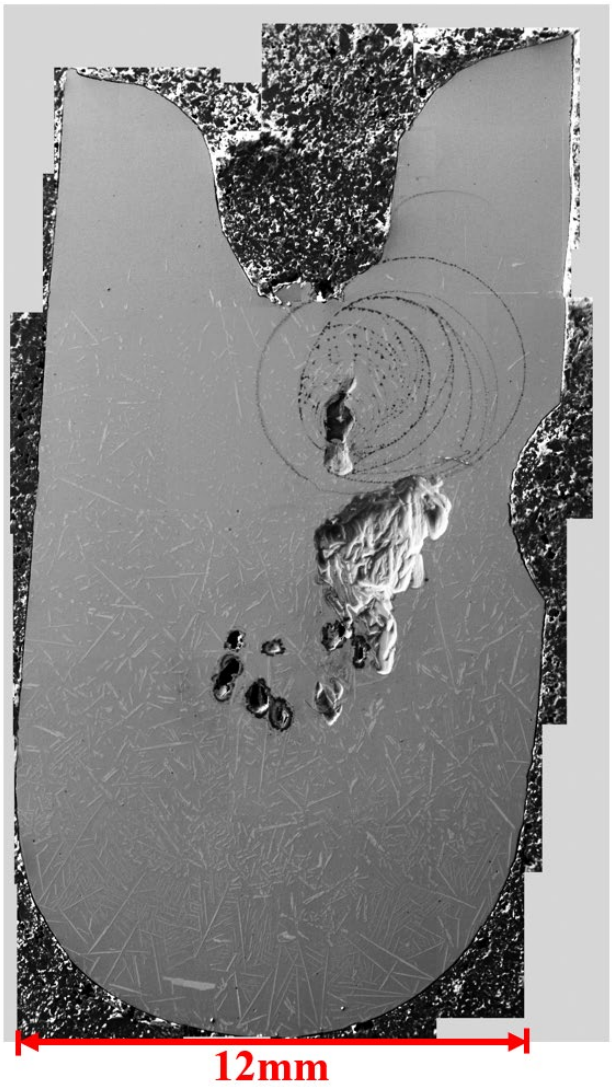

Figure III-24 Vertical cross-section of the solidified ingot of drop solution experiment: Cr in solvent Al. The image is a stitching of 40 photos taken by SEM-BSE. Two phases were identified in the ingot: the white needle-like phase is Al_7Cr and the grey background is Al.

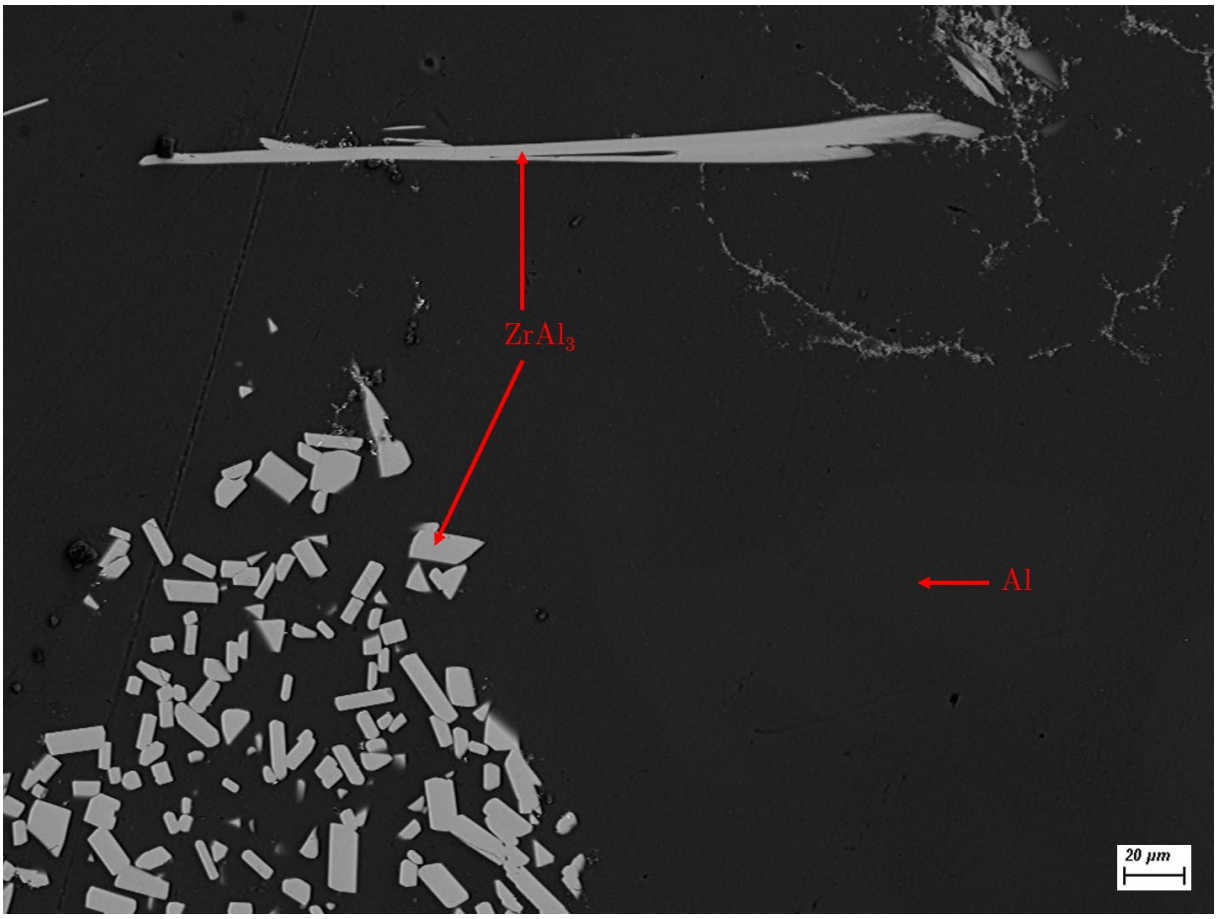

Figure III-25 Ingot of drop solution experiment: $ZrCr_2$ in solvent Al. The photo was taken by BSE under an accelerating voltage of 20kV, a working distance of 12.3mm

In early studies by Gajavalli *et al.* [57], [58], the enthalpy of solution of Zr in Al solvent at infinite dilution at 900°C has been carefully measured as $\Delta_{ds}\bar{H}^{\infty,1173K}_{Zr,298K} = -130 \pm 9kJ/mol$. According to the following Equation (III-2), the representative standard enthalpy of the formation of the $ZrCr_2$ compound is calculated as:

$$\Delta_f \boldsymbol{H_{ZrCr_2}} = \Delta_{ds}\boldsymbol{\bar{H}^{\infty,1173K}_{Zr,298K}} + \mathbf{2}\Delta_{ds}\boldsymbol{\bar{H}^{\infty,1173K}_{Cr,298K}} - \Delta_{ds}\boldsymbol{\bar{H}^{\infty}_{ZrCr_2}} \qquad \text{(III-2)}$$

$$\Delta_f H_{ZrCr_2} = -9.80 \pm 9.33\text{kJ/mol}$$

$$\text{as } \Delta_f H_{ZrCr_2} = -3.27 \pm 3.11\text{kJ/(mol.atom)}$$

The enthalpy of formation measured is less exothermic than the result reported by Matsui [36]. More recent experimental results of direct reaction calorimetry reported by Pavlů from a private communication of Meschel suggest that one can estimate the standard enthalpy of formation of $ZrCr_2$ (presumably in the most stable C15 structure) to be about −3 kJ mol^{-1} of atoms, i.e.

consistently with our results At this stage, the value reported by Pavlů is indicated to be only an estimate because the reaction in the calorimeter was not fully complete. The value for standard enthalpy of formation determined in a similar Cr_2Hf system, which is about -5 kJ mol^{-1} of atoms, could also support this estimated value [40].

In parallel with our experiments, some ab-initio calculations were performed to determine the enthalpy of the formation of $ZrCr_2$ for comparison with the measured value. For this purpose, DFT calculations were done for single isolated atoms Zr, Cr; single phases Zr of hcp structure, Cr of bcc structure and Laves phases C14/C15 of $ZrCr_2$ with the VASP code.

The calculations of cohesion energies of hcp Zr and bcc Cr were performed according to the details of the DFT simulations reported in Chapter II.

The cohesive energies per atom of Zr and Cr, are calculated by Equation (III-3):

$$\boldsymbol{NE_{coh} = E_{str}(N) - NE_{inf}} \qquad \text{(III-3)}$$

where N is the number of atoms in the simulation, E_{coh} is the cohesive energy per atom, E_{str} is the energy of the unary phase in its stable structure at 0K, i.e. hcp for Zr and bcc for Cr and E_{inf} is the energy of an isolated atom.

As a result, it is found that:

$$\mathrm{E_{coh,Zr}} = 6.34\ \mathrm{eV/atom} \text{ and } \mathrm{E_{coh,Cr}} = 4.03\ \mathrm{eV/atom}$$

The obtained cohesive energies of Zr and Cr are in agreement with the values reported by Brewer [59]: $\mathrm{E_{coh,Zr}} = 6.25\ \mathrm{eV/atom}$ and $\mathrm{E_{coh,Cr}} = 4.1\ \mathrm{eV/atom}$. For Cr, our results have a better agreement with Brewer values [59] than with Joseph and Haque's ones [60], Philipson and Baerends' ones [61]; for Zr, our results are close to the simulation of Baskes and Johnson [62], Kim *et al.* [63].

The DFT calculations of the C14 and C15 phases are performed according to the simulation details reported in Chap II. The calculated crystallographic parameters in our simulations are: for C14, a=b=5.0911Å, c=8.0551Å; for C15, a =7.1232Å. They can be compared to the crystallographic parameters experimentally determined in this work (Table III-7). The parameters calculated are not significantly different from those in the literature or from our experimental refinements.

The enthalpy of formation calculated are:

for C14 at 0 K,

$$\Delta_f H_{ZrCr_2\ C14,0K} = -7.625kJ/mol = -2.542kJ/(mol.atom)$$

for C15 at 0 K,

$$\Delta_f H_{ZrCr_2\ C15,0K} = -12.723kJ/mol = -4.241kJ/(mol.atom)$$

So, the energy of the $\mathrm{C15} \rightarrow \mathrm{C14}$ phase transition at 0K,

$$\Delta_{tr} H_{0K} = 5.098kJ/mol = 1.699kJ/(mol.atom)$$

These enthalpies of formation obtained by DFT are calculated at 0 K. To evaluate the enthalpies of formation at ambient temperature to be compared to our experimental result, an adjustment was done according to Equation (III-4) below.

$$\Delta_f \boldsymbol{H}^{\boldsymbol{298K}}_{\boldsymbol{ZrCr_2}} = \Delta_f \boldsymbol{H}^{\boldsymbol{0K}}_{\boldsymbol{ZrCr_2}} + \int_{\boldsymbol{0}}^{\boldsymbol{298}} \boldsymbol{C_{p,ZrCr_2}} \boldsymbol{dT} - \boldsymbol{2}\Delta \boldsymbol{H}^{\boldsymbol{298}}_{\boldsymbol{0,Cr}} - \Delta \boldsymbol{H}^{\boldsymbol{298}}_{\boldsymbol{0,Zr}} \qquad \text{(III-4)}$$

In the calculation, the $\Delta H^{298}_{0,Cr}$ and $\Delta H^{298}_{0,Zr}$ values were the enthalpy increment from 0K to room temperature, taken from SGTE [49]. The model of C_p for $ZrCr_2$ used in the previous equation is built from our experimental data, which will be detailed thereafter.

We obtained at room temperature:

for C14,

$$\Delta_f H^{298K}_{ZrCr_2\ C14} = -7.557kJ/mol = -2.519kJ/(mol.atom)$$

for C15,

$$\Delta_f H^{298K}_{ZrCr_2\ C15} = -12.352kJ/mol = -4.117kJ/(mol.atom)$$

Our DFT results are in quantitative agreement with our experimental result obtained by dissolution calorimetry as $-3.27 \pm 3.11\mathrm{kJ/(mol.\,atom)}$.

Thus, from two previously calculated enthalpies it is possible to calculate the enthalpy of transition between two phases C14 and C15 at ambient temperature:

$$\Delta_{tr} H_{298K} = 4.795\mathrm{kJ/mol} = 1.598kJ/(mol.atom)$$

The calculated enthalpy of transition is relatively low compared to the relatively important experimental uncertainty of (±10 kJ/mol) caused by the drop solution method. This could explain why the experimental results of C14 and C15 could not have been separated.

A comparison is made between our calculation of transition enthalpy to the other DFT values reported in the literature at 0K (Table III-12). The enthalpies of transition listed were calculated from the enthalpies of formation of C14 and C15 phases calculated by DFT reported in Table III-4 for the different authors. Though the enthalpies of formation in the literature were very different from our work, the enthalpy of transition values are in reasonable agreement.

Table III-12 Comparison of enthalpy of transition of $ZrCr_2$Laves phases C15 → C14 calculated by DFT at 0 K from the literature and this work

Author	**Enthalpy of Transition C15/C14**	
	kJ/mol	**kJ/(mol.at)**
Chen [40]	5.5	1.833
Pavlů [4]	4.98	1.660
Lu [5]	4.94	1.647
Sun [37]	7.6	2.533
This work (298.15 K)	5.098	1.699

Then, it is possible to correct our experimental result with our DFT enthalpy of transition to obtain two different values of enthalpy of formation for the C14 and C15 phases. It has to be reminded that the experimental value obtained by drop solution calorimetry was determined as a numerical average of the enthalpies of formation of the C14 and C15 phases.

With our DFT calculated transition enthalpy, the so-called "corrected" enthalpies of formation for both phases were calculated by Equation (III-5) as:

$$\Delta_f \boldsymbol{H}^{\boldsymbol{298K}}_{\boldsymbol{C14\ Corrected}} = \Delta^{\boldsymbol{298K}}_{\boldsymbol{f}} \boldsymbol{H}_{\boldsymbol{ZrCr_2}} + \frac{\boldsymbol{1}}{\boldsymbol{2}} \Delta_{\boldsymbol{tr}} \boldsymbol{H}_{\boldsymbol{298.15K}}$$
$$\Delta_f \boldsymbol{H}^{\boldsymbol{298K}}_{\boldsymbol{C15\ Corrected}} = \Delta^{\boldsymbol{298K}}_{\boldsymbol{f}} \boldsymbol{H}_{\boldsymbol{ZrCr_2}} - \frac{\boldsymbol{1}}{\boldsymbol{2}} \Delta_{\boldsymbol{tr}} \boldsymbol{H}_{\boldsymbol{298.15K}} \quad \text{(III-5)}$$

for C14,

$$\Delta_f H^{298K}_{C14\ Corrected} = -7.40 \pm 9.33\text{kJ/mol} = -2.47 \pm 3.11 kJ/(mol.atom)$$

for C15,

$$\Delta_f H^{298K}_{C15\ Corrected} = -12.20 \pm 9.33\text{kJ/mol} = -4.07 \pm 3.11 kJ/(mol.atom)$$

These corrected values will be used in our CALPHAD modeling to ensure a precise definition of Gibbs energy of the Laves phases.

III.3.3.2 Specific heat capacity (C_p) and entropy of formation

Heat capacities of Laves phases C14 and C15 were measured by semi-adiabatic thermal relaxation method using a PPMS in the low-temperature range (between 1.8 to 302 K) and by relaxation method using DSC in the high-temperature range (297 to 1063 K).

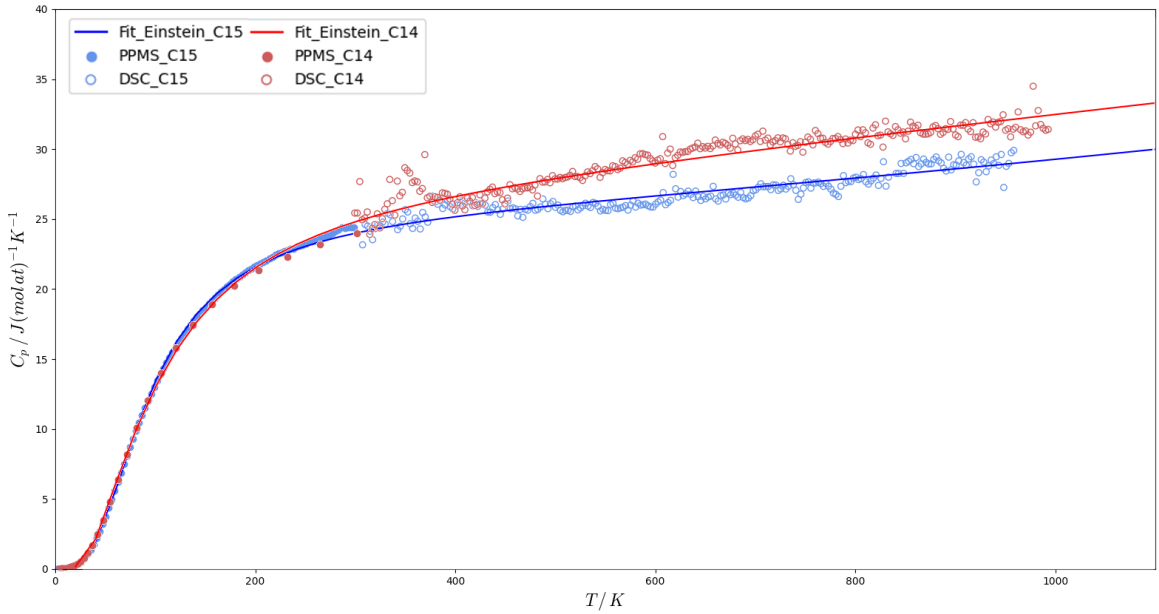

Figure III-26 Experimental C_p data of $ZrCr_2$ C14/C15 from 1.8K to 1063K

The results obtained by the two techniques show good compatibility around the ambient temperature. The abnormal peak in C14 C_p curve at room temperature is thought to be an artifact of the apparatus. The experimental data were fitted with a modified Einstein equation which is a sum of two terms, the first one coming from the classical Einstein model and the second one being a polynomial correction, as Equation (III-6) [64] [65].

$$\boldsymbol{C_p(T) = 3R\left(\sum_{i=1}^{2} a_i \left(\frac{\theta_E^i}{T}\right)^2 \frac{e^{(\theta_E^i/T)}}{\left(e^{(\theta_E^i/T)} - 1\right)^2}\right) + aT + bT^n} \qquad \text{(III-6)}$$

where C_p is the specific heat capacity; R is the perfect gas constant; a_i are the statistical weights; θ_E^i refers to the Einstein temperature and *a, b, n*: parameters, correction for non-

harmonic effects; T is the temperature in K. A relation $a_1 + a_2 = 1$ is required for the parameters a_1 and a_2 to adjust the sum of Einstein terms.

Fit parameters are listed in Table III-13 and the fit curves for C14 and C15 are represented by the red and blue lines, respectively in Figure III-26.

Table III-13 Fitting parameters of C_p data of C14 and C15 phases. N.points shows the number of experimental points fitted. Other parameters are related to Equation (III-6).

Phase	**C14**	**C15**
N. points	318	358
a_1	0.63±0.15	0.87 ± 0.038
a_2	0.37±0.15	0.13 ± 0.038
a	0.0077±0.0022	0.0044 ± 4.5E-05
θ_E^1	227.24±22.34	315.48 ± 5.74
θ_E^2	480.57±82.05	137.89 ± 19.62
b	0	2.15E-6±2.93E-7
n	2	2

Skripov *et al.* [34] performed heat capacity measurements of C15 type $ZrCr_2$ from 5.3K to 293K by adiabatic calorimetry, i.e. in a temperature range similar to ours (1.8K to 302K). Recently, Samanta and Jain [35] reported C15 phase heat capacity experimental data from 298K to 860K i.e. also in a temperature range similar to ours (298K to 1073 K). In Figure III-27, a comparison between the data of Skripov and ours is shown. It shows a very good quantitative agreement over the whole temperature interval. In Figure III-28, a comparison is made between the results reported by Samanta on C15 $ZrCr_2$ and the results of this work for both C14 and C15. The measurements of Samanta do not correspond to our data of C15 $ZrCr_2$ while they are similar to our C_p data of C14.

From our fits of C_p of C14 and C15 phases in the low-temperature interval, the entropy of formation of $ZrCr_2$ at 298.15K was calculated with Equation (III-7):

$$\Delta_f S_{ZrCr_2}^{298K} = \int_0^{T_0} \frac{C_p}{T} dT - S_{Zr}^{298K} - 2S_{Cr}^{298K} \qquad \text{(III-7)}$$

where T_0 is the ambient temperature (298.15K), C_p is the specific heat capacity of $ZrCr_2$, S_{Zr}^{298K} and S_{Cr}^{298K} are the entropy of pure Zr and Cr at room temperature respectively, which can be taken from SGTE [49].

As a result, we obtain:

$$\Delta_f S_{ZrCr_2,\mathrm{C14}}^{298K} = -0.892\, J\, mol^{-1}K^{-1} = -0.297\, J(mol.at)^{-1}K^{-1}$$

$$\Delta_f S_{ZrCr_2,\mathrm{C15}}^{298K} = -0.715\, J\, mol^{-1}K^{-1} = -0.238\, J(mol.at)^{-1}K^{-1}$$

The integration by trapezoidal interpolation method was slightly different from the integration of the Einstein model, see Table III-18.

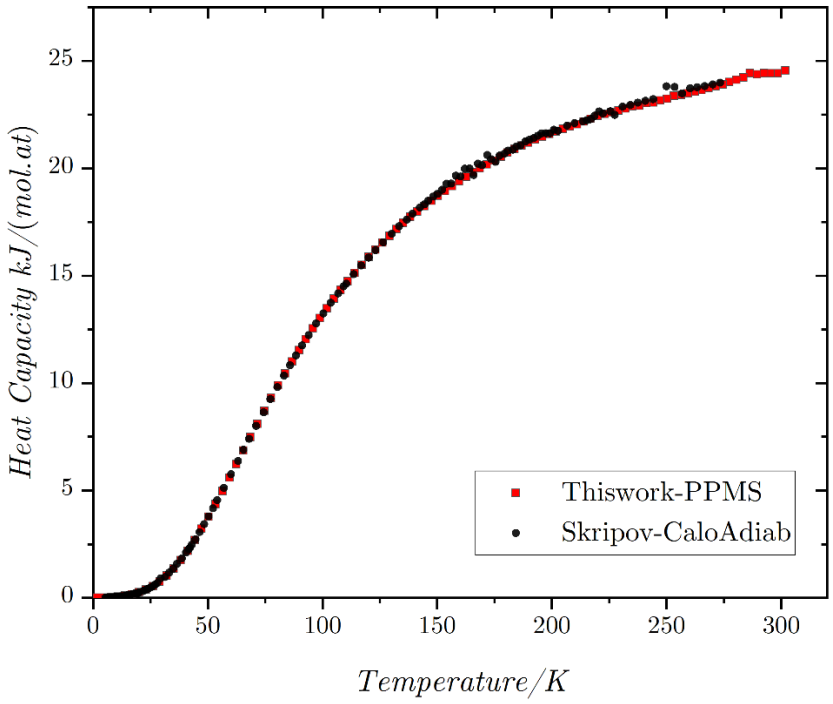

Figure III-27 Comparison of C_p of Laves phase C15 of $ZrCr_2$ at low temperatures (1.8K to 300K) obtained by PPMS (this work) and by adiabatic calorimeter (Skripov *et al.* [34]).

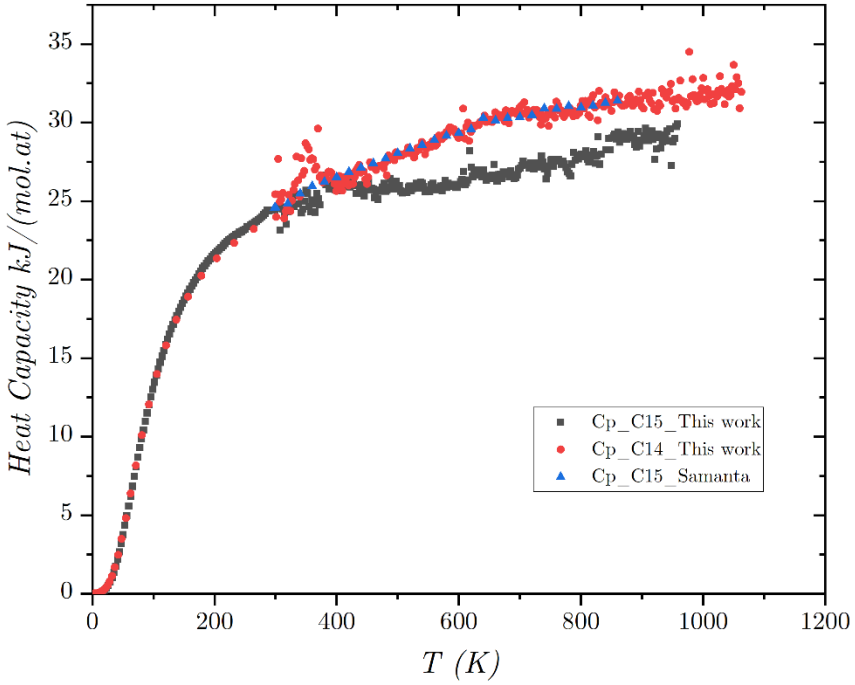

Figure III-28 Comparison of C_p of C14/C15 obtained in this work and the experimental data of C15 of Samanta and Jain [35].

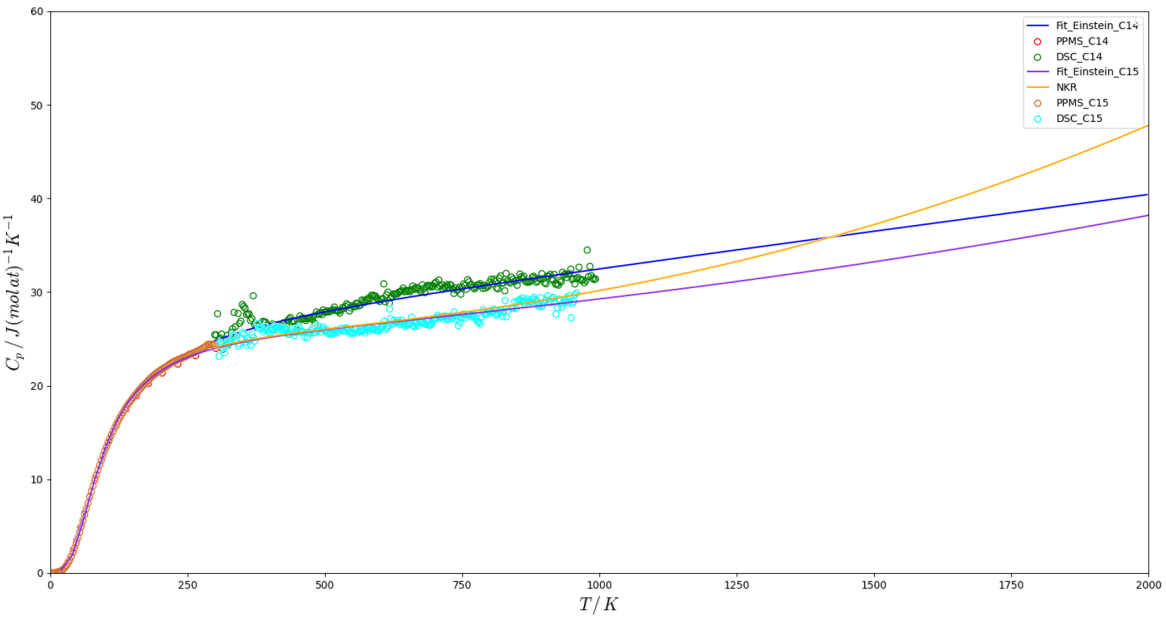

Figure III-29 Comparison of experimental data of C_p C14/C15 typed $ZrCr_2$ extended to 2000K, modeling with Equation (III-6) and Neumann-Kopp rule (hcp-Zr and bcc-Cr from data of SGTE).

In Figure III-29, our Einstein fit (prolonged till 2000K), is compared with the Kopp-Neumann approximation calculated with hcp Zr and bcc Cr. In 298.15K~1000K, the Kopp-Neumann approximation is consistent with our fit but provides values significantly lower than the experimental data of C14. As the temperature increases, the Kopp-Neumann approximation provides significantly higher values than our fits, for C14 as well as C15. A significant difference (about 10 J/(mol.at)/K) is found at 2000K between the approximation and our fits.

III.4 CALPHAD assessment

III.4.1 Definitions of phases

For the CALPHAD modelling, the five phases of the Zr-Cr binary system are noted as Liquid, HCP_A3 (for hcp Zr), BCC_A2 (for bcc Zr and bcc Cr), LAVES_C14 and LAVES_C15. The Gibbs energy of each phase of the system is required. The Gibbs energy of each of these phases is expressed as the sum of 3 terms, reference, ideal and excess.

The Liquid, HCP_A3 and BCC_A2 phases are described by the substitution solution model. The reference and ideal Gibbs energy are based on the SGTE pure element data [49]. The excess Gibbs energy is expressed by a Redlich-Kister polynomial. Polynomials of order 2 for the liquid and of order 1 for HCP_A3 and BCC_A2, with a temperature dependence for the regular term of Liquid and BCC_A2 are needed to reproduce the selected experimental data (III.4.2, III.4.3)

The Laves phases C14 and C15 are described with a two-sublattice model:

$$(\mathrm{Cr}, \mathrm{Zr})_2(\mathrm{Cr}, \mathrm{Zr})_1$$

The Gibbs energy of the $ZrCr_2$ stable end-members (C14 and C15) is described according to Equation (III-8).

$$\boldsymbol{G(T) = a + bT + cTln(T) + \sum dT^n} \qquad \text{(III-8)}$$

where a, b, c, d are coefficients and n are integers taken as 2, 3 and -1.

The c and d coefficients are parameters describing the C_p. They were fitted with our experimental data in the beginning and then fixed in the CALPHAD optimization. The a and b coefficients relate to the enthalpy of formation and the entropy of formation respectively, and were then optimized.

The Gibbs energies of the metastable end-members of the C14 and C15 phases, as $ZrZr_2$, $CrCr_2$ and $CrZr_2$ are fixed by taking into account the DFT values listed in

Table III-17. No entropic terms were added. The Gibbs energies of the metastable end-members are given in Table III-14, where the choices of parameter values will be explained later in III.4.3.

Table III-14 Definition of Gibbs energy of metastable end-members of Laves phases. GHSERCR and GHSERZR are the definitions of reference states of Cr and Zr according to SGTE, respectively.

Structure	Parameters
C14	G(LAVES_C14,CR:CR;0)=77750.00+3*GHSERCR
	G(LAVES_C14,ZR:ZR;0)=105283.33+3*GHSERZR
	G(LAVES_C14,ZR:CR;0)=284392.02+2*GHSERZR+GHSERCR
C15	G(LAVES_C15,CR:CR;0)=74079.44+3*GHSERCR
	G(LAVES_C15,ZR:ZR;0)=82882.67+3*GHSERZR
	G(LAVES_C15,ZR:CR;0)=296992.33+2*GHSERZR+GHSERCR

The ideal Gibbs energy is calculated classically with the arrangements of the constituents on the sublattices.

The excess Gibbs energy is expressed by Redlich-Kister polynomials. One parameter without temperature dependence for each of the 4 interactions has allowed to represent the homogeneity range.

III.4.2 Phase diagram experimental data selection

In this assessment, our measurements of the two eutectic temperatures and compositions (E1 & E2), the eutectoid temperature in the rich-zirconium part, the solubility domain of $ZrCr_2$ and the mutual solubilities of the pure elements were considered. Other important reactions were carefully chosen in the literature (Table III-15):

1. The temperature of melting of $ZrCr_2$ ($T_{melting}$): we would like to remind that we have not succeeded in measuring the melting temperature of the $ZrCr_2$ compound in our work, due to a limit of the facility and inevitable oxidation of the sample around 1700°C. The value of Petkov *et al.* [15] at 1670°C±10°C was considered in our modeling, consistent with other measurements of 1670°C in [26], 1675±10°C in [9], 1680°C in [12], and 1675°C in [10].

2. The transition temperature of $C14 \rightleftharpoons C15$ (T_{trans}): we also did not succeed in measuring the transition temperature between both polymorphs of $ZrCr_2$ due to a limit of our facility. The measurements of the transition temperature are not numerous. Gebhardt and Rexer [25] reported 1590°C while Svechnikov and Spektor [12] gave 1620°C. The result of Gebhardt was considered in our modeling, to increase the relative stability of the C14 phase.
3. Eutectoid point in the zirconium-rich part: the eutectoid point has been accurately studied by Domagala *et al.* [8] and Rumball and Elder [11]. These results are consistent. The result of Rumball was considered in our modeling with a value of 1.44±0.22% at. Cr. It could be the most accurate measurement as the slight oxidation of samples and O impurity of raw materials were taken into consideration. No maximum solubility of Cr in hcp Zr was reported in the article, but the monophasic sample of hcp Zr with the richest Cr composition reported was 0.35% at. Cr, so the value was reasonably taken into account in our model. The temperature of the eutectoid reaction was measured in our work by DTA and retained in our modeling.
4. The transition temperature of the reaction hcp Zr $\rightleftharpoons$ bcc Zr was adopted from the SGTE data.

Table III-15 Invariant reactions in the Zr-Cr system

Reaction	**Temperature/K**	**Compositions % at. Cr**			**Reference**
$L \rightleftharpoons ZrCr_2\ (C14)$	1943.15	66.8	66.8		Petkov [15]
$L \rightleftharpoons ZrCr_2(C14) + bcc\ Cr$	1881.15	80	68	99.5	This work
$L \rightleftharpoons ZrCr_2(C15) + bcc\ Zr$	1618.15	27.2	64.8	7.1	This work
$ZrCr_2(C14) \rightleftharpoons ZrCr_2(C15)$	1863.15				Gebhardt [25]
$bcc\ Zr \rightleftharpoons hcp\ Zr + ZrCr_2\ (C15)$	1078.15	1.44	0.35		Rumball [11]
$bcc\ Zr \rightleftharpoons hcp\ Zr$	1139	0	0		This work* SGTE [49]

* Temperature was measured in this work by DTA, and compositions were taken from Rumball.

III.4.3 Thermodynamic data selection

With the definition of the Gibbs energy model of the $ZrCr_2$ solution phase, DFT calculations were performed on the metastable end-members as Cr_2Cr, Zr_2Zr, and Zr_2Cr for both C14 and C15 structures. The lattice parameters and atomic positions calculated of C14 and C15 $ZrCr_2$ were used and fixed in these calculations. The atoms in some positions were replaced by corresponding elements to meet the compositions of meta-stable phases e.g. to calculate the Gibbs energy of the metastable phase Cr_2Cr, all the Zr atoms of Cr_2Zr were replaced by Cr atoms.

The enthalpies at room temperature of these end-member phases were calculated by adding the enthalpy increment ΔH_0^{298} to the DFT results. The enthalpy increments ΔH_0^{298} were taken from SGTE (Zr and Cr) and calculated with the Kopp-Neumann rule (see Table III-16).

A comparison of our results with the literature is made in Table III-17. The results showed an acceptable consistency, though some differences were found in phases Zr_2Zr and Zr_2Cr for the C14 phase. Our DFT calculations are considered to establish the description of the Gibbs energy of end-members.

Table III-16 DFT calculation of energies for pure metal and Laves phases (2nd and 3rd columns) and enthalpy corrections (4th column).

Compound	H_{0K}**(eV/atom)**	H_{0K}**(kJ/mol)**	ΔH_0^{298} **(kJ/mol)**	**Reference***
Zr HCP_A3	-8.48	-818.04	5.57	SGTE
Cr BCC_A2	-9.50	-916.99	4.05	SGTE
$ZrCr_2$ C15	-27.62	-2664.74	14.04	THIS WORK
$CrCr_2$ C15	-27.74	-2676.89	12.15	NKR
$ZrZr_2$ C15	-24.58	-2371.22	16.70	NKR
$CrZr_2$ C15	-23.38	-2256.07	15.18	NKR
$ZrCr_2$ C14	-27.56	-2659.64	13.73	THIS WORK
$CrCr_2$ C14	-27.71	-2673.22	12.15	NKR
$ZrZr_2$ C14	-24.34	-2348.82	16.70	NKR
$CrZr_2$ C14	-23.51	-2268.67	15.18	NKR

*Reference indicates the source of values for the value calculated in column ΔH_0^{298}

Table III-17 Comparison of DFT enthalpy of formation of metastable end-members of Laves phases in literature and this work.

Structure	$\Delta_f H$ kJ/mol			
	Cr_2Cr	**Zr_2Zr**	**Zr_2Cr**	**Author**
C14	77.75	105.28	284.39	This work
C14	85.89	61.53	200.19	Pavlů [4]
C14	83.4	59.1		Sluiter [66]
C15	74.08	82.88	296.99	This work
C15	83.16	68.4	299.28	Pavlů [4]
C15	79.2	79.5		Sluiter [66], Wang, [67]

Table III-18 reported the entropies of formation of C14 and C15 $ZrCr_2$ assessed in the recently published CALPHAD modeling. The authors agreed with a positive value of around 10 J/mol/K, except for the result of Samanta which is much larger than the others. These results are very different from our experiments indicating that the value is very slightly negative. We will reasonably take into account our results in the CALPHAD modeling, considering the fact that firstly it was supported by an accurate experimental measurement by the semi-adiabatic thermal relaxation method and, secondly, it was also consistent with the C_p data reported by Skripov and Mirmelstein [34] at low temperatures.

This different choice of entropy of formation causes a huge stability disparity at high temperatures, and would greatly affect the optimization of interaction parameters of the Gibbs energy of Laves phases as well as the parameters of the bcc and liquid phases. Therefore, as a result, we have obtained parameters for liquid and bcc phases different from the previous modeling.

Table III-18 Comparison of entropy of formation of C14 and C15 $ZrCr_2$ in literature and with this work integrated by two methods: analytically with the model of Equation (III-6) and numerically from the experimental data by the trapezoidal rule.

Reference	$\Delta_f S$				Method
	C14		C15		
	J/(mol K)	J/(mol.at K)	J/(mol K)	J/(mol.at K)	
Lafaye [7]	14.1375	4.713	11.422	3.807	CALPHAD
Pavlu [4], Yang [6]	8.988	2.996	6.531	2.177	CALPHAD
Lu [5]	11.85	3.950	9.22	3.073	CALPHAD
Samanta [35]			33.433*	11.144	Exp/model
This work (Einstein model)	-0.892	-0.297	-0.715	-0.238	Exp
This work (Numerical integration)**	-1.362	-0.454	-0.860	-0.287	Exp

* Calculated with the published value $S^{298K}_{ZrCr2,C15} = 119.7\ J\ mol^{-1}K^{-1}$ reported in the publication.

** Calculated by direct numerical integration from experimental heat capacity data.

III.4.4 Results and discussions

The optimized parameters and the calculated phase diagram are shown in Table III-19 and Figure III-30 respectively. An overall consistency is obtained between our modeling and the selected experimental data.

Table III-19 Optimized thermodynamic parameters of the system.

Phases	Parameters
LIQUID	$L(LIQUID,CR,ZR;0)=-1.3819*10^4+3.5*T$
	$L(LIQUID,CR,ZR;1)= 4.99*10^3$
	$L(LIQUID,CR,ZR;2)= 3.0469*10^2$
BCC_A2	$L(BCC\_A2,CR,ZR:VA;0)= -1*10^4+25*T$
	$L(BCC\_A2,CR,ZR:VA;1)= -2.00*10^4+18.2*T$
HCP_A3	$L(HCP\_A3,CR,ZR:VA;0)= 2.1*10^4$
	$L(HCP\_A3,CR,ZR:VA;1)= -4*10^3$
LAVES_C14	$G(LAVES\_C14,CR:ZR;0)= -5.12*10^4+ 4.17937367*10^2*T - 73.71417*T*Ln(T) -1.188*10^{-2}*T^2+ 2.25834*10^5*T^{-1}$
	$L(LAVES\_C14,CR,ZR:ZR;0)= -2.3*10^4$
	$L(LAVES\_C14,CR :CR,ZR;0)= -4*10^4$
LAVES_C15	$G(LAVES\_C15,CR:ZR;0)= -6.23*10^4+ 4.00591217*10^2*T - 71.5567789*T*LN(T)-7.98940884*10^{-3}*T^2+ 1.88795668*10^5*T^{-1}$
	$L(LAVES\_C15,CR,ZR:ZR;0)= -7*10^3$
	$L(LAVES\_C15,CR:CR,ZR;0)= -4*10^4$

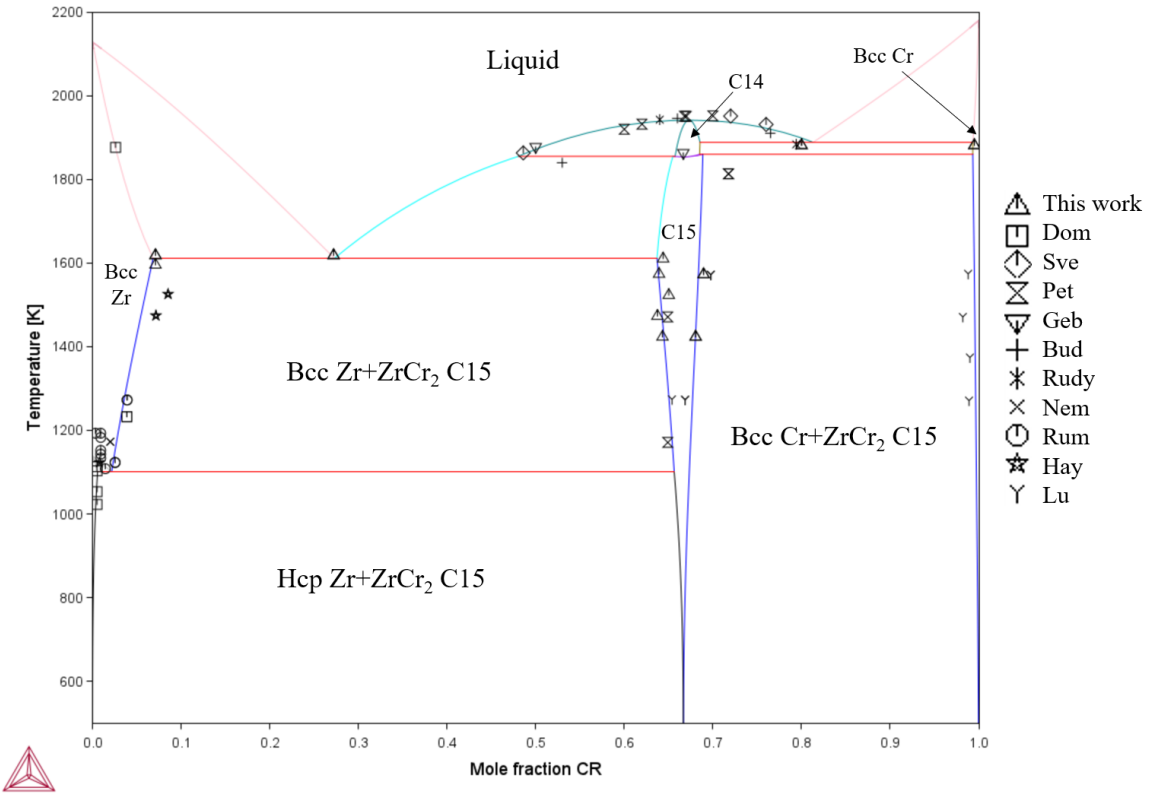

Figure III-30 Calculated phase diagram Zr-Cr of this work. In the legend: Domagala *et al.* [8], Svechnikov and Spektor [12], Petkov *et al.* [15], Gebhardt and Rexer [25], Rudy [14], Nemoshkalenko *et al.* [26], Rumball and Elder [11], Hayes *et al.* [13], Lu *et al.* [5].

A comparison of the fitting results of C_p with modified Einstein model and with CALPHAD and experimental data are illustrated in Figure III-31 below. A good consistency of experimental points and fitting lines was obtained. Some differences in fitting results are shown at low temperatures (limits of the Redlich-Kister model) and at very high temperatures for the C15 phase (no experimental data support).

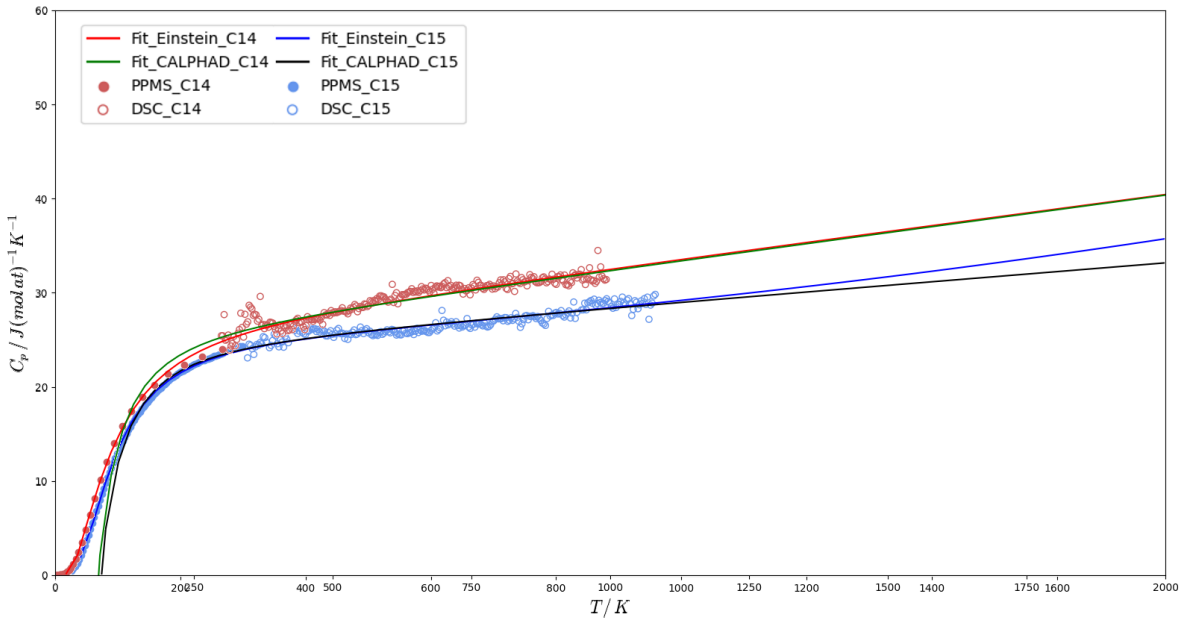

Figure III-31 Comparison of experimental points, Einstein fitting and CALPHAD fitting lines of the heat capacities of C14 and C15

However, as no experimental data were available in high temperatures (2000K), large "flexibility" in the model parameters has been identified for the high-temperature region. As a result, it should be regretful to say that our modeling of Gibbs energy of Laves phases at very high temperatures may be less accurate than at temperatures <1000K.

Table III-20 Optimized and experimental thermodynamic properties of polymorphs of $ZrCr_2$ at 298K.

	Optimization		**Experiment**	
Phase	C14	C15	C14	C15
$\Delta_f H$ / $kJ\ (mol.at)^{-1}$	-8.88	-12.99	-3.27±3.11	
S / $J\ (mol.at)^{-1}\ K^{-1}$	28.465	28.518	28.458	28.517
$\Delta_f S$/ $J\ (mol.at)^{-1}\ K^{-1}$	-0.290	-0.238	-0.297	-0.238

Thermodynamic properties of $ZrCr_2$ phases calculated in our model are reported in Table III-20 with the experimental determinations performed in this work.

More exothermic values than the experimental ones are required for our modeling to reproduce the stability of Laves phases and to fit the liquidus temperatures reported in the literature. As our measurements of the enthalpies of formation were determined with relatively large uncertainty, the deviation between the model and the experimental data has been considered to be the better compromise to obtain good consistency with the other selected experimental data.

It was chosen to well reproduce our measured entropies of formation of $ZrCr_2$, whereas the calculated enthalpies of formation are more negative than the experimental data.

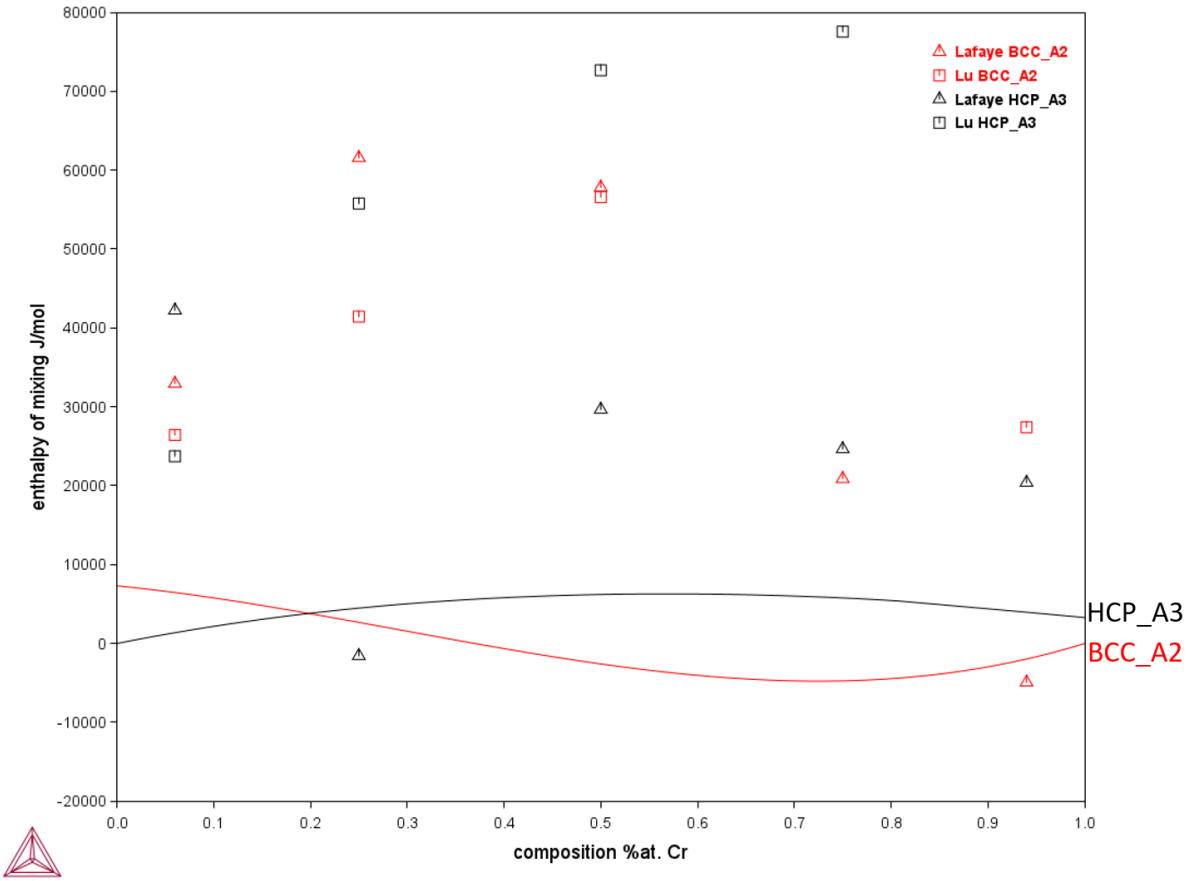

Figure III-32 Calculated mixing enthalpies at 298 K of HCP_A3 (black line) or BCC_A2 (red line) solid solutions in the Zr-Cr system compared to SQS results by Lafaye *et al.* [7] and Lu *et al.* [5]. The reference state of the solid lines is the SER of the pure elements.

Figure III-32 shows a comparison of the calculated mixing enthalpies of HCP_A3 or BCC_A2 solid solutions in our modeling of Zr-Cr with the DFT-SQS results of Lu and Lafaye. As shown, the mixing enthalpies of the bcc and hcp solid solutions are strongly different from the DFT results of Lu or Lafaye. This is because the interaction parameters of BCC_A2 and HCP_A3 phases were optimized together with the Gibbs energy of Laves phases, based on our experimental data whereas Lafaye or Lu considered different descriptions of the $ZrCr_2$ polymorphs. This difference impacts the optimization of all the phases, and then the mixing enthalpies.

Figure III-33 shows a comparison of our model for Zr-Cr and the last assessed phase diagram of Lafaye *et al.* [7]. The main differences between the two studies can be summarized as follows:

- ✓ The C36 phase, considered in Lafaye's model, is not modeled in our work which therefore only includes the two polymorphs of Laves phase, C14 and C15.
- ✓ The shape of the $ZrCr_2$ phase stability domain and transition temperatures of Laves phases thus differ.
- ✓ The optimized temperatures and compositions of the eutectic points of our modeling correspond to our experimental values and are slightly different from Lafaye's calculated values.
- ✓ The solubility of Zr in Cr is considerably smaller in our model.

Thanks to our new experimental measurements, the optimized Gibbs energy functions, particularly for the Laves phases, should be more accurate than the previous assessments, which rely more on DFT calculations and estimated heat capacities.

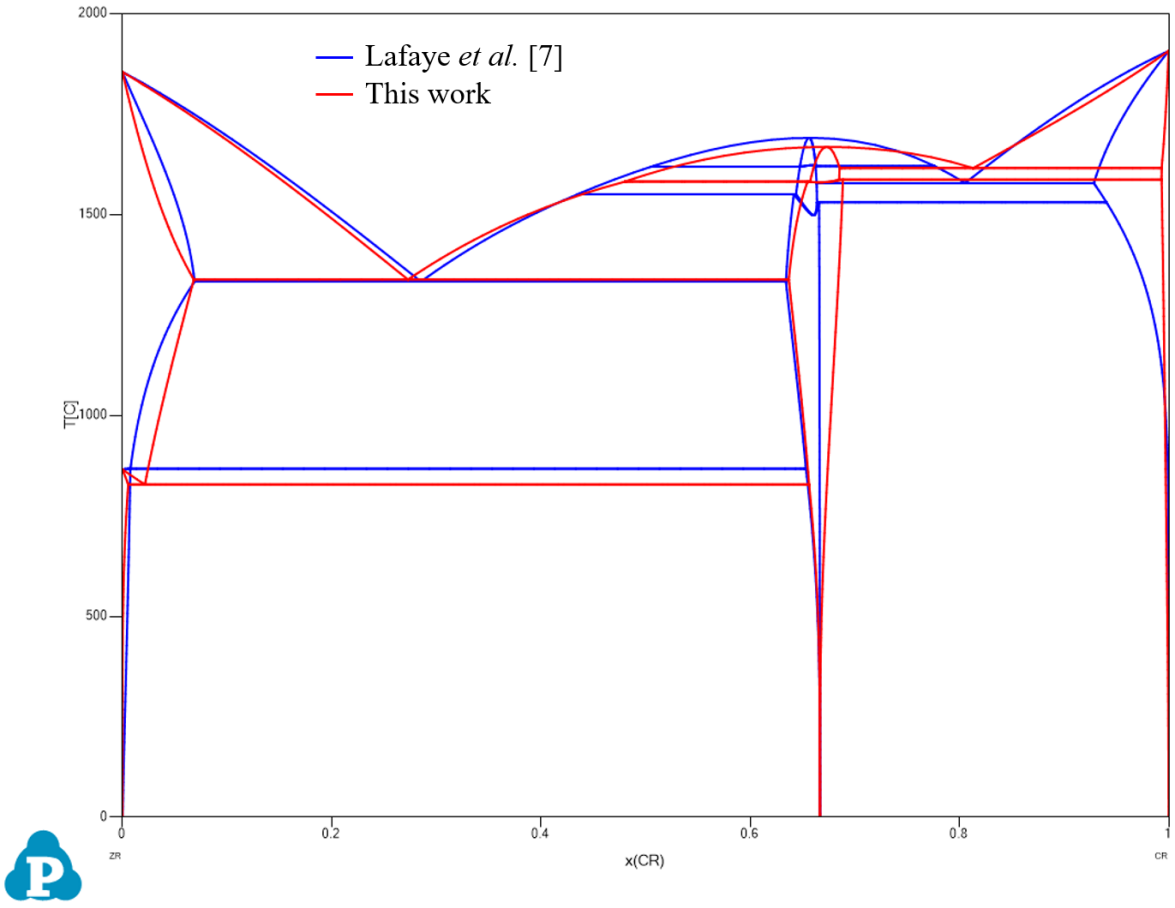

Figure III-33 Comparison between our calculated phase diagram and the modeling of Lafaye *et al.* [7].

III.5 Conclusion and prospective studies

In this chapter, we have presented an extensive study of the binary system Zr-Cr.

1. A phase diagram investigation was performed to better evaluate the temperatures and compositions of the eutectic reactions, the temperature of the eutectoid reaction in the zirconium-rich part, the mutual solubility of pure elements and the non-stoichiometry domain of $ZrCr_2$.The main results of this work are summarized in Table III-21.

Table III-21 Selection of main phase diagram outputs of this work.

	Values
Zr-rich eutectic point	27.2 ± 0.1% at. Cr
	1322.4 ± 0.7°C
Cr-rich eutectic point	80 ± 0.1% at. Cr
	1608 ± 7°C
Eutectoid point	852.2 ± 0.4°C
Stability domain of $ZrCr_2$	64.8~68.0% at. Cr
Solubility of Cr in (Zr)	7.1 ± 0.1% at. Cr
Solubility of Zr in (Cr)	~0.5% at. Zr

2. The stability of the $ZrCr_2$ polymorphs was studied. It was not possible to confirm the stability of the C36 phase, which was therefore not modeled in the CALPHAD modeling of the system.
3. The enthalpies of formation and heat capacities of the C14 and C15 phases were measured using a combination of calorimetric methods. The heat capacity data is in agreement with previous measurements which are surprisingly not taken into account in the existing CALPHAD models. The measured enthalpies of formation are slightly exothermic. The entropies of formation of these two phases were calculated by integrating heat capacity data from low temperatures.
4. DFT calculations were performed to estimate the enthalpy of formation of the stable and metastable end-members of the Laves phases. The results for $ZrCr_2$ were also used to estimate the enthalpy of the transition between the C15 and C14 structures. The calculations

also provided starting values for the interaction coefficients involved in the sub-lattice model describing the non-stoichiometry around the $ZrCr_2$ composition.

5. The Zr-Cr system was reassessed with all the above results using the CALPHAD method and Thermo-Calc software.

This assessment will be used in the next chapter for the modeling of the Zr-Cr-O ternary system.

Additional research would be greatly valuable in improving the results of this work. They are related:

- To the determinations of the C14/C15 transition temperature and the melting temperature of $ZrCr_2$.
- To reduce, if possible, the uncertainties on the measurements of the enthalpy of formation of $ZrCr_2$.
- To the determination of liquidus points in the high-temperature region.

Reference

[1] D. Arias and J. P. Abriata, 'The Cr−Zr (Chromium-Zirconium) system', *Bulletin of Alloy Phase Diagrams*, vol. 7, no. 3, pp. 237–244, Jun. 1986, doi: 10.1007/BF02868997.

[2] K. Zeng, M. Hamalainen, and R. Luoma, 'A Thermodynamic Assessment of the Cr-Zr system', *International Journal of Materials Research*, vol. 1, no. 84, pp. 23–28, 1993.

[3] Ansara, I., Dinsdale, A.T., and Rand, M.H., 'Cost 507: Thermochemical Database for Light Metal Alloys. Vol.2'. Office for Official Publications of the European Communities, 1998.

[4] J. Pavlů, J. Vřešt'ál, and M. Šob, 'Stability of Laves phases in the Cr–Zr system', *Calphad*, vol. 33, no. 2, pp. 382–387, Jun. 2009, doi: 10.1016/j.calphad.2008.11.003.

[5] H.-J. Lu, Wen-Bo Wang, Nan Zou, Jian-Yun Shen, Xiao-Gang Lu, and Yan-Lin He, 'Thermodynamic modeling of Cr–Nb and Zr–Cr with extension to the ternary Zr–Nb–Cr system', *Calphad*, vol. 50, pp. 134–143, 2015, doi: 10.1016/j.calphad.2015.06.002.

[6] Y. Yang, L. Tan, H. Bei, and J. T. Busby, 'Thermodynamic modeling and experimental study of the Fe–Cr–Zr system', *Journal of Nuclear Materials*, vol. 441, no. 1–3, pp. 190–202, Oct. 2013, doi: 10.1016/j.jnucmat.2013.05.061.

[7] P. Lafaye, C. Toffolon-Masclet, J.-C. Crivello, and J.-M. Joubert, 'Experimental investigations and thermodynamic modelling of the Cr–Nb–Sn–Zr system', *Calphad*, vol. 64, pp. 43–54, Mar. 2019, doi: 10.1016/j.calphad.2018.11.002.

[8] R. F. Domagala, D. J. McPherson, and M. Hansen, 'System Zirconium-Chromium', *Journ. Metals*, vol. 5, pp. 279–283, 1953.

[9] P. B. Budberg, S. P. Alisova, and R. S. Musayev, 'Phase diagram of the Zr-Cr system', *IZV AKAD NAUK SSSR METALLY*, vol. 3, no. may-juin, pp. 222–223, 1968.

[10] V. N. Svechnikov and A. Ts. Spektor, 'Phase Diagram of Chromium-Zirconium System', *Voprosy fiz. metallov i metalloved*, no. 17, p. 174, 1963.

[11] W. M. Rumball and F. G. Elder, 'Phase equilibria in zirconium-rich zirconium-chromium-oxygen alloys', *Journal of the Less Common Metals*, vol. 19, no. 4, pp. 345–358, Dec. 1969, doi: 10.1016/0022-5088(69)90180-5.

[12] V. N. Svechnikov and A. Ts. Spektor, 'The $ZrCr_2$ Region of the Cr-Zr phase diagram', *Russian Metallurgy (English Translation) (1971)*, vol. 4, p. 141, 1971.

[13] E. T. Hayes, A. H. Roberson, and M. H. Davies, 'Zirconium-Chromium Phase Diagram', *Journal of metals*, vol. 4, no. 3, pp. 304–306, Mar. 1952, doi: 10.1007/BF03397695.

[14] E. Rudy, *Ternary phase equilibria in transition metal-boron-carbon-silicon systems: part V. compendium of phase diagram data*, vol. III. 1969.

[15] V. V. PetKov, S. B. Prima, L. A. Tretyachenko, and O. A. Kocherzhinskij, 'New data on the laves phases in Zr-Cr systems', *Metallofiz. Noveishie Tekhnologii*, vol. 46, p. 80, 1973.

[16] E. Gebhardt, J. Rexer, and G. Petzow, 'Das System Zirknoium-Tantal-Chrom', *International Journal of Materials Research*, vol. 58, no. 8, pp. 534–541, 1967, doi: 10.1515/ijmr-1967-580807.

[17] S. Kanazawa, Y. Kaneno, H. Inoue, W.-Y. Kim, and T. Takasugi, 'Microstructures and defect structures in $ZrCr_2$ Laves phase based intermetallic compounds', *Intermetallics*, vol. 10, no. 8, pp. 783–792, Aug. 2002, doi: 10.1016/S0966-9795(02)00057-2.

[18] M.K. Mcquillan, 'Survey of the constitutional diagram of the chromium-zirconium system', Commonwealth of Australia, SM.165, Jan. 1951.

[19] F. Laves and H. J. Wallbaum, 'Über den Einfluß geometrischer Faktoren auf die stöchiometrische Formel metallischer Verbindungen, gezeigt an der Kristallstruktur des KNa $_2$', *Z. Anorg. Allg. Chem.*, vol. 250, no. 1, pp. 110–120, Jul. 1942, doi: 10.1002/zaac.19422500110.

[20] H. J. Wallbaum, 'Uber weitere Zirkonium verbindungen mit Ubergangs elementen', *Naturwissenschaften*, vol. 30, no. 9–10, pp. 149–149, Feb. 1942, doi: 10.1007/BF01475390.
[21] Y. Kitano, M. Takata, and Y. Komura, 'High resolution electron microscopy of partial dislocations in the Laves phase structure', *Journal of Microscopy*, vol. 142, no. 2, pp. 181–190, May 1986, doi: 10.1111/j.1365-2818.1986.tb02755.x.
[22] C. B. Jordan and P. Duwez, 'Progress Report, 20-196, CIT Jet propulsion Laboratory', *J.Inst.Metals*, vol. 20, p. 196, Jun. 1953.
[23] S. P. Alisova, P. B. Budberg, and K. I. Shakhova, 'On the polymorphism of the $ZrCr_2$ Compound', *Kristollografiya*, vol. 9, no. 3, p. 419, 1964.
[24] Y.-S. Shen and O. G. Paasche, 'On the transformation of $ZrCr_2$', *Transactions of the metallurgical*, vol. 242, no. 2242, Oct. 1968.
[25] E. Gebhardt and J. Rexer, 'Der Aufbau des Systems $ZrCr_2$-$TaCr_2$', *J. Less-Common Metals*, vol. 11, no. 4, 1968.
[26] B. B. Nemoshkalenko, A. P. Nesepyuk, and B. P. Krivitsky, 'Polymorphism phases of Laves in the system Zirconia-Chromium and its Q-reflection in X-ray emission spectra', *Metallofiika*, 1974.
[27] W. Rostoker, 'Allotropy in the Phase $ZrCr_2$', *Trans.AIME*, vol. 197, p. 304, 1953.
[28] R. P. Elliot and W. Rostoker, 'The occurrence of Laves-Type Phase Among Transition Elements', *Trans. ASM*, vol. 50, pp. 617–633, 1958.
[29] J. Bodega, J. F. Fernández, F. Leardini, J.R. Ares, and C. Sánchez, 'Synthesis of hexagonal C14/C36 and cubic C15 $ZrCr_2$ Laves phases and thermodynamic stability of their hydrides', *Journal of Physics and Chemistry of Solids*, vol. 72, no. 11, pp. 1334–1342, 2011, doi: 10.1016/j.jpcs.2011.08.004.
[30] Xian Ying Meng and D. O. Northwood, 'Polytype structures in Zr-Cr-Fe laves phase', *Journal of the Less Common Metals*, vol. 125, pp. 33–44, Nov. 1986, doi: 10.1016/0022-5088(86)90078-0.
[31] V. N. Svechnikov and A. Ts. Spektor, 'The polymorphism of the Intermetallic Compound $ZrCr_2$', *Phase Transformations*, vol. 22, p. 64, 1968.
[32] W. Pearson, *A handbook of lattice spacings and structures of metals and alloys*. 1964.
[33] T. Massalski, J. Murray, L. Bennett, and H. Baker, 'Binary alloy phase diagram', Metals Park (OH): American Society for Metals, 1986, p. 882.
[34] A. V. Skripov and A. V. Mirmelstein, 'The heat capacity of C15-type $ZrCr_2H_x$: evidence for low-energy localized excitations', *J. Phys.: Condens. Matter*, vol. 5, no. 48, pp. L619–L624, Nov. 1993, doi: 10.1088/0953-8984/5/48/001.
[35] B. Samanta and A. Jain, 'Experimental investigation of lattice thermal expansion and specific heat capacity of C15–Cr_2Zr Laves phase intermetallic compound by HTXRD and DSC', *Intermetallics*, vol. 148, p. 107634, Sep. 2022, doi: 10.1016/j.intermet.2022.107634.
[36] T. Matsui, 'Vaporization study on M, Zr (M = Fe and Cr) by a mass-spectrometric method', *Journal of Nuclear Materials*, vol. 201, pp. 278–283, 1993, doi: 10.1016/0022-3115(93)90184-Z.
[37] J. Sun and B. Jiang, '*Ab initio* calculation of the phase stability, mechanical properties and electronic structure of $ZrCr_2$ Laves phase compounds', *Philosophical Magazine*, vol. 84, no. 29, pp. 3133–3144, Oct. 2004, doi: 10.1080/14786430410001720345.
[38] P. Y. Chevalier and E. Fischer, 'Thermodynamic modelling of the O-U-Zr system', *Journal of Nuclear Materials*, vol. 257, no. 3, pp. 213–255, 1998.
[39] Q. Yao, H. Xing, S. Liu, and J. Sun, 'Theoretical Prediction of Ternary Site Occupancies in $ZrCr_2$ and $NbCr_2$ Laves Phases', *Materials Science Forum*, vol. 546–549, pp. 1451–1454, 2007, doi: 10.4028/www.scientific.net/MSF.546-549.1451.

[40] X.-Q. Chen, W. Wolf, R. Podloucky, and P. Rogl, '*Ab initio* study of ground-state properties of the Laves phase compounds $TiCr_2$, $ZrCr_2$, and $HfCr_2$', *Phys. Rev. B*, vol. 71, no. 17, p. 174101, May 2005, doi: 10.1103/PhysRevB.71.174101.
[41] M. Krčmar and C. L. Fu, 'First-principles study of point-defect structures in C15 $ZrCo_2$ and $ZrCr_2$ and B2 ZrCo', *Phys. Rev. B*, vol. 68, no. 13, p. 134110, Oct. 2003, doi: 10.1103/PhysRevB.68.134110.
[42] A. Kellou, T. Grosdidier, C. Coddet, and H. Aourag, 'Theoretical study of structural, electronic, and thermal properties of Cr (Zr,Nb) Laves alloys', *Acta Materialia*, vol. 53, no. 5, pp. 1459–1466, Mar. 2005, doi: 10.1016/j.actamat.2004.11.039.
[43] S. Curtarolo, 'AFLOWLIB.ORG: A distributed materials properties repository from high-throughput ab initio calculations', *Computational Materials Science*, vol. 58, pp. 227–235, 2012, doi: 10.1016/j.commatsci.2012.02.002.
[44] J. E. Saal, S. Kirklin, M. Aykol, B. Meredig, and C. Wolverton, 'Materials Design and Discovery with High-Throughput Density Functional Theory: The Open Quantum Materials Database (OQMD)', *JOM*, vol. 65, no. 11, pp. 1501–1509, Nov. 2013, doi: 10.1007/s11837-013-0755-4.
[45] R. Sarhaddi, H. Arabi, and F. Pourarian, 'Structural, stability and electronic properties of C15- AB_2 (A = Ti , Zr ; B = Cr) intermetallic compounds and their hydrides: An *ab initio* study', *Int. J. Mod. Phys. B*, vol. 28, no. 17, p. 1450105, Jul. 2014, doi: 10.1142/S0217979214501057.
[46] J. Rodriguez-Carvajal, 'Recent developments of the program FULLPROF, commission on powder diffraction', *IUCr Newsl.*, vol. 26, Jan. 2001.
[47] I. I. Kornilov, P. B. Budberg, K. I. Shakhova, and S. P. Alisova, 'The equilibrium diagram of $TiCr_2$ - $ZrCr_2$', *Doklady Akademii Nauk SSSR*, vol. 161, no. 6, pp. 1378–1381, 1965.
[48] P. A. Suprunenko, V. Ya. Markiv, and T. M. Tsvetkova, 'Magnetic and X-ray diffraction study of Laves phases in the ternary systems {Ti, Zr, Hf}-Cr-Al', *Russian Metallurgy (English Translation)*, vol. 1, pp. 207–210, 1984.
[49] A. T. Dinsdale, 'SGTE DATA FOR PURE ELEMENTS', *Calphad*, vol. 15, no. 4, pp. 317–425, Oct. 1991, doi: 10.1016/0364-5916(91)90030-N.
[50] T. Maciąg and K. Rzyman, 'Calorimetric studies of the enthalpies of formation of alloys from Ni75Al25- Ni75Cr25 and Ni75Al25-Ni85Cr15 sections at 873 K', *Journal of Achievements in Materials and Manufacturing Engineering*, vol. 55, no. 2, p. 5, 2012.
[51] J. L. Murray, 'The Al-Cr (aluminum-chromium) system', *JPE*, vol. 19, no. 4, pp. 367–375, Aug. 1998, doi: 10.1007/BF02735058.
[52] Y. Esin *et al.*, 'Enthalpies of Formation of Molten Binary Aluminum Alloys with Yttrium, Zirconium, Vanadium, and Chromium', *Splavy Redk. Met. s Osobymi Fiz.-Khim*, vol. 177, no. 80, 1975.
[53] S. Kek, K. Rzyman, and F. Sommer, 'Determination of the enthalpy of formation of ternary Ni_3Al-based alloys', *Ann. Phys. B*, vol. 86, pp. 31–38, 1990.
[54] B. C. Sudavtsova, A. V. Shuvalov, and N. O. Sharkina, 'Thermochemical properties of liquid binary alloys of Al-(Cr, Ni) systems', *Rasplvy*, no. 1, pp. 97–99, 1990.
[55] A. A. Zubkov, 'Dissolution enthalpies of 3d transition metals in liquid aluminium', *The Journal of Chemical Thermodynamics*, vol. 26, no. 12, pp. 1267–1274, Dec. 1994, doi: 10.1006/jcht.1994.1144.
[56] P. Saltykovt, I. Arpshofen, H. J. Seifert, and F. Aldinger, 'Enthalpy of Mixing of Liquid Al-Cr and Cr-Ni Alloys', *J. Mater. Sci. Technol.*, vol. 18, no. 2, pp. 167–170, 2002.
[57] K. Gajavalli, M. Barrachin, P. Benigni, J. Rogez, G. Mikaelian, and E. Fischer, 'Determination of solution enthalpy of zirconium in liquid aluminum', *The Journal of Chemical Thermodynamics*, vol. 135, pp. 198–204, Aug. 2019, doi: 10.1016/j.jct.2019.03.037.

[58] M. Barrachin *et al.*, 'Critical evaluation of experimental data of solution enthalpy of zirconium in liquid aluminum', *The Journal of Chemical Thermodynamics*, vol. 128, pp. 295–304, Jan. 2019, doi: 10.1016/j.jct.2018.08.010.
[59] L. Brewer, 'The cohesive energies of the elements', Lawrence Berkeley National Laboratory, 1977.
[60] E. Joseph and M. Haque, 'The Cohesive Energy Calculations of Some BCC (Li, Cr, Fe, Mo) Lattices Using Density Functional Theory', *AJOPACS*, vol. 1, no. 2, pp. 1–10, Jan. 2016, doi: 10.9734/AJOPACS/2016/30695.
[61] P. H. T. Philipsen and E. J. Baerends, 'Cohesive energy of 3 *d* transition metals: Density functional theory atomic and bulk calculations', *Phys. Rev. B*, vol. 54, no. 8, pp. 5326–5333, Aug. 1996, doi: 10.1103/PhysRevB.54.5326.
[62] M. I. Baskes and R. A. Johnson, 'Modified embedded atom potentials for HCP metals', *Modelling and Simulation in Materials Science and Engineering*, vol. 2, no. 1, p. 147, Jan. 1994, doi: 10.1088/0965-0393/2/1/011.
[63] Y.-M. Kim, B.-J. Lee, and M. I. Baskes, 'Modified embedded-atom method interatomic potentials for Ti and Zr', *Physical Review B*, vol. 74, no. 1, p. 014101, 2006.
[64] I. Bajenova *et al.*, 'Third-generation CALPHAD description of pure GeO_2 at 1 atm', *Calphad*, vol. 74, p. 102299, Sep. 2021, doi: 10.1016/j.calphad.2021.102299.
[65] Z. He, B. Kaplan, H. Mao, and M. Selleby, 'The third generation Calphad description of Al–C including revisions of pure Al and C', *Calphad*, vol. 72, p. 102250, Mar. 2021, doi: 10.1016/j.calphad.2021.102250.
[66] M. H. F. Sluiter, 'Ab initio lattice stabilities of some elemental complex structures', *Calphad*, vol. 30, no. 4, pp. 357–366, Dec. 2006, doi: 10.1016/j.calphad.2006.09.002.
[67] Y. Wang *et al.*, 'Ab initio lattice stability in comparison with CALPHAD lattice stability', *Calphad*, vol. 28, no. 1, pp. 79–90, Mar. 2004, doi: 10.1016/j.calphad.2004.05.002.

Chapter IV

Zr-Cr-O ternary system

Chapter IV. Zr-Cr-O ternary system

IV.1 Introduction

In this chapter, we focus on studying the Zr-Cr-O ternary system. Few experimental data were published on this system and no CALPHAD modelling was published. The final objective of this work is to provide the first CALPHAD modeling of the system based on reliable phase relations and thermodynamic data. To reach this objective, experimental investigation of the phase equilibria at high temperature will be performed as well as measurements of thermodynamic properties of the only identified compound, Zr_3Cr_3O, in the system. The ternary CALPHAD model will be based on the models of the binary systems Zr-Cr (detailed in Chapter III), Zr-O, and Cr-O (these two latter systems are currently modeled in the NUCLEA database developed at IRSN), and the optimization of the ternary parameters according to our experimental data. The sub-sections of this chapter are devoted to the following topics:

In sub-section IV.2, a literature review is presented:

- ✓ A summary of the current state of the modeling of the Zr-O and Cr-O binary systems is presented in sections IV.2.1.1 and IV.2.1.2.
- ✓ The available experimental phase diagram of the ternary system Zr-Cr-O is presented in section IV.2.2.
- ✓ A review of the quasi-binary system ZrO_2-Cr_2O_3 is introduced in section IV.2.3.
- ✓ Literature found on the ternary phase $Zr_3Cr_3O_x$ is summarized in section IV.2.4.

In sub-section IV.3, the aims and methods are presented.

Our results are then presented and discussed in sub-section IV.4:

- ✓ Some basic experiments on the quasi-binary system ZrO_2-Cr_2O_3 are detailed in IV.4.1.1.
- ✓ The phase relation studies of isothermal sections at 1200°C and 1500°C are presented in IV.4.1.2.
- ✓ A thorough study of the ternary phase $Zr_3Cr_3O_x$ is presented in IV.4.1.3.2, including the preparation method, the crystal structure study, and the measurements of thermodynamic properties.

A CALPHAD modeling is then made with all these experimental results, our assessed Zr-Cr system, and Zr-O/Cr-O descriptions of NUCLEA. The assessed model is presented in IV.4.2.

At last, conclusions and perspective works are proposed in IV.5.

IV.2 Literature review

Our review of the ternary system Zr-Cr-O starts with the three sub binary systems:

- ✓ The Zr-Cr binary system has been experimentally investigated and reassessed in this work (Chapter III). The new CALPHAD modeling was worked out with our experimental data and will be used in the assessment of the ternary system.
- ✓ Two binary systems Zr-O and Cr-O have been the subject of many investigations and a brief review of the current state of these systems is presented in sub-sections IV.2.1.1 and IV.2.1.2. The systems are integrated into the NUCLEA database, currently developed at IRSN. The modeling of NUCLEA for two binary systems will be used in our assessment of the ternary system.

The only publication of the Zr-Cr-O ternary phase diagram displayed manually assessed isothermal sections at 1200, 1500 and 1700°C with sparse experimental points [1]. No CALPHAD assessments have been published till now. A short review of this work will be presented in IV.2.2.

The quasi-binary system ZrO_2-Cr_2O_3 also drew attention. A review of the available publications is presented in sub-section IV.2.3.

$Zr_3Cr_3O_x$ was the only ternary compound reported in the ternary system Zr-Cr-O [1]. Little is known about this phase till now. Its structure and stoichiometric composition are still not fully determined and its thermodynamic properties such as the heat capacity or the enthalpy of formation are still unknown. A review of this phase is presented in sub-section IV.2.4.

IV.2.1 Assessed Zr-O and Cr-O systems

IV.2.1.1 Zr-O system

A first detailed review of the experimental phase equilibrium and thermodynamic information for the Zr–O system was given by Abriata *et al.* [2]. With the development of the CALPHAD approach, several descriptions of the system were reported, e.g. Liang *et al.* [3], Arroyave *et al.* [4], Chen *et al.* [5], Wang *et al.* [6], and Chevalier *et al.* [7]. These descriptions differ in the choice of thermodynamic models for the different phases, particularly for cubic zirconia and liquid. The work of Wang *et al.* [8] (Figure IV-2) is considered by some reviewers [9] as the

most comprehensive one. The Wang's model was developed from Abriata's data and some experimental data from thermodynamic studies [10]–[13]. A model $(Zr^{+2}, Zr^{+4})(O^{-2}, Va)_2$ is adopted for cubic ZrO_2 while an ionic model is applied for the liquid phase. Most of the experimental phase equilibria and thermodynamic data are reproduced very well. The CALPHAD model for the Zr-O system considered in this work is taken from the NUCLEA thermodynamic database currently developed at IRSN in the framework of severe accident research and development. It has been published by Chevalier *et al.* [7]. The choice of this last model is dictated by the fact that the modeling of the Zr-Cr-O system that will be carried out in this work is intended to be integrated into the NUCLEA database.

The condensed solutions and stoichiometric compounds, considered in this description are the following:

- ✓ the liquid phase, L
- ✓ the cubic ZrO_{2-x} solid solution (fcc_C1)
- ✓ the tetragonal zirconium dioxide compound ZrO_2(tet)
- ✓ the monoclinic zirconium dioxide compound ZrO_2(mon)
- ✓ the solid solutions based on the two allotropes of pure zirconium, Zr(hcp_A3); Zr(bcc_A2)

A three sub-lattice model $(Zr)(O, Va)_2(Va, O)$ is applied to cubic zirconia while an associate model (O, ZrO_2, Zr) is taken into account for the liquid phase. The calculated phase diagram with the superimposed experimental data is reported in Figure IV-3. The calculated invariant points are reported in Table IV-1. Different versions of the phase diagram are shown below as the Abriata's assessment (Figure IV-1) and the Wang's model (Figure IV-2). A difference between the Wang's and Chevalier's models is the curvature of the liquidus line of ZrO_{2-x}. Up to very recently no measurement was available to fit this line. Based on solubility measurements, Veshchunov [14] tentatively reported liquidus points at high temperatures (T > 2400 K) in the ZrO_2-rich region of the ZrO_2-Zr partial phase diagram. Very recent experimental data from Brunel *et al.* [15], should be considered in the future to improve the model in this zone.

Table IV-1 Invariant equilibrium in the Zr-O system

Reaction	T(K)	Type	Phase	Composition(at.%)	
				O	Zr
L=FCC_C1	2985	melting	L,FCC_C1	66.7	33.3
FCC_C1=L+G	2979		FCC_C1	66.9	33.1
			L	66.9	33.1
			G	99.9	0.1
FCC+C1=TET_OXIDE	2650	allotropic	FCC_C1,TET_OXIDE	66.7	33.3
FCC_C1,TET_OXIDE,G	2646		FCC_C1,TET_OXIDE	66.7	33.3
			G	100.0	0
HCP_A3=L	2446	melting	HCP_A3,L	29.9	70.1
L=FCC_C1+HCP_A3	2372	eutectic	L	41.2	58.8
			FCC_C1	61.7	38.3
			HCP_A3	31.2	68.8
L+BCC_A2=HCP+A3	2244	peritectic	L	10.5	89.5
			BCC_A2	10.4	89.6
			HCP_A3	18.4	81.6
L=BCC_A2	2127.86	melting	L,BCC_A2	0	100.0
FCC_C1=TET_OXIDE+HCP_A3	1797	eutectoid	FCC_C1	63.7	36.3
			TET_OXIDE	66.7	33.3
			HCP_A3	30.6	69.4
TET_OXIDE=O2ZR1(S)Monoclinic	1478	allotropic	TET_OXIDE,O2ZR1(S)Monoclinic	66.7	33.3
TET_OXIDE=O2ZR1(MON)+HCP_A3	1478	eutectoid	TXT_OXIDE	66.7	33.3
			O2ZR1(S)Monoclinic	66.7	33.3
			HCP_A3	29.9	70.1
TET(OX),O2ZR1(S)Monoclinic,G	1478		TXT_OXIDE,	66.7	33.3
			O2ZR1(S)Monoclinic	100.0	0
			G		
BCC_A2=HCP_A3	1139	allotropic	BCC_A2,HCP_A3	0.0	100.0

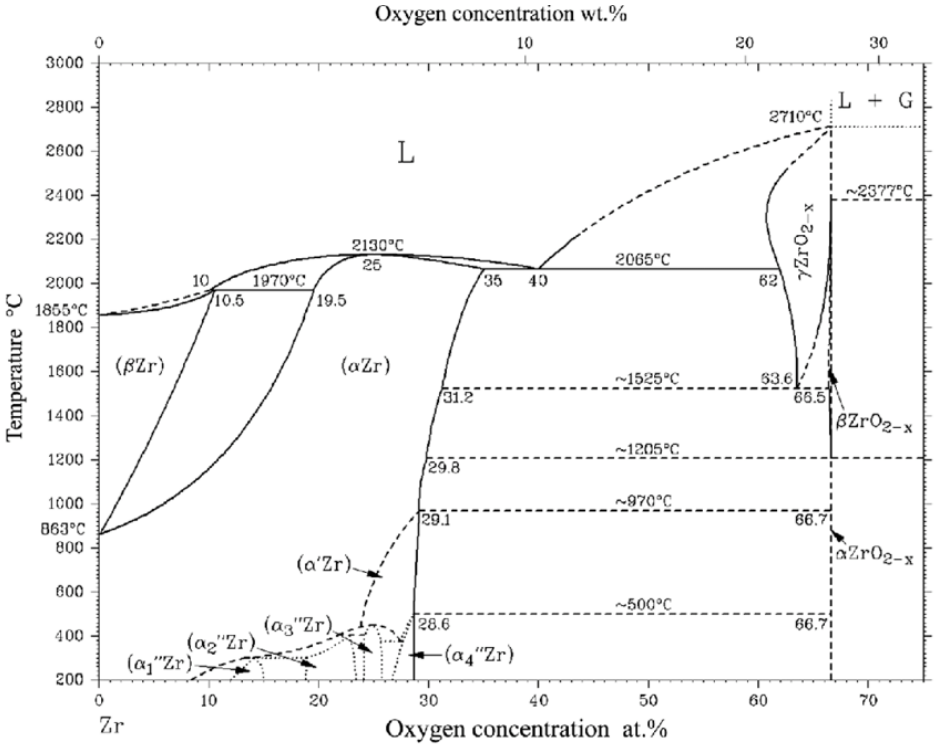

Figure IV-1 Phase diagram of Zr-O binary system [2]

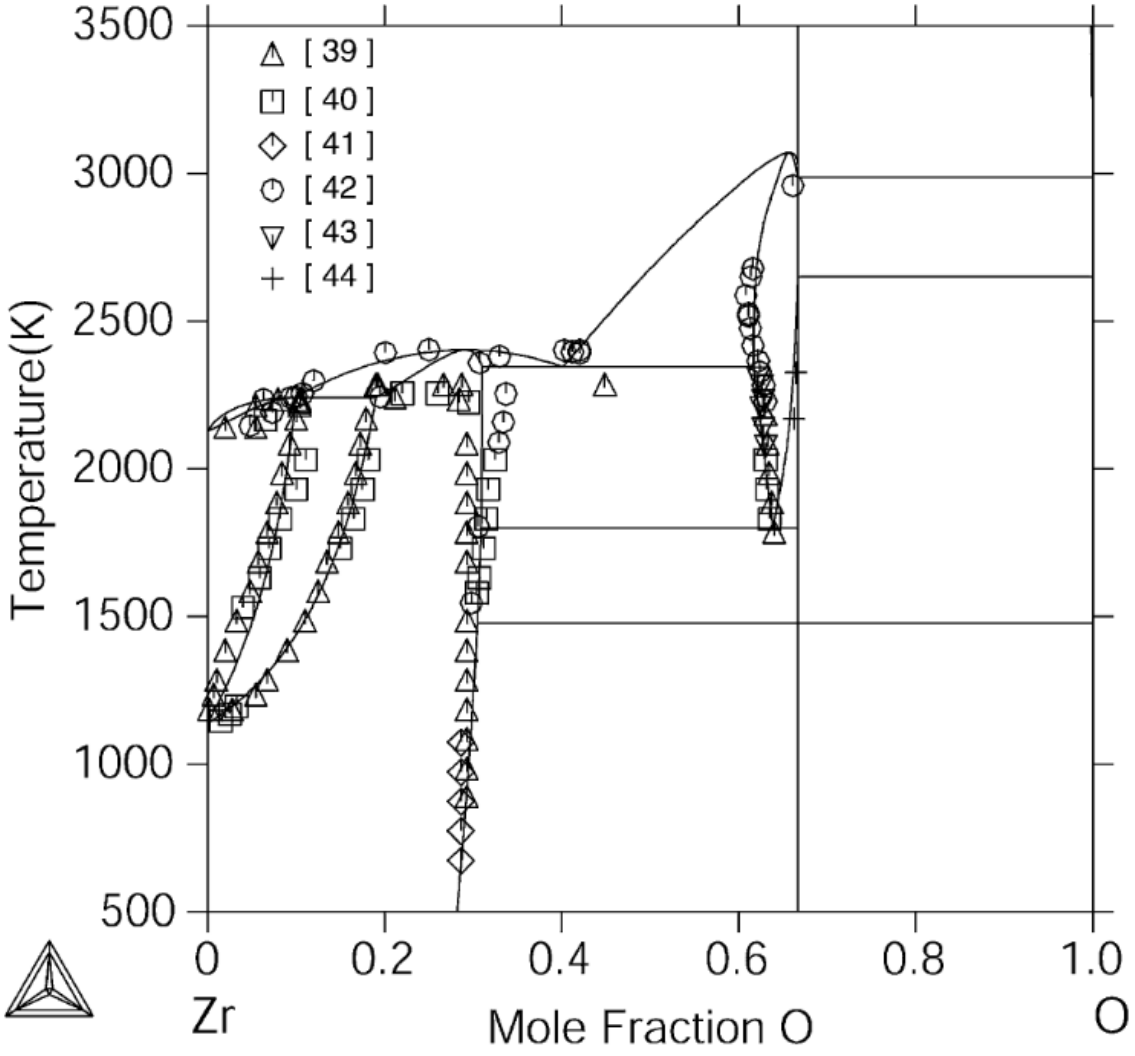

Figure IV-2 Assessed the Zr-O binary system of Wang [8] with experimental data [39]=Domagala and McPherson [16], [40]= Gebhardt *et al.* [17], 41=Holmberg *et al.* [18], [42] Ackermann *et al.* [19], [43] R.J. Ackermann *et al.* [20], [44]=Rauh and Garg [21] superimposed.

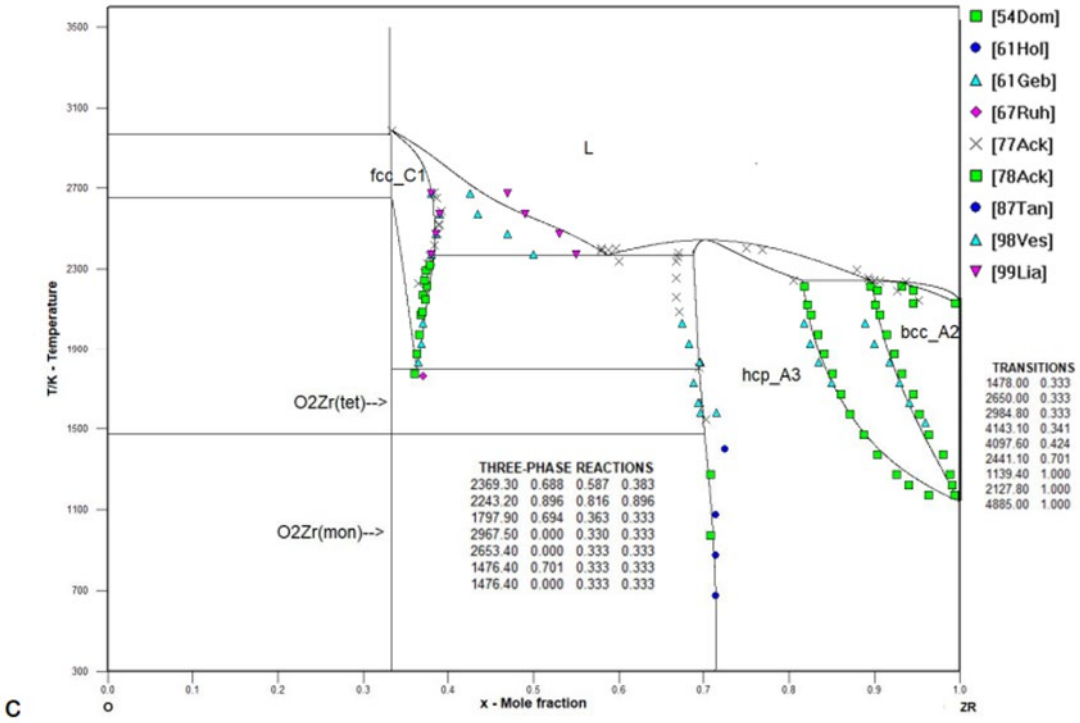

Figure IV-3 Zr-O binary system modeled by Chevalier *et al.* [7] retained in this work

IV.2.1.2 Cr-O system

The publications on the binary system Cr-O are scarce compared to those on Zr-O. Banik *et al.* [22] first established a phase diagram of the system with a sub-regular solution model for the liquid phase. Taylor and Dinsdale [23] described the liquid phase with a two sub-lattice ionic model $(Cr^{+3})_p(O^{-2},Va^{-q})_q$, with only one valence for chromium (Figure IV-4).

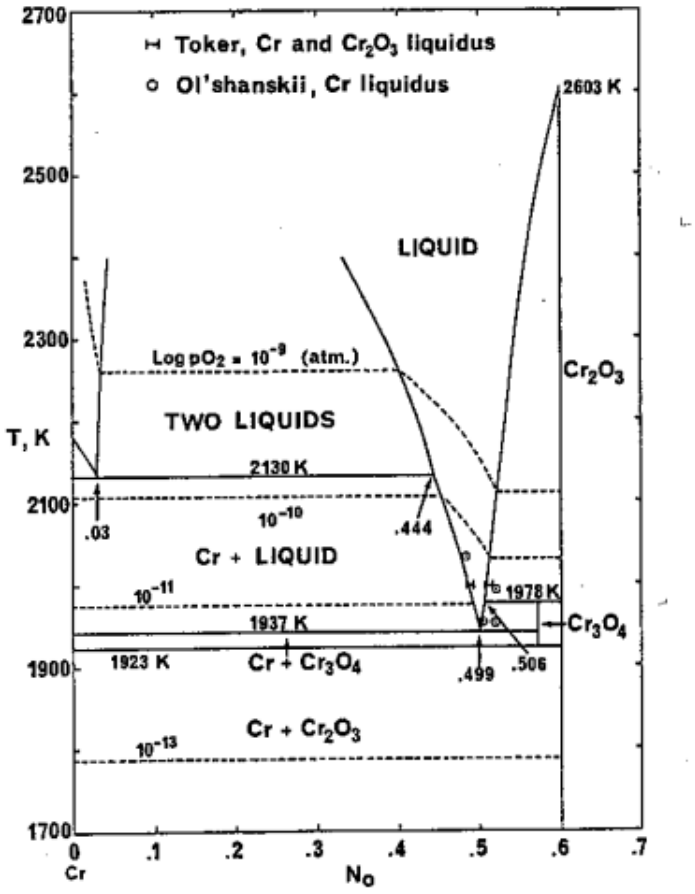

Figure IV-4 Modelled Cr-O binary system of Taylor [23]

Later on, Kowalski and Spencer [24] modeled the liquid solution with a single associated species $CrO_{1.5}$. In Figure IV-5, the published phase diagram of Kowalski is compared with that of Taylor and Dinsdale [23]. Kowalski corrected the non-physical miscibility gap appearing at high temperatures in the Taylor's model.

The calculated phase diagram only contained the two stoichiometric oxides Cr_2O_3 and Cr_3O_4, the latter oxide which was identified by Toker *et al.* [25]. Some other Cr oxides such as CrO_2, Cr_5O_{12}, Cr_6O_{15}, and CrO_3 were reported in the literature, but not included in these phase diagrams [26].

Povoden *et al.* [27] described the liquid phase with an ionic model including 2 sublattices, with valences 2 and 3 for chromium $(Cr^{+3},Cr^{+2})_P(O^{-2},Va^{-q})_q$. The calculated Cr-O phase diagram is shown in Figure IV-6. Povoden obtained a better agreement with the experimental data than before.

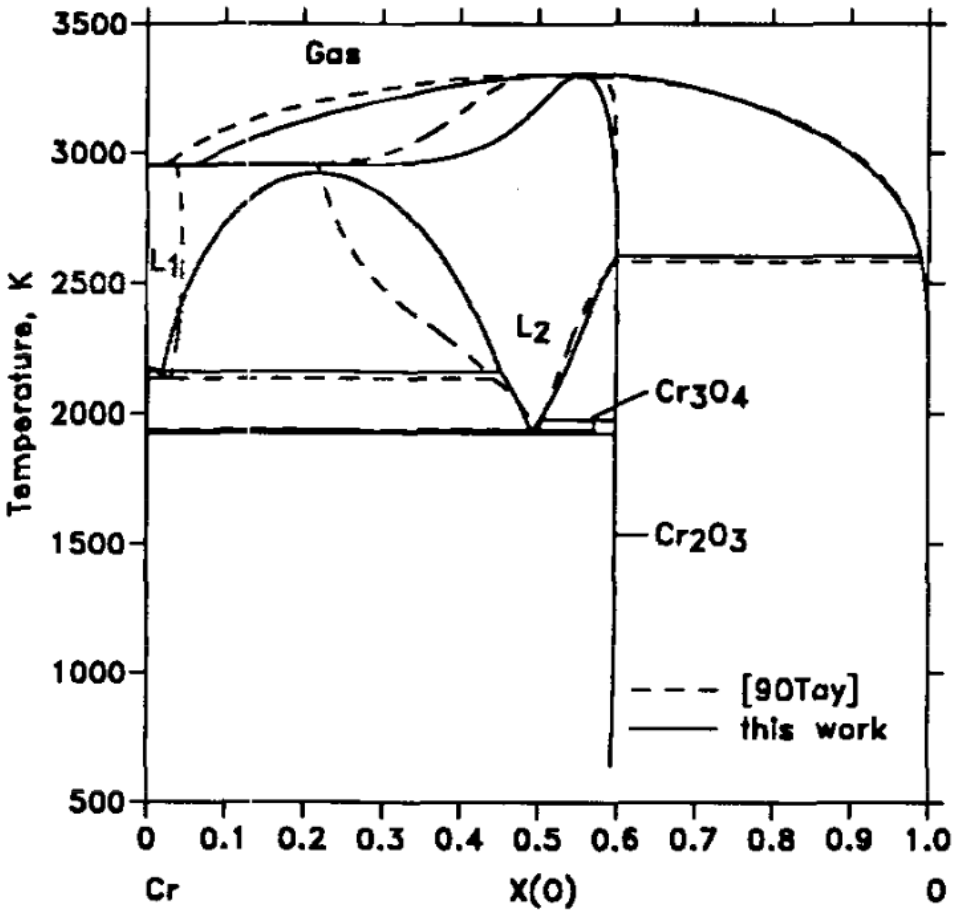

Figure IV-5 Phase diagram of Cr-O system [24] compared to [23]

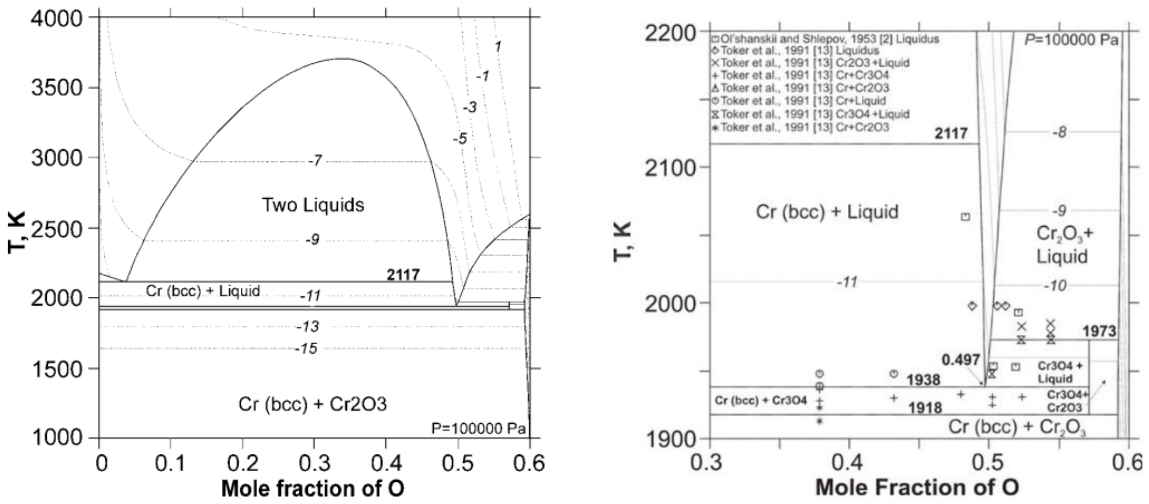

Figure IV-6 Calculated Cr-O phase diagram with oxygen isobars by Povoden *et al.* [27]. The gas phase was not included in the calculation. Enlargement of the calculated Cr-O phase diagram close to the CrO composition, with experimental data and oxygen isobars included.

The CALPHAD model for the Cr-O system considered in this work is taken from the NUCLEA thermodynamic database currently developed at IRSN (the calculated invariant reactions are reported in Table IV-2). The choice of this particular model is motivated by the fact that the modeling of the Zr-Cr-O system that will be carried out in this work is intended to be integrated into the NUCLEA database. In this model, the Cr_2O_3 and Cr_3O_4 are modeled as stoichiometric compounds. The associate model is applied to the liquid phase with 4 associates (CrO, Cr_2O_3, O, Cr). The Cr-O phase diagram of NUCLEA is illustrated in Figure IV-7 (without gas phase) and Figure IV-8 (with gas phase). The comparison between the modeling and the experimental data (Figure IV-9 and Figure IV-10) is satisfactory.

Table IV-2 Invariant equilibria and special points in the Cr-O system in the NUCLEA database.

Reaction	T(K)	Type	Phase	Composition(at.%)	
				Cr	O
L1+G=L1+L2	2779.5		L1	56.9	43.1
			G	98.8	1.2
			L2	90.3	9.7
L+G=Corundum	2569		L	40.3	59.7
			G	0.8	99.2
			Corundum	40.0	60.0
L=bcc_a2	2180	melting	L, bcc_a2	100.0	0.0
L1=L2+bcc_a2	2127	monotectic	L1	96.7	3.3
			L2	52.0	48.0
			bcc_a2	100.0	0.0
L+Corundum=Spinel	1978	peritectic	L	49.4	50.6
			Corundum	40.0	60.0
			Spinel	42.9	57.1
L=bcc_a2+Spinel	1934	eutectic	L	50.2	49.8
			bcc_a2	100.0	0.0
			Spinel	42.9	57.1
Spinel=bcc_a2+Corundum	1917	eutectoid	Spinel	42.9	57.1
			bcc_a2	100.0	0.0
			Corundum	40.0	60.0
Corundum+G=CrO_2	443		Corundum	40.0	60.0
			G	0.0	100.0
			CrO_2	33.3	66.7

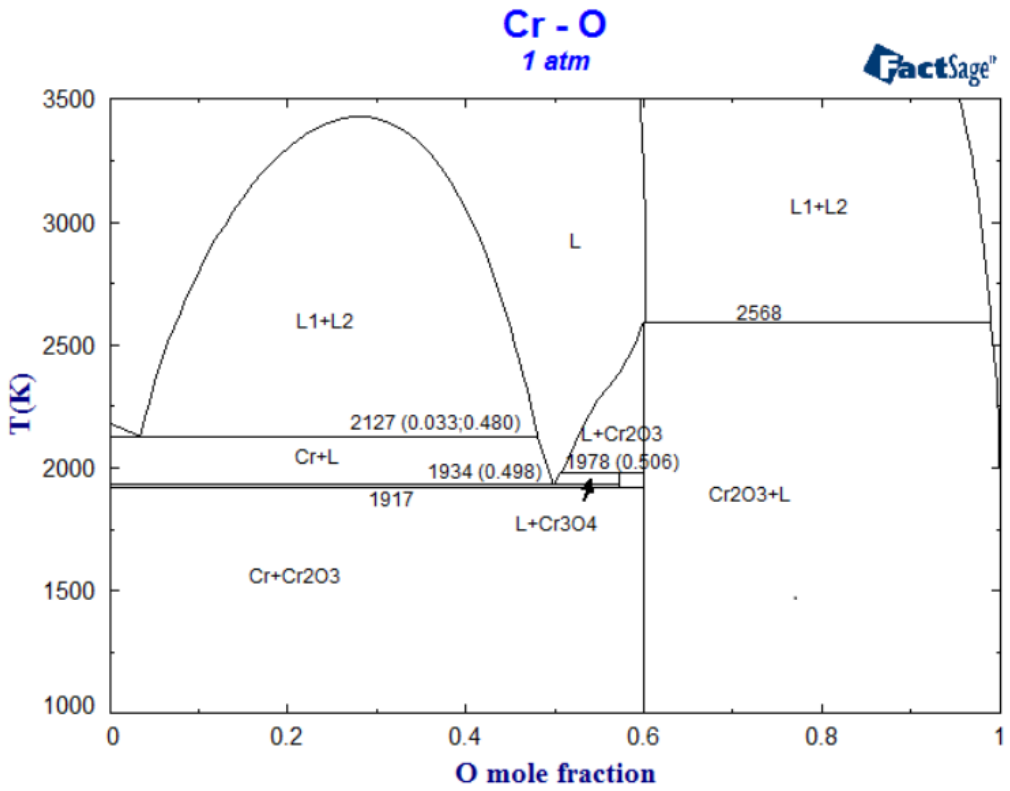

Figure IV-7 Cr-O binary system modeled in NUCLEA [28] (without gas phase) retained in this work

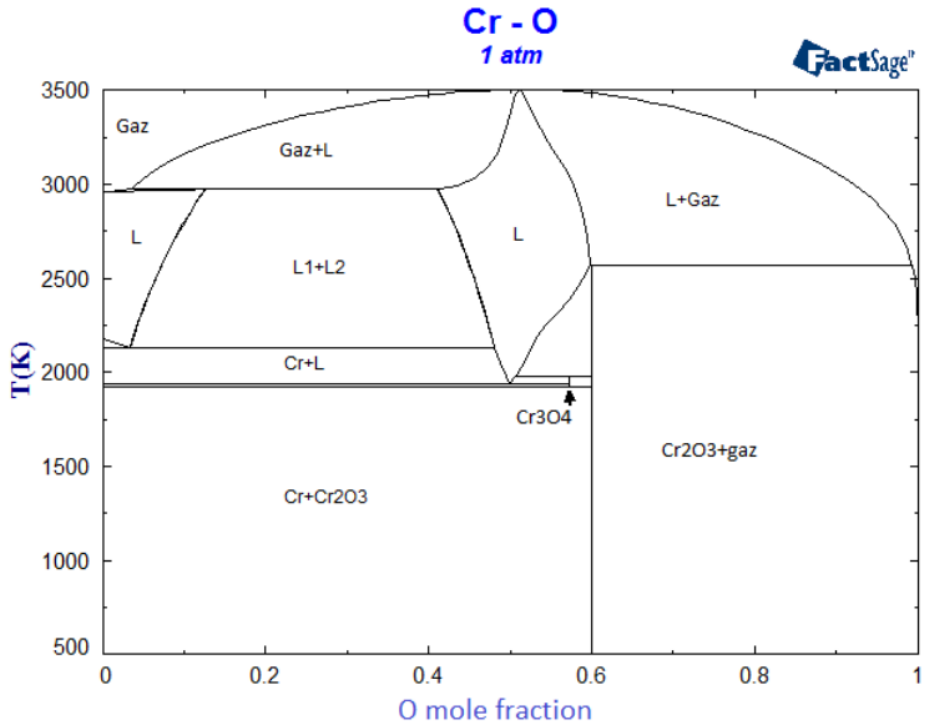

Figure IV-8 Cr-O binary system modeled in NUCLEA [28] (with gas phase) retained in this work

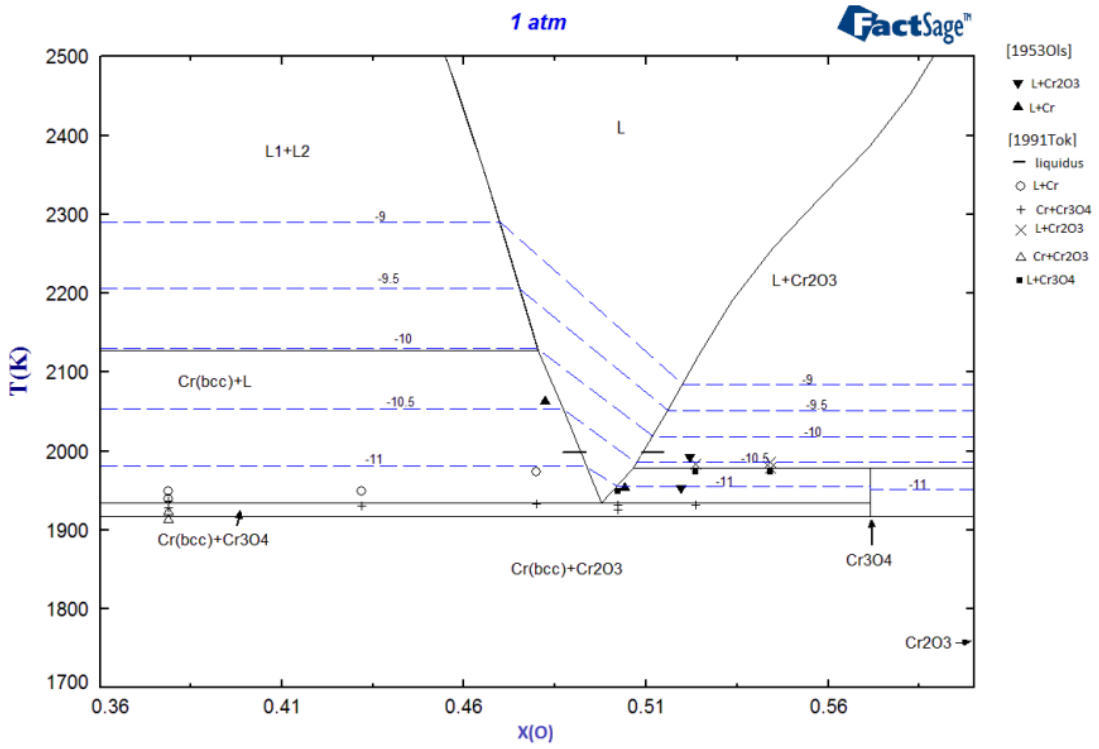

Figure IV-9 Zoom of the Cr-O phase diagram calculated in NUCLEA, with the experimental points [1991Tok]=Toker *et al.* [25], [1953Ols]=Ol'shanskii and Shlepov [29] and the $P(O_2)$ isobars in atm superimposed

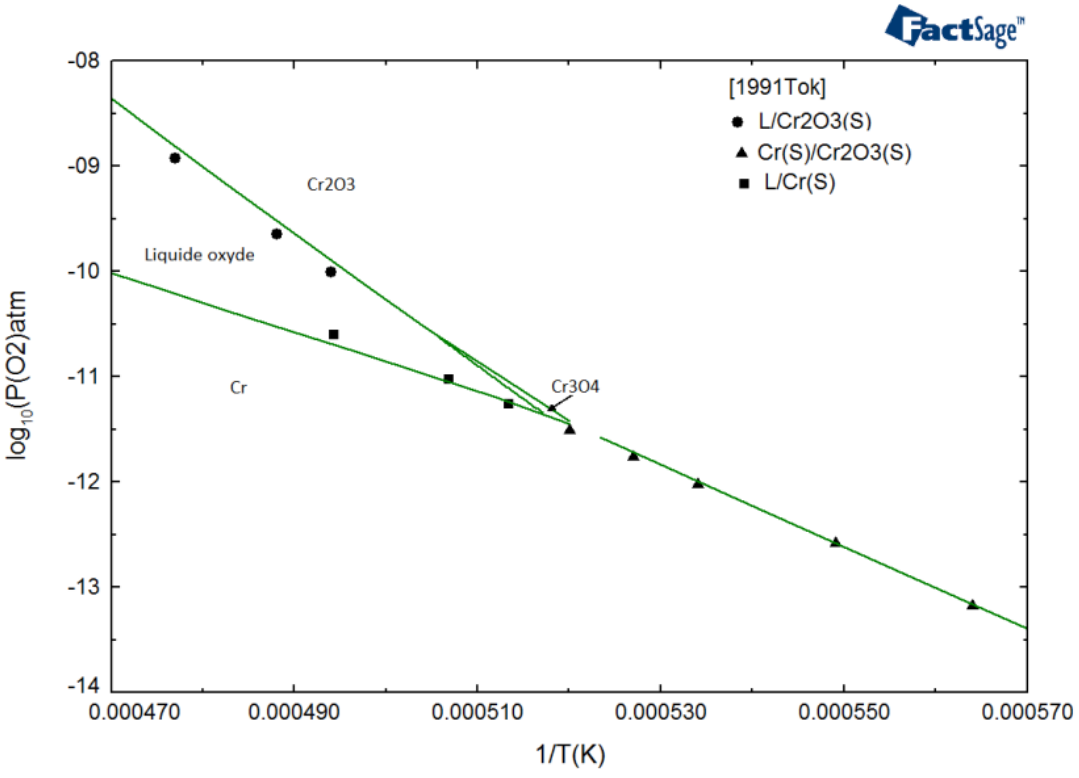

Figure IV-10 Oxygen partial pressure calculated for two-phase equilibria, compared with experimental values from Toker *et al.* [25]

IV.2.2 Ternary phase diagram

To our knowledge, Rhee and Hoch [1] are the only authors to have studied the ternary Zr-Cr-O. The isothermal sections at 1200°C, 1500°C and 1700°C are reproduced in Figure IV-11, Figure IV-12 and Figure IV-13 respectively. Samples were synthesized by melting pure Zr and Cr metals and ZrO_2 and Cr_2O_3 powders by induction heating under argon. Samples were mainly studied with XRD, their compositions being reported by black points in the Figures.

Isothermal sections at 1200°C and 1500°C are very similar, the main difference being the presence at 1500°C of a liquid domain originating at the Zr-Cr binary border and extending moderately into the ternary. The results of Hayes *et al.* [30] and Domagala *et al.* [31] on the binary system Zr-Cr were accepted in the Rhee's assessment.

The isothermal section at 1700°C showed different phase relations. In particular, an important liquid region appears while the ternary compound Zr_3Cr_3O is still stable at this temperature.

Another important point to declaim is that no Cr_3O_4 phase was formed in the system till 1660°C.

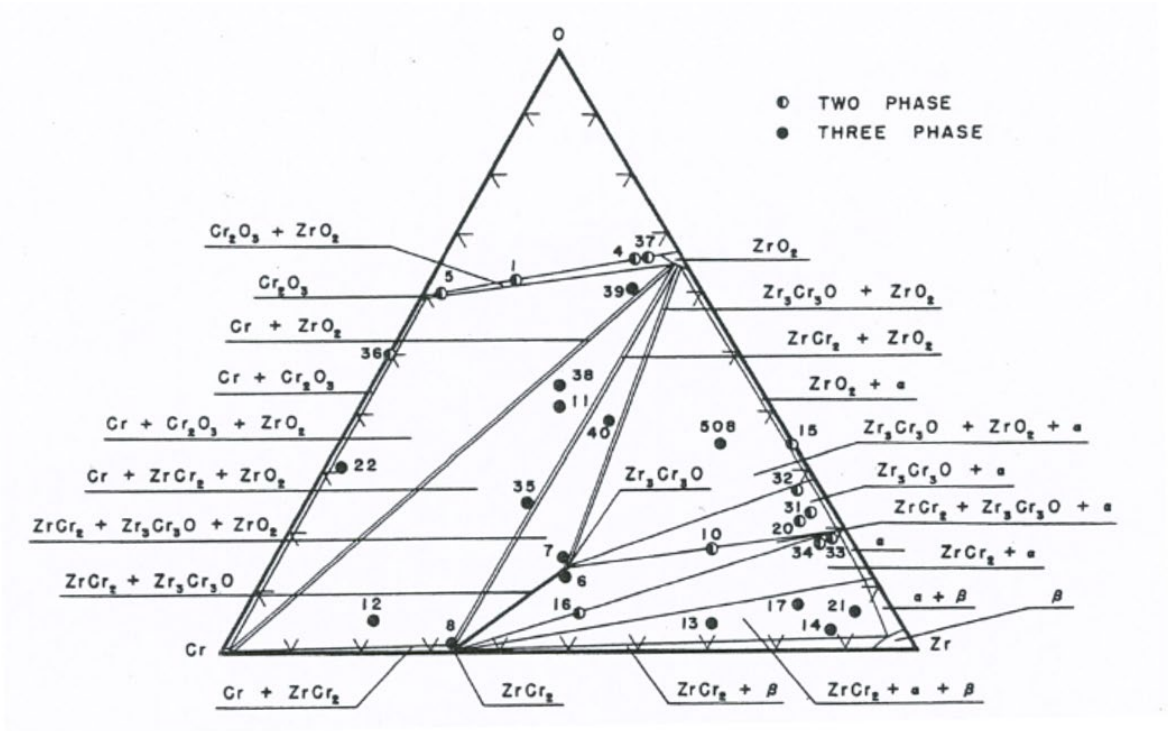

Figure IV-11 Isothermal section of Zr-Cr-O system at 1200°C [1]

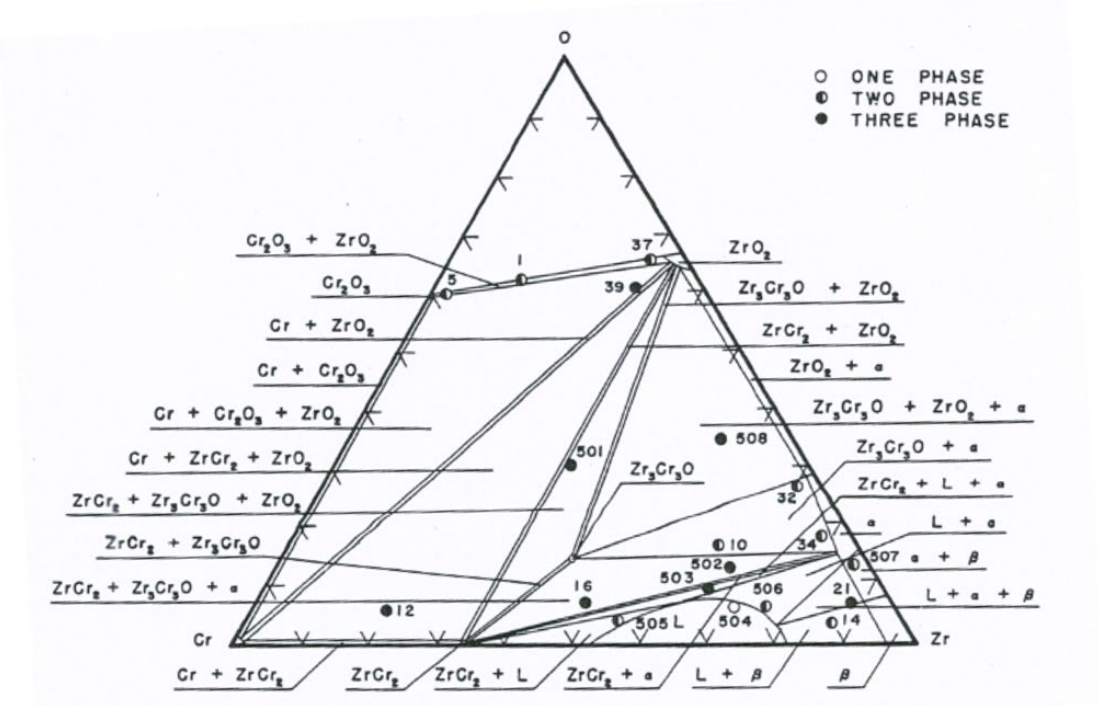

Figure IV-12 Isothermal section of Zr-Cr-O system at 1500°C [1]

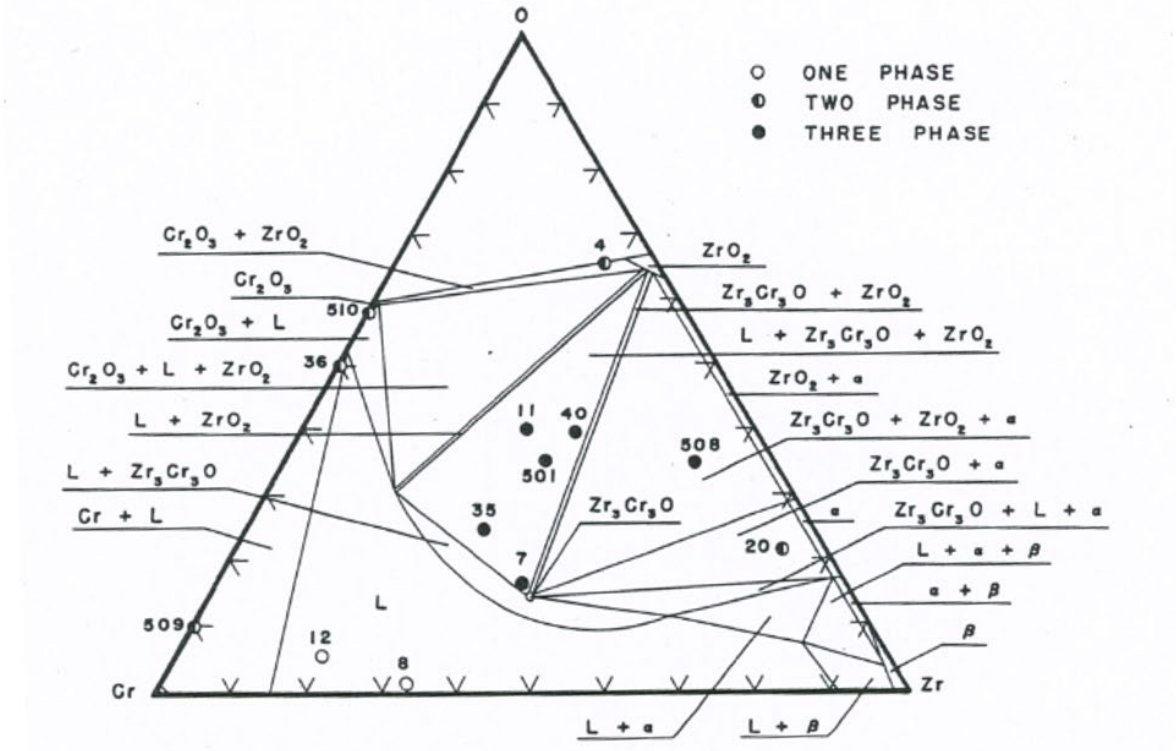

Figure IV-13 Isothermal section of Zr-Cr-O system at 1700°C [1]

Very recently, a CALPHAD modeling of the Zr-Cr-O system [32] has been presented and isothermal sections calculated at 1200°C, 1500°C, and 1700°C were shown.

IV.2.3 Quasi-binary system ZrO_2-Cr_2O_3

The ZrO_2-Cr_2O_3 section is a quasi-binary section in the ternary Cr-Zr-O system. It was studied by some researchers from the 1930s [33]. These early experiments indicated a simple eutectic reaction in the system, with no intermediate compound (See Figure IV-14). The eutectic point was found at 50% wt. ZrO_2 (as 55.23% mol. ZrO_2) and 2300°C.

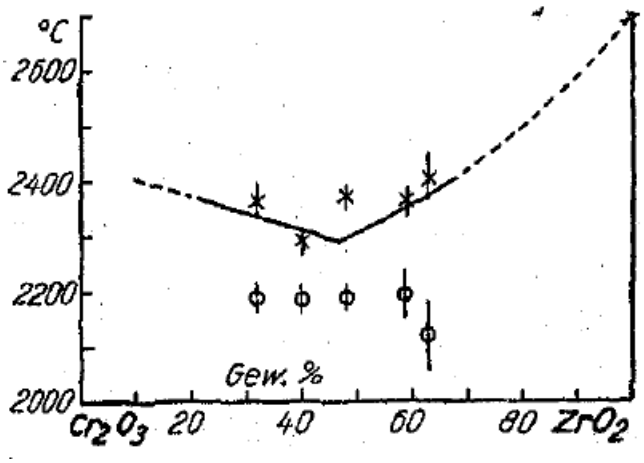

Figure IV-14 Phase diagram of the system ZrO_2-Cr_2O_3 reported by Wartenberg and Werth [33]

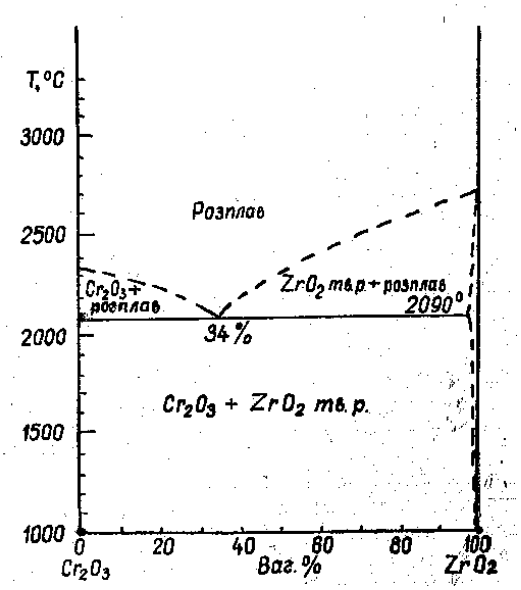

Figure IV-15 Phase diagram of the system ZrO_2-Cr_2O_3 reported by Berezhenoi and Gulko [34]

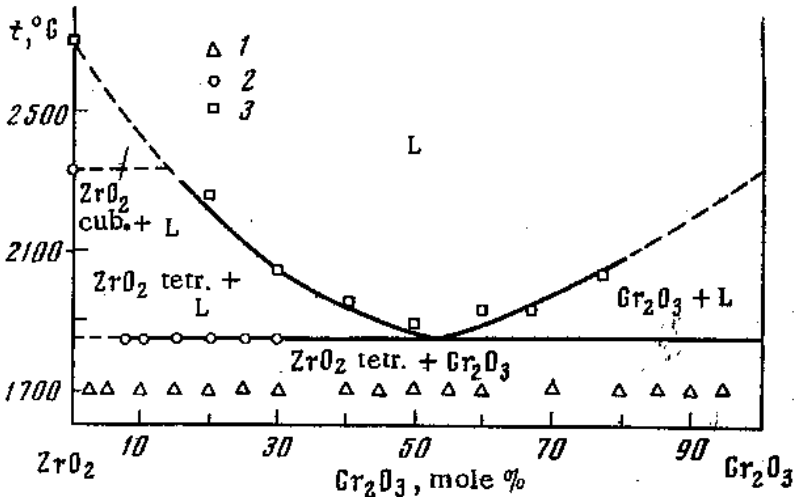

Figure IV-16 Phase diagram of the system ZrO_2-Cr_2O_3 constructed by Lopato *et al.* [35]; (1)= annealing and quenching, (2) = DTA method, (3) = improved DTA method

The eutectic character of the system was then confirmed by Berezhnoi and Gul'ko [34], Smachnaya and Saldau [36] and Lopato *et al.* [35] (Figure IV-16). The eutectic composition and temperature were reported as 66% wt. Cr_2O_3 and 2090°C by Berezhnoi and as 61.1% at. Cr_2O_3 and 1850±10°C by Smachnaya and Lopato. Several other studies determined the characteristics of the eutectic reaction of the system, revealing in Cr_2O_3: 59%wt. (53.85% mol.) and 1880°C in [36], [37]; 55% wt. (49.77% mol.) and 2320°C in [38]; 50% wt. (44.77% mol.) and 1950°C in [39].

Wartenberg and Werth [33] and Rhee and Hoch [1] both found a slight solubility of ZrO_2 in Cr_2O_3 solid solution, without providing numerical values, whereas Smachnaya *et al.* [36], [37] reported high solubility up to 38% wt. (43.1% mol.) of ZrO_2 in Cr_2O_3 solid solution in the temperature range 800-1900°C. The result of Collins and Ferguson [40] was more in agreement with Smachnaya. In his study, Collins used a coprecipitation synthetic route coupled with X-ray analysis to find the maximum of 30% mol. of ZrO_2 in Cr_2O_3 solid solution at 900°C. The recent study by Jerebtsov *et al.* [39] reported a solubility of 40±7% wt. (45.17% mol.) of ZrO_2 in Cr_2O_3 solid solution below the eutectic temperature.

The low solubility of Cr_2O_3 in the ZrO_2 solid solution was reported in several publications [1], [33], [41] or no solubility was mentioned in some studies [36], [37]. Turkin and Maslova [42] reported a solubility of Cr_2O_3 in the ZrO_2 solid solution equal to 0.5-3% wt. (0.41% to 2.45% mol.). Recently, Jerebtsov *et al.* [39] found a maximum solubility of 9±2% wt. (7.42% mol.) of Cr_2O_3 in the ZrO_2 solid solution below the eutectic temperature of 1950°C, at 1840°C.

As previously mentioned, the more recent study was performed by Jerebtsov *et al.* [39]. Jerebtsov et al. have studied the system by DTA in the composition range from 0 to 40 mass % Cr_2O_3, in a molybdenum crucible under argon atmosphere. The molybdenum concentrations in the samples increase with the rise of Cr_2O_3. The eutectic is observed at 1950 °C (2223 K) and 50 wt% ZrO_2 (38 mol% $CrO_{1.5}$-ZrO_2), and ZrO_2 and Cr_2O_3 form extensive solid solutions. The diagram is shown in Figure IV-17. Eutectoid transitions were identified at 1115°C and 1840°C, respectively. Though it was reported that some pollution problem due to molybdenum was encountered during the experiments, this study is still the most complete description of this quasi-binary system till now.

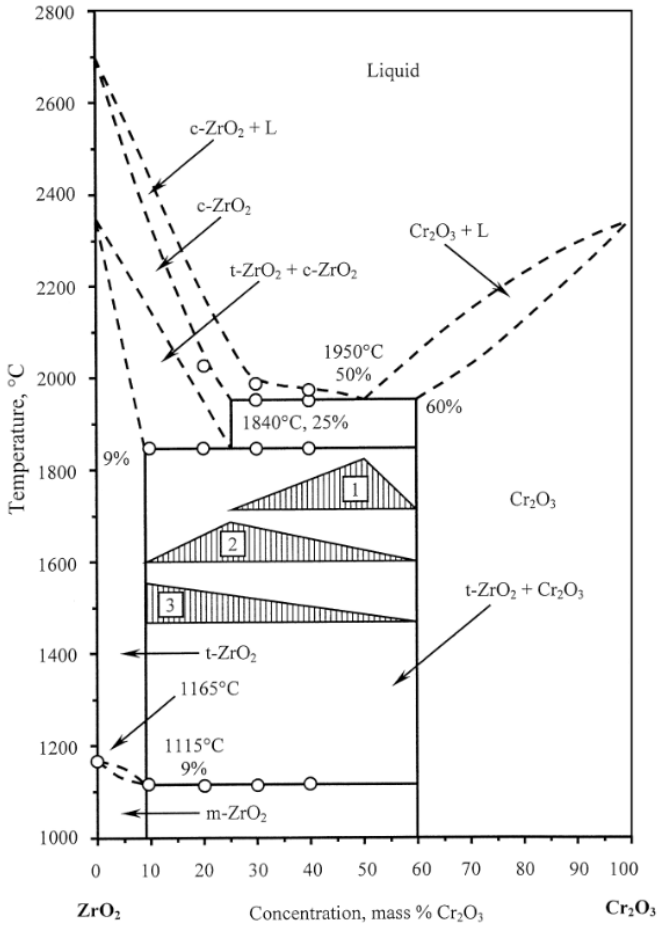

Figure IV-17 Phase diagram of quasi-binary system ZrO_2-Cr_2O_3 by Jerebtsov *et al.* [39]. Triangles show the expected peak areas for 1) eutectic at 1950°C; 2) eutectoid at 1840°C; 3) eutectoid at 1115°C.

No CALPHAD modeling of the quasi-binary system ZrO_2-Cr_2O_3 has been published till now.

IV.2.4 Ternary phase $Zr_3Cr_3O_x$

To the best of our knowledge, Rhee and Hoch [1] were the first to identify the phase $Zr_3Cr_3O_x$ that was characterized by powder XRD with a prototype Ti_2Ni type, also known as η-carbide.

The lattice parameter was reported as a = 11.958±0.002Å. The phase has been confirmed stable at 1500°C, and still solid at 1700°C, according to Rhee.

The $Zr_3Cr_3O_x$ phase was also characterized with a η-carbide structure by Zavaliy [43], very similar to the $Zr_3V_3O_x$ phase, where x= 0.2 to 1.0. A lattice parameter of this phase was reported as 11.953±0.001Å. in agreement with Rhee.

The variation of oxygen content in the Ti_2Ni type phase has been mentioned in Nevitt *et al.* [44], [45]. The possibility of oxygen vacancy in the $Zr_3Cr_3O_x$ structure attracted our attention. This is the reason why the phase is noted as $Zr_3Cr_3O_x$ in this work, assumed to be x=0.2 to 1.0 roughly similar to $Zr_3V_3O_x$.

As far as we know, no pure Zr_3Cr_3O sample was prepared in the previous studies, besides Zavaliy [43] (reported 'minor' impurity in samples). Although the value of the lattice parameter was first reported by Rhee and confirmed by Zavaliy, the exact positions of the atoms in the structure have not been studied until now. In addition, the thermodynamic properties of this phase are not known. It was therefore concluded that the data available in this phase were insufficient for accurate modeling of the ternary system.

IV.3 Study objective and methodology

The main objective of our study is to propose a CALPHAD modeling of the Zr-Cr-O ternary system. The experimental work will be focused on the ternary Zr-Cr-O system for which there are very few data and sometimes in disagreement in particular concerning the ZrO_2-Cr_2O_3 pseudo-binary sections:

1. An experimental investigation of the quasi-binary system ZrO_2-Cr_2O_3 will be focused on the mutual solubility of these oxides. Some uncertainties still exist on the eutectic temperature of the ZrO_2-Cr_2O_3 section, but our experimental facilities do not allow us to accurately determine its value.

2. For the isothermal sections of the ternary system, phase relation will be studied at 1200°C and 1500°C to check the result published by Rhee and Hoch [1]. Experiments at higher temperatures cannot be performed due to the limitations of our experimental facility.

3. $Zr_3Cr_3O_x$, the only ternary phase in this system, was not extensively studied. The first objective will be the development of a method to prepare samples of $Zr_3Cr_3O_x$ with the

highest possible purity. A reliable, stable and repeatable preparation method would benefit the further characterizations. Once the $Zr_3Cr_3O_x$ samples were prepared, an extensive study should be realized on this phase, including the determination of the lattice parameter and the atomic positions, the determination of its enthalpy of formation and its heat capacity. Regarding the ability of this phase to accommodate easily oxygen vacancy, particular attention will be paid to its oxygen content.

4. In parallel, DFT calculations will be performed on the Zr_3Cr_3O structure for comparison with experimental data.

Based on these new results, a CALPHAD model of the ternary system is developed using the model of the Zr-Cr binary subsystem presented in Chapter III, and models of the Zr-O and Cr-O subsystems extracted from IRSN's NUCLEA database [28].

IV.4 Results and discussions

IV.4.1 Experimental results

IV.4.1.1 Quasi-binary system ZrO_2-Cr_2O_3

The experimental study presented here aims to determine the mutual solubility of ZrO_2 and Cr_2O_3.

For this purpose, two samples were prepared by mixing ZrO_2 and Cr_2O_3 powders that were then pressed into pellets. The composition of the samples is listed in Table IV-3. The samples were then annealed at 1200°C for 10h, and further examined by powder XRD and SEM-EDS.

The powder XRD patterns are shown in Figure IV-18. The samples are all composed of Cr_2O_3 and monoclinic ZrO_2, with a ratio slightly changed after annealing.

The lattice parameters obtained at room temperature after annealing agreed with the results of Fukui (ZrO_2, [46]) and of Baster (Cr_2O_3, [47]). According to the literature, the mutual solubility of the two oxides is not negligible at 1200°C. Our observation can be probably explained by the full exsolution of the dissolved oxides during cooling.

Table IV-3 DRX fitting results of ZrO_2-Cr_2O_3 samples annealed at 1200°C.

	ZrO_2 40 mol% + Cr_2O_3 60 mol%		**ZrO_2 90 mol% + Cr_2O_3 10 mol%**	
Phases	ZrO_2 monoclinic	Cr_2O_3	ZrO_2 monoclinic	Cr_2O_3
Initial composition *	40.00	60.00	90.00	10.00
Space group	P 2_1/c	R $\bar{3}$ c	P 2_1/c	R $\bar{3}$ c
Lattice parameters	a=5.147(1) b=5.204(1) c=5.314(1)	a=b=4.957(1) c=13.590(1)	a=5.145(1) b=5.205(1) c=5.312(1)	a=b=4.957(1) c=13.587(1)
Refined phase fractions	45.12(0.32)	54.88(0.40)	91.88(1.07)	8.12(0.36)
χ^2	6.4	4.98	11.8	8.81

* Calculated with mass.

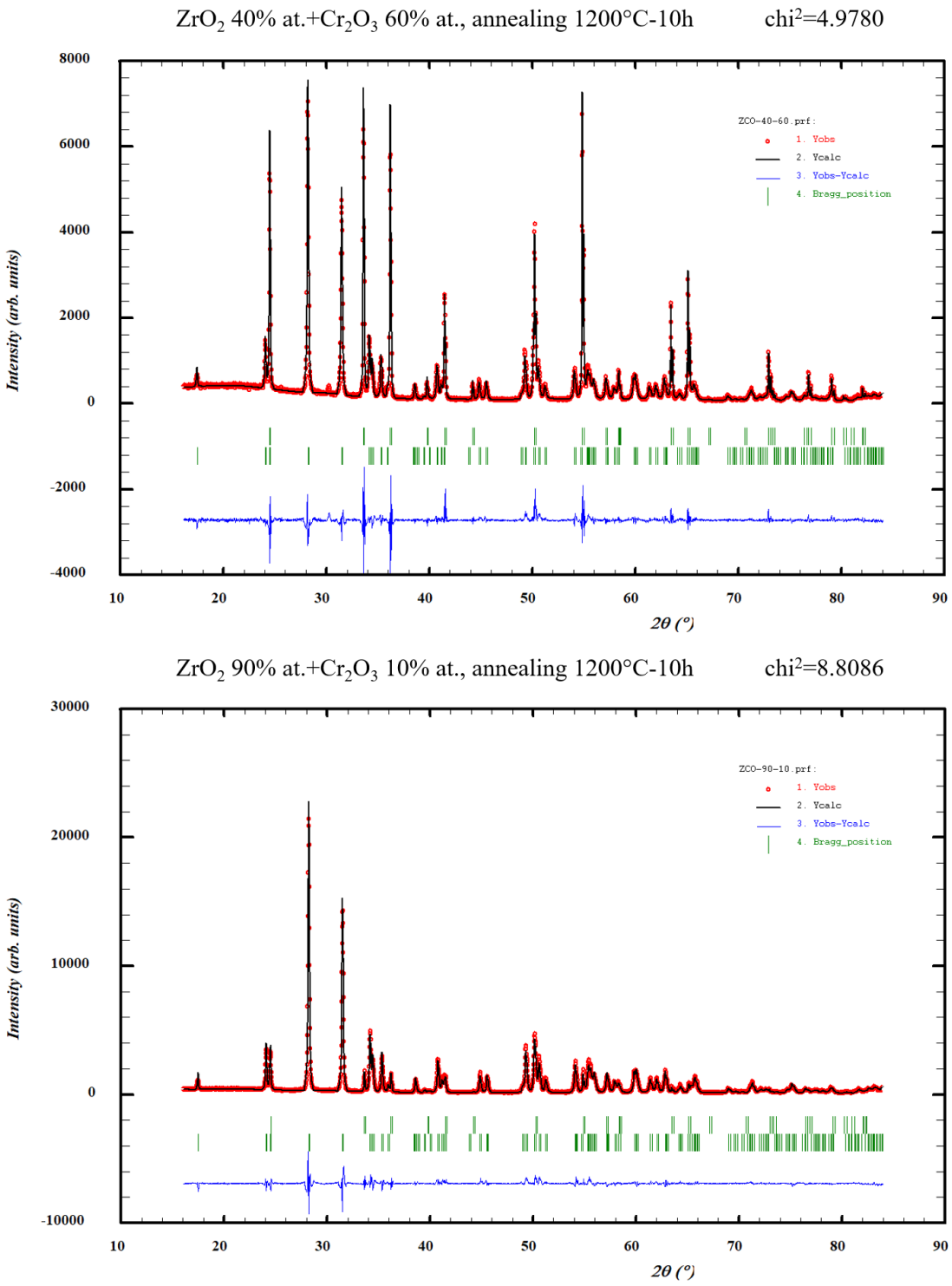

Figure IV-18 Rietveld plots of two samples (above: 40 ZrO_2% at. 60 Cr_2O_3 %at., below: 90 ZrO_2% at. 10 Cr_2O_3 % at.: annealed at 1200°C for 10h.

SEM images of the samples are shown in Figure IV-19.

As the m-ZrO_2 phase fractions determined by Rietveld refinement (45.12 and 91.88% ZrO_2) are close to the nominal ZrO_2 contents of the samples (40 and 90% ZrO_2 respectively), the mutual solubility of the two oxides should be low at room temperature. The small differences observed between these two pairs of values could be explained by a loss of Cr_2O_3 by vaporization during annealing.

The compositions of these phases were measured by SEM-EDS in at least 5 different locations and an average of measurements was taken. However, due to the significant charge-up effect during measurement, a relatively important measurement error was found inevitable. Difficulties were also encountered in polishing the sample surfaces because they were fully brittle. Though the measurements were performed again after careful surface polishing as well as possible and carbon coating with 200µm thickness, the situation was not significantly ameliorated.

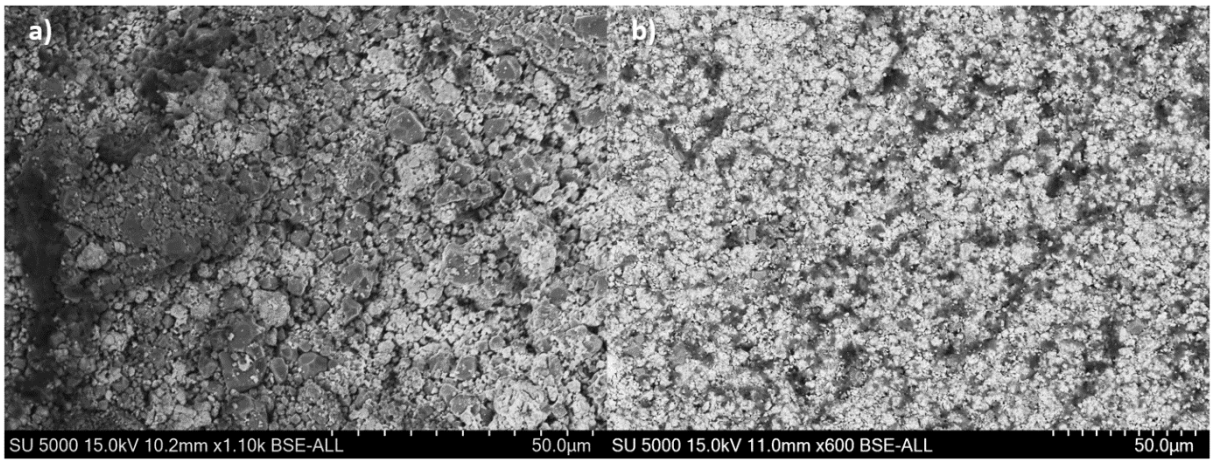

Figure IV-19 The SEM images of two samples. The images were taken by SEM-BSE under 15kV. In the figures, a) ZrO_2 40% at. + Cr_2O_3 60% at.; b) ZrO_2 90% at. + Cr_2O_3 10% at.

The solubility measured are:

$$\mathrm{Sol}(\mathrm{ZrO_2\ in\ Cr_2O_3}) = 29.07 \pm 10.27\%\ \mathrm{mol\ ZrO_2}.$$

$$\mathrm{Sol}(\mathrm{Cr_2O_3\ in\ ZrO_2}) = 9.24 \pm 8.30\%\ \mathrm{mol\ Cr_2O_3}.$$

In considering the measurement uncertainties, these results are consistent with Jerebtsov *et al.* [39] (45.13% at ZrO_2 in Cr_2O_3; 7.42% at Cr_2O_3 in ZrO_2). Though the measurements of this work were less accurate due to the charge effect and unsatisfactory surface preparation, this work is still of interest as experimental confirmation of measurements obtained by XFM used in Jerebtsov's study, which is a different analytical technique from EDS. However, for the best

accuracy of modeling, the values of solubility determined by Jerebtsov will be used in our CALPHAD modeling work.

IV.4.1.2 Phase relations in Zr-Cr-O system at 1200°C and 1500°C

As-cast samples were prepared by melting Zr, Cr metals and $ZrCr_2$, ZrO_2 and Cr_2O_3 powders using an arc furnace. The samples were polished and analyzed by SEM-EDS. Overall compositions of the samples were measured as listed in the 'Initial Composition' column of Table IV-4. Because of the vaporization of Cr/Cr_2O_3 during arc melting, the composition of Cr was often lower than expected.

Some samples were not homogeneous after melting, especially the samples mixed with ZrO_2 powder, which has a melting temperature of up to 2715°C. Results of as-cast samples are presented in the sub-section "**As-cast states**".

To deal with this problem, the samples were crushed, ground as fine as possible, mixed and pressed into pellets. The pellets were annealed at 1200°C for 48-72h and 1500°C for 6-10h to improve the homogeneity. However, the ground particles were non-uniform in size, shape and hardness, causing problems in sample polishing. EDS measurements could not give reliable results on overall compositions or individual phases. The overall compositions of annealed pellets were considered close to their compositions in as-cast states, as no significant mass changes were determined before or after annealing. Samples 12 and 13 were prepared directly in pellets, so no EDS measurements were available for them. The phase identification was performed by XRD, listed in the 'Phase Identified' column in Table IV-4. Results of annealed pellet samples are presented in the sub-section "**Annealing states**".

- **As-cast states**

Some samples were found to be inhomogeneous after arc melting, especially the samples prepared with large amounts of ZrO_2 powder, which has a melting temperature of up to 2715°C. An example is shown in Figure IV-20 with SEM images of a sample Zr17Cr75O8. Though the sample seemed homogenous at first glance (a), a large number of ZrO_2 spheres was found after magnification (b). The sphere shape indicates that ZrO_2 was melted in the arc furnace, but was not homogeneously integrated with other raw materials. In Figure IV-21, images of different zones of the same sample Z17Cr75O8 using the EDS mapping mode are reported. Green spheres in these figures corresponding to the ZrO_2 composition were widespread in the sample.

Table IV-4 Summary of prepared compositions in Zr-Cr-O system and phase identified with XRD.

	Prepared Formula	**$X_{Initial}$ EDS % at. Zr/O/Cr**	**$T_{Annealing}$ °C**	**Phase Identified**
1	Zr3Cr3O	39.6/17.3/43.1	1200/1500	Zr_3Cr_3O
2	Zr4Cr2O	53.7/16.6/29.7	1200	$ZrCr_2$+Zr(O)*+Zr_3Cr_3O
2	Zr4Cr2O	53.7/16.6/29.7	1500	Zr(O)+Zr_3Cr_3O
3	Zr3Cr2O3**	38.26/31.37/30.36 43.1/52.8/4.1	As-cast	$ZrCr_2$+Zr_3Cr_3O+ZrO_2 Zr(O)+Zr_3Cr_3O+ZrO_2
4	ZrCr2O	24.6/28.9/46.5	1200/1500	Cr+$ZrCr_2$+ZrO_2
5	Zr75Cr12.5O12.5	67/23.2/9.8	1200/1500	$ZrCr_2$+ Zr(O)
6	Zr67Cr27O6	64.9/14.6/20.5	1200	$ZrCr_2$+ Zr(O)
6	Zr67Cr27O6	64.9/14.6/20.5	1500	L+Zr(O)
7	Zr33Cr60O7	34.5/7.6/57.9	1200/1500	$ZrCr_2$+Zr_3Cr_3O+ZrO_2
8	Zr50Cr25O25	51.9/27.2/20.9	1200/1500	Zr_3Cr_3O+ZrO_2+ Zr(O)
9	Zr17Cr75O8	17/5.5/77.5	1200/1500	Cr+$ZrCr_2$+ZrO_2
10	Zr20Cr30O50	17.2/49.3/33.4	1200/1500	Cr+Cr_2O_3+ZrO_2
11	Zr5Cr47.5O47.5	5.4/50.7/43.9	1200/1500	Cr+Cr_2O_3+ZrO_2
12	Zr38.5Cr23O38.5		1200/1500	Zr_3Cr_3O+ZrO_2+ Zr(O)
13	Zr37.5Cr37.5O25		1200/1500	$ZrCr_2$+Zr_3Cr_3O+ZrO_2

* Zr hcp with a certain percentage of solubility of O within.

** The sample was not homogeneously mixed; two parts of the samples were analyzed separately.

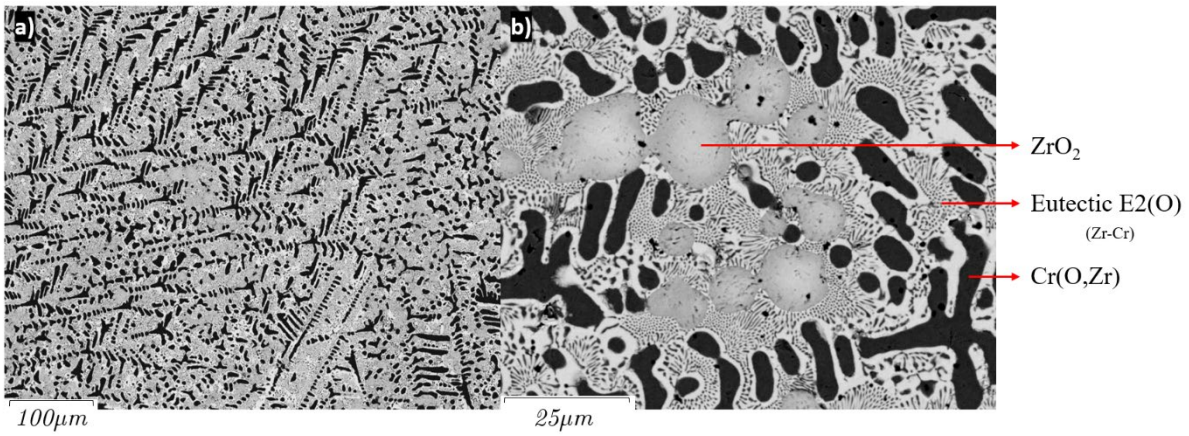

Figure IV-20 SEM images of sample Zr17Cr75O8 (composition as Zr 17.9% at.; Cr 75.0% at.; O 7.2% at. by EDS average of image a). Images a) taken under 15kV with a magnification of 200x and a working distance of 12mm; b) taken under 15kV with a magnification of 1200x and a working distance of 12mm.

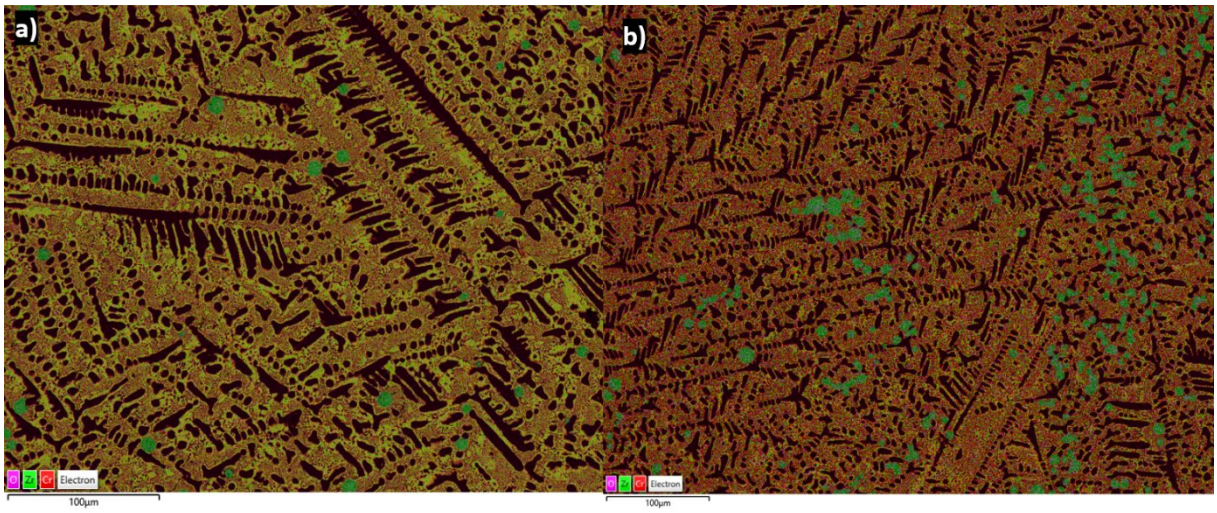

Figure IV-21 SEM images of the sample Zr17Cr75O8 (composition as Zr 17.9% at.; Cr 75.0% at.; O 7.2% at. by EDS). Mapping mode: Pink for O, green for Zr and red for Cr. Images taken under 15kV and magnification x300.

Another measurement performed on as-cast samples was related to the solubilities of binary phases in the ternary system. In the bcc Cr phase, a solubility maximum of Zr of 0.2±0.17% at. and a solubility of O as 3.2±0.26% at have been measured by EDS. In the ZrO_2 phase, a maximum solubility of Cr of 0.76±0.16% at. has been measured; in the eutectic structure corresponding to E2 (mentioned in Zr-Cr binary system, composition 80% at. Cr), an overall solubility maximum of O as 3.74±0.66% at. has been measured. All the solubility values were determined by averaging at least 10 measurements.

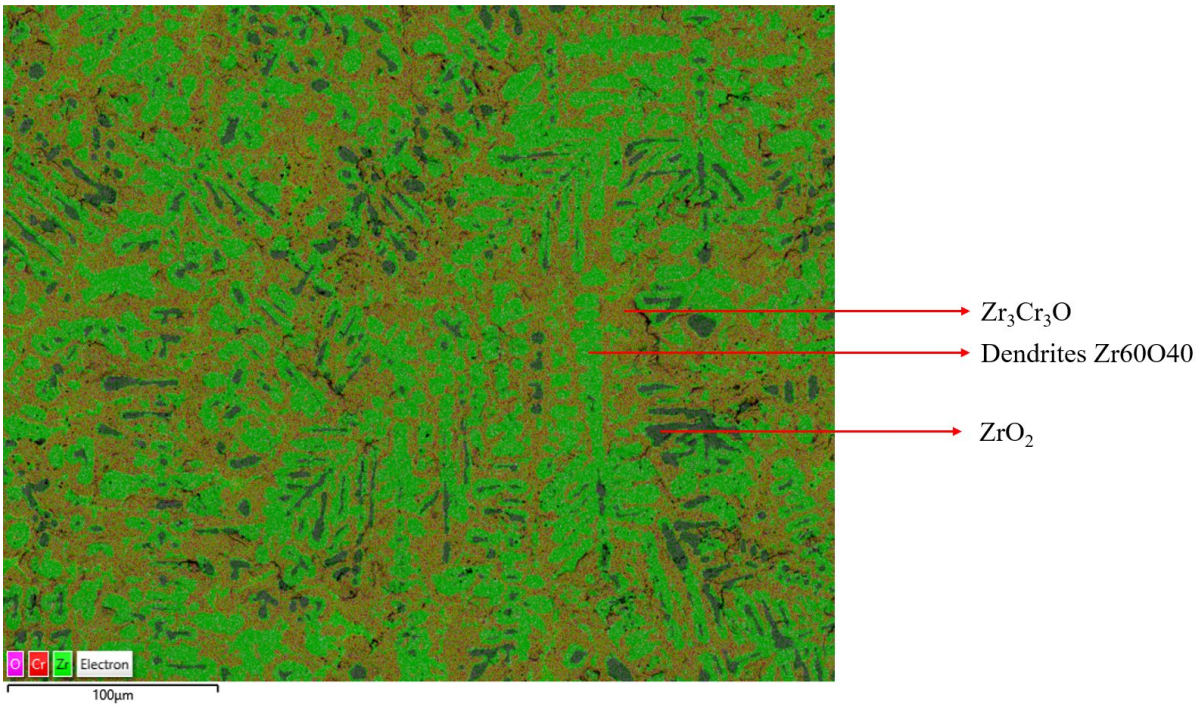

Figure IV-22 Reconstructed elemental X-map of sample Zr50Cr25O25 (composition as Zr 51.9% at.; Cr 20.8% at.; o 27.3% at. by EDS). Mapping code: Pink for O, red for Cr and green for Zr.

A reconstructed elemental X-map of the sample Zr50Cr25O25 (composition Zr 51.9% at.; Cr 20.8% at.; O 27.3% at. measured by EDS) is shown in Figure IV-22. EDS measurements showed that the sample was composed of Zr_3Cr_3O phase, dendrites with a composition (Zr 60% at.; O 40% at.) and ZrO_2 phase**.** Distribution of the dendrites and ZrO_2 phase corresponds to a typical peritectic reaction.

The solubility limit of Cr in ZrO_2 measured in this sample was consistent with that of sample Zr17Cr75O8. The solubility limit of Cr in the eutectic structure Zr-O was measured as 1.3±0.8% at.

With another sample Zr33Cr60O7 (composition as Zr 34.5% at.; Cr 57.8% at.; O 7.7% at. by EDS), the solubility limit of O in $ZrCr_2$ phase was measured as 2.8±0.3% at.

As these solubilities were measured on as-cast samples, they were estimated at melting temperatures of the solvent phases.

- **Annealing states**

As shown in Table IV-4, the phase identification and composition for most of the annealed pellet samples were similar at both temperatures 1200°C and 1500°C. Our measurements are reported

in Figure IV-23 and Figure IV-24 for 1200°C and 1500°C, respectively. The same phase relations are obtained at these two temperatures, whereas a liquid zone is found with sample 6: Zr67Cr27O6 at 1500°C near the Zr-Cr border in a very restricted area between 50% at Zr and 80% at. Zr. This liquid zone is a small extension of the liquid domain in the Zr-Cr binary system Zr-Cr around the E1 point into the ternary Zr-Cr-O system.

The phase relations determined in our work are in satisfactory agreement with the results published by Rhee and Roch [1]. The main difference at 1500°C is the extension of the liquid zone.

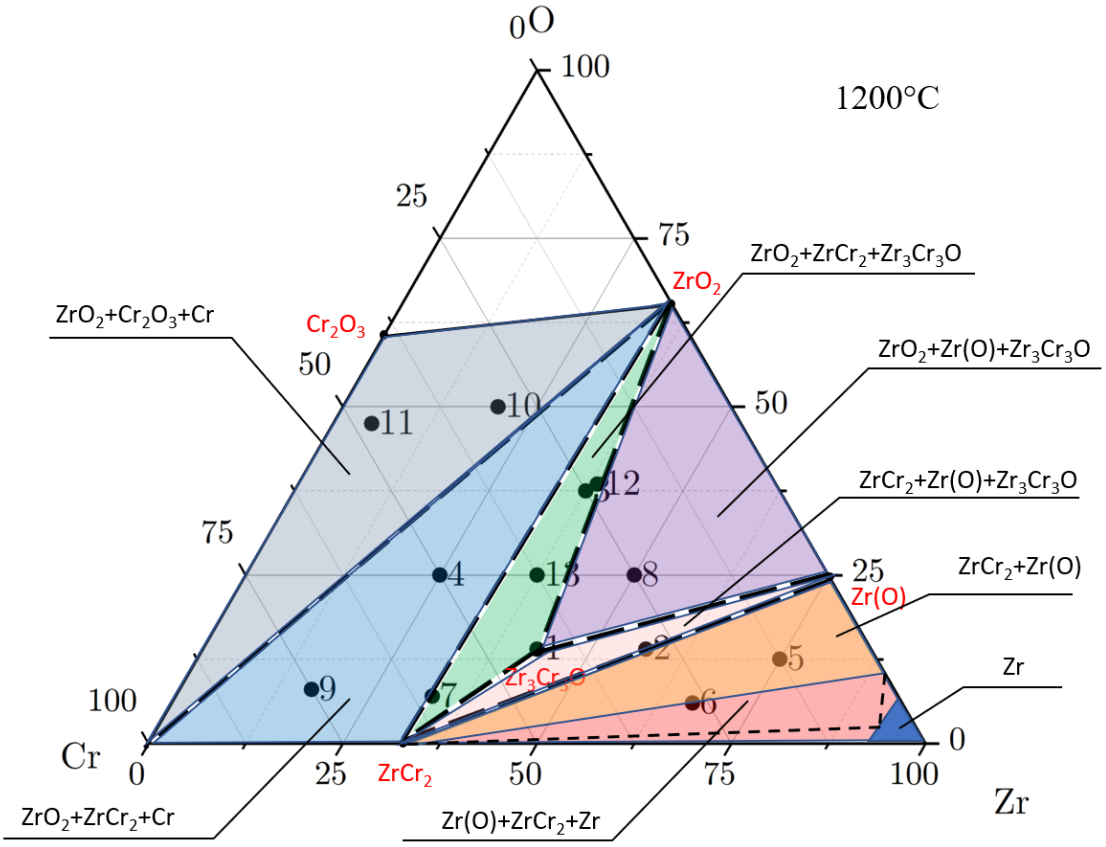

Figure IV-23 Phase relation on the isothermal section at 1200°C of the Zr-Cr-O system. Dashed lines are tentative limits of the Zr(O) + $ZrCr_2$ + β-Zr three phase domain.

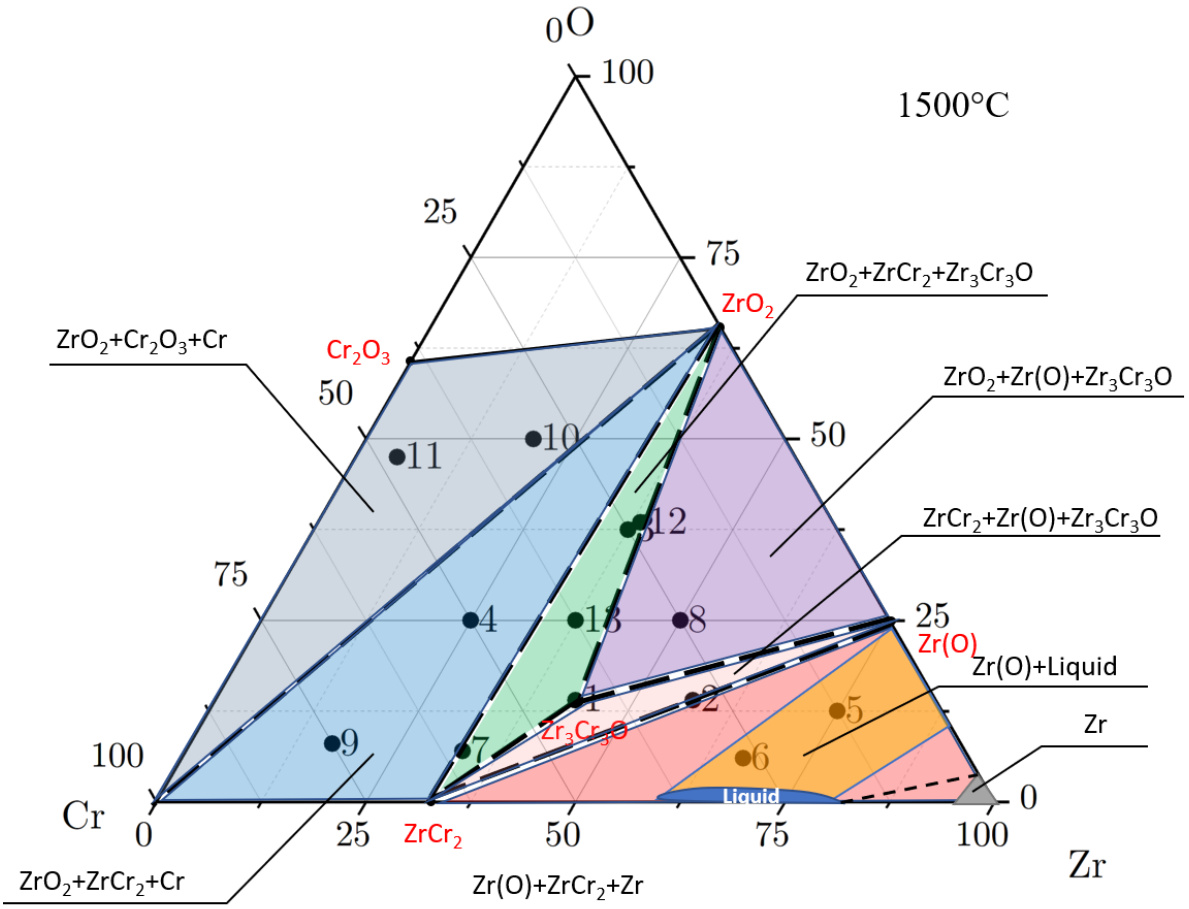

Figure IV-24 Phase relation on the isothermal section at 1500°C of the Zr-Cr-O system. Dashed line is the tentative limit of the liquid + Zr(O) + β-Zr three phase domain.

Regarding our experimental results, the following additional information and comments can be provided:

- The slight solubilities (e.g. Cr in ZrO_2, O in $ZrCr_2$…) were not presented in these figures to simplify our first CALPHAD modeling of the ternary system. These solubilities can be included in the future by modifying additional sub-lattices in phase definitions.
- The $ZrCr_2$ phase was identified at 1200°C in sample 2 (Zr4Cr2O) but disappeared at 1500°C, due to a slight oxidation of the sample.
- The sample 6 (Zr67Cr27O6) was solid at 1200°C and partially melted/melted at 1500°C. This composition at 1500°C thus is located in a liquid zone or a biphasic zone Liquid+Zr(O). The DRX result with the recovered sample indicated mainly the Zr(O) phase. We tended to

conclude that the sample was partially melted and should be located in a biphasic zone of Liquid+Zr(O) at 1500°C regarding our observation. In the Rhee's work, two samples (so-called 504 and 506 in his publication) allowed the author to determine the extension of the liquid zone (Figure IV-25). The melting extension (characterized by the visual identification of the liquid amount in the sample, either weak or strong) of these samples was determined macroscopically. The possible conflicting point is the Rhee's 504 composition, which was characterized as "strongly" melted and located in the biphasic zone in our work.

- The Rhee & Roch's sample (502 and 503) compositions were located in the same zone as our sample 6, but were reported to be solid at 1500°C. In our work, we proposed a liquid zone more restricted than Rhee at 1500°C with a larger biphasic zone Liquid+Zr(O) around sample 6.

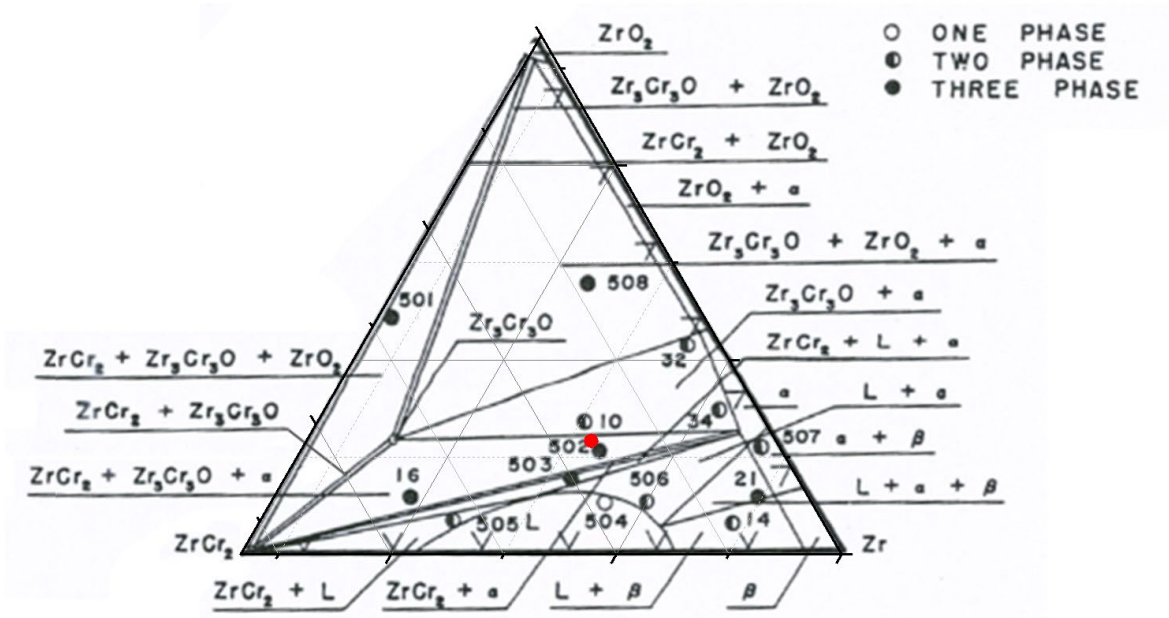

Figure IV-25 Partial phase diagram in the range of Zr-ZrO_2-$ZrCr_2$ at 1500°C [1]. Red point: sample 6 (Zr67Cr27O6).

IV.4.1.3 The ternary phase $Zr_3Cr_3O_x$

IV.4.1.3.1 Sample preparation

A preparation method for obtaining high-purity $Zr_3Cr_3O_x$ samples was determined. The pellets were prepared by mixing Zr metal, $ZrCr_2$ and Cr_2O_3 powders with an atomic ratio of 11:7:2.

Annealing attempts under argon atmosphere at different temperatures (1200°C to 1500°C) and for different times were considered in a resistance furnace. The purity of the $Zr_3Cr_3O_x$ sample was often affected by:

1) Oxidation of sample. Though all precautions were taken before the annealing, oxidation of samples was found to be inevitable during the annealing at these high temperatures. The oxidation level of the sample depends on both the annealing temperature and time that influenced the final state of the sample which is not fully predictable. When the oxidation is presumably excessive, it transforms excess $ZrCr_2$ to ZrO_2 impurity, during a vaporization of Cr.
2) Vaporization of Cr_2O_3. It becomes significant at the isothermal stage of annealing. An isothermal stage long enough at the annealing temperature is necessary to homogenize the sample. However, the longer the stage lasts, the more Cr_2O_3 would be vaporized, which leads directly to a loss of Cr and O constituents in the sample. The target phase was then mixed with a certain percent of impurity as $ZrCr_2$ or Zr if so.

Due to these two effects, it became challenging to achieve a preparation of this compound with high purity.

The attempts of preparation, their prepared compositions, annealing temperatures and dwells, and DRX results are listed below in Table IV-5:

Table IV-5 Initial compositions of Zr_3Cr_3O samples, annealing parameters, phase fractions of the various phases and lattice parameters of Zr_3Cr_3O obtained by Rietveld refinement of XRD patterns of the samples.

Initial composition	**Physical state**	**Annealing parameters**		**Phase fractions from XRD / % wt.**				
		Temperature /°C	**Time**	**Zr_3Cr_3O**	**Zr hcp**	**ZrO_2 monoclinic**	**$ZrCr_2$**	**Lattice parameter of Zr_3Cr_3O /Å**
Zr3Cr3O	Chunk	As-cast	As-cast	47.39	15.53		37.08	
Zr3Cr3O	Pellet	1200	48h	75.04(0.37)	11.23(0.10)	8.73(0.26)	5.00(0.07)	11.957 (1)
Zr3Cr3O	Pellet	1500	6h	89.45(0.72)		9.98(0.12)	0.57(0.06)	11.962 (1)
Zr3Cr3O	Pellet	1500	48h	85.94(0.92)	8.34(0.21)	5.3(0.35)	0.41(0.15)	11.962 (1)
Zr3Cr3O	Pellet	1200	6h	82.58(1.13)		13.34(0.76)	4.07(0.25)	11.954(2)
Zr3Cr3.3O	Pellet	1200	48h	93.53(0.93)	2.22(0.10)		4.25(0.21)	11.953(1)
Zr3Cr3.3O	Pellet	1500	6h	95.93(1.02)		4.07(0.11)		11.958(1)
Zr3Cr3.5O	Pellet	1200	48h	83.67(0.34)	2.01(0.05)	2.78(0.12)	11.54(0.10)	11.955(1)
Zr3Cr3.5O	Pellet	1500	6h	89.33(1.09)		3.91(0.20)	6.76(0.13)	11.960(1)
Zr3Cr3.1O	Pellet	1200	6h	68.87(0.77)	9.49(0.13)	5.18(0.18)	16.60(0.19)	11.956(1)
Zr3Cr3.2O	Pellet	1200	6h	81.72(0.56)	3.15(0.15)	4.91(0.25)	10.22(0.17)	11.954(1)
Zr3Cr3.3O	Pellet	1400	6h	84.17(2.52)	3.33(0.10)		12.50(0.28)	11.956(1)
Zr3Cr3.3O0.875	Pellet	1400	3h	92.11(1.19)	0.72(0.08)		7.17(0.27)	11.954(1)
Zr3Cr3.3O0.75	Pellet	1400	3h	95.05(3.17)			4.95(0.16)	11.959(1)
Zr3Cr3.3O	Pellet	1400	3h	99.30(1.24)			0.70(0.10)	11.956(1)
Zr3Cr3.3O	Chunk	1400	3h	88.80(0.63)			11.20(0.15)	11.957(1)
Zr3Cr3.3O	Pellet	1400	6h	95.93(0.59)	2.14(0.08)		1.93(0.08)	11.957(1)
Zr3Cr3.1O	Chunk	1400	6h	70.98(0.37)	5.97(0.10)	10.97(0.17)	12.07(0.12)	11.960(1)
Zr3Cr3.3O	Pellet	1400	4.5h	95.21(0.51)		1.11(0.13)	3.68(0.18)	11.958(1)
Zr3Cr3.3O	Chunk	1400	4.5h	88.40(0.57)	3.14(0.14)		8.46(0.14)	11.958(1)
Zr3Cr3.3O	Pellet	1400	5.25h	97.24(0.65)			2.76(0.27)	11.956(1)
Zr3Cr3.3O	Pellet	1400	5.25h	91.33(1.42)		3.87(0.46)	4.81(0.27)	11.952(1)
Zr3Cr3.3O	Pellet	1400	5.25h	96.36(1.28)			3.64(0.22)	11.954(1)
Zr3Cr3.3O	Pellet	1400	5.25h	98.07(1.42)			1.93(0.17)	11.954(1)
							Average	**11.957**

Regarding Table IV-5, the following comments can be made:

1. The purity of Zr_3Cr_3O obtained from pellets is far higher than that obtained from as-cast samples. The highest purity obtained of the former is 99.30±1.24% wt. (98.42% at. with impurity $ZrCr_2$), whereas the purity of as-cast samples never reaches 90% wt.
2. The best initial composition to consider before the annealing procedure is determined as $Zr_3Cr_{3.3}O$. The excess mass of Cr is added to compensate for the vaporization of Cr and slight oxidation in the annealing.
3. Based on the discussion of different difficulties encountered in our elaboration tests, the best annealing temperature and duration found was at 1400°C for a dwell time lower than 4h under Ar flooding.

An average of the measured lattice parameter was found as $a = 11.957 \pm 0.002$Å. The result is consistent with the results reported by Rhee and Roch [1] (11.958(2) Å) and Zavaliy *et al*. [43] (11.953(1) Å). The variance of the measured lattice parameters is $\sigma^2 = 7.15 \times 10^{-6}$. It shows that the lattice parameter of Zr_3Cr_3O was constant regardless of the equilibrium states of the different samples. Thus, it can be interpreted that, in our study, no solubility domain was identified for this ternary phase.

IV.4.1.3.2 O content in $Zr_3Cr_3O_x$

According to the literature, O atoms may not occupy all of the 16d positions in the structure of the unit cell of η-carbide phases [44], [45]. For this reason, the oxygen content of the phase was investigated.

An EPMA-WDS analysis was performed on two different $Zr_3Cr_3O_x$ samples. The details of the measurement procedure have been introduced in Chapter II. Figure IV-26 shows the measurement results at different locations of the samples. No significant variation in oxygen content was found.

The average of these measurements leads to a mean composition equal to Zr 42.85% at., Cr 41.99% at. and O 15.14% at. The compound could be written as $Zr_3Cr_{2.94}O_{1.06}$. When we consider the measured error due to the overlap of diffraction peaks of Cr and O, and the difficulty in baseline fitting at low voltage, it could be concluded that the measured composition corresponds to the theoretical one Zr_3Cr_3O. Thus, it is concluded that a ratio of Zr: Cr: O=3:3:1

is always kept in the $Zr_3Cr_3O_x$ compound, and the composition formulae can be expressed as Zr_3Cr_3O.

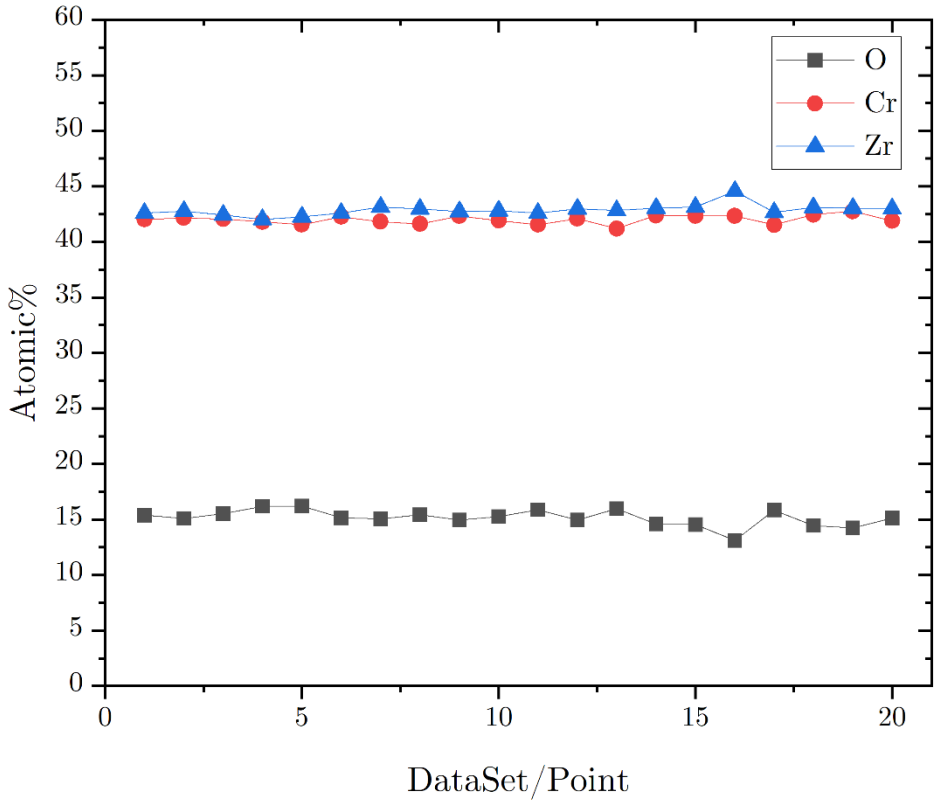

Figure IV-26 EPMA results of Zr_3Cr_3O samples

A complementary determination of O content in Zr_3Cr_3O by neutron diffraction is planned in the future.

IV.4.1.3.3 Crystal structure

A structural study was made based on powder XRD using the Rietveld fitting with the help of the FULLPROF software. The Rietveld plot is given in Figure IV-27.

As a result, the compositions of the sample are fitted with the results reported in Table IV-6. Regarding the Bragg R-factor and RF-factor, it could be said that the three phases are all well-fitted. The .cif files of $ZrCr_2$ C15 and Zr hcp are both detailed in Chapter II. The Zr_3Cr_3O structure was refined from the Zr_3V_3O atomic positions [43], by replacing the V atoms with Cr

ones and modifying the lattice parameter (i.e. 11.958Å). In the Rietveld fitting, both lattice parameters and atomic positions are refined. The fitting results are also listed in Table IV-6.

Table IV-6 Phase fractions and crystallographic parameters of the phases obtained by Rietveld fitting of the diffraction pattern of the Zr_3Cr_3O sample.

Phases	**Zr_3Cr_3O**	**Impurities**	
		$ZrCr_2$ C15	**Zr hcp**
Fraction/% wt.	95.79(4)	2.50(0)	1.72(4)
Fraction/% at.	87.16	5.19	7.65
Lattice parameters/Å	11.959(1)	7.209(1)	a=3.249(1) c=5.205(1)
Space group	$Fd\bar{3}m$	$Fd\bar{3}m$	$P6_3/mmc$
Bragg R-factor	8.681	23.28	11.49
RF-factor	4.062	10.73	7.437

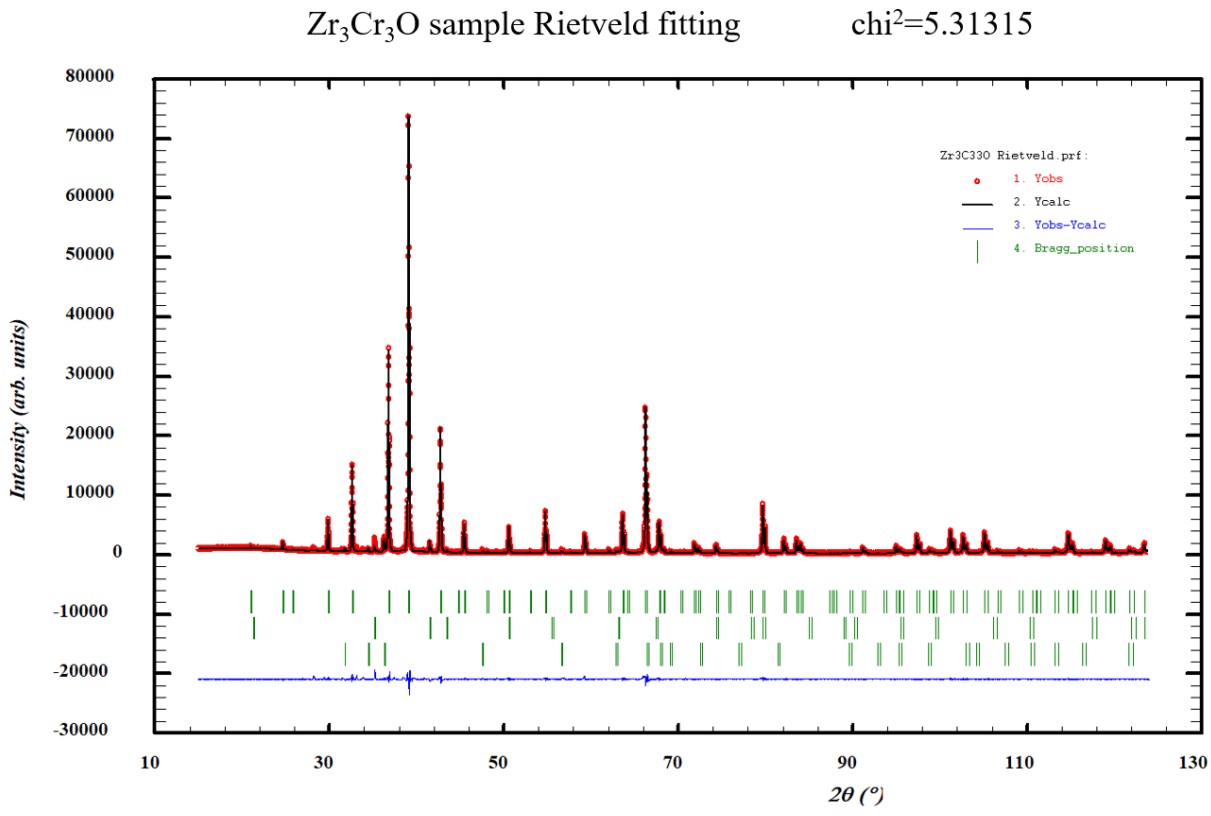

Figure IV-27 Rietveld fitting of the XRD scan of the Zr_3Cr_3O sample annealed 3 h at 1400°C (purity 99.3 wt.%).

Table IV-7 Lattice parameters and atom positions of Zr_3Cr_3O ternary phase

Zr_3Cr_3O	**a**		
	11.95895(1)		
$Fd\bar{3}m$	x	y	z
Zr1 – 48f	0.18293(1)	3/8	3/8
Cr2 – 32e	0.20249(1)	0.20249(1)	0.20249(1)
O - 16d	½	½	½
Cr1 – 16c	0	0	0

The Rietveld fitting results of the Zr_3Cr_3O lattice are listed in Table IV-7. Two types of Cr atoms occupy the Wyckoff positions 16c and 32e; O atoms occupy the 16d position; Zr atoms occupy the 48f positions. The site occupancy of O in position 16d was fitted and was found not significantly different from 1.

As far as it is known, this result is the first work devoted on the characterization of the atom positions in the Zr_3Cr_3O phase.

The structure of the compound is shown below in Figure IV-28.

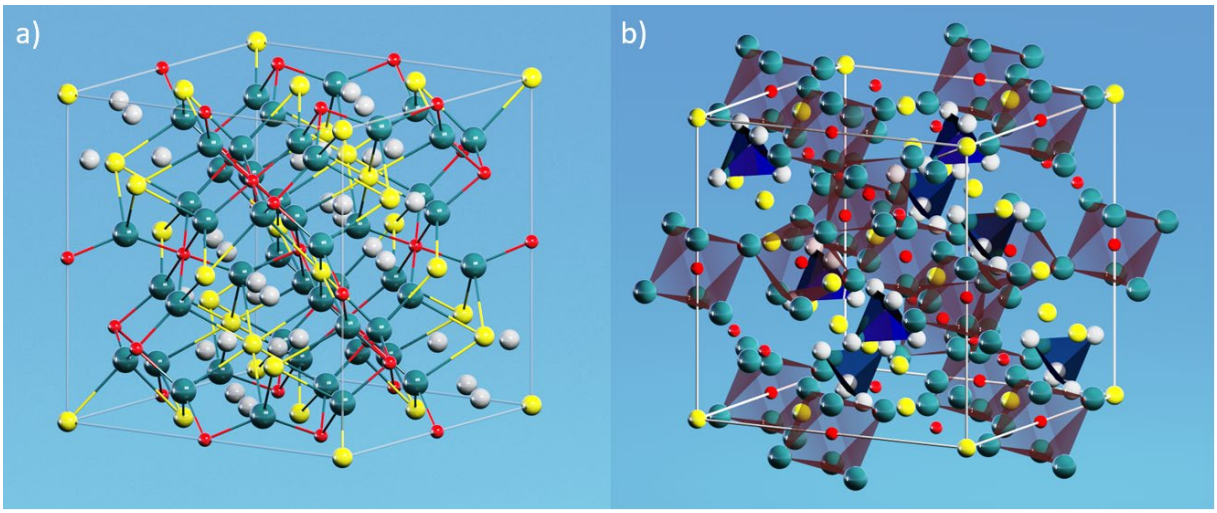

Figure IV-28 a) Perspective view of the crystal structure of Zr_3Cr_3O phase. b) Perspective view of Zr_3Cr_3O enlighten the Zr6O polyhedral details. Red spheres stand for oxygen atoms; green spheres stand for Zr atoms; yellow spheres stand for Cr atoms in 16c positions; white spheres stand for Cr in 32e positions.

Table IV-8 Atomic environments in Zr_3Cr_3O structure

Atoms	wy.	Comp.	Distance/Å	Solid angles/%
Zr1	48f	Cr2O2		
Cr2	32e	Cr6	2.551 for Cr1 2.6207 for Cr2	10.6872 for Cr1 7.8873 for Cr2
O1	16d	Zr6	2.2607	16.5837
Cr1	16c	Cr6	2.551	10.6872

The structure of the unit cell and polyhedral of Zr_3Cr_3O is shown in Figure IV-28. Similar to other η-carbide type compounds [48]–[50], a unit cell of Zr_3Cr_3O contains 48 atoms of Zr, 48 atoms of Cr and 16 O. Eight regular octahedra and eight regular tetrahedra are formed in such a unit cell. In Figure IV-28 b), it can be seen that the regular tetrahedra are formed by Cr atoms in Wyckoff positions 32e, centered in a diamond cubic lattice, as the Wyckoff positions 8a. 16 Cr atoms in Wyckoff positions 16c are coordinated in each surface of these Cr tetrahedra. The eight regular octahedra are formed by Zr atoms in 48f positions, centered with a translated unit cell of the cubic diamond lattice with a vector (1/2, 1/2, 1/2). The lattice interpenetrates with the first-mentioned diamond lattice. In the center of each regular octahedra of Zr, an atom of O in position 16d is settled. The atom environments with detailed atomic distances and solid angles are listed in Table IV-8.

DFT calculations using the VASP code have been performed from these refined crystallographic data of Zr_3Cr_3O (i.e. shown in Table IV-7). More details of the simulation are already presented in Chapter II.

The DFT relaxed structure is stabled with a lattice parameter $a = 11.749Å$. The atomic positions are detailed below in Table IV-9.

Table IV-9 Relaxed structure of Zr_3Cr_3O obtained by DFT

$Fd\bar{3}m$	x	y	z
Zr1 – 48f	0.18100	3/8	3/8
Cr2 – 32e	0.20146	0.20146	0.20146
O - 16d	½	½	½
Cr1 – 16c	0	0	0

It could be seen that the assessed atomic positions are rather similar to the experimental ones but that the lattice parameter is significantly smaller than the experimental result. This difference could be qualitatively expected because the DFT calculation is performed at 0K.

IV.4.1.3.4 Thermodynamic studies

In this subsection, we present our experimental work related to the determination of the enthalpy of formation and the heat capacity of Zr_3Cr_3O.

- **Specific heat and entropy**

The specific heat capacity was measured in our work by a combination of relaxation calorimetry (PPMS) and DSC. The measurement was carried out on a Zr_3Cr_3O sample of high purity 98.07(1.72) % wt. (95.70% at. with $ZrCr_2$ impurities).

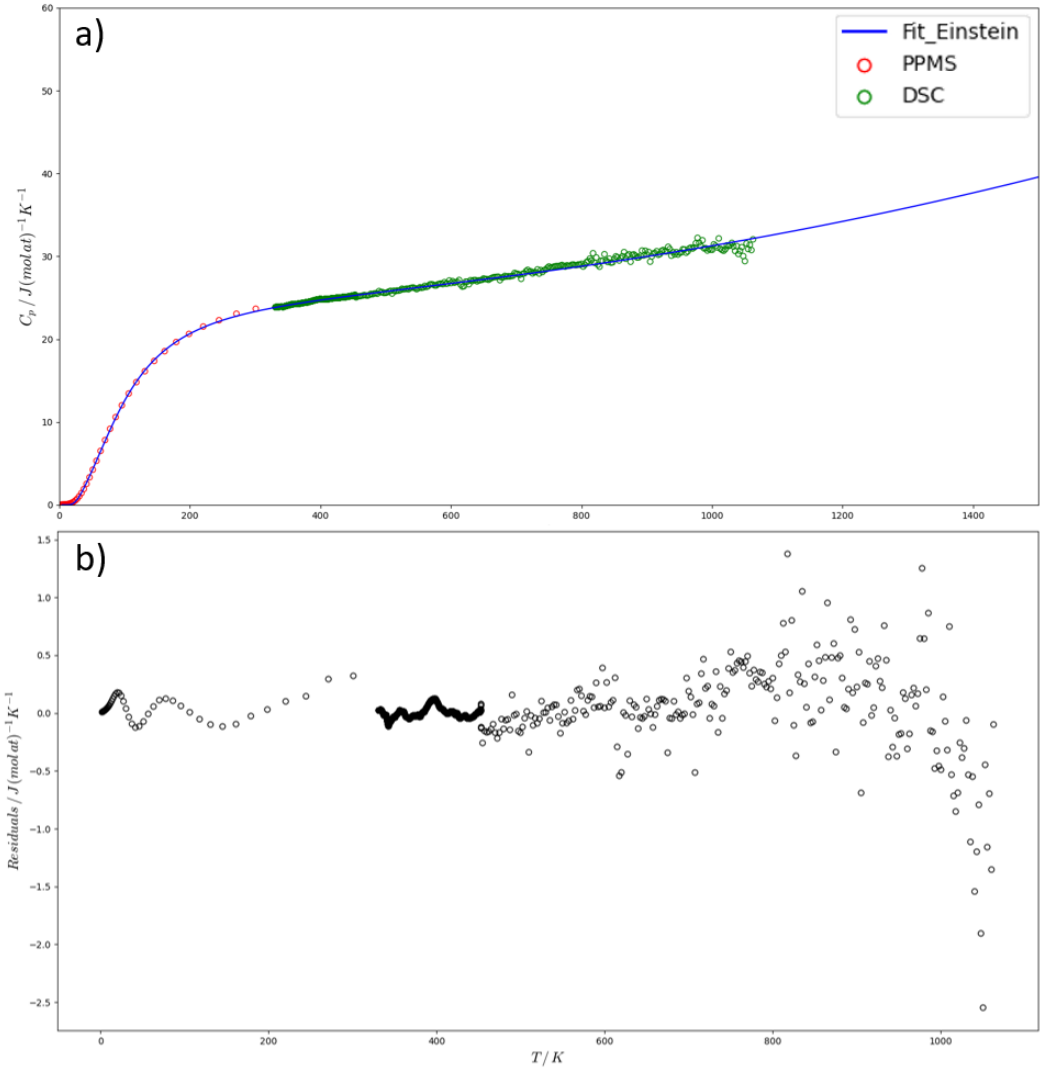

Figure IV-29 Heat capacity of Zr_3Cr_3O versus temperature. a) Experimental points with the fitting line according to the modified Einstein model in blue. b) difference points between measured and calculated points.

The C_p measurements are reported in Figure IV-29. A good agreement was found around room temperature between the two, PPMS and DSC, calorimetric techniques. The experimental points are fitted with a modified Einstein equation, which is a sum of two Einstein terms and a polynomial correction [51] [52].

$$\boldsymbol{C_p(T) = 3R\left(\sum_{i=1}^{2} a_i \left(\frac{\theta_E^i}{T}\right)^2 \frac{e^{(\theta_E^i/T)}}{\left(e^{(\theta_E^i/T)} - 1\right)^2}\right) + aT + bT^n} \qquad \text{(IV-1)}$$

where C_p is the specific heat capacity; R is the perfect gas constant; a_i are the statistical weights; θ_E^i refers to the Einstein temperatures and a, b, n: parameters, correction for non-harmonic effects; T is the temperature in K. The constraint $a_1 + a_2 = 1$ is used to ensure that the sum of the Einstein terms tends towards the Dulong-Petit limit.

Fittings parameters are listed below in Table III-13 and the resulting equation is represented by the blue line in Figure IV-29. In the fitting parameters, the n integer parameter was fixed to 2.

Table IV-10 Fitting parameters of C_p data of Zr_3Cr_3O according to the modified Einstein model. N.points shows the number of experimental points fitted. Other parameters share the same definition as in Equation (III-6).

Phase	**Zr_3Cr_3O**
N. points	2381
a_1	0.636±0.023
a_2	0.364±0.023
a	0
θ_E^1	378.250±4.428
θ_E^2	173.652±5.255
b	6.545E-6±1.454E-8
n	2

Analytical integration of C_p/T was done with the modified Einstein model with n=2 between 0 and 298 K to obtain the Zr_3Cr_3O entropy at 298K.

$$S_{Zr_3Cr_3O}^{298K} = \int_T^{298K} \frac{C_p}{T} dT$$

The Zr_3Cr_3O entropy at ambient temperature is equal to:

$$S_{Zr_3Cr_3O}^{298K} = 188.569\, J/mol/K = 26.938\, J/(mol.atom)/K$$

The entropy of the formation of Zr_3Cr_3O is thus calculated according to the following Equation (III-7).

$$\Delta_f^{298K} S_{Zr_3Cr_3O} = S_{Zr_3Cr_3O}^{298K} - 3S_{Zr}^{298K} - 3S_{Cr}^{298K} - \frac{1}{2}S_{O_2}^{298K} \qquad \text{(IV-2)}$$

where S_{Zr}^{298K}, S_{Cr}^{298K} and $S_{O_2}^{298K}$ are the entropy of pure Zr, Cr and O_2 at 298K and 1 bar, taken from SGTE [53].

The entropy of the formation of Zr_3Cr_3O is equal to:

$$\Delta_f^{\circ} S_{Zr_3Cr_3O} = -102.120\, J/mol/K = -14.588\, J/(mol.atom)/K$$

- **Enthalpy of formation**

The enthalpy of the formation of Zr_3Cr_3O was measured by the drop solution method in an aluminum solvent at 900°C/1173K. To reach this objective, the drop solution enthalpies of Zr, Cr and Zr_3Cr_3O have to be determined. The drop solution enthalpies of pure Zr and Cr have already been measured in Gajavalli[54] and Chapter III of this document, respectively. Then the Zr_3Cr_3O drop solution needs to be measured. Chunks of three high-purity Zr_3Cr_3O samples were used in the drop solution experiments, with purities of 98.07% wt. (95.70% at.), 96.36% wt. (92.06% at.) and 97.24% wt. (93.91% at.) confirmed by powder XRD.

The three dissolution reactions to be considered in the determination of the enthalpy of the formation of Zr_3Cr_3O by drop solution method are:

$$< Cr >_{298K} + \left((\quad)\right)_{Al,1173K} \rightarrow \left((Cr)\right)_{Al,1173K} \qquad \text{(IV-3)}$$

$$< Zr >_{298K} + \left((\quad)\right)_{Al,1173K} \rightarrow \left((Zr)\right)_{Al,1173K} \qquad \text{(IV-4)}$$

which correspond to reactions involved in the Cr and Zr dissolution process.

$$Zr_3Cr_3O_{298K} + \frac{2}{3}Al_{1173K} + \left((\quad)\right)_{Al,1173K} = \frac{1}{3}Al_2O_{3\,1173K} + 3\left((Zr,Cr)\right)_{Al,1173K} \qquad \text{(IV-5)}$$

which corresponds to the dissolution of Zr_3Cr_3O in the aluminum solvent.

In the second reaction, we assume that zirconium dissolution is complete. As reported by Gajavalli *et al.* [54], when metallic zirconium is put in contact with liquid aluminum, $ZrAl_3$ can be formed in the solvent during the dissolution, rather quickly. In the situation in which all the Zr fraction is transferred into $ZrAl_3$, the reaction would be:

$$\boldsymbol{Zr_3Cr_3O_{298K}} + \left(\frac{2}{3} + 9\right)\boldsymbol{Al_{1173K}} + (( ))_{\mathbf{Al,1173K}} = \frac{1}{3}\boldsymbol{Al_2O_3}_{\mathbf{1173K}} + 3\boldsymbol{ZrAl_3}_{1173K} + 3((\boldsymbol{Cr}))_{Al,1173K} \quad \text{(IV-6)}$$

The recent assessment of the Al-Zr system of Dezellus *et al.* [55] measured the solubility of Zr in Al at 900°C as 0.3% at. In our study, we carefully controlled our dropping masses, in order to reach a final bath composition of Zr in Al <0.05% at., and tried to prevent the formation of $ZrAl_3$ in the solvent.

The results of 4 drop solution experiments are reported in Table IV-11 and Figure IV-30. Each experiment consists of 4 to 5 drops. A linear fitting is made with all experimental points, with an intercept fixed at 0 (zero heat effect expected if no mass is dropped). The linear fitting represents the relation between the dropped quantity (in mg or mmol) and the measured heat (in J) during the drop dissolution, so the slope of the fitting line corresponds to the drop solution enthalpy (as the compositions reached after dropping were always enough low). Though an R^2=0.98 was obtained, it is clear that several points are located out of the confidence band of our linear fitting. The divergence of experimental points cannot be fully explained by measurement errors but possibly indicates an unexpected thermal effect in the dissolution process.

Table IV-11 Data of drop solution experiments

Drop amount(mg)	**Drop amount(mmol)**	$\boldsymbol{\Delta Q}$**(J)**	
7.79	0.017	-6.03	Exp.1
19.72	0.044	-20.18	
24.91	0.056	-20.75	
26.32	0.059	-22.09	
27.06	0.061	-26.71	Exp.2
16.9	0.038	-19.55	
18.29	0.041	-21.60	
10.54	0.024	-12.44	
12.46	0.028	-10.18	Exp.3
15.36	0.034	-12.42	
18.7	0.042	-15.01	
24.3	0.055	-26.00	
13.51	0.030	-13.52	Exp.4
12.73	0.029	-13.38	
13.85	0.031	-11.26	
12.54	0.028	-10.35	
8.56	0.019	-7.30	

A hypothetical mechanism is proposed to explain the experimental values: though the total mass of dropping samples was carefully controlled to limit the overall Zr composition in the Al solvent, precipitation of $ZrAl_3$ could be occurred in some oversaturated zones of the Al bath. This partial or total reaction of Zr and Al to $ZrAl_3$ corresponds to the situation of most of the dissolution experiments of Zr in Al solvent, where the subsequent dissolution of $ZrAl_3$ is known to be slow and endothermic [56]. In the situation of partial dissolution of $ZrAl_3$, the deduced enthalpy will be much more negative than that expected for a complete dissolution.

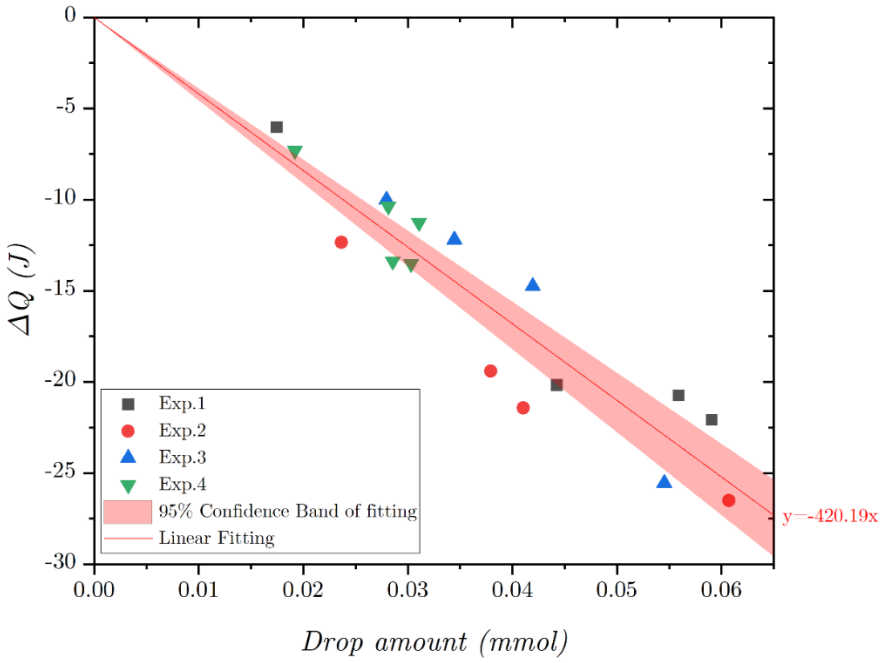

Figure IV-30 Heat change of Zr_3Cr_3O versus drop amount in Al bath at 900°C

During our experiments, two types of thermal curves were identified as illustrated in Figure IV-31. In this figure, the first endothermic peak corresponds to the heating of the sample up to the calorimeter temperature; the following exothermic peak corresponds to the dissolution of the sample. In almost half of our measurements, a second endothermic peak appeared after the exothermic dissolution peak, before the signal finally returned to the baseline. Based on our experience with the dissolution of Zr samples in liquid Al [54], the second endothermic corresponds to the dissolution of $ZrAl_3$ initially formed by reaction (IV-6). For the other half of the measurements, this second peak was absent. In this second situation, either $ZrAl_3$ dissolution is too slow to be detected, or it does not occur at all.

According to the above interpretation, the measurements were classified into two groups: Group A (measurements with a second endothermic peak) and Group B (measurements without the second endothermic peak).

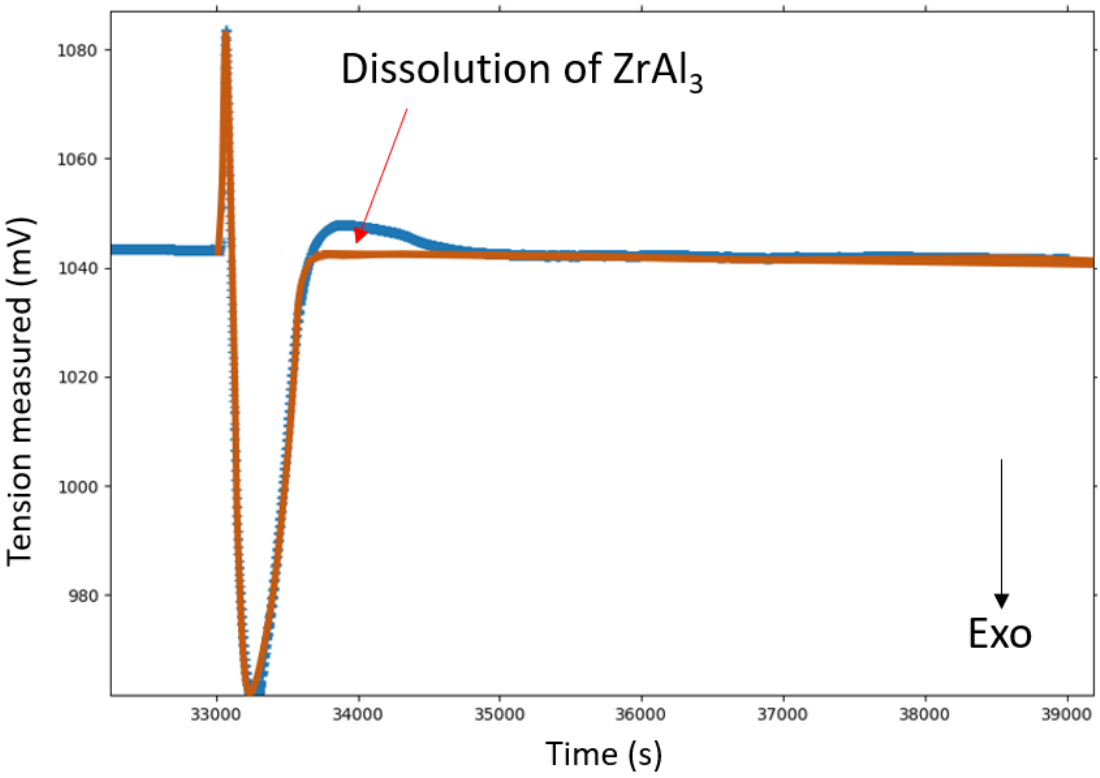

Figure IV-31 Schematic view of two types of thermal curves obtained in the drop solution experiments of Zr_3Cr_3O. The blue curve corresponds to drops in which the $ZrAl_3$ formed is subsequently dissolved, while the orange curve corresponds to drops in which the $ZrAl_3$ formed is not dissolved.

The numbers of measurements in the two groups A and B were nearly equal. Linear fittings were made for these two groups and are shown in Figure IV-32 and the fitting parameters are listed in Table IV-12.

As Pearson's r is close to -1 and R^2 close to 1, the Group A measurements can be represented by a straight line. The intercept at 0 (zero heat effect expected if no mass is dropped) is fixed. The fitted slope of Group A corresponds to the least negative slope possible for all measurements. It corresponds to the less negative enthalpy of dissolution measured, which may be linked to the situation in which formed $ZrAl_3$ was fully dissolved.

The Group B measurements are more scattered than Group A and showed worse linearity than Group A. It possibly corresponds to the situation in which the formed $ZrAl_3$ was not fully dissolved. This assumption may be supported by different arguments:

1) Partial dissolution is expected to be more negative than the situation of the full $ZrAl_3$ dissolution. → The fitting slope is effectively more negative than the slope for Group A.

2) Partial dissolution is expected to change with different amounts of $ZrAl_3$ residue. → The experimental points are effectively more scattered than for Group A.

3) For Group B, we were able to detect undissolved $ZrAl_3$ clusters in solidified Al ingots after the experiments, but no crystal.

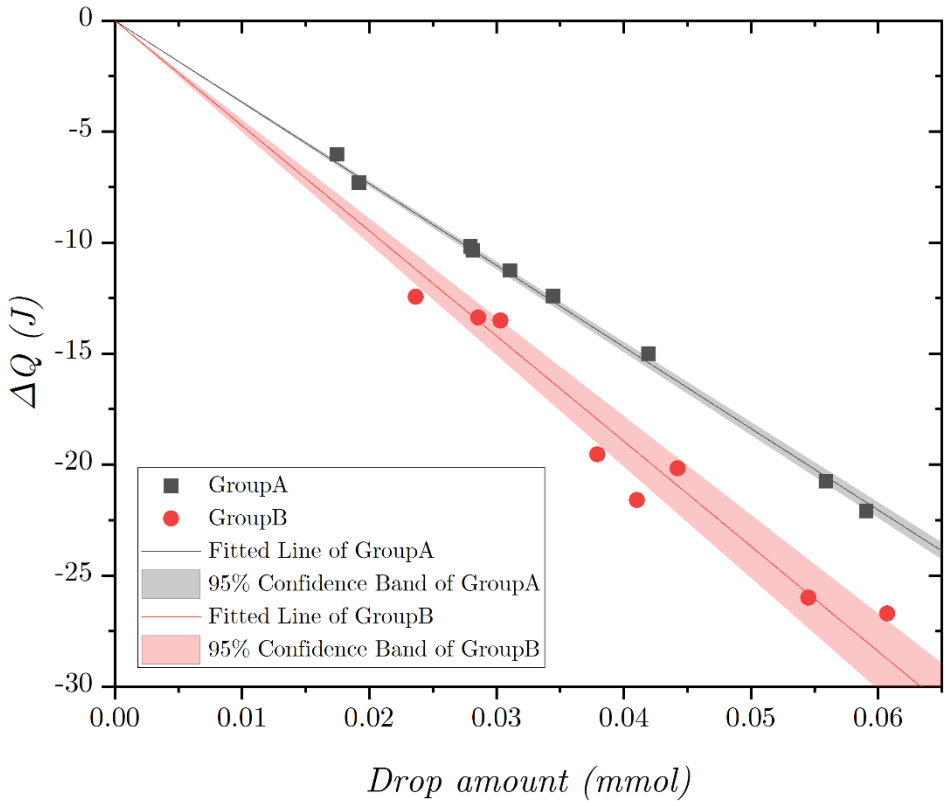

Figure IV-32. Linear fitting of experimental points for Zr_3Cr_3O drop solution experiments when the experimental points are divided into two data subsets (groups A and B)

Table IV-12 Fitting parameters and uncertainties

Parameters	**Group A**
Slope	-367.43287
Error	2.56571
Residual Sum of Squares	0.67274
Pearson's r	-0.99981
R-Square (COD)	0.99961
Adj. R-Square	0.99956

The solidified ingots of the drop solution of experiments “exp.1” and “exp.2” (same notation as Figure IV-30) were cut, polished, and observed by SEM. The compositions of different phases are measured by EDS.

Micrographs of the cross-section of exp. 1 and exp. 2 ingots are shown in Figure IV-33 and Figure IV-34.

At the bottom of the exp. 1 ingot, white needle-like phases are distributed in the bottom half of the ingot, identified as $ZrAl_3$; black spots are distributed in the bottom half of the ingot, identified as Al_2O_3.

In the bottom of the exp. 2 ingot, white tabular phases clustered in a limited area, identified as $ZrAl_3$; white needle-like phases distributed in the bottom half of the ingot, also identified as $ZrAl_3$; black spots also distributed in the bottom half of the ingot, identified as Al_2O_3. As for the needle-like $ZrAl_3$ that existed in the two ingots, its shape suggested that its formation may have undergone a fast cooling procedure when the crucible was pulled out of the calorimeter.

The millimetric cluster of $ZrAl_3$ was only found in a limited area of the exp 2 ingot. The form and distribution of the cluster are similar to the result of [56], where the mechanism of formation and growth of $ZrAl_3$ is explained. This cluster was the undissolved residue of $ZrAl_3$ formed at the calorimeter temperature.

Though one experimental point of exp.1 was categorized in Group B, no $ZrAl_3$ was found in the micrograph. The cluster may exist in another part of the ingot, not detectable on the cross-section examined.

Our hypothesis of $ZrAl_3$ formation during dissolution is confirmed. The diverged tendencies between the different experimental points can be explained by an effect of full/partial dissolution of $ZrAl_3$ formed in the calorimeter. The experimental points in Group A correspond to a situation of a full dissolution of $ZrAl_3$, so the reaction needed to be considered corresponds to Equation (IV-5). The points in Group B correspond to the situation in which only very partial dissolution of $ZrAl_3$ occurs in Equation (IV-6).

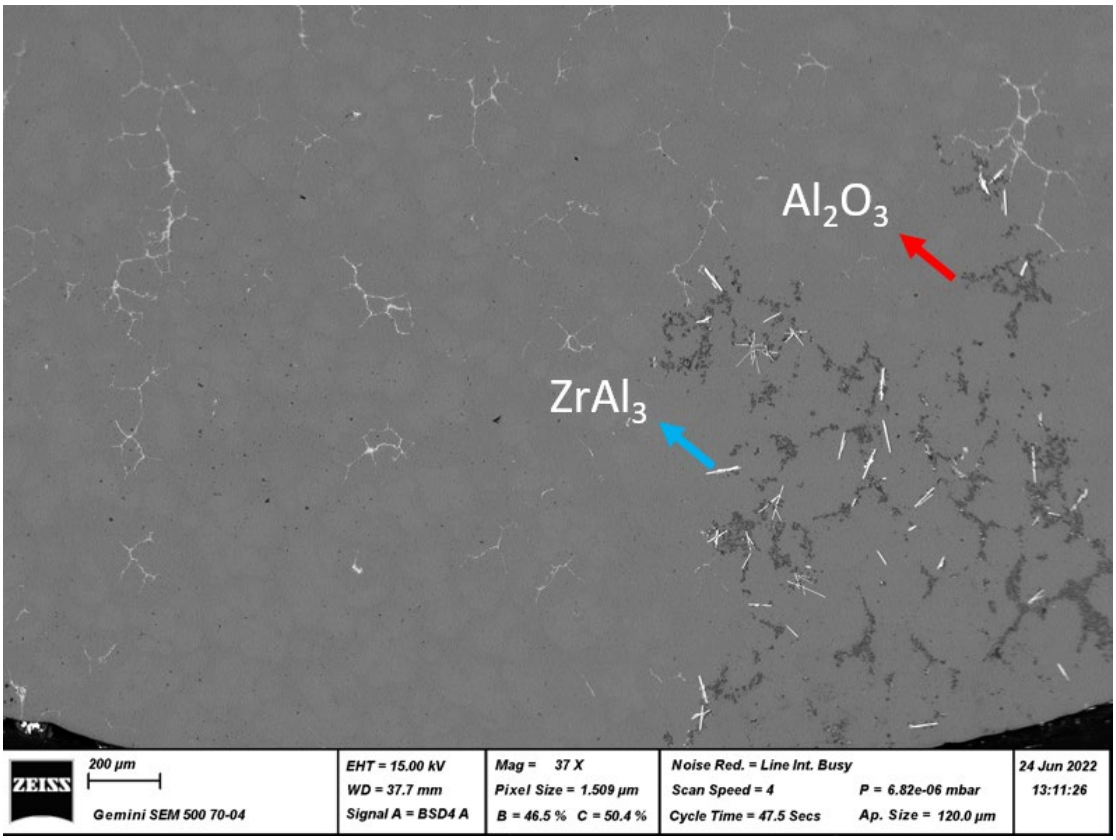

Figure IV-33 Bottom of an ingot exp.1 of drop solution experiment of Zr_3Cr_3O

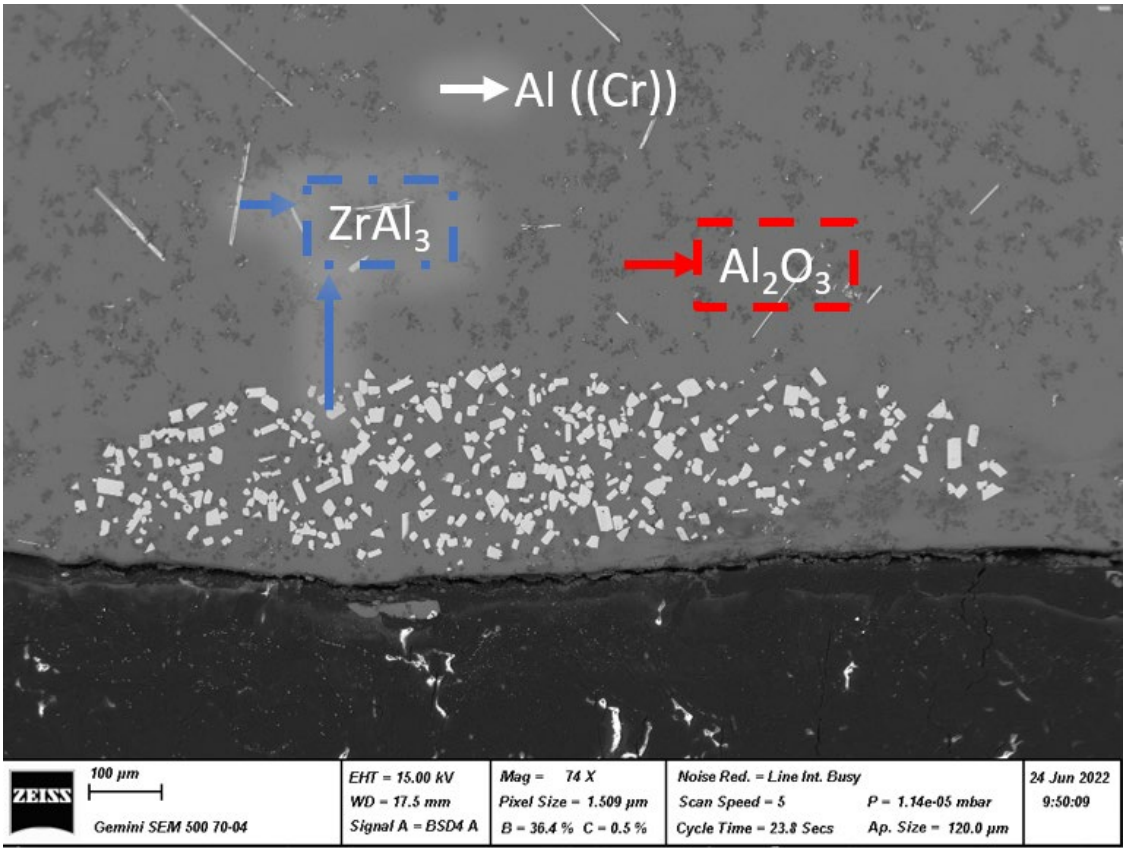

Figure IV-34 Bottom of an ingot exp.2 of drop solution experiment of Zr_3Cr_3O

By using the fitting value of Group A as the enthalpy of the drop solution of Zr_3Cr_3O, it is found:

$$\Delta_{ds}H_{Zr_3Cr_3O} = -367.43 \pm 1.68\ kJ/mol = 52.49 \pm 0.24\ kJ.mol^{-1}.atom^{-1}$$

The enthalpy of the formation of Zr_3Cr_3O is calculated by Equation (IV-7):

$$\Delta_f \boldsymbol{H}^{\boldsymbol{298K}}_{\boldsymbol{Zr_3Cr_3O}} = \boldsymbol{3\Delta_{ds}\bar{H}^{\infty}_{Zr} + 3\Delta_{ds}\bar{H}^{\infty}_{Cr} + \frac{1}{3}\Delta_f H^{298K}_{Al_2O_3} - \Delta_{ds}H_{Zr_3Cr_3O}} + \boldsymbol{\frac{1}{3}\Delta H_{Al_2O_3} - \frac{2}{3}\Delta H_{Al}} \quad \text{(IV-7)}$$

where $\Delta_f H^{298K}_{Zr_3Cr_3O}$ and $\Delta_f H^{298K}_{Al_2O_3}$ are the enthalpy of formation of Zr_3Cr_3O and Al_2O_3 at room temperature, respectively; $\Delta_{ds}\bar{H}^{\infty}_{M}$ (M=Zr, Cr) is the drop solution enthalpy at infinite dilution of M at 1173K; $\Delta_{ds}H_{Zr_3Cr_3O}$ is the drop solution enthalpy of Zr_3Cr_3O at 1173K. $\Delta H_{Al_2O_3}$ and ΔH_{Al} are the change of enthalpy between 298K and 1173K.

Here, the values of $\Delta_{ds}\bar{H}^{\infty}_{M}$ (M=Zr, Cr) is taken from our results in Chapter III, as $\Delta_{ds}\bar{H}^{\infty}_{Zr} = -130 \pm 9\ kJ/mol$ and $\Delta_{ds}\bar{H}^{\infty}_{Cr} = -18.65 \pm 1.07 kJ/mol$. $\Delta_f H^{298K}_{Al_2O_3}$ and $\Delta H_{Al_2O_3}$ are taken or calculated according to the JANAF database [57]. ΔH_{Al} is calculated with C_p of Al of the SGTE database [53]. In detail, we used $\Delta_f H^{298K}_{Al_2O_3} = -1675.69\ kJ/mol$, $\Delta H_{Al_2O_3} = 99.84\ kJ/mol$ and $\Delta H_{Al} = 36.45\ kJ/mol$

As a result, we have the enthalpy of formation of Zr_3Cr_3O at ambient temperature as:

$$\Delta_f H^{298K}_{Zr_3Cr_3O} = -89.73 \pm 3.89\ kJ.mol^{-1}.atom^{-1}$$

Heat increment experiments

Heat increment experiments were performed with a Zr_3Cr_3O sample (purity 98.07% wt. as 95.70 % at. by XRD). The calorimeter was calibrated with Al_2O_3 chunks of different masses. Next, two experiments with each 4 pieces of Zr_3Cr_3O samples of different masses are dropped successively into an empty crucible maintained at 900°C/1173.15K.

The experimental points and the linear fitting of these points are reported in Table IV-14 and Figure IV-35. The fitting parameters are listed in Table IV-13. A perfect linearity was found since both Pearson's R and adjusted R^2 values are very close to 1. It can be seen that all the experimental points are settled in the 95% prediction band of the fitting.

Table IV-13 Linear fitting parameters of the drop heating measurements

Linear fitting parameters	
Pearson's r	0.99969
Adj. R-Square	0.99928
Intercept	-0.42129 ± 0.08746
Slope	181.15213 ± 1.83448

Table IV-14 Data of drop heating experiments

Drop amount(mg)	**Drop amount(mmol)**	***ΔQ*(J)**	
7.92	0.018	2.74	Exp.1
19.93	0.045	7.78	
25.3	0.057	9.84	
26.6	0.060	10.31	
9.8	0.022	3.60	Exp.2
19.74	0.044	7.59	
24.98	0.056	9.66	
26.35	0.059	10.40	

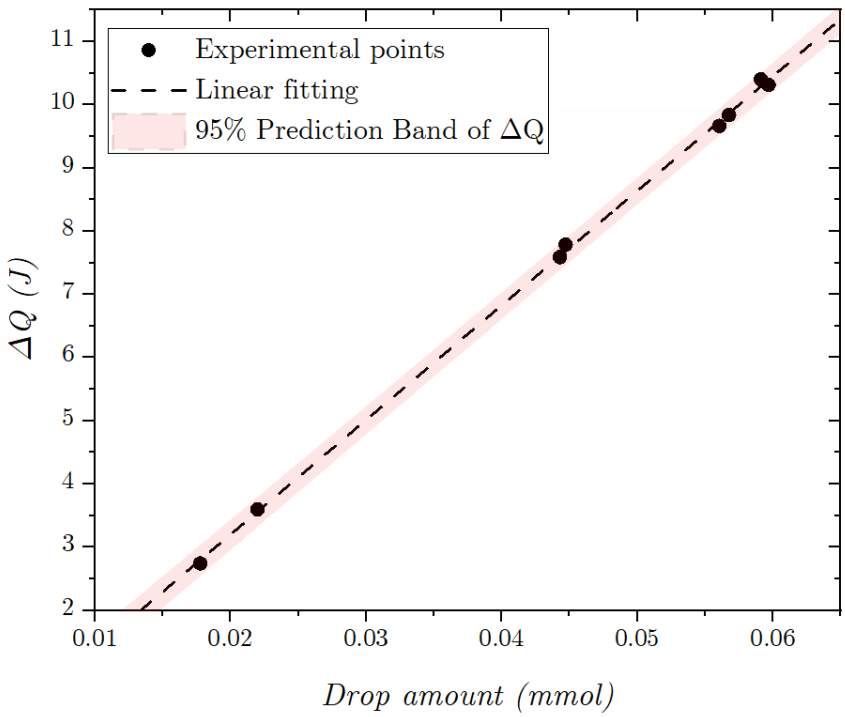

Figure IV-35 Drop heating measurements of Zr_3Cr_3O at 900°C and linear fitting of the obtained values

Enthalpy change of Zr_3Cr_3O with temperature from room temperature to 900°C/1173.15K calculated as:

$$\Delta H_{298K,Zr_3Cr_3O}^{1173K} = 172.80 \pm 0.85\ kJ/mol$$

The integration of C_p with the modified Einstein model of Equation (III-6) and Table III-13 was calculated and referenced at ambient temperature to make a comparison with the previous result. The results are illustrated in Figure IV-36. The red point in the figure is the enthalpy obtained by the drop heating method, which shows good consistency with the value obtained by temperature integration of the measured C_p. This proves the accuracy and consistency of our experimental work which includes different techniques.

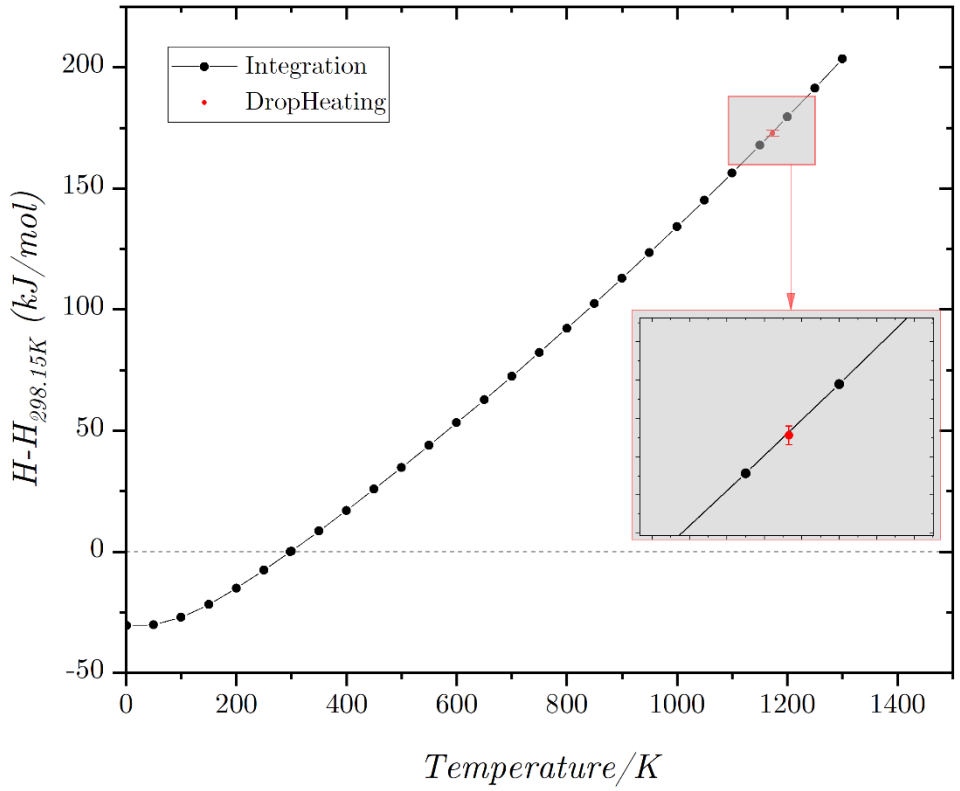

Figure IV-36 Comparison of integration of C_p measurements and the result of drop heating experiments

IV.4.1.4 DFT results

DFT calculations have been realized to support the experimental measurement of the enthalpy of formation of Zr_3Cr_3O. Results are listed below in Table III-13.

Table IV-15 DFT calculations related to the enthalpy of formation of Zr_3Cr_3O

Compound	H_{0K}	
	eV/atom	kJ/mol
$O_{2,mag}$*	-4.928	-475.454
Zr	-8.478	-818.036
Cr	-9.514	-917.993
Cr_{mag}*	-9.504	-916.988
Zr_3Cr_3O	-64.504	-6223.814
$Zr_3Cr_3O_{mag}$*	-64.371	-6211.046

* In the calculations the antiferromagnetism of Cr and paramagnetism of oxygen at low temperatures were considered.

The enthalpy of formation at 0K was calculated according to the following equation (IV-8).

$$\Delta_f H^{0K}_{Zr_3Cr_3O} = H^{0K}_{Zr_3Cr_3O} - 3H^{0K}_{Zr} - 3H^{0K}_{Cr} - \frac{1}{2}H^{0K}_{O_2} \qquad \text{(IV-8)}$$

The O_2, Cr and Zr_3Cr_3O compounds were calculated with or without considering their magnetism at low temperatures. Slight differences in calculated enthalpy values were found in these calculations.

Calculated with the data $O_{2,mag}$, Zr, Cr and Zr_3Cr_3O, we have:

$$\Delta_f H^{0K}_{Zr_3Cr_3O} = -540.273 \text{ kJ/mol} = -77.19 \text{ kJ/mol/atom}$$

Calculated with the data $O_{2,mag}$, Zr, Cr_{mag} and $Zr_3Cr_3O_{mag}$, we have:

$$\Delta_f H^{0K}_{Zr_3Cr_3O} = -530.520 \text{ kJ/mol} = -75.79 \text{ kJ/mol/atom}$$

It can be concluded that the differences caused by magnetism were negligible compared with the important exothermic enthalpy of formation of Zr_3Cr_3O (difference <2%).

The enthalpy of formation is calculated at room temperature starting with $\Delta_f H^{0K}_{Zr_3Cr_3O} = -530.520\ \text{kJ/mol}$ and the enthalpy increments ΔH_0^{298} from SGTE (shown in Table IV-16), and Equation (IV-9):

Table IV-16 Data of enthalpy increments ΔH_0^{298} used for the correction of DFT result

Compound	ΔH_0^{298} (kJ/mol)	Source
$1/2O_2$*	4.341	SGTE [53]
Zr	5.566	SGTE
Cr	4.050	SGTE
Zr_3Cr_3O	30.181	This work

* $1/2O_2$ (Gas) in the database

$$\Delta_f \boldsymbol{H^{298K}_{Zr_3Cr_3O}} = \Delta_f^{0K} \boldsymbol{H_{Zr_3Cr_3O}} + \Delta \boldsymbol{H^{298K}_{0K,Zr3Cr3O}} - \boldsymbol{3}\Delta \boldsymbol{H^{298K}_{0K,Zr}} - \boldsymbol{3}\Delta \boldsymbol{H^{298K}_{0K,Cr}} - \frac{\boldsymbol{1}}{\boldsymbol{2}} \Delta \boldsymbol{H^{298K}_{0K,O_2}} \quad \text{(IV-9)}$$

As a result, we have at room temperature:

$$\Delta_f H^{298K}_{Zr_3Cr_3O} = -533.530\ \text{kJ/mol} = -76.219\ \text{kJ/mol/atom}$$

The formation enthalpy calculated by DFT is found to be less exothermic than the calorimetric value ($\Delta_f H^{298K}_{Zr_3Cr_3O} = -89.96 \pm 3.89\ kJ.mol^{-1}.atom^{-1}$).

IV.4.2 CALPHAD modeling

The CALPHAD modeling of the ternary system Zr-Cr-O was based on the binary modeling of Zr-O, Cr-O and Zr-Cr. Zr-Cr is described in Chapter III whereas Zr-O and Cr-O systems were taken from the NUCLEA database of IRSN [28].

The system was defined with 3 elements (Zr, Cr, O), 12 species and 15 phases. Mutual solubilities of ZrO_2 and Cr_2O_3 were defined by adding second sub-lattices in the definitions and optimized with an interaction parameter. The phase Cr_3O_4 was defined in the model but was not stabilized until 1700°C.

For the modeling of the ternary system, the Zr_3Cr_3O ternary compound was introduced, with its thermodynamic properties as determined in this work. The calculated enthalpy of formation and entropy at room temperature of this compound in this modeling is:

$$\Delta_f H^{298K}_{Zr_3Cr_3O} = -90.039\ kJ.mol^{-1}.atom^{-1}$$

$$S^{298K}_{Zr_3Cr_3O} = 26.96\ J/(mol.atom)/K$$

They agreed with our experimental data. The entropy of formation of this compound is calculated to be, in agreement with our determination. Finally, the modelled heat capacity agrees with our measurements.

The interaction parameters of the liquid phase have been optimized to model the extension of the liquid domain in the ternary section.

Three isothermal sections of phase diagrams at 1200°C, 1500°C and 1700°C are presented below in Figure IV-37, Figure IV-38 and Figure IV-39. The different three solid-phase equilibria of the ternary isothermal sections at 1200, 1500°C and 1700 °C agree with our data and the experimental information reported by Rhee and Roch [1].

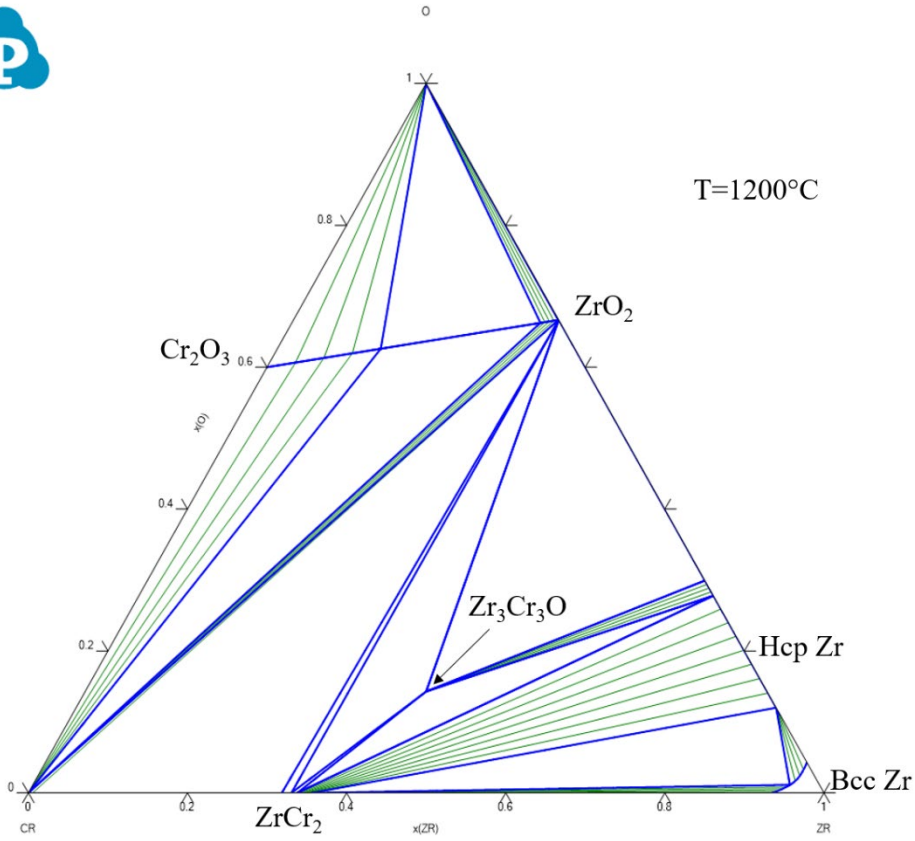

Figure IV-37 Isothermal section of the Zr-Cr-O ternary system at 1200°C

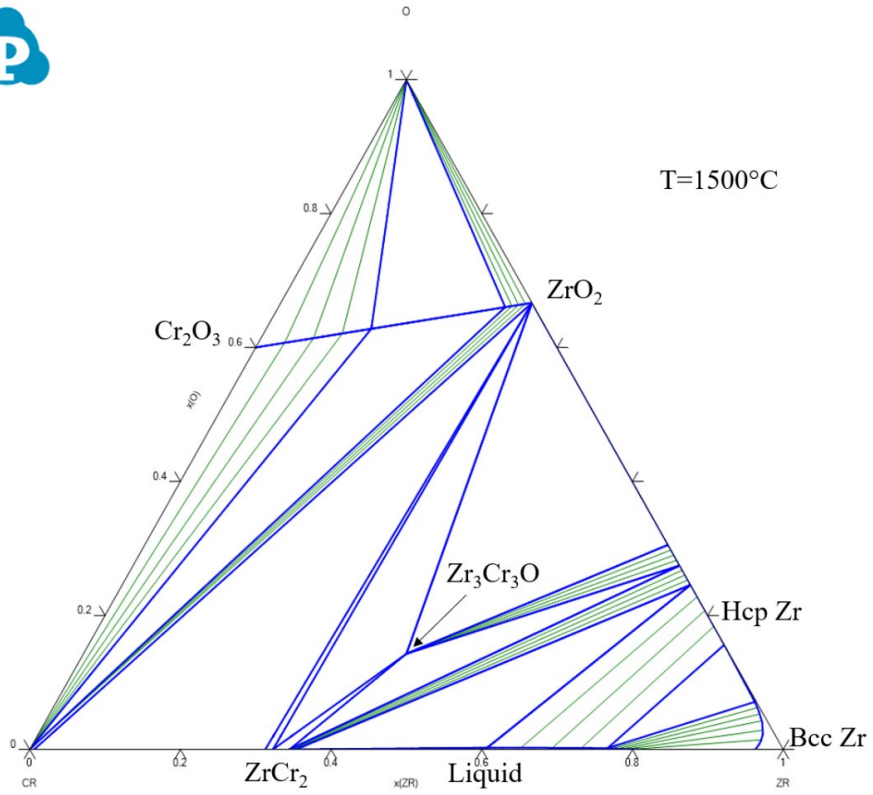

Figure IV-38 Isothermal section of the Zr-Cr-O ternary system at 1500°C

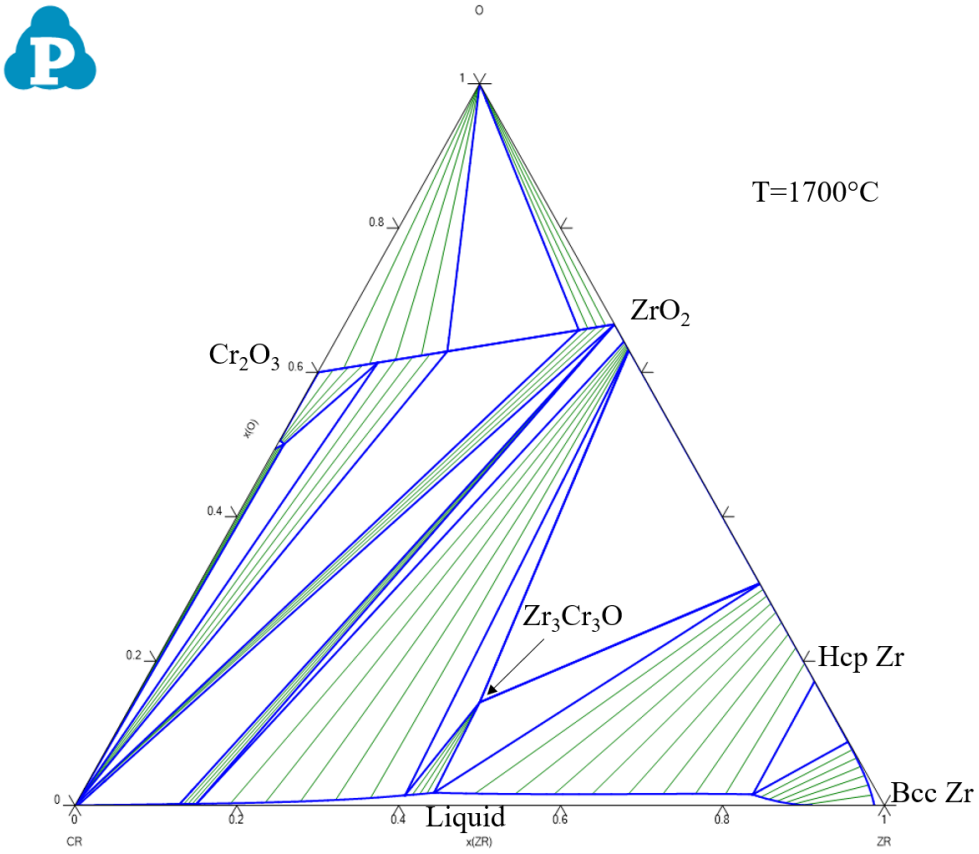

Figure IV-39 Isothermal section of the Zr-Cr-O ternary system at 1700°C

The parameters of modeling are optimized and reported as in Table IV-17:

Table IV-17 Modeling parameters of the Zr-Cr-O system

Liquid	
Components and associates	Cr, CrO, $CrO_{1.5}$, O, ZrO_2, Zr
Parameters	°L ($CrO_{1.5}$, ZrO_2) = -39186.20
	°L CrO, ZrO_2 = 20000
	°L Cr, ZrO_2 = 100000
	°L CrO, Zr = 50000
	°L $CrO_{1.5}$, Zr = 100000
Fcc_C1	
Components	$CrO_{1.5}$, O, ZrO_2, Zr
Parameters	°Gfcc_C1 $CrO_{1.5}$ = +27000 -3.7*T+ °G$CrO_{1.5}$(rho)
	°Lfcc_C1 $CrO_{1.5}$,ZrO_2 = -9301.81
Tetra(oxide)	
Components	$CrO_{1.5}$, ZrO_2
Parameters	°Gtetra $CrO_{1.5}$ = +25000 -3.7*T +°GCrO1.5(rho)
	°Ltetra $CrO_{1.5}$,ZrO_2 = 4002.9
CrO1.5(ss)	
Components	$CrO_{1.5}$, ZrO_2
Parameters	°GCrO1.5 ZrO_2 = +25000 -3.7*T+ °GZrO2(fcc_C1)
	°LCrO1.5 ZrO_2 = -54658.27 + 16.8444*T
Zr_3Cr_3O	
Parameters	°G Cr_3OZr_3 = -680000 + 838*T -149.75884*T*LN(T)-0.03388*T^2
	+311432.88*T^{-1}

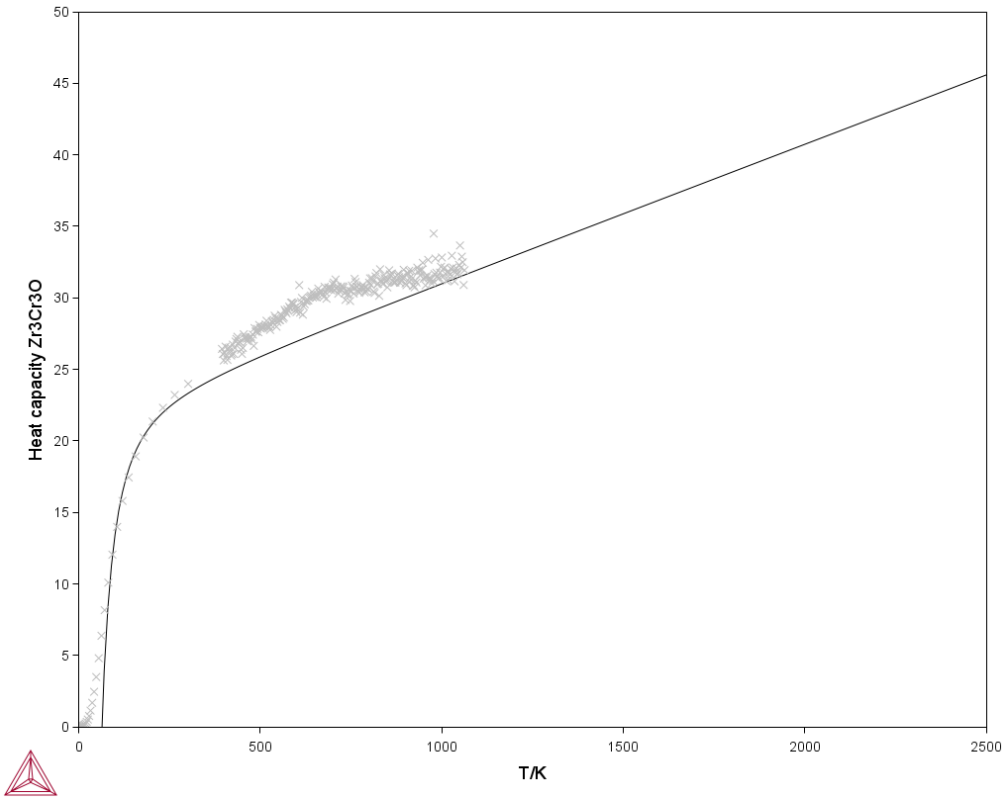

Figure IV-40 Comparison of C_p calculated from CALPHAD model and experimental points of the ternary phase Zr_3Cr_3O

The C_p fitting result is shown in Figure IV-40. An acceptable consistency is found for the experimental data at low temperatures and a reasonable agreement at high temperatures. The difficulty in fitting was caused by dispersed points at around 1000°C, which led to a huge uncertainty in the slope determination. The resulting line presented in the figure was fitted to meet the points at low temperatures [1.8K to 300K] and the mean slope of data at high temperatures around [300K to 1063K]. Attempts of fitting with only PPMS points or only with DSC points were made but the results were not better. A more consistent fitting may be achieved with more assessments and more prudent selections of the fitting data. It would surely affect the stability of the Zr_3Cr_3O phase at high temperatures. Thus, the interaction parameters of the other phases would require further modifications, especially for the liquid phase.

Further development of the modeling would be to consider solubility measurements of oxygen in $ZrCr_2$ or Cr, and Cr in hcp Zr phase into the model. This will help to improve the description of extensions of binary phases in the ternary system.

IV.5 Conclusion and prospective works

Up to now, very few studies have been devoted to the Zr-Cr-O ternary system. In particular, the ternary compound Zr_3Cr_3O was poorly characterized. The results reported in this chapter aimed to fill these lacks, at least partially. The main results obtained in this work are the following:

1. For the quasi-binary system ZrO_2-Cr_2O_3, a study was made by annealing pellets of mixed powders of ZrO_2 and Cr_2O_3 to validate the mutual solubility of these two end-members. Difficulties were encountered for EDS measurements due to a strong charge-up effect. Despite this, we were able to confirm the Cr_2O_3 solubility in ZrO_2 and ZrO_2 solubility in Cr_2O_3 at 1200°C, as:

$$\mathrm{Sol}(\mathrm{ZrO_2\ in\ Cr_2O_3}) = 29.07 \pm 10.27\%\ \mathrm{mol.}$$
$$\mathrm{Sol}(\mathrm{Cr_2O_3\ in\ ZrO_2}) = 9.24 \pm 8.30\%\ \mathrm{mol.}$$

2. The study of the phase equilibrium of the ternary system Zr-Cr-O performed from annealed pellet samples aimed for the determination of the isothermal sections at 1200°C and 1500°C. The phase relations have been studied in the metallic-to-oxide composition part of the system. The solid-state relationships are consistent with the isothermal sections published by Rhee and Roch [1] while the liquid zone is more limited at 1500°C in the present assessment. Some ternary extensions of binary phases were also measured, mainly for the isopleth section of Cr_2O_3-ZrO_2.
3. A reproducible preparation method of the Zr_3Cr_3O ternary phase was achieved starting from an initial composition of $Zr_3Cr_{3.3}O$ firstly arc-melted, then the resulting ingot was crushed into powder that was cold-pressed, and finally, the green pellet was annealed at 1400°C for less than 4h under high purity Ar. The phase purity of Zr_3Cr_3O is above 95% at. as confirmed by powder XRD refinement.
4. The crystal structure of Zr_3Cr_3O was refined using the Rietveld method allowing the refinement of the atomic positions within the filled Ti_2Ni structure. No solubility domain around the stoichiometric composition was found. WDS results confirm the stoichiometry of Zr: Cr: O = 3: 3: 1 without a detectable homogeneity range.
5. The specific heat capacity C_p of Zr_3Cr_3O was studied by coupling semi-adiabatic relaxation calorimetry (PPMS) and DSC methods over a wide range, of 2-1100K. The C_p data was fitted with a modified Einstein model. From these data, the entropy of the formation of the compound was calculated. The heat increment of the compound between 25°C/298K and

900°C/1173K was measured by isothermal calorimetry, and the result proved consistent with the value obtained by integrating C_p data as a function of temperature.

6. The enthalpy of the formation of Zr_3Cr_3O was measured by drop solution calorimetry in liquid Al at 1173K. A data processing based on a careful analysis and interpretation of the thermal curves obtained and the microstructure of ingots was performed. The enthalpy of formation was deduced as $\Delta_f^{298K} H_{Zr_3Cr_3O} = -89.96 \pm 3.98\ kJ.mol^{-1}.atom^{-1}$
7. DFT calculations were made on the Zr_3Cr_3O phase. Results were compared with the experimental data for both atomic arrangement and enthalpy of formation. The results are in fair agreement with our experiments, considering the simulation carried out at 0K.

With all these experimental and DFT results, a CALPHAD modeling of the ternary system was established from the binary description of Zr-Cr assessed in Chapter III and Zr-O, Cr-O descriptions of the NUCLEA thermodynamic database of IRSN, the optimization of some interaction parameters of the liquid phase and the thermodynamic data of the ternary compound Zr_3Cr_3O. The isothermal sections calculated at 1200°C and 1500°C agreed with our experimental results and also with Rhee and Roch [1] whereas the section at 1700°C has a more restricted liquid area.

The following avenues for future work are proposed:

1. CALPHAD modeling could be further refined with more experimental data at high temperatures such as 1700°C and by introducing more interaction parameters to model the extension of $ZrCr_2$ into the ternary.
2. In this respect, a more detailed study of equilibria involving the liquid phase would be useful to support the modeling.
3. The determination of the melting temperature of Zr_3Cr_3O by an appropriate technique would be very valuable.

IV.6 Reference

[1] S. K. Rhee and M. Hoch, 'The system chromium-zirconium-oxygen at 1200, 1500, and 1700°C', *Trans. AIME*, vol. 230, no. 7, pp. 1687–1690, Dec. 1964.

[2] J. P. Abriata, J. Garcés, and R. Versaci, 'The O−Zr (Oxygen-Zirconium) system', *Bulletin of Alloy Phase Diagrams*, vol. 7, no. 2, pp. 116–124, Apr. 1986, doi: 10.1007/BF02881546.

[3] P. Liang *et al.*, 'Thermodynamic Assessment of the Zr–O Binary System', *International Journal of Materials Research*, vol. 92, no. 7, pp. 747–756, Feb. 2022, doi: 10.1515/ijmr-2001-0140.

[4] R. Arroyave, L. Kaufman, and T. W. Eagar, 'Thermodynamic modeling of the Zr-O system', *Calphad*, vol. 26, no. 1, pp. 95–118, Mar. 2002, doi: 10.1016/S0364-5916(02)00027-5.

[5] M. Chen, B. Hallstedt, and L. Gauckler, 'Thermodynamic modeling of the ZrO_2–$YO_{1.5}$ system', *Solid State Ionics*, vol. 170, no. 3–4, pp. 255–274, May 2004, doi: 10.1016/j.ssi.2004.02.017.

[6] C. Wang, M. Zinkevich, and F. Aldinger, 'On the thermodynamic modeling of the Zr–O system', *Calphad*, vol. 28, no. 3, pp. 281–292, Sep. 2004, doi: 10.1016/j.calphad.2004.09.002.

[7] P.-Y. Chevalier, E. Fischer, and B. Cheynet, 'Progress in the thermodynamic modelling of the O–U–Zr ternary system', *Calphad*, vol. 28, no. 1, pp. 15–40, Mar. 2004, doi: 10.1016/j.calphad.2004.03.005.

[8] Y. Wang *et al.*, 'Ab initio lattice stability in comparison with CALPHAD lattice stability', *Calphad*, vol. 28, no. 1, pp. 79–90, Mar. 2004, doi: 10.1016/j.calphad.2004.05.002.

[9] H. Okamoto, 'Section III: Supplemental Literature Review', *JPE*, vol. 19, no. 5, pp. 486–486, Oct. 1998, doi: 10.1007/BF02700865.

[10] M. V. Nevitt, Y. Fang, and S.-K. Chan, 'Heat Capacity of Monoclinic Zirconia between 2.75 and 350 K', *J American Ceramic Society*, vol. 73, no. 8, pp. 2502–2504, Aug. 1990, doi: 10.1111/j.1151-2916.1990.tb07619.x.

[11] T. Tsuji and M. Amaya, 'Heat capacity measurement on ZrO_x (x = 0–0.31) from 325 to 905 K. Part I. Heat capacity anomaly due to thermal non-equilibrium state at low temperature', *Thermochimica Acta*, vol. 259, no. 1, pp. 1–12, Jul. 1995, doi: 10.1016/0040-6031(95)02264-3.

[12] T. Tojo, T. Atake, T. Mori, and H. Yamamura, 'Heat capacity and thermodynamic functions of zirconia and yttria-stabilized zirconia', *The Journal of Chemical Thermodynamics*, vol. 31, no. 7, pp. 831–845, Jul. 1999, doi: 10.1006/jcht.1998.0481.

[13] C. Degueldre, P. Tissot, H. Lartigue, and M. Pouchon, 'Specific heat capacity and Debye temperature of zirconia and its solid solution', *Thermochimica Acta*, vol. 403, no. 2, pp. 267–273, Jul. 2003, doi: 10.1016/S0040-6031(03)00060-1.

[14] M. Veshchunov, 'Analysis of the FZK previous tests and pretest calculations of the FZK new tests on ZrO_2 dissolution by molten Zircaloy', Minutes of the 4th CIT project meeting, Pisa, In vessel cluster INV-CIT(98)-M006, Jun. 1998.

[15] A. Brunel, A. Quaini, T. Alpettaz, C. Bonnet, R. Guillou, and L. Cormier, 'Experimental investigation of the phases transitions on O-rich side of the Zr–O system', *Calphad*, vol. 79, p. 102490, Dec. 2022, doi: 10.1016/j.calphad.2022.102490.

[16] R. F. Domagala and D. J. McPherson, 'System zirconium-oxygen', *JOM*, vol. 6, no. 2, pp. 238–246, Feb. 1954, doi: 10.1007/BF03398005.

[17] E. Gebhardt, H.-D. Seghezzi, and W. Dürrschnabel, 'Untersuchungen in system Zirkonium-Sauerstoff teil 2 untersuchungen zur kinetik der reaktion zwischen Zirkonium und sauerstoff, sowie über die konstitution des systems Zirkonium-Sauerstoff', *Journal of*

Nuclear Materials, vol. 4, no. 3, pp. 255–268, Aug. 1961, doi: 10.1016/0022-3115(61)90075-7.
[18] B. Holmberg, T. Dagerhamn, and L. Kaarina, 'X-ray studies on solid solutions of oxygen in a-zirconium', *Acta Chem. Scand*, vol. 15, no. 4, p. 14, 1961.
[19] O. R. J. Ackermann, S. P. Garg, and E. G. Rauh, 'High-Temperature Phase Diagram for the System Zr.', *J American Ceramic Society*, vol. 60, no. 7–8, pp. 341–345, Jul. 1977, doi: 10.1111/j.1151-2916.1977.tb15557.x.
[20] R. J. Ackermann, S. P. Garg, and E. G. Rauh, 'The Lower Phase Boundary of ZrO_{2-x}', *J American Ceramic Society*, vol. 61, no. 5–6, pp. 275–276, May 1978, doi: 10.1111/j.1151-2916.1978.tb09303.x.
[21] E. G. Rauh and S. P. Garg, 'The ZrO_{2-x} (cubic)-ZrO_{2-x} (cubic+tetragonal) Phase Boundary', *J American Ceramic Society*, vol. 63, no. 3–4, pp. 239–240, Mar. 1980, doi: 10.1111/j.1151-2916.1980.tb10711.x.
[22] G. Banik, T. Schmitt, P. Ettmayer, and B. Lux, 'Thermodynamische Betrachtungen über das System Cr-Cr2O3', *International Journal of Materials Research*, vol. 71, no. 10, pp. 644–645, Oct. 1980, doi: 10.1515/ijmr-1980-711004.
[23] J. R. Taylor and A. Dinsdale, 'A thermodynamic assessment of the Ni-O, Cr-O and Cr-Ni-O systems using the ionic liquid and compound energy models', *Zeitschrift Fur Metallkunde*, vol. 81, pp. 354–366, 1990.
[24] M. Kowalski and P. J. Spencer, 'Thermodynamic reevaluation of the C-O, Fe-O and Ni-O systems: Remodelling of the liquid, BCC and FCC phases', *Calphad*, vol. 19, no. 3, pp. 229–243, doi: 10.1016/0364-5916(95)00024-9.
[25] N. Y. Toker, L. S. Darken, and A. Muan, 'Equilibrium phase relations and thermodynamics of the Cr-O system in the temperature range of 1500 °C to 1825 °C', *Metallurgical Transactions B*, vol. 22, no. 2, pp. 225–232, Apr. 1991, doi: 10.1007/BF02652487.
[26] H. Okamoto, 'Cr-O (chromium-oxygen)', *Journal of Phase Equilibria*, vol. 18, no. 4, p. 402, Aug. 1997, doi: 10.1007/s11669-997-0072-0.
[27] E. Povoden, A. N. Grundy, and L. J. Gauckler, 'Thermodynamic Reassessment of the Cr-O System in the Framework of Solid Oxide Fuel Cell (SOFC) Research', *Journal of Phase Equilibria & Diffusion*, vol. 27, no. 4, pp. 353–362, Aug. 2006, doi: 10.1361/154770306X116289.
[28] 'Thermodynamic database for nuclear applications, NUCLEA'.
[29] Y. I. Ol'shanskii and V. K. Shlepov, 'Sistema Cr-Cr_2O_3', *DOKLADY AKADEMII NAUK SSSR*, vol. 91, no. 3, pp. 561–564, 1953.
[30] E. T. Hayes, A. H. Roberson, and M. H. Davies, 'Zirconium-Chromium Phase Diagram', *Journal of metals*, vol. 4, no. 3, pp. 304–306, Mar. 1952, doi: 10.1007/BF03397695.
[31] R. F. Domagala, D. J. McPherson, and M. Hansen, 'System Zirconium-Chromium', *Journ. Metals*, vol. 5, pp. 279–283, 1953.
[32] T. M. Vu, J.-M. Joubert, and C. Toffolon-Masclet, 'Thermodynamic database for zirconium alloys used in Pressurized Water Reactors', Conference CALPHAD, Boston, 2023.
[33] H. V. Wartenberg and H. Werth, 'Schmelzdiagramme höchstfeuerfester Oxyde. II', *Z. Anorg. Allg. Chem.*, vol. 190, no. 1, pp. 178–184, May 1930, doi: 10.1002/zaac.19301900116.
[34] A. S. Berezhnoi and N. V. Gul'ko, 'Phase diagrams of the systems Cr_2O_3-TiO_2 and Cr_2O_3-ZrO_2 (in russian)', *Dopov. Akad. Nauk. Ukr. RSR*, vol. Ser. B (3), no. 30, pp. 250–253, 1968.
[35] L. M. Lopato, V. A. Shevchenko, and I. M. Maister, 'Reaction of ZrO_2 with Cr_2O_3', *Izv. Akad. Nauk SSSR*, vol. 13, no. 10, pp. 1822–1824, 1977.

[36] V. F. Smachnaya and P. Y. Saldau, *Zap. Len. Gorn. Inst.*, vol. 24, no. 153, 1950.
[37] V. F. Smachnaya, 'Study of Physico-chemistry of the Ternary Cr_2O_3-ZrO_2-SiO_2 system', *Iz Vysshikh Ucheb Zaved Chern Met.*, vol. 11, pp. 191–195, 1962.
[38] S. M. Lang, R. S. Roth, and C. L. Fillmore, 'Some properties of porcelains and phase relations in the ternary systems of beryllia and zirconia with titania, ceria, and chromia', *J. RES. NATL. BUR. STAN.*, vol. 53, no. 4, p. 201, Oct. 1954, doi: 10.6028/jres.053.025.
[39] D. A. Jerebtsov, G. G. Mikhailov, and S. V. Sverdina, 'Phase diagram of the system: ZrO_2–Cr_2O_3', *Ceramics International*, vol. 27, no. 3, pp. 247–250, Jan. 2001, doi: 10.1016/S0272-8842(00)00071-7.
[40] J. F. Collins and F. Ferguson, 'Lattice parameter variations in mixed oxides with the monoclinic zirconia structure: the systems ZrO_2–Fe_2O_3, ZrO_2–SnO_2, and ZrO_2–Cr_2O_3', *Journal of the Chemical Society*, vol. A: Inorganic, Physical, Theoretical, pp. 4–5, 1968.
[41] J. Stocker and R. Collongues, 'Sur la préparation de solution solides cubiques de la zircone', laboratoire de Vitry du CNRS, Aug. 1957.
[42] I.A. Turkin and T. N. Maslova, 'Sintering and Phase Composition of the Aluminum--Chromium-Zirconium Oxide Systems [in Russian]', Dep. VINITI, Leningrad, 2797, 1984.
[43] I. Y. Zavaliy, 'New Hydrides of Zr-Based Intermetallic Compounds', *MRS Proc.*, vol. 547, p. 469, 1998, doi: 10.1557/PROC-547-469.
[44] M. V. Nevitt, J. W. Downey, and R. A. Morris, 'A further study of Ti 2Ni-type phases containing titanium, zirconium or hafnium', *Trans. Met. Soc. AIME*, vol. 218, 1960.
[45] M. V. Nevitt, 'Stabilization of Certain Ti_2Ni-Type Phases by Oxygen', *Trans. Met. Soc. AIME*, vol. 218, 1960.
[46] H. Fukui, M. Fujimoto, Y. Akahama, A. Sano-Furukawa, and T. Hattori, 'Structure change of monoclinic ZrO_2 baddeleyite involving softenings of bulk modulus and atom vibrations', *Acta Crystallogr B Struct Sci Cryst Eng Mater*, vol. 75, no. 4, pp. 742–749, Aug. 2019, doi: 10.1107/S2052520619007923.
[47] M. Baster, F. Bourée, A. Kowalska, and Z. Latacz, 'The change of crystal and exchange parameters in the vicinity of TN in Cr_2O_3', *Journal of Alloys and Compounds*, vol. 296, no. 1–2, pp. 1–5, Jan. 2000, doi: 10.1016/S0925-8388(99)00511-3.
[48] W. B. Pearson, 'Metal Compounds: *Interstitial Alloys*', *Science*, vol. 162, no. 3850, pp. 251–251, Oct. 1968, doi: 10.1126/science.162.3850.251.b.
[49] L. E. Toth, *Transition Metal Carbides and Nitrides*. in Pure and Applied Mathematics. Academic Press, 1971. [Online]. Available: https://books.google.fr/books?id=-pYvAQAAIAAJ
[50] D. V. Suetin, I. R. Shein, and A. L. Ivanovskii, 'Structural, electronic and magnetic properties of η carbides (Fe_3W_3C, Fe_6W_6C, Co_3W_3C and Co_6W_6C) from first principles calculations', *Physica B: Condensed Matter*, vol. 404, no. 20, pp. 3544–3549, Nov. 2009, doi: 10.1016/j.physb.2009.05.051.
[51] I. Bajenova *et al.*, 'Third-generation CALPHAD description of pure GeO_2 at 1 atm', *Calphad*, vol. 74, p. 102299, Sep. 2021, doi: 10.1016/j.calphad.2021.102299.
[52] Z. He, B. Kaplan, H. Mao, and M. Selleby, 'The third generation Calphad description of Al–C including revisions of pure Al and C', *Calphad*, vol. 72, p. 102250, Mar. 2021, doi: 10.1016/j.calphad.2021.102250.
[53] A. T. Dinsdale, 'SGTE DATA FOR PURE ELEMENTS', *Calphad*, vol. 15, no. 4, pp. 317–425, Oct. 1991, doi: 10.1016/0364-5916(91)90030-N.
[54] K. Gajavalli, M. Barrachin, P. Benigni, J. Rogez, G. Mikaelian, and E. Fischer, 'Determination of solution enthalpy of zirconium in liquid aluminum', *The Journal of Chemical Thermodynamics*, vol. 135, pp. 198–204, Aug. 2019, doi: 10.1016/j.jct.2019.03.037.

[55] O. Dezellus, B. Gardiola, and J. Andrieux, 'On the Solubility of Group IV Elements (Ti, Zr, Hf) in Liquid Aluminum Below 800°C', *J. Phase Equilib. Diffus.*, vol. 35, no. 2, pp. 120–126, Apr. 2014, doi: 10.1007/s11669-013-0278-2.
[56] M. Barrachin *et al.*, 'Critical evaluation of experimental data of solution enthalpy of zirconium in liquid aluminum', *The Journal of Chemical Thermodynamics*, vol. 128, pp. 295–304, Jan. 2019, doi: 10.1016/j.jct.2018.08.010.
[57] Thomas C. Allison, 'NIST-JANAF Thermochemical Tables - SRD 13'. National Institute of Standards and Technology, Jan. 01, 2013. doi: 10.18434/T42S31.

Chapter V

U-Cr-O ternary system

Chapter V. U-Cr-O ternary system

V.1 Introduction

This chapter is devoted to our work on the U-Cr binary system and the U-Cr-O ternary system. It is as follows:

Section V.2 presents our experimental work on the U-Cr binary system. The first sub-section is devoted to the literature review (Section V.2.1) revealing doubt points to be resolved. A second sub-section describes the experimental results (Section V.2.2). The last section includes the CALPHAD modeling of the binary system (Section V.2.3)

Section V.3, gives a short overview of the literature about the U-O system and a complete analysis of the available data about U-Cr-O:

- ✓ Sub-section V.3.1 presents a viewpoint of the U-O system of the NUCLEA database.
- ✓ V.3.2 gives an exhaustive review of the U-Cr-O ternary system examining successively the available isothermal sections and the 3 ternary phases reported to date, namely, $UCrO_4$, Cr_2UO_6 and CrU_3O_{10-x}

In V.4 the main objectives of the investigation performed in this work are listed.

The results of the work and finally outputs and outcomes are presented in V.5 and V.6, respectively.

V.2 U-Cr binary system

V.2.1 Literature review

The U-Cr system is a simple eutectic system involving the invariant eutectic reaction $L \rightleftharpoons bcc\ Cr + \gamma U$. Experimental studies are limited to the U-rich side, up to 44 at. % Cr. A critical assessment of the experimental phase diagram studies has been published by Venkatraman *et al.* [1], based on the experimental works of Saller *et al.* [2], Daane and Wilson [3], Badaeva and Kuznetsova [4], Chapman [5], Provow and Pisher [6], and Townsend and Burke [7]. The eutectic invariant reaction was characterized in [2]–[4], [6], [7] and the eutectic temperatures and compositions reported in these works are listed in Table V-1. This table shows values in the composition and temperatures ranges 853-895°C (1126-1168K) and 80-82.5% at. U respectively. Despite a rather good agreement of the eutectic temperature within ±10°C/K and

±1%, Badaeva *et al.* [4] and Terekhov and Aleksandrova [8] measured a slightly higher eutectic temperature at 895°C and at 880°C using DTA, respectively. There is no clear explanation for this discrepancy at this stage. Venkatraman *et al.* [1] assumed that the temperature reported by Badaeva more likely corresponded to a liquidus temperature for a composition near the eutectic one. A new measurement would help to solve this controversy.

Table V-1 Reported temperature of the eutectic reaction of the U-Cr system in the literature

Temperature of eutectic reaction		**Composition**	**Reference**
°C	K	% at. U	
859	1132	80.6	Saller [2]
859±10	1132±10	80	Daane [3]
895	1168	82.5	Badaeva [4]
870±3	1143±3	80.7	Provow [6]
853	1126	81.9	Townsend [7]
880	1153	82	Terekhov[8]

Two eutectoid reactions were induced by uranium polymorphism, as $\gamma U \rightleftharpoons \text{bcc Cr} + \beta U$ and $\beta U \rightleftharpoons \text{bcc Cr} + \alpha U$. (with α, the orthorhombic structure, β, the tetragonal one, and γ, the cubic one):

- ✓ The temperature of the eutectoid reaction $\gamma U \rightleftharpoons \text{bcc Cr} + \beta U$ was determined in the interval 737-745°C (1010-1018 K) [3], [5], [7], [8]; Some authors [2], [4], [6] nevertheless reported slightly higher temperatures, respectively 765°C, 752±10°C, and 756±2°C.
- ✓ For $\beta U \rightleftharpoons \text{bcc Cr} + \alpha U$, the eutectoid temperatures reported in the literature were in the range of 612-652°C (885-925K) [2]–[8].

Measurements of the eutectoid compositions corresponding to these two reactions are difficult because they were both very close to pure U. Finally, only Badaeva and Kuznetsova [4] reported eutectoid compositions of 98.4% at. U for $\gamma U \rightleftharpoons \text{bcc Cr} + \beta U$ and 99.1% at. U for $\beta U \rightleftharpoons \text{bcc Cr} + \alpha U$.

Daane and Wilson [3], Badaeva and Kuznetsova [4], and Terekhov and Aleksandrova [8] reported the solubility of Cr in γU, as 96% at. U, 98.1% at. U and 95.5% at. respectively. They agreed with a solubility of Cr in βU estimated at 1% at. U and null solubility in αU.

The assessed phase diagram of Venkatraman *et al.* [1], is shown in Figure V-1. More recently, the U-Cr phase diagram was optimized with the CALPHAD method by Berche *et al.* [9](Figure

V-2), based on the Venkatraman's assessment of the eutectic temperature as well as the chromium solubility in uranium-rich solid solutions and on the experimental data of Daane and Wilson [3] and Badaeva and Kuznetsova [4] for the description of the liquidus line in the composition range [0.40% at. Cr]. As no thermodynamic information was found in the literature, the approach of Miedema [10] was used to evaluate the thermodynamic properties of the liquid phase. A good overall agreement was found between the experimental data and the model. The main difference between the Venkatraman and Berche's phase diagrams is the shape of the liquidus line in the chromium-rich part. An inflection of the liquidus line is seen in the CALPHAD description of Berche. This inflection arises from the *bcc* miscibility gap over the whole composition range [11].

Very recently experimental data have been reported by Santhosh *et al.* [12]. They used dynamic calorimetry under slow heating (1 K/min.) in a pure flowing Ar-atmosphere in an alumina crucible. The high-temperature phase stability characteristics of U–xCr (x = 0, 1, 2, 3, 4, 5, 7, 9, 15 wt%) alloys have been investigated. The temperatures of various eutectic, eutectoid solid state phase transformations and melting have been measured as a function of Cr-content. They are superimposed on the Berche's model in Figure V-2 and show a good agreement (within ±15°C) with the assessment, except for the liquidus temperatures corresponding to the compositions the richest in chromium (9 and 15 wt.%) which exhibited a small upward shift (30°C) as compared to equilibrium phase diagram model. Also, Santhosh *et al.* provided for the first time, thermodynamic data in terms of phase transformation enthalpies at the different compositions.

In conclusion, a rather good description of the binary system and a CALPHAD model able to reproduce satisfactorily the experimental data are available. However, the U-rich part of the phase diagram could be improved with accurate chromium solubility measurements in β and γ U polymorphs. Liquidus temperatures in the chromium-rich part or/and thermodynamic data of the liquid phase could also increase the reliability of the thermodynamic description.

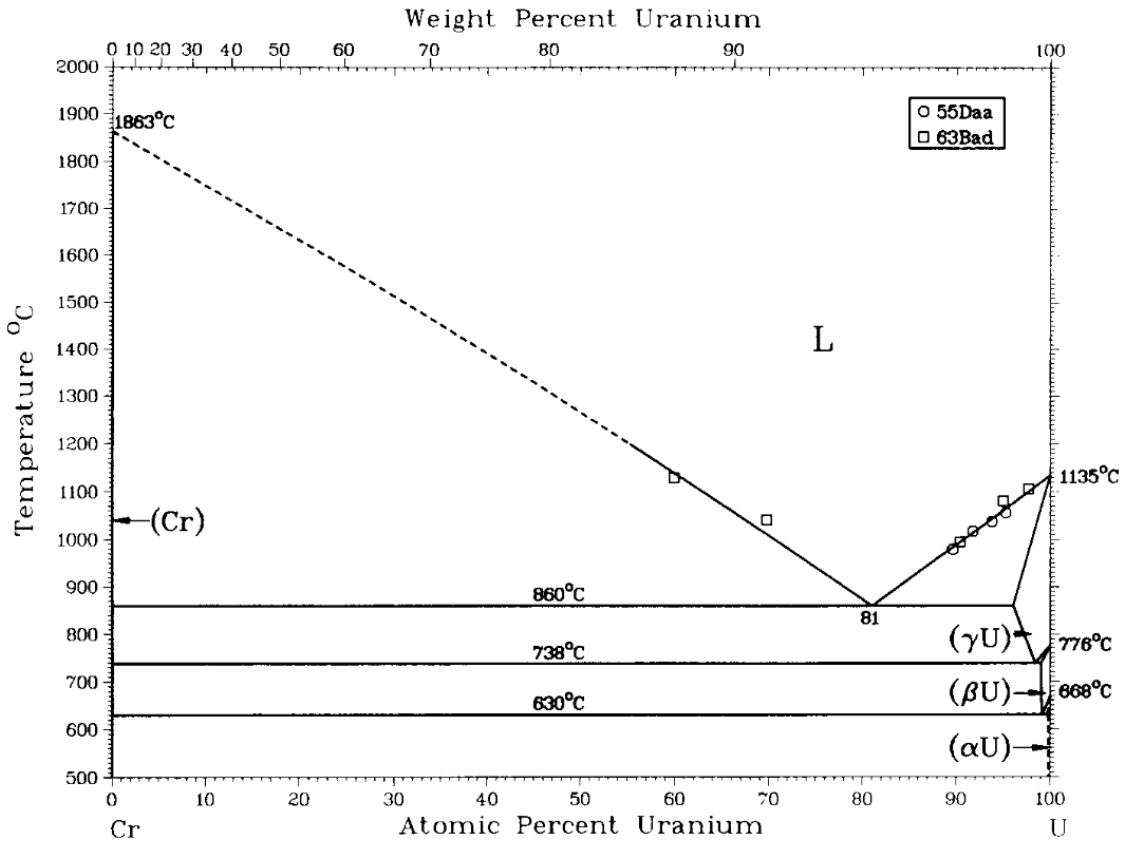

Figure V-1 Phase diagram of the U-Cr system assessed by Venkatraman *et al.* [1]

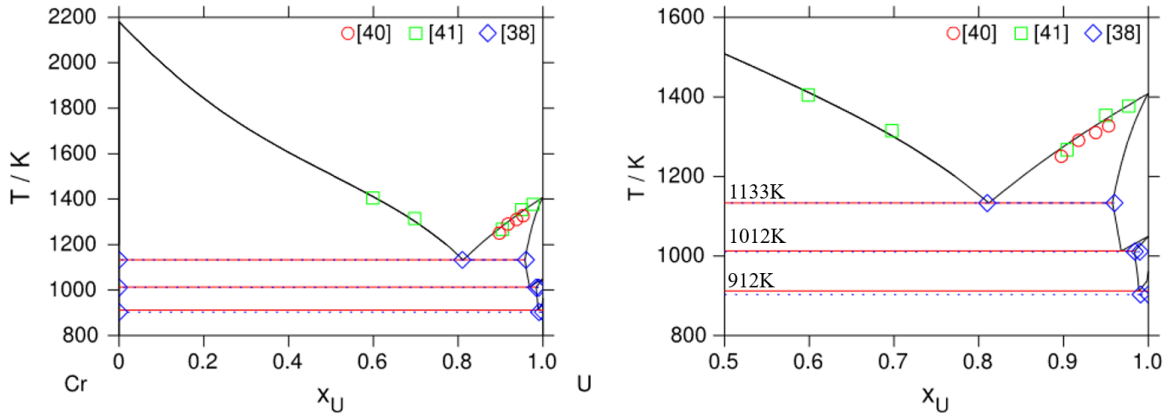

(a) Full composition range. (b) Zoom of the area studied experimentally.

Figure V-2 Assessed U-Cr phase diagram by Berche *et al.* [9]. In the legend at the top right of the graphs, [38] is the publication of Venkatraman *et al.* [1], [40] is the publication of Daane *et al.* [3], [41] is the publication of Badaeva and Kuznetsova [4].

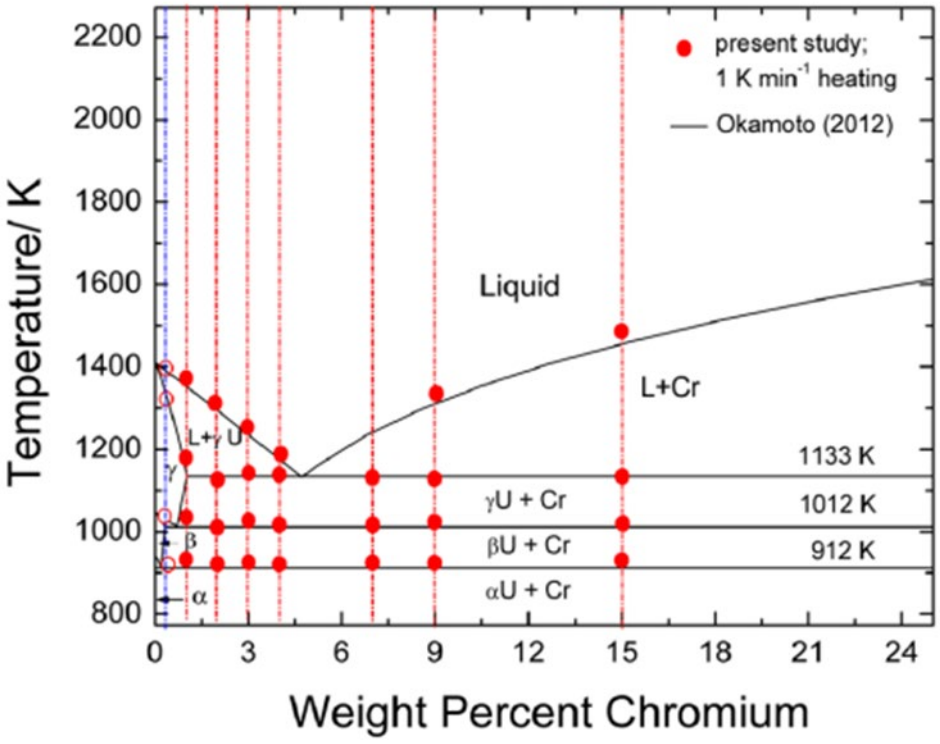

Figure V-3 U–Cr binary phase diagram from the assessment of Okamoto [13] which was retained in Berche's model. The circles represent the measured on-heating transformation arrest temperatures (Figure from Santhosh *et al.* [12])

Finally, very recently a rather complete investigation of the U-Cr system has been published [14]. The solid-state phase transformation and phase stability were measured experimentally using DSC, XRD, SEM, and EDX. The liquidus temperature in the composition ranges from 25 to 100 at. % U were measured by DSC. The temperatures corresponding to $\gamma U \rightleftharpoons \text{bcc Cr} + \beta U$ and $\beta U \rightleftharpoons \text{bcc Cr} + \alpha U$ were found to be 1018 ± 2 K and 920 ± 2 K, respectively. The measured eutectic transformation was found to be 1132 ± 5 K.

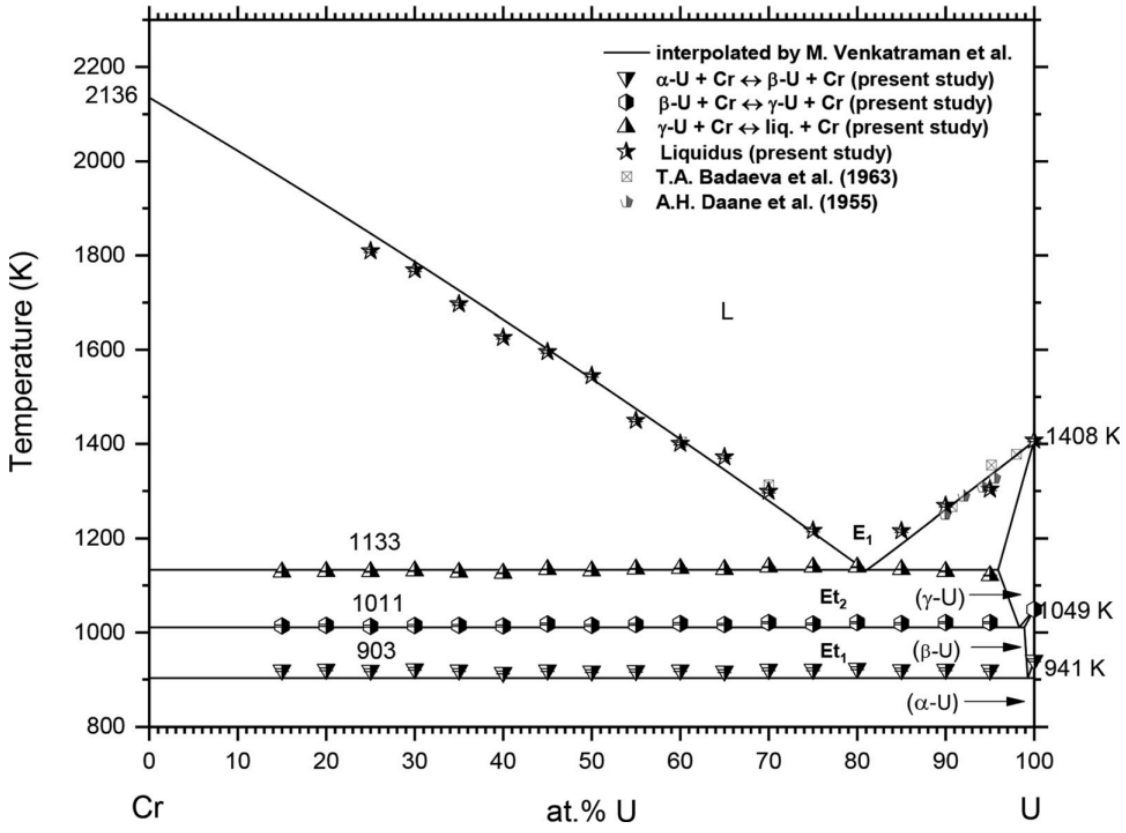

Figure V-4 Experimentally measured liquidus and invariant equilibria in the Cr-U system along with available literature data by Samanta *et al.* (Figure taken from [14])

V.2.2 Experimental studies

Experimental measurements focusing on the eutectic point and the eutectoid temperatures of the U-Cr binary system were carried out to compare with the CALPHAD model.

Samples U77Cr23 (78.4% at. U measured by EDS) and U86Cr14 (87.6% at. U measured by EDS) were prepared by arc-melting. The corresponding micrographs are shown in Figure V-5 and Figure V-6:

- ✓ In Figure V-5, a minor surface fraction of U dendrites (white petals) is visible in a broad background of lamellar eutectic structure;
- ✓ In Figure V-6, U dendrites (white zones) occupy a very large fraction of the observed surface area, while a small fraction of eutectic structure is seen between the dendrites.

  The eutectic composition and the solubility of chromium in the uranium-rich solution were measured. Average values were taken with at least 10 measurements of individual zones.

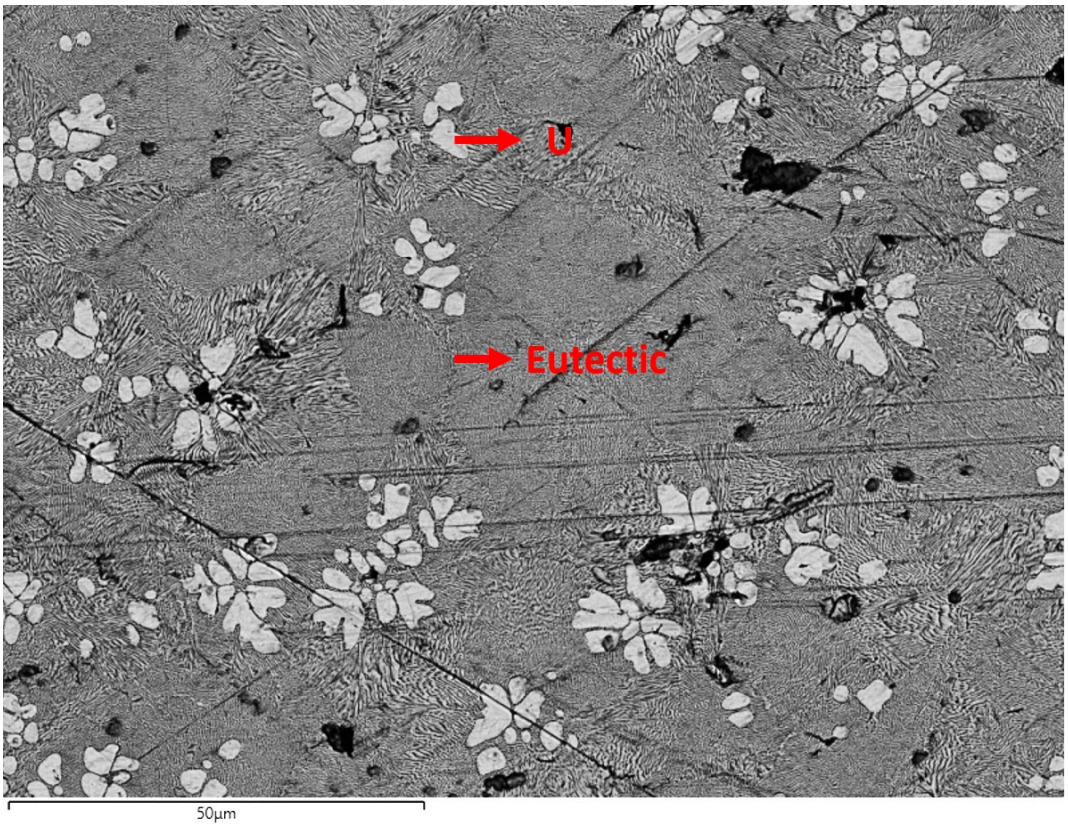

Figure V-5 SEM image in BSE mode of U77Cr23 sample (composition as 78.4% at. U by EDS).

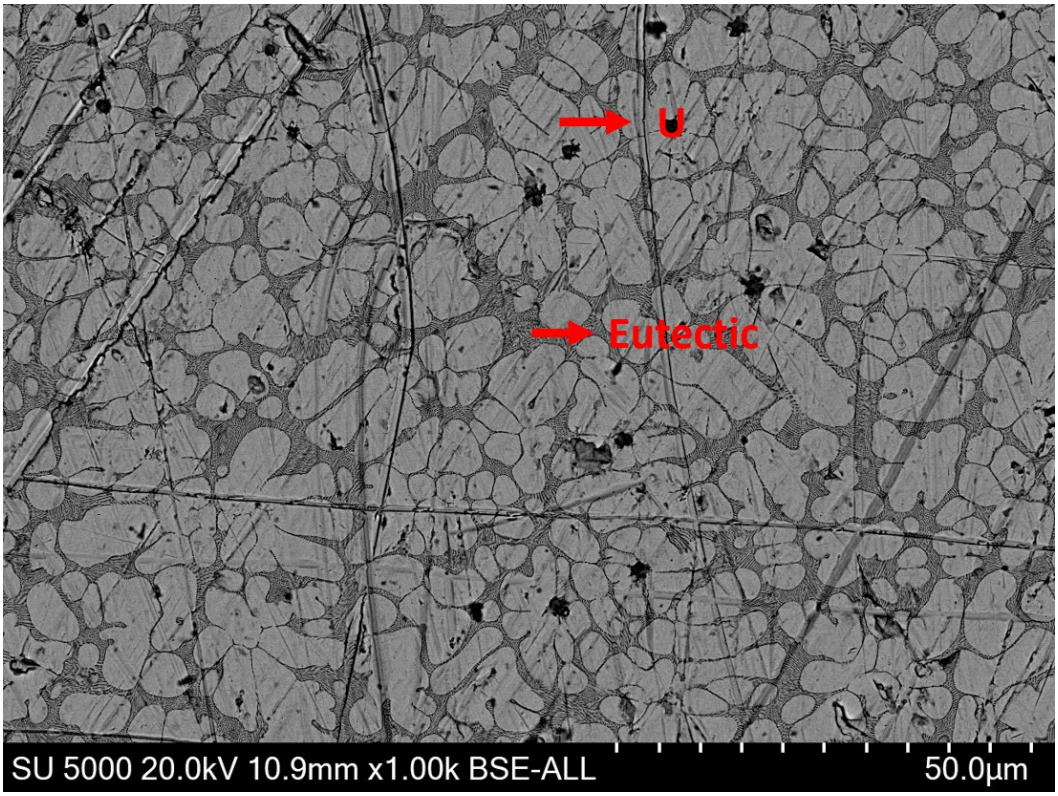

Figure V-6 SEM image in BSE mode of U86Cr14 sample (composition as 87.6% at. U by EDS).

The eutectic composition and the solubility of chromium in uranium at the eutectic temperature are respectively:

$$X_{Eutectic}(U) = 77.9 \pm 0.4\% \text{ at. U}$$

$$Sol(Cr)_{\gamma U} = 5.2 \pm 0.3\% \text{ at. Cr}$$

Regarding the fast cooling of these as-cast samples, these compositions are regarded as representative of the eutectic reaction. The measured eutectic composition is slightly lower than the published values. This measurement is consistent with the micrograph of Figure V-5 showing primary U dendrites, which is clear evidence of the hypereutectic character of the U77Cr23 (78.4% at. U measured by EDS) alloy. The solubility of chromium in uranium is consistent with previous experimental data within ±1% at., e.g. reported by Daane and Wilson [3] and very recently by Samanta and Yadav [14], around 4% at. Cr.

A sample with composition U95Cr5 was prepared by arc melting, and then wrapped in a W foil for annealing at 800°C for 10 days in a fused silica tube. After annealing, the tube was quenched in cold water.

Figure V-7 shows the micrographs collected with BSE and SE detectors. The overall composition amounts to 94.90% at. U. As shown in Figure V-7 a) and b), black dendrites are distributed randomly on a homogeneous grey matrix. A difficulty was found in measuring the compositions of these dendrites because of their narrow shapes and the intense disruption of the response of U around them. The dendrites were reasonably identified as Cr in regarding their shape, distribution and color under BSE, as Figure V-7 b). Besides, biphasic areas (Cr+U) were found in some intergranular areas, as shown in Figure V-7 c) and d). These areas were also too small/thin to realize accurate measurements of compositions.

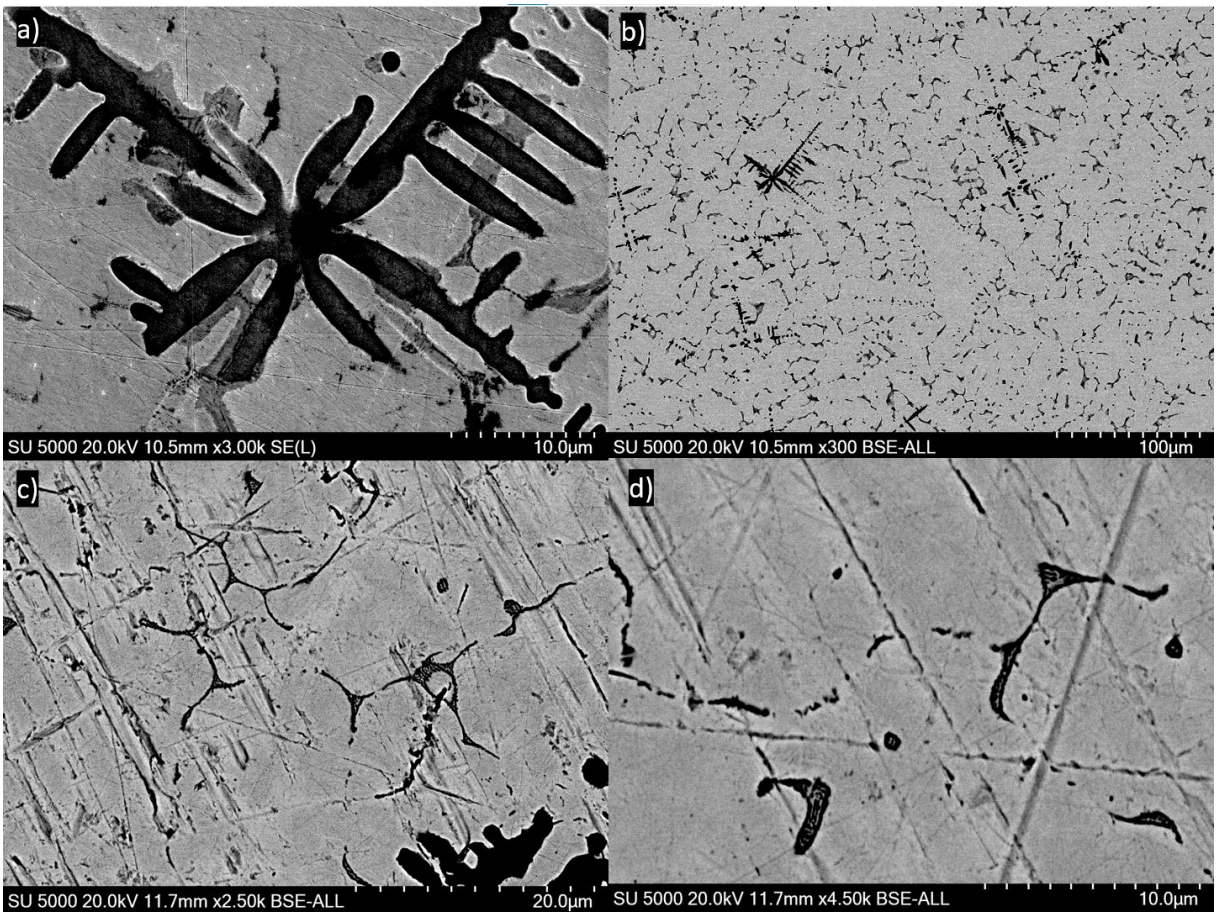

Figure V-7 Microstructure of annealing sample U95Cr5 (composition as 94.9% at. U by EDS)

EDS measurements of the U-based matrix (grey areas) were applied for more than 40 different locations giving an average value of 95.6±0.4% at. U. This composition is not significantly different from the overall composition measured.

No deviation of Cr compositions was determined near or far from the dendrite-like areas/biphasic intergranular areas. No oxidation of the sample was determined.

The composition measured as 95.6(0.4)% at. U is lower than the published phase diagrams (around 97.2% at. in Venkatraman *et al.* [1] and around 96.1% in Berche *et al.* [9]). It will be used as the lower boundary of the equilibrium $\mathrm{bcc\ Cr} + \gamma\mathrm{U} \rightleftharpoons \gamma\mathrm{U}$ at 800°C for the CALPHAD modeling.

DTA measurements were performed on the U86Cr14 sample (87.6% at. U by EDS) at the as-cast state (without any prior homogenization before the DTA experiment). The sample was heated from room temperature to 800°C under Ar, cooled to room temperature and reheated to 800°C at 5°C/min.

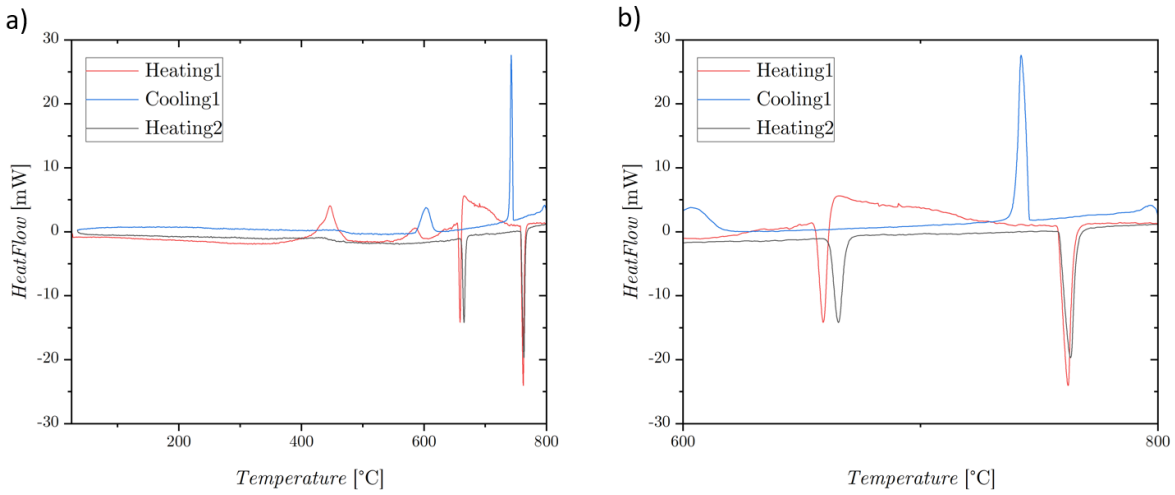

Figure V-8 DTA curves of sample U86Cr14 (87.6% at. U by EDS). a) complete view of the investigated temperature interval; b) zoomed view in the range 600-800°C. An exothermic effect is seen as an upward deflection from the baseline.

The DTA curves are shown in Figure V-8. In Figure V-8 a), Two exothermic peaks were found during the first heating (red line) at about 400 and 600°C. Two endothermic peaks are also seen on heating 1 and detected again during heating 2 as shown in Figure V-8 a). These two endothermic effects correspond fairly well to the two exothermic peaks detected during the first cooling (cooling 1 in Figure V-8 b). The onset temperatures of the peaks of these two reproducible thermal effects listed below in Table V-2 could be associated with the following reactions, according to the phase diagram:

$$T_{\alpha\rightleftharpoons\beta}^{U,Cr}: \alpha\ U + \text{bcc Cr} \rightleftharpoons \beta\ U$$

$$T_{\beta\rightleftharpoons\gamma}^{U,Cr}: \beta\ U + \text{bcc Cr} \rightleftharpoons \gamma U$$

Table V-2 Transition temperatures measured by DTA in sample U86Cr14.

Run	$T_{\alpha\rightleftharpoons\beta}^{U,Cr}$ / °C	$T_{\beta\rightleftharpoons\gamma}^{U,Cr}$ / °C
Heating1	655.4	757.8
Cooling1	617.2	746.0
Heating2	661.0	758.3

The temperature values measured on heating and cooling for the $T_{\beta\rightleftharpoons\gamma}^{U,Cr}$ transition was consistent. The slight difference between the two values should disappear for rates of temperature change of 0.001°C/s (0.06°C/min) according to Chapman [5].

For the $T_{\alpha\rightleftharpoons\beta}^{U,Cr}$ transition, the temperature measured on cooling (617°C) at 0.083°C/s (5°C/min) is ≈40°C lower than the value measured on heating (658±3°C). This experimental value on heating is in very good agreement with the dilatometric investigation of Chapman [5] (shown in Figure V-9 below) and the value on cooling is close to the result of Chapman at 0.001°C/s (617.6°C, read from the figure). From this figure, the equilibrium value of the transition temperature would be expected to lie in the range of 620-650°C and is estimated to be 630±10°C by Chapman.

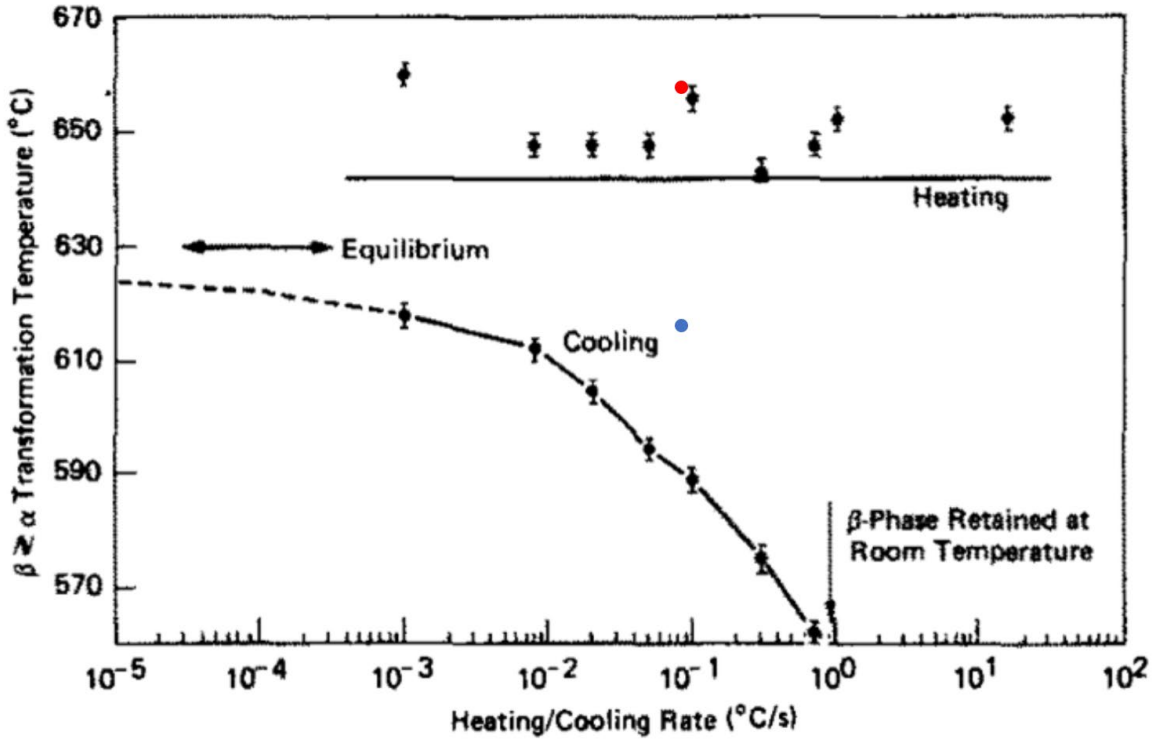

Figure V-9 The $T_{\alpha\rightleftharpoons\beta}^{U,Cr}$ temperatures measured in different heating or cooling rates by Chapman [5]. The red and blue points in the figure are our measurements of heating or cooling, respectively

These preliminary measurements can be reinforced with more DTA measurements at lower heating/cooling rates and calibrations of temperature with pure metals (U and Cr). More thermal cycles applied in each measurement would also help with the accuracy.

For the preliminary measurements obtained so far, a simple treatment of data was made by taking averages of values on heating. We have:

$$T_{\alpha\rightleftharpoons\beta}^{U,Cr} = 658.2 \pm 2.8°C$$

$$T_{\beta\rightleftharpoons\gamma}^{U,Cr} = 758.1 \pm 0.3°C$$

As reported in Table V-3, the temperature measured $T_{\alpha\rightleftharpoons\beta}^{U,Cr}$ is consistent with Provow and Pisher [6], but slightly higher than other reported values; the temperature $T_{\beta\rightleftharpoons\gamma}^{U,Cr}$ agrees with [2], [6], but slightly higher than [3], [5], [7], and lower than [4].

Table V-3 Reported transition temperatures $T_{\alpha\rightleftharpoons\beta}^{U,Cr}$ and $T_{\beta\rightleftharpoons\gamma}^{U,Cr}$ in the literature and the methods

Temperature β ⇌ γ		**Temperature α ⇌ β**		**Reference**	**Method**
°C	K	°C	K		
752±10	1025±10	640±10	913±10	Saller [2]	Metallography
737	1010	612	885	Daane [3]	XRD, metallography
765	1038	640	913	Badaeva [4]	DTA, metallography
756±2	1029±2	652±2	925±2	Provow [6]	Resistivity
739	1012	638	911	Townsend [7]	DTA, metallography
738±2	1011±2	630±10	903±10	Chapman [5]	Dilatometry
745	1018	640	913	Terekhov [8]	DTA
745±2	1018±2	647±2	920±2	Samanta [14]	DSC
738±10	1011±10	630±10	903±10	Venkatraman [1]	Assessment
739	1012	637	912	Berche [9]	CALPHAD
758	1031	658	931	This work	DTA

V.2.3 CALPHAD modeling

The binary system U-Cr has been reassessed by the CALPHAD method based on our experimental work and a selection of the data previously published.

Five phases are modeled: Liquid, Bcc_A2 (for both bcc Cr and γU), Tetragonal_U (for βU), and Orthorhombic_A20 (for αU).

All the phases were defined with a single sublattice (Cr, U), as in the work of Berche *et al*. [9].

The optimization was carried out considering mainly the experimental results of [3], [4], [7] that are gathered in Table V-4. Lattice stabilities were taken from the SGTE database [15].

Table V-4 Experimental data of invariant reactions imported in the modeling

Reaction	Temperature/°C	Reference	Compositions/at. U	Reference
$L = bcc\ Cr + \gamma U$	860±10	[1]	77.9/0/94.8	This work
$\gamma U = bcc\ Cr + \beta U$	758.1±0.3	This work	98.4/0/99	[4]
$\beta U = bcc\ Cr + \alpha U$	658.2±2.8	This work	99.1/0/100	[4]

The assessment started with the equilibrium of the liquid phase and Bcc_A2 by optimizing the eutectic reaction $L = bcc\ Cr + \gamma U$. The interaction parameters of the liquid phase and Bcc_A2 phase were then assessed. The DTA-measured eutectoid temperatures were considered to optimize the interaction parameters of the Tetragonal_U phase. The estimated enthalpy of transition $\beta U \rightleftharpoons \gamma U$ of Berche *et al.* [9] (13200 J/mol) was accepted in the modeling. The assessed parameters are listed in Table V-5. Other parameters were taken from the SGTE database [15].

Table V-5 Assessed parameters in this work for the CALPHAD modeling of the U-Cr system

Phase	Parameters
Liquid	$L^0_{Cr,U} = 10500 - 4 * T$ $L^1_{Cr,U} = 9000 - 4 * T$ $L^2_{Cr,U} = 4000$
Bcc_A2	$L^0_{Cr,U} = 62000$ $L^1_{Cr,U} = 38000$
Tetragonal_U	$G_{\beta U} - G_{BCC} = 13200$ $L^0_{Cr,U} = 19000$

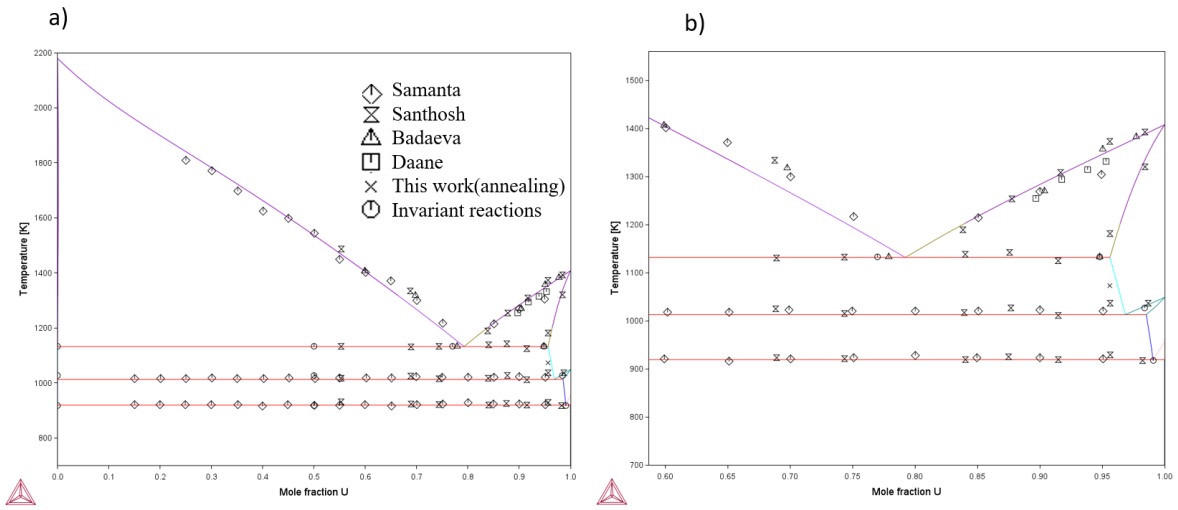

Figure V-10 Assessed phase diagram of the U-Cr binary system in this work. a) Global view; b) Zoomed diagram in the U-rich side.

The assessed phase diagram is shown in Figure V-10 a). A good overall agreement has been obtained with experimental data. An enlarged partial section of the diagram in Figure V-10 b) compares equilibrium lines and experimental data.

Our modeling fits well our new measurements and, by considering the new experimental measurements recently published by Samanta and Yadav [14] and Santhosh *et al.* [12], is more accurate in the description of the liquidus line U-rich part. Compared to the description of Berche *et al.* [9], more interaction parameters are used for the liquid phase to better fit the data points.

V.3 Literature review of ternary system U-Cr-O

V.3.1 U-O binary system

Among the three sub-systems of the U-Cr-O ternary system, the U-Cr and Cr-O have been discussed yet. The U-O system will be presented briefly.

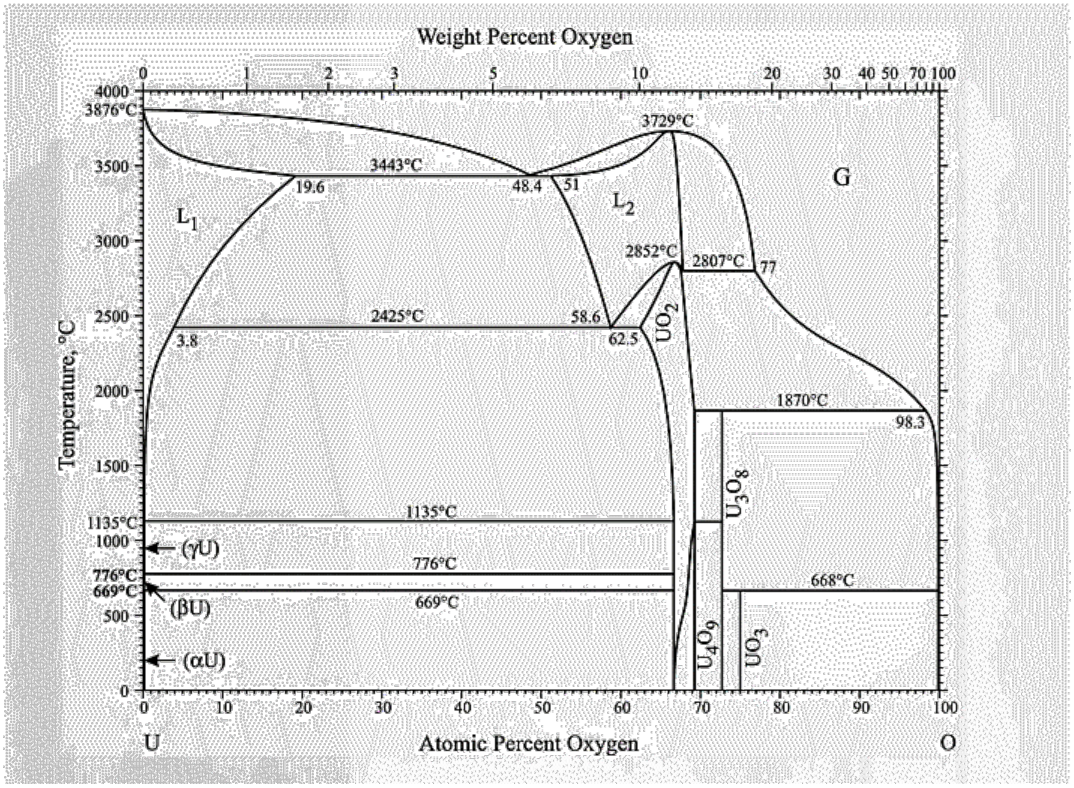

Figure V-11 Assessed phase diagram of the U-O system [16]

The system U-O has drawn great attention for its significance in understanding the behavior of nuclear fuel [17] including modeling.

In some early compilations (Levin *et al.* [18] and Roth *et al.* [19]), different versions of the phase diagrams manually assessed have been reported. The stoichiometric substances and phases reported in these phase diagrams are inherited till today, i.e. liquid, UO_2, U_4O_{9-y}, U_3O_{8-z}, UO_3, $U_5O_{13\pm x}$, U_8O_{21}, $UO_{2.61}$, α-U(Orthorhombic), β-U(Tetragonal) and γ-U(Bcc). The system is complex with several intermediate compounds and a quite large domain of non-stoichiometry around the UO_2 composition.

Two main CALPHAD models of this system are available today, the first one by Guéneau *et al.* [20] and the second one by Chevalier *et al.* [16]. The phase diagram calculated by Chevalier

et al. [16] and illustrated in Figure V-11 will be considered here, taking into account the fact it is integrated into the NUCLEA database. The presented version in this Figure was published after the improvement of their early works [21], [22]. Very numerous data on thermodynamic properties, both experimental data and simulations, were considered into the modeling of 4 selected oxides UO_2, U_4O_9, U_3O_8 and UO_3. The assessments of data were detailed in [22]. The thermodynamic description of pure condensed phases of uranium was taken from the SGTE database [15]. The liquid phase was modeled with a non-ideal associate model.

The main incoherency initially found in the experimental data was the solubility limit of oxygen in liquid uranium, between the temperature of the eutectic reaction $L_1 \rightleftharpoons UO_2 + \gamma U$ and the temperature of the monotectic reaction $L_2 \rightleftharpoons UO_2 + L_1$. Two possible values of the solubility limit were reported in the literature, which affected both the liquidus temperature of U-rich compositions and the extension of the liquid miscibility gap. However, it was difficult at that time to tell which reported value was better. Therefore, two different sets of parameters were initially published [21] corresponding to a small or higher oxygen solubility of oxygen in liquid uranium. A small solubility of oxygen in liquid uranium (and hence a wide liquid miscibility gap) was finally chosen in agreement with new experimental results obtained by Gueneau *et al*. [23] and Maurizi *et al.* [24].

The modeling allows a good reproduction of the thermodynamic properties of UO_{2+x} solid solution and also has a good consistency in phase equilibria and oxygen potential with published experimental data. The work has also been used for an extension to the ternary system U-Zr-O, which is the key system for severe accident comprehension for core degradation.

V.3.2 U-Cr-O ternary system

Although there is no phase diagram for the Cr-U-O system as such, mixed phases have been identified by various authors. A significant number of studies devoted to the U-Cr-O ternary system were mainly focused on the characterization of ternary compounds, namely, $UCrO_4$ identified by Felten *et al.* [25] obtained by mixing between UO_2 and Cr_2O_3 and annealing the mixture between 1200 and 1600°C under air. Cr_2UO_6 is assumed to be stable in air until at least 950°C [26] and CrU_3O_{10-x}, is stable below 700°C under air [27]. The only isothermal ternary section was reported by Yamanaka *et al.* [28], [29] at 1000°C.

V.3.2.1 Ternary phase diagram

The 1000°C isothermal section was investigated by Yamanaka *et al.* [28], [29]. The phase relations were based on powder X-ray diffraction collected for samples annealed at 1000°C for a period of 10 to 200h under a vacuum. The isothermal section is shown in Figure V-12. The existence of a binary liquid phase containing only uranium and chromium was confirmed.

The three ternary compounds $UCrO_4$, UCr_2O_6 and CrU_3O_{10-x} did not appear in the section and no thermodynamic data were discussed in this experimental assessment. Doubts about the correctness of the phase relations have been expressed [30].

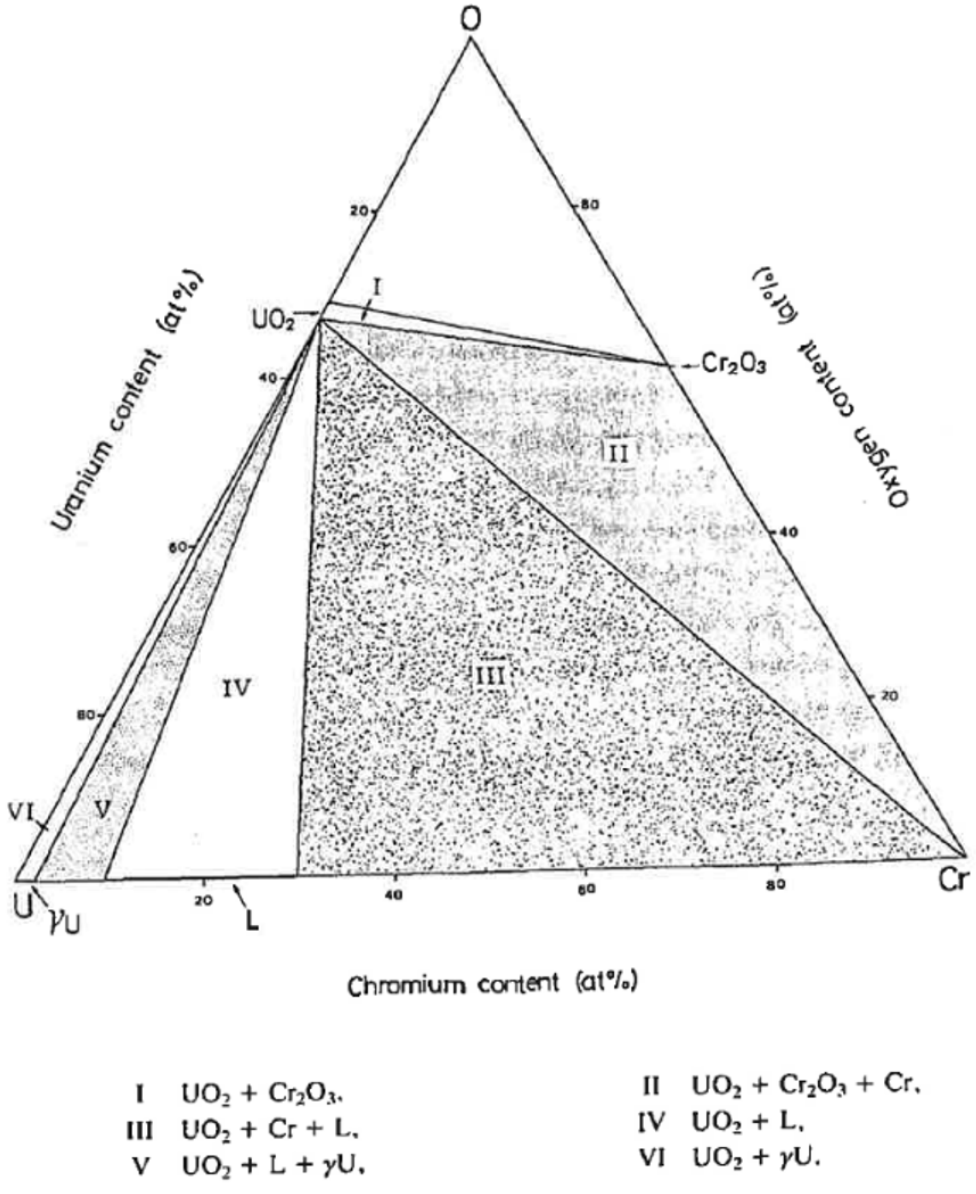

Figure V-12 Experimental isothermal section of U-Cr-O ternary system at 1000°C by Yamanaka *et al.* [29]

V.3.2.2 $UCrO_4$ ternary phase

In the early study of Borchardt [31], the reactions of uranium oxides, such as U_3O_8 and UO_2 with Cr/Cr_2O_3 were investigated. It was found that Cr reduces U_3O_8 rapidly below 1000°C. No reaction occurred after heating a UO_2+Cr_2O_3 mixture for 2h at 1000°C under argon. Meanwhile, a new phase was formed by the reaction between U_3O_8 and Cr_2O_3 under the same conditions. X-ray diffraction peaks were reported in the article but the composition was only given approximatively as $UCrO_x$.

Bacmann *et al.* [32] obtained the phase by heating a pellet with appropriate amounts of UO_2 and Cr_2O_3 at 1200°C in air. The phase formed was confirmed as $UCrO_4$, determined as an orthorhombic structure with the $BiVO_4$-type with lattice parameters at room temperature equal to a=4.87(1) b=11.78(7) c=5.05(3). The result was consistent with Borchardt [31], Felten *et al.* [25] and Smith *et al.* [33].

Hoekstra *et al.* [34] performed a study of uranium oxides with multiple transition elements. By mixing ground U_3O_8 and Cr powders in air, the $UCrO_4$ phase was obtained after heating for a day at 1000°C to 1100°C. The phase was reconfirmed as an orthorhombic structure with a *Pbcn* (#66) group space and the $BiVO_4$ type.

Sampath *et al.* [27] found that $UCrO_4$ decomposes under vacuum or hydrogen above 1000°C to a mixture of Cr_2O_3 and UO_2.

The $UCrO_4$ phase was determined as a collinear antiferromagnetic compound by Wolfers *et al.* [28]. Greenblatt *et al.* [36] reported the Neel temperature of 44.5K.

Guo *et al.* [37] measured the enthalpy of the formation of $UCrO_4$ by calorimetry as $-1824.6 \pm 4.5\ \mathrm{kJ/mol}$. This value is obtained from measurements realized on $UCrO_4$ samples, related binary oxides Cr_2O_3, UO_2 and γ-UO_3 in molten $3Na_2O{\cdot}4MoO_3$ at 802°C (the enthalpy of formation of $UCrO_4$ from the oxides is $-33.4 \pm 1.3\ \mathrm{kJ/mol}$ at 298.15 K). The corresponding DFT calculation from the oxides was also realized and gave a value less exothermic, -29.9 $\mathrm{kJ/mol}$.

V.3.2.3 Ternary phase Cr_2UO_6

Hoekstra and Siegel [26] reported the Cr_2UO_6 phase that was synthesized by hydrothermal methods by the reaction of uranium trioxide with chromium (III) nitrate solution at 325–425°C. The composition of the phase was confirmed by dissolving the oxide in an HCl-$HClO_4$ mixture.

The X-ray diffraction analysis yields indexation in the $P\bar{3}1m$ hexagonal space group with lattice parameters a=4.988(1) Å, c=4.620(1) Å, compatible with the $PbSb_2O_6$ type. A DTA measurement showed that the phase decomposed between 950°C to 1050°C, following the reaction (V-1):

$$\mathbf{4Cr_2UO_6 \rightarrow 2Cr_2O_3 + 4UCrO_4 + O_2} \quad \text{(V-1)}$$

V.3.2.4 CrU_3O_{10-x} ternary phase

Sampath *et al.* [27] studied the ternary system by co-precipitating mixtures of chromium (III) hydroxide and ammonium diuranate (ADU) powders that were heat-treated in air, vacuum and under hydrogen in the temperature range of 500-1600°C. The uranium to chromium ratio was set in the range of 3:1 to 1:6. Mixture of powders with a ratio of 1:3 heated at 700°C in the air formed the new phase. The product was examined by XRD showing a hexagonal symmetry with lattice parameters a=7.835 Å, c=16.575 Å and a density of 4.8g/cm^3. The phase starts to decompose at 700°C by slowly losing oxygen. The x value in CrU_3O_{10-x} was calculated on weight loss of its final decomposition at 1000°C as reaction (V-2), and found as ~0.3.

$$\mathbf{4CrU_3O_{10-x} \rightarrow UCrO_4 + U_3O_8} \quad \text{(V-2)}$$

V.3.2.5 Cr_2O_3 doped UO_2 fuel

Leenaers *et al.* [38] worked on the solubility limit of Cr_2O_3 in UO_2 under different sintering conditions. The samples were sintered at 1600, 1660, and 1760°C under fixed oxygen potential, and then examined by XRD and EPMA. As a result, the solubility limits of Cr in UO_2 were found as 0.065±0.002, 0.086±0.003 and 0.102±0.004 % wt. Cr at 1600, 1660, and 1760°C, respectively. The effect on crystal structures related to these solubilities was linear to the lattice parameters, corresponding to a true solid solution. However, the results were not sufficiently conclusive to determine if the solid solution was substitutional or interstitial.

Riglet-Martial *et al.* [39] published a study of the Cr_2O_3-doped fuel with a discussion about the solubility and speciation analysis of Cr, CrO and Cr_2O_3 in UO_2 at different temperatures and oxygen potential conditions. A thermodynamic model of solubilities was established with this experimental work and reliable data from the literature. It was determined that the temperature and oxygen potential were the only two main factors that influenced the solubility. In all

sintering conditions, the metallic chromium Cr and oxidized chromium CrO, and Cr_2O_3 solubilities in UO_2 were always in a single soluble chemical form of $CrO_{3/2}$ where the degree of oxidation of Cr was +3.

Peres *et al.* [40] studied chromium volatilization from Cr_2O_3 and Cr_2O_3-doped UO_2 at high temperatures with DTA and thermogravimetry experiments. The mass loss during a linear temperature increase to 1700°C was mainly caused by the dissociation of Cr_2O_3 into metallic Cr gas and O_2; liquid CrO depending on the atmosphere composition. The volatilization process of Cr_2O_3 doped UO_2 is the result of different processes (1) decomposition of non-solubilized Cr_2O_3; (2) volatilization of Cr solubilized in UO_2 before the porosity closure; (3) volatilization of Cr solubilized in UO_2 ceramic matrix after the porosity closure.

Smith *et al.* [41] studied the fundamental chemistry of Cr_2O_3-doped UO_2 fuel ($Cr^{(3+)}{}_2O_3$–doped $U^{(4+)}O_2$) with multiple advanced spectroscopy methods. Cr^{2+} directly substitutes for U^{4+}, compensated with U^{5+} and oxygen vacancy. A mixed $Cr^{2+/3+}$ oxidation state with more than one physical form of Cr was found in the heat-treated sample.

Milena-Pérez *et al.* [42] studied the oxidation of Cr_2O_3-doped UO_2 with thermal treatments ranging from room temperature to 700°C under oxygen partial pressure 1% and 21%. The results showed no effect under 21% oxygen composition (air), but a reduction of oxidation degree under 1% oxygen partial pressure.

V.4 Objective of the study and methodology

To date, the ternary phase equilibria in the U-Cr-O system are still poorly described.

The objectives of the study focus on two main points:

1) To establish phase relations for temperatures above 1000°C using a classical approach coupling DRX and SEM-EDS analyses.
2) To measure the heat capacity of pure $UCrO_4$ samples in the low-temperature range from 2 K to room temperature using semi adiabatic relaxation method.

V.5 Results and discussions

V.5.1 Sample preparation and phase-equilibrium

U-Cr-O samples were prepared from U and Cr pieces and UO_2 and Cr_2O_3 powders. The UO_2 powder was obtained by reducing U_3O_8 under a stable flow of Ar/H_2 gas. The purity and oxygen sub-stoichiometry were deduced from powder XRD.

Four as-cast samples were prepared, with composition within different zones from II to V of the phase diagram of Yamanaka *et al.* [29]. The samples are denoted U10Cr50O40, U40Cr30O30, U55Cr10O35 and U75Cr5O20 according to their target compositions in at. %. Some oxide-rich samples were difficult to melt and the mass loss resulting from Cr/Cr_2O_3 vaporization was determined after arc melting. The samples were then annealed at 1000°C for 6h under high-purity Ar gas. No significant mass loss was determined before and after annealing.

Table V-6 shows a comparison of the UO_2 lattice parameter as well as the phase composition determined by Rietveld refinement for the three samples that could be crushed into powder. The fluorite lattice parameters fall into the range of stoichiometric UO_2, (Barrett *et al.* [43]) (Leinders *et al.* [44]). and Cr-doped UO_2. (In comparison, Cordara *et al.* [45] reported a=5.4772(6)Å with 1200ppm of dopant)

Table V-6 Phase fractions in U-Cr-O samples determined by XRD.

Sample/% at.	**Zone***	**XRD phase fractions****				**Lattice of UO_2/Å**
		Cr	Cr_2O_3	UO_2	α-U	
U10Cr50O40	II	24.83(0.27)	32.48(0.38)	42.69(0.25)		5.468(1)
U40Cr30O30	III	4.54(1.23)		91.86(1.93)	3.60(0.22)	5.471(1)
U55Cr10O35	IV			92.99(0.44)	7.01(0.26)	5.471(1)
U75Cr5O20***	V					

* According to the notation of Yamanaka *et al.* [28], [29]

** Results in % wt. Errors are shown in brackets.

*** Sample U75Cr5O20 is ductile and could not be grounded for subsequent powder XRD analysis.

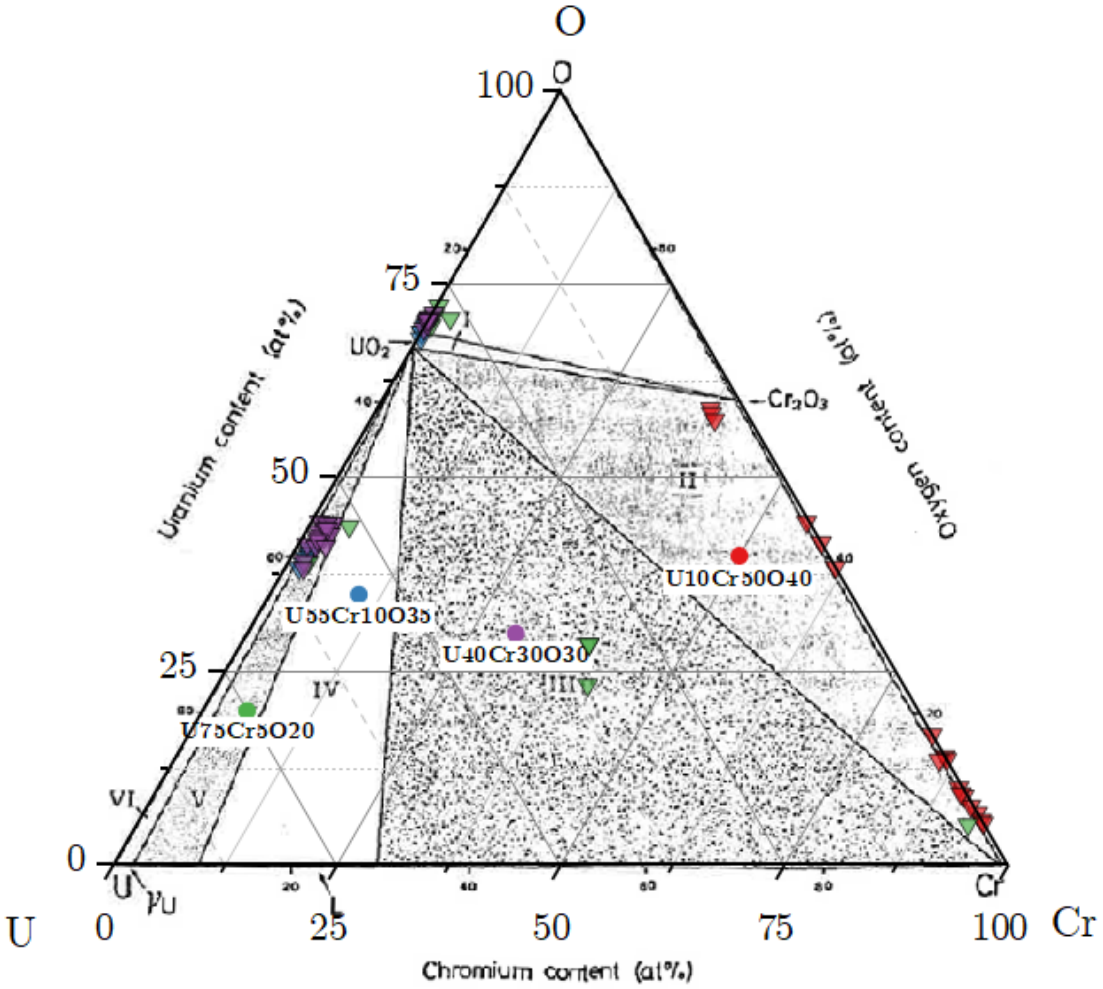

Figure V-13 Prepared samples and EDS measured compositions (%at.) in different areas of each sample reported in the phase diagram of Yamanaka *et al.* [28]. In the figure, dots are prepared compositions of each sample and triangles are measurements by EDS. Symbols with the same color are for the same sample.

Figure V-13 shows the superimposition of the target composition and EDS analyses in the ternary phase diagram of Yamanaka *et al.* [19]. The figure includes 17 measured points of U10Cr50O40, 24 measured points of U40Cr30O30, 9 measured points of U55Cr10O35, and 11 measured points of U75Cr5O20.

Because of the macro-segregated state of the samples, it was difficult to obtain representative overall compositions. The situations were similar for all the ternary samples prepared.

Analysis of these results will be presented in the next sub-sections.

V.5.1.1 U10Cr50O40

The SEM micrographs are displayed in Figure V-14, the sample exhibits two regions of different compositions separated by a clear front plane. Spherules of the darker zone extend into the two-phase eutectic zone on the right of the image. It indicates that the two regions have been formed by liquid-liquid phase separation, confirming the full melting of the sample

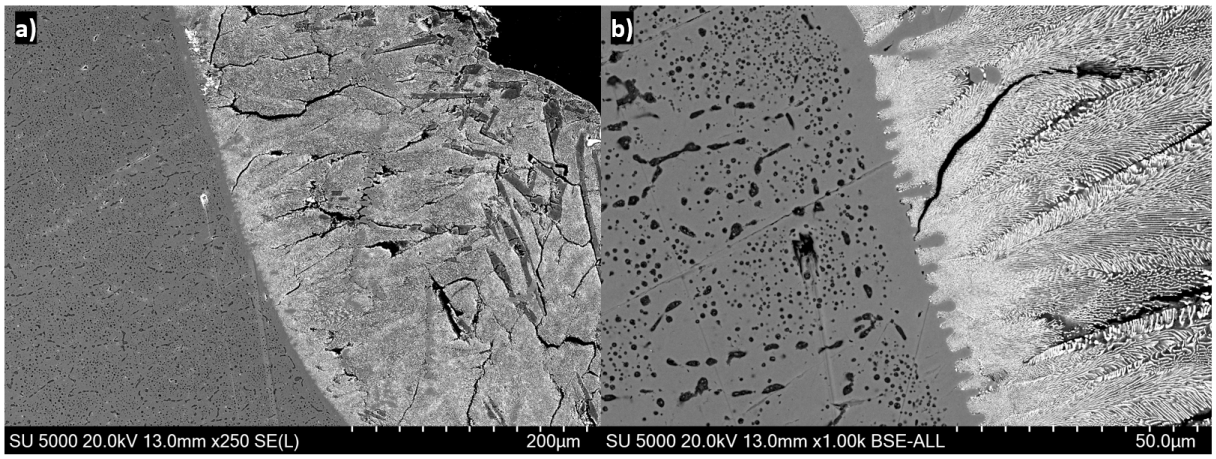

Figure V-14 SEM-BSE micrograph of sample U10Cr50040. a) magnification x250; b) magnification x1000

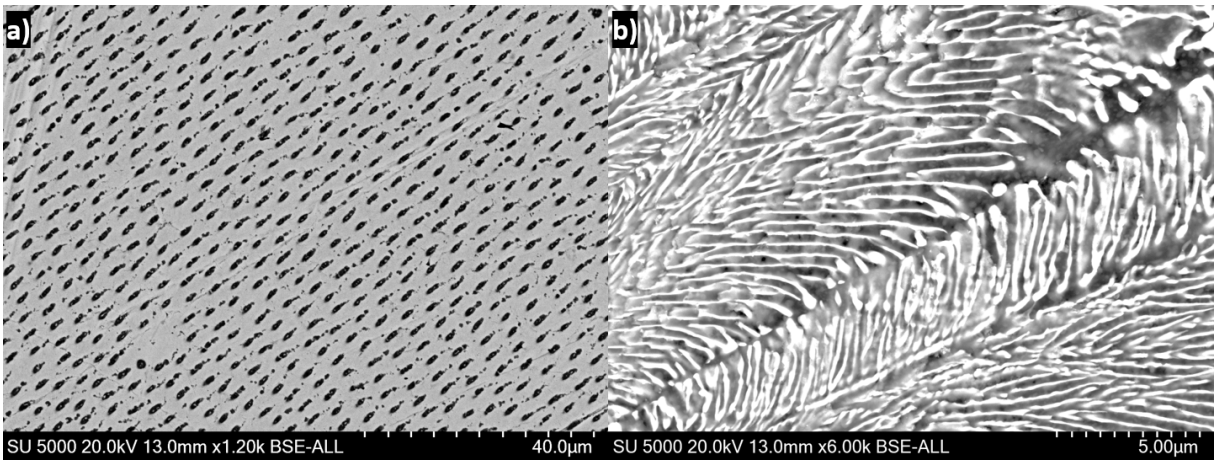

Figure V-15 Detailed view of the two separated regions of sample U10Cr50O40

The two regions of the sample are shown in Figure V-15 at higher magnification.

The region seen on the left of the micrograph of Figure V-14, is shown in Figure V-15 a) and is Cr-rich. The black spots seen on the surface in BSE mode were confirmed to be holes by the

SE detector. Shapes of these holes are more ellipsoidal on the outside of the sample and become more spherical when approaching the front between the two regions.

The change in the shape of the bubbles correlates with the decrease in the cooling rate from the surface to the core of the ingot.

The homogeneous grey area of Figure V-15a) was measured by EDS and a composition of Cr 94.3% at., O 5.7% at. on average. The oxygen compositions measured correspond to systematic error enhanced by the presence of holes. Since no solubility of O in Cr was reported the grey area is considered to be solid Cr.

Figure V-15 b) is the ceramic-like region of the sample. The sample showed a eutectic structure. EDS measurements in large zones were performed yielding overall composition U 3.9% at., O 58.3% at., Cr 37.8% at. on average. It likely indicates the presence of a eutectic composition between UO_2 and Cr_2O_3 phases.

V.5.1.2 U40Cr30O30

The sample U40Cr30O30 is in zone III of the phase diagram of Yamanaka *et al.*

A SEM image of the microstructure of this sample is shown in Figure V-16. As for the U10Cr50O40 sample, the structure was formed by liquid-liquid phase separation. The sample can be divided into a ceramic-like gangue (dark area on the left of the image) and a metallic kernel (grey area on the right of the image). The presence of the spherical ceramic in the metallic part demonstrates that the whole sample was fully melted, including the oxides.

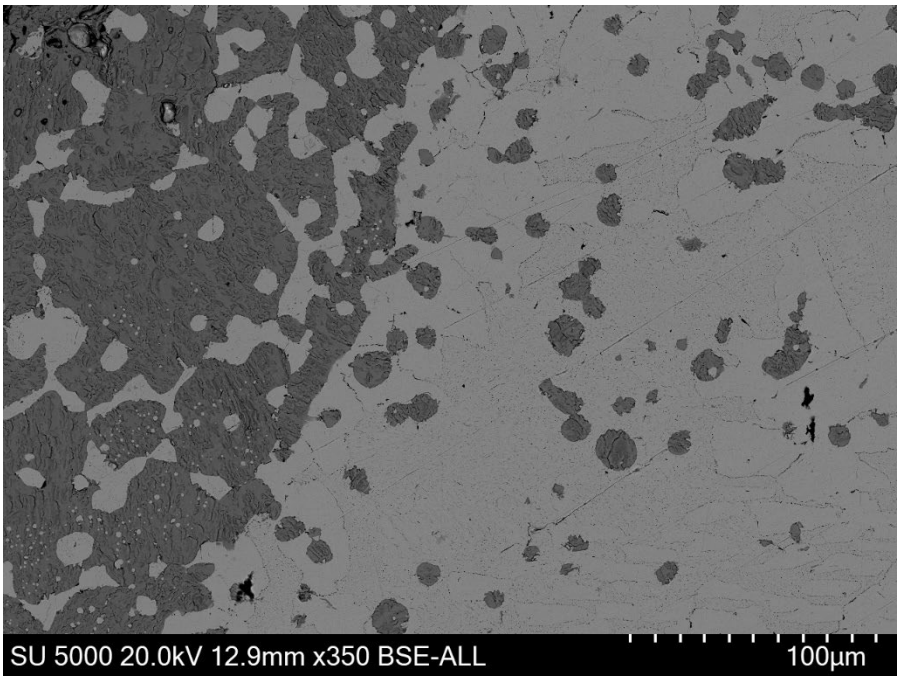

Figure V-16 SEM-BSE micrograph of sample U40Cr30O30

Figure V-17 shows images of (a) the gangue and (b) the kernel taken at a lower magnification. Two different compositions were measured by EDS: U57.5O39.6Cr2.9 (light grey precipitations) and U29.6O70.4Cr0.1 (dark grey background). The same compositions were determined in the light grey and dark grey areas in Figure V-17 b), respectively.

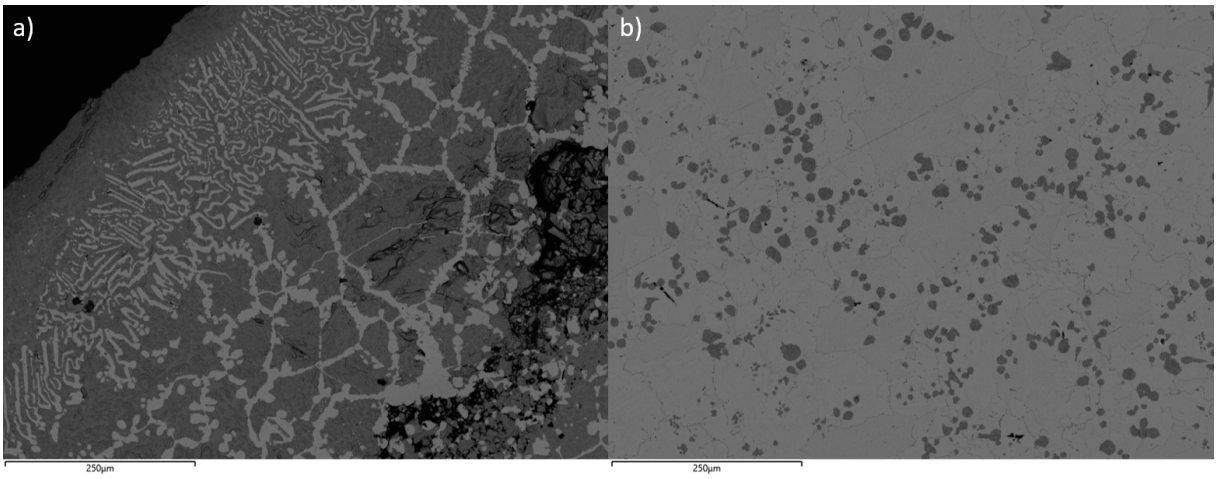

Figure V-17 SEM-BSE images in two regions of sample U40Cr30O30

V.5.1.3 U55Cr10O35

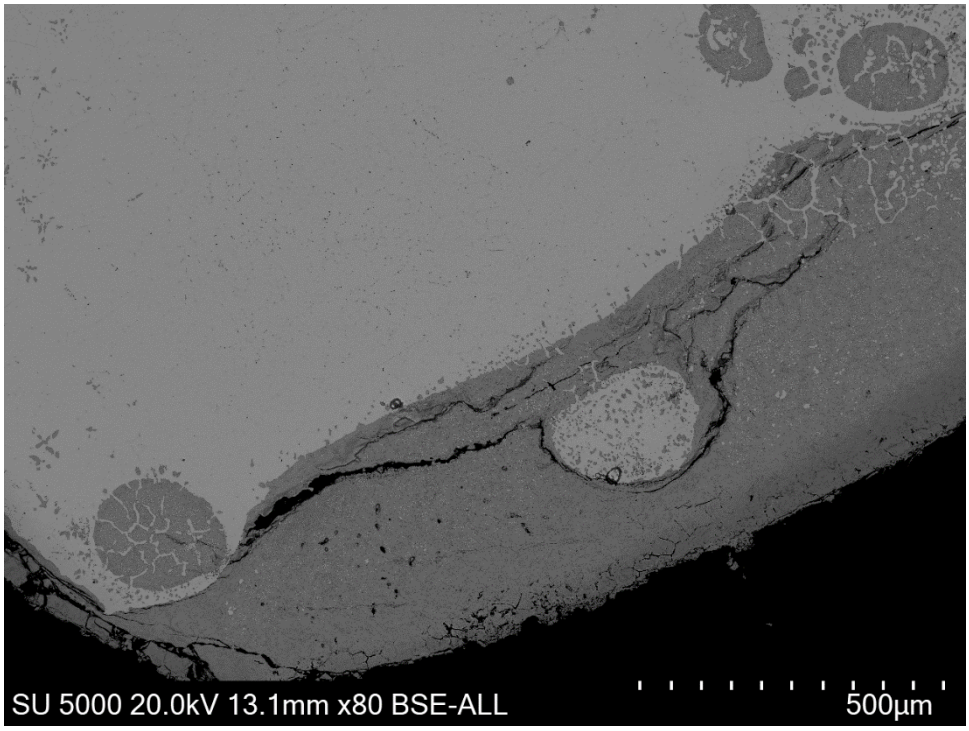

Figure V-18 SEM-BSE images of sample U55Cr10O35

The liquid demixing was also found in this sample with a clear frontier. As shown in Figure V-18, the light grey metallic kernel above and dark grey gangue below are illustrated. Several spherules of one phase were retained in the other phase during demixing. The difference in thermomechanical properties results in a lot of cracks. The compositions were measured for the light and dark grey areas by EDS: In the light grey areas, it was measured as U59.2O39.0Cr1.8 and in the dark grey areas, it was found as U30.0O69.9Cr0.1

V.5.1.4 U75Cr5O25

The sample U75Cr5O25 was prepared in zone V. The ductility of this sample makes it impossible to grind it. Therefore, the sample was only examined by SEM-EDS. An image of the sample surface is shown below in Figure V-19.

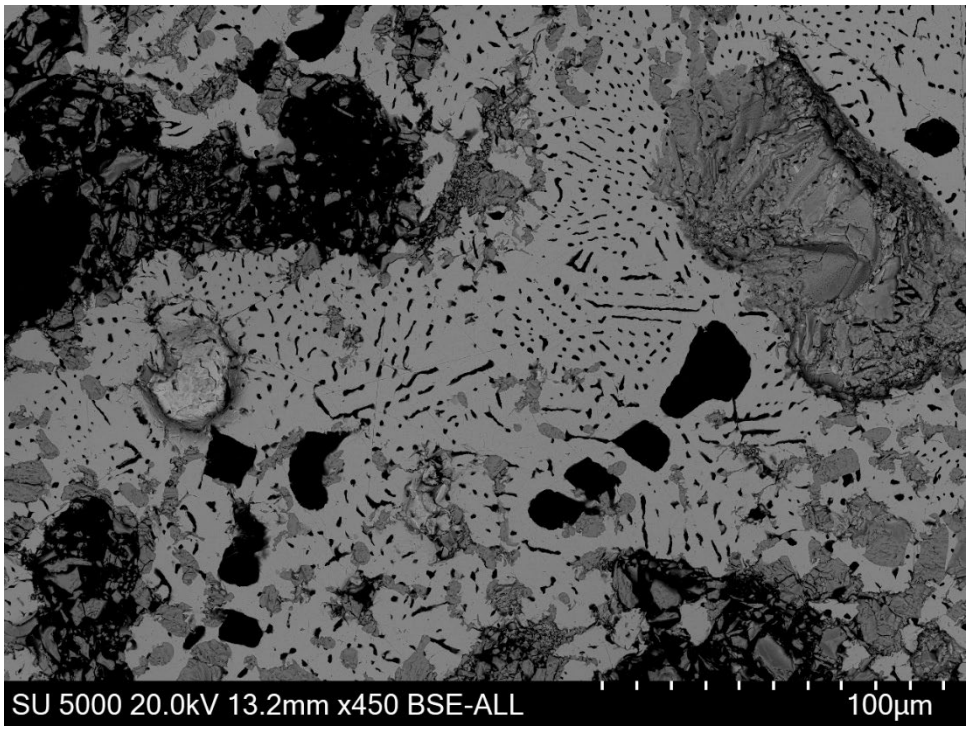

Figure V-19 SEM-BSE image of sample U75Cr5O25

In Figure V-19, black areas were determined as holes by observing the surface in SE mode. Light grey areas were homogeneous, measured with a composition of U58.6O39.1Cr2.3; dark grey areas showed a composition of U28.6O70.9Cr0.4.

The liquid phase demixing that occurred in this sample did not with a clear dividing line as the previous ones. In this sample, the majority of the volume was occupied by one type of liquid (as the light grey area in the figure) with a limited volume of another liquid distributed inside (as the dark grey areas in the figure). The surface of the dark grey phase was rougher than that of the light grey phase after polishing because the hardness of the dark grey phase was significantly lower than the other one.

V.5.1.5 Summary

The four samples prepared U10Cr50O40, U40Cr30O30, U55Cr10O35, and U75Cr5O20 all showed separated zones with ceramic and metallic parts resulting from liquid demixing. Clear frontiers were visible in samples U10Cr50O40 and U55Cr10O35. A separation of ceramic gangue and metallic kernel was found in samples U40Cr30O30 and U55Cr10O35.

The sample U10Cr50O40 has demixed into a metallic Cr phase and a eutectic phase with a global composition U3.9Cr37.8O58.3, supposed to be a eutectic mixture of UO_2 and Cr_2O_3.

For other samples, similar compositions of ceramic and metallic parts were measured with:

-an area with an average composition of U59O40Cr1 for the metallic zone. With this composition, the area is not supposed to be monophasic, but more likely biphasic as a mixture of ($U+UO_2$). This assumption also corresponds to the XRD results of samples U40Cr30O30 and U55Cr10O35.

-an area with an average of U29.5O70Cr0.5 for the ceramic zone. Regarding the low content of Cr and the U to O ratio, this ceramic phase is considered mainly composed of a crystallized fluorite phase. The examination of the lattice parameters refined for the 3 samples suggested that it corresponds to UO_2.

No Cr-rich phase was found in samples U40Cr30O30, U55Cr10O35 and U75Cr5O20. For samples U55Cr10O35 and U75Cr5O20, a small quantity of Cr should be contained in U and UO_2, but the composition was underestimated (misidentified as oxygen) as EDS is less accurate in identifying Cr and O. This assumption also corresponds to the XRD result of sample U55Cr10O35, as only UO_2 and U was identified.

For sample U40Cr30O30, 4.54(1.23)% at. of Cr was also identified in it by XRD. It's reasonable to suppose that the bcc Cr phase exists in some very limited area and volume of the sample, which was presented in the XRD powder of this sample, but not presented on the polished surface of SEM.

More studies at high temperatures should be performed to determine the liquid characteristics and the accurate liquid regions in the system.

From a general thermodynamic point of view, it is possible to anticipate a rather large miscibility gap between the oxide and metallic liquid phases considering the large miscibility gaps at high temperatures in both U-O and Cr-O systems.

V.5.2 Ternary phase $UCrO_4$

$UCrO_4$ samples were prepared by annealing pellets of UO_2 and Cr_2O_3 powder mixtures under air at 1200°C for 6h, following the procedure of Bacmann and Lewy-Bertaut [46].

The purity of $UCrO_4$ samples was examined by XRD (Figure V-20). The purity of the sample was determined by the Rietveld method as 96.63 ± 0.91% wt. with 3.37 ± 0.23% wt. of U_3O_8 (98.55±0.93% at. with 1.45±0.10% at. of U_3O_8).

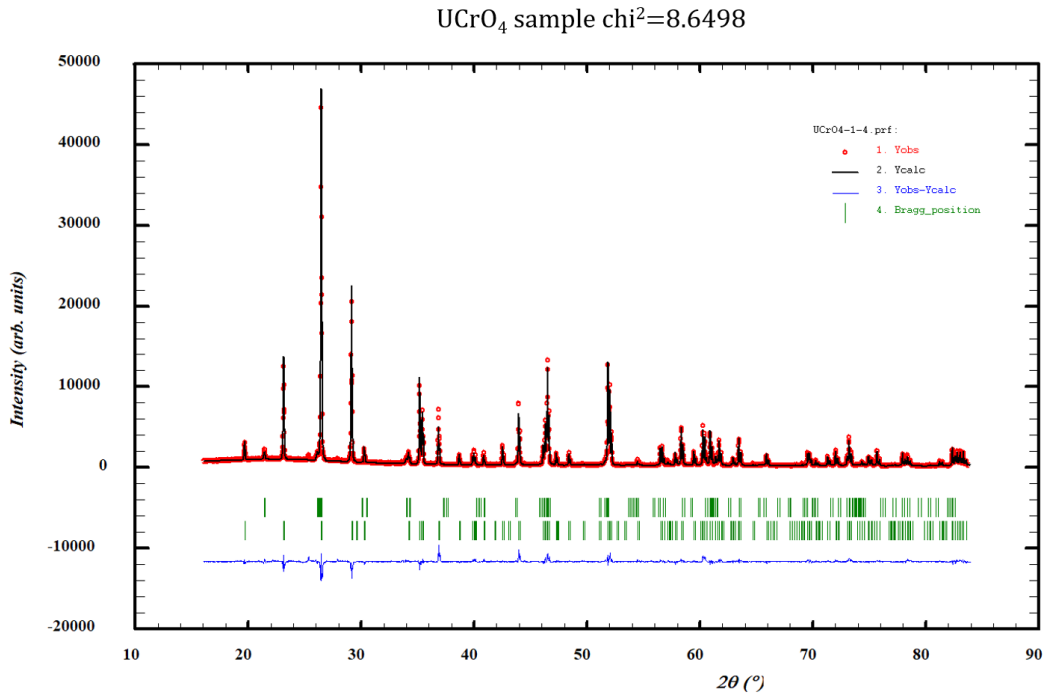

Figure V-20 XRD pattern of $UCrO_4$ sample

The $UCrO_4$ phase has an orthorhombic symmetry with the *Pbcn* space group. Lattice parameters are a=4.875 (1), b=11.801 (1) and c=5.062 (1) which are consistent with the reported values of the literature [32], [46].

The atomic positions, site occupations and multiplicities are listed below (Table V-7). The results are consistent with the published data [32]. In a unit cell of the $UCrO_4$ phase, U and Cr atoms are localized on 4c Wyckoff positions and the two independent O atoms per asymmetric unit are on 8d Wyckoff positions. The atomic coordinates are given in Table V-5.

Table V-7 Atomic parameters fitted of $UCrO_4$ sample

Name	**Wyckoff position**	**x**	**y**	**z**
U1	4c	0	0.166 (1)	0.25
Cr1	4c	0	0.436(1)	0.25
O1	8d	0.7678(3)	0.451 (1)	0.553(3)
O2	8d	0.781(3)	0.316(1)	0.107(3)

The C_p at low temperatures was measured by the semi-adiabatic method (PPMS).

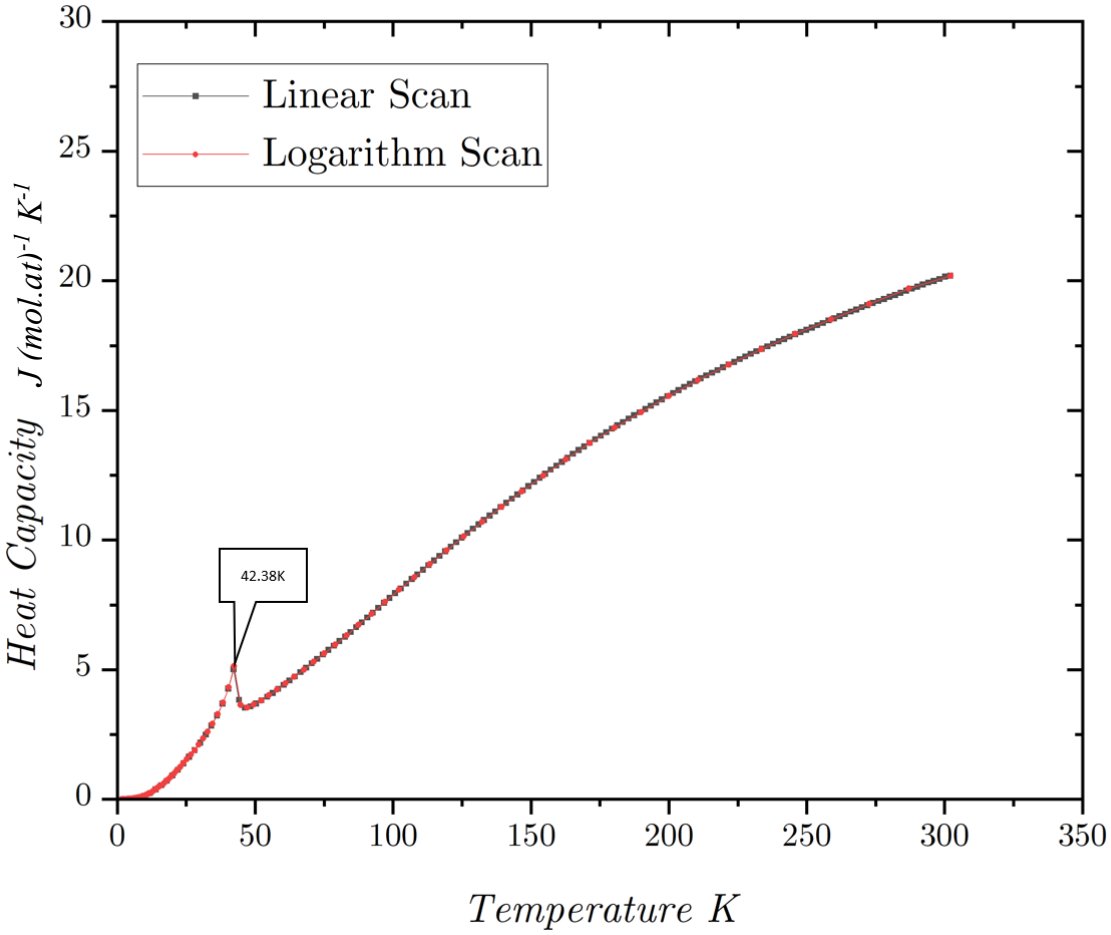

Figure V-21 Heat capacity of $UCrO_4$ from 1.8K to 300K measured by relaxation method (PPMS)

The variation of C_p vs. temperature is displayed in Figure V-21. Two measurements were realized with the same sample $UCrO_4$ from 300K down to 1.8K, according to the cool down procedure a linear decrease and a logarithm decrease. The results of the two measurements are fully consistent. The peak of C_p was determined as a temperature of 42.4(1) K. The temperature corresponds to the Néel temperature of $UCrO_4$, reported as 44.5K by Greenblatt *et al.* [36]. The C_p peak thus corresponds to the transition of $UCrO_4$ from an antiferromagnetic state to a paramagnetic state as the temperature is increased above the Néel temperature.

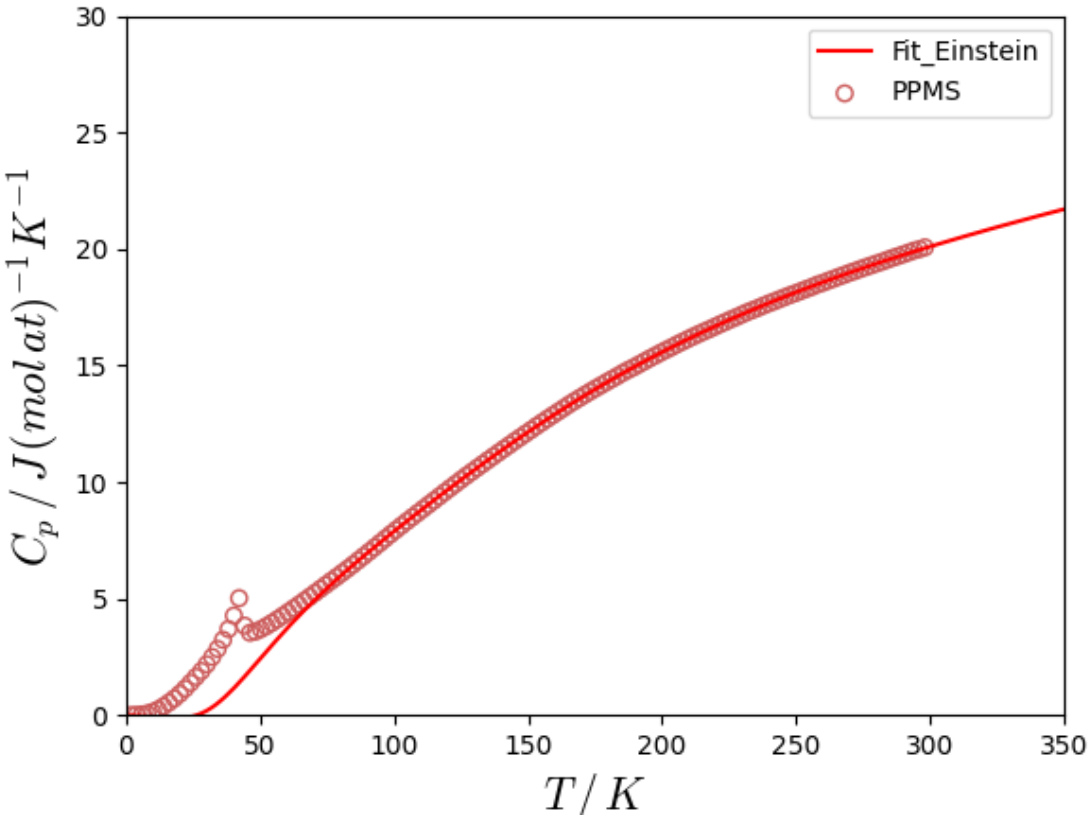

Figure V-22 Fitted C_p of $UCrO_4$ with modified Einstein model

The heat capacity was fitted by the modified Einstein model (defined in the Zr-Cr chapter) with data from 80K to 300K. We obtained a fairly good fitting of C_p data above 80 K. At low temperatures, the magnetic interactions contribute significantly to the C_p.

Table V-8 Fitting parameters of the modified Einstein model of $UCrO_4$ C_p.

Phase	**$UCrO_4$**
N. points	116
a_1	0.55±0.01
a_2	0.45±0.01
a	-0.0078±0.0011
θ_E^1	661.29±9.55
θ_E^2	219.40±4.34
b	2.7^{e}-5±3^{e}-6
n	2

The entropy of $UCrO_4$ at 298K was therefore calculated with the numerical integration of $\frac{C_p}{T}$:

$$S_{UCrO_4}^{298K} = 21.63\, J\,(mol.at)^{-1}\, K^{-1}$$

The entropy calculated will be useful in the definition of the Gibbs energy function of the compound for subsequent CALPHAD modeling.

V.6 Conclusion and perspective

In this section, our results in the U-Cr binary and U-Cr-O ternary systems are summarized.

In the U-Cr system, the main following results were obtained:

- The composition of the eutectic point was measured as 77.9% at. U and the solubility of Cr in γU was measured as 94.8% at. U on as-cast samples.
- DTA measurements determined the eutectoid temperatures of polymorphs U:

$$T_{\alpha \rightleftharpoons \beta}^{U,Cr} = 658.2 \pm 2.8°C$$

$$T_{\beta \rightleftharpoons \gamma}^{U,Cr} = 758.1 \pm 0.3°C$$

- A new CALPHAD modeling of the U-Cr system was performed by combining the results of our experimental investigation and carefully selected data in the literature.

In the U-Cr-O system:

- 4 samples were prepared with compositions corresponding to different three-phase fields of Yamanaka's isothermal section. All samples Show liquid demixing. The sample U10Cr50O40 was demixed to a metallic Cr phase and a eutectic region with a composition U3.9Cr37.8O58.3, supposed to be UO_2 - Cr_2O_3; the samples U40Cr30O30, U55Cr10O35 and U75Cr5O20 display same composition for the two liquids:
  - A solidified liquid with a average composition of U59O40Cr1, which is supposed to be a mixture of (U+UO_2).
  - A solidified liquid with a average composition of U29.5O70Cr0.5, which is supposed to be UO_2 regarding the low content of Cr, the U to O ratio and XRD results.
  - Underestimation of Cr may be possible in these two compositions. Bcc Cr phase may exist in limited areas and volumes of sample U40Cr30O30 by XRD but is not detected on SEM-EDS analysis.
- The $UCrO_4$ sample was prepared by powder metallurgy from UO_2 and Cr_2O_3 powder mixture heated at 1473 K for 6h under air. The purity of the sample revealed by the Rietveld method amounts to 96.63 ± 0.91% wt. (98.55±0.93% at.). The lattice parameters and atomic positions were also fitted and were consistent with the reported crystallographic parameters of the $BiVO_4$ type. The C_p of $UCrO_4$ was measured by relaxation calorimetry between 1.8 and 300K. The Néel temperature corresponding to the antiferromagnetic/paramagnetic transition on heating was measured at 42.4(1) K. By numerical integration of the heat capacity data, the entropy of $UCrO_4$ at 298K was calculated as 21.63kJ/(mol.atom)/K.

These preliminary results need to be completed. Nevertheless, these first experiments on the U-Cr-O ternary system as well as the measurement of $UCrO_4$ heat capacity are encouraging to further study of this ternary system.

Future work should concern:

- The determination of melting temperatures of ternary compositions by high-temperature DTA or laser Flash thermal analysis to better define the shape of the liquid/liquid miscibility gap.
- Measurements of the thermodynamic properties of the ternary phase $UCrO_4$, which is the most stable ternary phase in the system. The enthalpy of formation has been already measured by Guo *et al.* [37]. Measurement of the heat capacity and/or enthalpy increment at high temperatures would be of great help for further CALPHAD modeling of the Gibbs energy of this phase.
- Studies of the stability domain and thermodynamic properties of other ternary phases, namely CrU_2O_6 and CrU_3O_{10-x} would be positive.
- The CALPHAD modeling of the phase diagram. The modeling will be made based on phase relation data, thermodynamic properties of ternary phases and models of the 3 binary subsystems U-Cr, U-O and Cr-O. The demixing of liquid should be carefully considered in the modeling, using delicate definitions of phases/compounds and well-selected interaction parameters, to ensure compatibility with binary systems and experimental data.

All these works will be planned for the development of the NUCLEA database of IRSN.

V.7 Reference

[1] M. Venkatraman, J. P. Neumann, and D. E. Peterson, 'The Cr-U (Chromium-Uranium) system', *Bulletin of Alloy Phase Diagrams*, vol. 6, no. 5, pp. 425–429, Oct. 1985, doi: 10.1007/BF02869502.

[2] H. A. Saller, R. F. Dickerson, and W. E. Murr, 'Preparation of irradiation specimens of the Uranium-Chromium eutectic alloy', Aug. 1954, [Online]. Available: https://www.osti.gov/biblio/4350284

[3] A. H. Daane and A. S. Wilson, 'Uranium-Chromium System', *JOM*, vol. 7, no. 11, pp. 1219–1220, Nov. 1955, doi: 10.1007/BF03379031.

[4] T. A. Badaeva and R. I. Kuznetsova, 'Structure and Properties of Alloys of Uranium, Thorium and Zirconium', *O.S. Ivanov (Ed.)*, pp. 87–91, 1963.

[5] L. R. Chapman, 'Revision of the eutectoid isotherms of the uranium-chromium system', *Journal of Nuclear Materials*, vol. 116, no. 2–3, pp. 328–331, Jun. 1983, doi: 10.1016/0022-3115(83)90122-8.

[6] D. M. Provow and R. W. Pisher, 'The electrical resistivity of solid and molten uranium-chromium eutectic', *Journal of the Less Common Metals*, vol. 6, no. 4, pp. 313–321, 1964, doi: 10.1016/0022-5088(64)90128-6.

[7] R. D. Townsend and J. Burke, 'The effects of thermal history on the kinetics of the β → α phase change in uranium and uranium-chromium alloys', *Journal of Nuclear Materials*, vol. 17, no. 3, pp. 215–226, 1965, doi: 10.1016/0022-3115(65)90165-0.

[8] G. I. Terekhov and L. N. Aleksandrova, 'Phase diagrams of U-V and U-Cr', *IZV AKAD NAUK SSSR METALLY*, vol. 5, pp. 197–200, 1988.

[9] A. Berche, N. Dupin, C. Guéneau, C. Rado, B. Sundman, and J. C. Dumas, 'Calphad thermodynamic description of some binary systems involving U', *Journal of Nuclear Materials*, vol. 411, no. 1–3, pp. 131–143, Apr. 2011, doi: 10.1016/j.jnucmat.2011.01.043.

[10] A. R. Miedema, P. F. De Châtel, and F. R. De Boer, 'Cohesion in alloys — fundamentals of a semi-empirical model', *Physica B+C*, vol. 100, no. 1, pp. 1–28, Apr. 1980, doi: 10.1016/0378-4363(80)90054-6.

[11] N. Dupin, C. Guéneau, and S. Chatain, 'Thermodynamic Assessments of Cr-U and Pu-Si Systems', Materials Models and Simulations for Nuclear Fuels Workshop, Poster Session, 2006.

[12] R. Santhosh, S. Raju, A. K. Rai, N. V. Shanthi, and S. Saroja, 'Differential Scanning Calorimetry Study of U–Cr Alloys', *Trans Indian Inst Met*, vol. 68, no. S2, pp. 305–308, Sep. 2015, doi: 10.1007/s12666-015-0601-1.

[13] H. Okamoto, 'Supplemental Literature Review of Binary Phase Diagrams: B-Fe, Cr-Zr, Fe-Np, Fe-W, Fe-Zn, Ge-Ni, La-Sn, La-Ti, La-Zr, Li-Sn, Mn-S, and Nb-Re', *J. Phase Equilib. Diffus.*, vol. 37, no. 5, pp. 621–634, Oct. 2016, doi: 10.1007/s11669-016-0465-z.

[14] B. Samanta and R. K. Yadav, 'Experimental Investigation of Phase Equilibria and Phase Transformation Kinetics in the U-Cr System by Using DSC, XRD, and SEM', *J. Phase Equilib. Diffus.*, vol. 44, no. 1, pp. 28–42, Feb. 2023, doi: 10.1007/s11669-022-01021-z.

[15] A. T. Dinsdale, 'SGTE DATA FOR PURE ELEMENTS', *Calphad*, vol. 15, no. 4, pp. 317–425, Oct. 1991, doi: 10.1016/0364-5916(91)90030-N.

[16] P.-Y. Chevalier, E. Fischer, and B. Cheynet, 'Progress in the thermodynamic modelling of the O–U–Zr ternary system', *Calphad*, vol. 28, no. 1, pp. 15–40, Mar. 2004, doi: 10.1016/j.calphad.2004.03.005.

[17] P. C. Burns, R. C. Ewing, and A. Navrotsky, 'Nuclear Fuel in a Reactor Accident', *Science*, vol. 335, no. 6073, pp. 1184–1188, Mar. 2012, doi: 10.1126/science.1211285.

[18] E. M. Levin, C. R. Robbins, H. F. McMurdie, and M. K. Reser, *Phase Diagrams for Ceramists. 1969 Supplement*. in Phase Diagrams for Ceramists : 1969 Supplement.

American Ceramic Society, 1969. [Online]. Available: https://books.google.fr/books?id=yVngtAEACAAJ
[19] R. S. Roth *et al.*, *Phase Diagrams for Ceramists: Volume V*. in Phase diagrams for ceramists. American Ceramic Society, 1983. [Online]. Available: https://books.google.fr/books?id=ILXJAQAACAAJ
[20] C. Guéneau *et al.*, 'Thermodynamic modelling of advanced oxide and carbide nuclear fuels: Description of the U–Pu–O–C systems', *Journal of Nuclear Materials*, vol. 419, no. 1–3, pp. 145–167, Dec. 2011, doi: 10.1016/j.jnucmat.2011.07.033.
[21] P. Y. Chevalier and E. Fischer, 'Thermodynamic modelling of the O-U-Zr system', *Journal of Nuclear Materials*, vol. 257, no. 3, pp. 213–255, 1998.
[22] P. Y. Chevalier, E. Fischer, and B. Cheynet, 'Progress in the thermodynamic modelling of the O–U binary system', *Journal of Nuclear Materials*, vol. 303, no. 1, pp. 1–28, May 2002, doi: 10.1016/S0022-3115(02)00813-9.
[23] C. Guéneau, V. Dauvois, P. Pérodeaud, C. Gonella, and O. Dugne, 'Liquid immiscibility in a (O, U, Zr) model corium', *Journal of nuclear materials*, vol. 254, no. 2–3, pp. 158–174, 1998.
[24] A. Maurisi *et al.*, 'Experimental determination of the liquidus L/(U, Zr)O_{2-x} in the (U, Zr, O) system at T=2273K', Proc. Int. Conf. EUROMAT, Oct. 1996.
[25] E. J. Felten, E. F. Juenke, and S. F. Bartram, 'The system Cr_2O_3-UO_2-O_2', *Journal of Inorganic and Nuclear Chemistry*, vol. 24, no. 7, pp. 839–845, 1962, doi: https://doi.org/10.1016/0022-1902(62)80104-3.
[26] H. R. Hoekstra and S. Siegel, 'Preparation and properties of Cr_2UO_6', *Journal of Inorganic and Nuclear Chemistry*, vol. 33, no. 9, pp. 2867–2873, Sep. 1971, doi: 10.1016/0022-1902(71)80048-9.
[27] S. Sampath, A. Chadha, and D. M. Chackraburtty, 'Thermal behaviour of co-precipitated mixtures of chromium(III) and uranium(VI)', *Thermochimica Acta*, vol. 55, no. 2, pp. 249–251, Jun. 1982, doi: 10.1016/0040-6031(82)85159-9.
[28] S. Yamanaka, J. Shimizu, and M. Miyake, 'Thermodynamic study of the compatibility of oxide fuel with metals', *Journal of Nuclear Materials*, vol. 201, pp. 27–34, May 1993, doi: 10.1016/0022-3115(93)90156-S.
[29] Yamanaka Shinsuke, Kawano, Masaya, Shimizu, Juntaroh, Katsura, Masahiro and M. Miyake, 'Study of the uranium-transition metal-oxygen ternary system', *Technology Reports of the Osaka University*, vol. 40, pp. 179–187, Oct. 1990.
[30] J. Song, S. An, J.-Y. Kim, M. Barrachin, B. Piar, and B. Michel, 'Morphology and phase distributions of molten core in a reactor vessel', *Journal of Nuclear Materials*, vol. 542, p. 152471, Dec. 2020, doi: 10.1016/j.jnucmat.2020.152471.
[31] H. J. Borchardt, 'Observations on reactions of uranium compounds', *Journal of Inorganic and Nuclear Chemistry*, vol. 12, no. 1–2, pp. 113–121, Dec. 1959, doi: 10.1016/0022-1902(59)80100-7.
[32] M. Bacmann, E. F. Lewy-Bertaut, and G. Bassi, 'Paramètres atomiques et structures magnétiques de $UCrO_4$', *bulmi*, vol. 88, no. 2, pp. 214–218, 1965, doi: 10.3406/bulmi.1965.5838.
[33] D. K. Smith, C. F. Cline, and D. E. Sands, 'X-ray Data for the Chrome-Urania System, $Cr_2O_3 \cdot 2UO_3$', *Nature*, vol. 192, no. 4805, pp. 861–862, Dec. 1961, doi: 10.1038/192861b0.
[34] H. R. Hoekstra and R. H. Marshall, 'Some Uranium-Transition Element Double Oxides', in *Lanthanide/Actinide Chemistry*, in Advances in Chemistry, no. 71, vol. 71. AMERICAN CHEMICAL SOCIETY, 1967, pp. 211–227. doi: 10.1021/ba-1967-0071.ch016.

[35] P. Wolfers, M. Bacmann, and E. F. Bertaut, 'STRUCTURE MAGNÉTIQUE DE LA SOLUTION SOLIDE $UFe_{0,75}Cr_{0,25}O_4$', *J. Phys. Colloques*, vol. 32, no. C1, pp. C1-859-C1-860, Feb. 1971, doi: 10.1051/jphyscol:19711301.
[36] M. Greenblatt, R. M. Hornreich, and B. Sharon, 'Magnetoelectric compounds with two sets of magnetic sublattices: $UCrO_4$ and $NdCrTiO_5$', *Journal of Solid State Chemistry*, vol. 10, no. 4, pp. 371–376, Aug. 1974, doi: 10.1016/0022-4596(74)90046-2.
[37] X. Guo *et al.*, 'U(v) in metal uranates: a combined experimental and theoretical study of $MgUO_4$, $CrUO_4$, and $FeUO_4$', *Dalton Trans.*, vol. 45, no. 11, pp. 4622–4632, 2016, doi: 10.1039/C6DT00066E.
[38] A. Leenaers, L. de Tollenaere, C. Delafoy, and S. Van den Berghe, 'On the solubility of chromium sesquioxide in uranium dioxide fuel', *Journal of Nuclear Materials*, vol. 317, no. 1, pp. 62–68, Apr. 2003, doi: 10.1016/S0022-3115(02)01693-8.
[39] Ch. Riglet-Martial *et al.*, 'Thermodynamics of chromium in UO_2 fuel: A solubility model', *Journal of Nuclear Materials*, vol. 447, no. 1–3, pp. 63–72, Apr. 2014, doi: 10.1016/j.jnucmat.2013.12.021.
[40] V. Peres *et al.*, 'High temperature chromium volatilization from Cr_2O_3 powder and Cr_2O_3-doped UO_2 pellets in reducing atmospheres', *Journal of Nuclear Materials*, vol. 423, no. 1–3, pp. 93–101, Apr. 2012, doi: 10.1016/j.jnucmat.2012.01.001.
[41] H. Smith *et al.*, 'Cr^{2+} solid solution in UO_2 evidenced by advanced spectroscopy', *Commun Chem*, vol. 5, no. 1, p. 163, Dec. 2022, doi: 10.1038/s42004-022-00784-3.
[42] A. Milena-Pérez, L. J. Bonales, N. Rodríguez-Villagra, M. B. Gómez-Mancebo, and H. Galán, 'Oxidation of accident tolerant fuels models based on Cr-doped UO_2 for the safety of nuclear storage facilities', *Journal of Nuclear Materials*, vol. 582, p. 154502, Aug. 2023, doi: 10.1016/j.jnucmat.2023.154502.
[43] S. A. Barrett, A. J. Jacobson, B. C. Tofield, and B. E. F. Fender, 'The preparation and structure of barium uranium oxide $BaUO_{3+x}$', *Acta Crystallogr B Struct Sci*, vol. 38, no. 11, pp. 2775–2781, Nov. 1982, doi: 10.1107/S0567740882009935.
[44] G. Leinders, T. Cardinaels, K. Binnemans, and M. Verwerft, 'Accurate lattice parameter measurements of stoichiometric uranium dioxide', *Journal of Nuclear Materials*, vol. 459, pp. 135–142, Apr. 2015, doi: 10.1016/j.jnucmat.2015.01.029.
[45] T. Cordara *et al.*, 'Hot Isostatic Pressing (HIP): A novel method to prepare Cr-doped UO_2 nuclear fuel', *MRS Advances*, vol. 5, no. 1–2, pp. 45–53, Jan. 2020, doi: 10.1557/adv.2020.62.
[46] M. Bacmann and E. F. Lewy-Bertaut, 'Structure de $UCrO_4$', *Bulletin de la Société française de Minéralogie et de Cristallographie*, vol. 87, no. 2, pp. 275–276, 1964, doi: 10.3406/bulmi.1964.5735.

Chapter VI

General conclusions

Chapter VI. General conclusions

The context of this thesis has been the studies on new conceptions of ATF (accident tolerant fuel) in LWR under severe accident conditions. More precisely, the work has been concerned with the new conceptions which are considered today in France, i.e. Cr-coated zirconium-based cladding and Cr_2O_3-doped UO_2 fuel. After the Fukushima Daichi accident, nuclear industry was asked to improve the fuel elements in order to reach the general objective of increasing the coping time in case of accident. In this framework, the Cr-coated cladding concept has been developed to increase the oxidation resistance and to improve the behavior of cladding at high temperatures whereas the Cr_2O_3-doped UO_2 fuel concept has been proposed to increase the retention of fission gas in the fuel grains.

To better understand the behavior of these advanced materials, in particular under accident conditions, the knowledge of thermodynamics of the quaternary system Zr-Cr-U-O at high temperatures is a key step. Regarding the large uncertainties existing on this system, there was a need of experimental investigations. These experiments constituted the core of our project. In parallel, modelling activities, significant part of this work, have been developed to complement the experimental studies to have an overview of thermodynamics of the Zr-Cr-U-O system. Among these modelling activities, the CALPHAD method which is a suitable approach for the assessment of phase diagrams based on a stepwise progression from unary, then binary, then ternary systems to fulfill the thermodynamic comprehension of complex systems has been used. This approach is currently considered in the development and improvement of the IRSN NUCLEA thermodynamic database, in which our work will be integrated in a next future.

This thesis aimed to contribute both experimental and modeling studies of the Zr-Cr, U-Cr, Zr-Cr-O and U-Cr-O systems. Regarding the binary systems, even if the Zr-Cr system has been already overwhelmingly studied, there were still conflicting descriptions; the U-Cr system, mainly investigated in the uranium-rich part, is a simple eutectic phase diagram previously modelled by Berche *et al.* [1]; The Zr-Cr-O and U-Cr-O systems were poorly studied in the literature, with for each of them, a unique investigation carried out by Rhee and Hoch [2] and Yamanaka *et al.* [3], respectively.

For the Zr-Cr system, the main experimental outputs of this work are:

1. The phase equilibria were carefully re-examined in order to try to determine more accurately the temperatures and the compositions of the eutectic reactions, the temperature

of the eutectoid reaction, the mutual solubility of pure elements and the non-stoichiometry domain of $ZrCr_2$.

2. The $ZrCr_2$ C36 polymorph was disregarded after careful examination of heat-treated samples using diffraction techniques.
3. The enthalpies of formation of the C14 and C15 phases were measured by dissolution calorimetry and the heat capacities of the C14 and C15 phases were determined using a semi-adiabatic method (PPMS, 1.8K to 298K) and relaxation method (DSC, room temperature to 1063K). The entropies of formation of these compounds were calculated from heat capacity integration.
4. DFT calculations were performed to estimate the enthalpy of formation of the stable and metastable end-members of the Laves phases. These calculations provided starting values for the definition of the Gibbs energy of the $ZrCr_2$ compound in the modelling of Zr-Cr.
5. A CALPHAD optimization was performed according to our experimental investigation and selected literature data.

To deepen the study of the Zr-Cr system (in spite of the numerous works that already exist), some additional studies could be proposed:

- Measurement of the C14/C15 transition temperature and the melting temperature of $ZrCr_2$.
- Determination of the enthalpy of formation of $ZrCr_2$ C14/C15 with better accuracy.
- Measurements high-temperature liquidus points.

The Zr-Cr-O system was scarcely studied in the literature. A ternary phase of Zr_3Cr_3O composition was reported in several publications, but its thermodynamic properties were unknown.

The main results of this work can be summarized as follows:

1. Regarding the quasi-binary ZrO_2-Cr_2O_3 system, despite difficulties encountered for EDS measurements due to a strong charge-up effect, the oxide mutual solubilities at 1200°C were estimated as:

$$\mathrm{Sol}(ZrO_2 \text{ in } Cr_2O_3) = 29.07 \pm 10.27\% \text{ mol.}$$
$$\mathrm{Sol}(Cr_2O_3 \text{ in } ZrO_2) = 9.24 \pm 8.30\% \text{ mol.}$$

2. Isothermal sections were assessed for 1200°C and 1500°C for the concentration region in the metallic-oxidic part of the system. The results are in agreement with the work of Rhee and Hoch [2], except for a slight discrepancy in the liquid extension at 1500°C.

3. Samples of high-purity Zr_3Cr_3O could be prepared according to powder metallurgy from an initial composition of $Zr_3Cr_{3.3}O$ annealed at 1400°C for less than 4h under high purity Ar. The crystal structure of Zr_3Cr_3O was refined using the Rietveld method, confirming the filled Ti_2Ni structure type with a lattice parameter, $a = 11.959(1)$ Å at room temperature. No solubility domain around the stoichiometric composition was found.
4. The enthalpy of the formation of Zr_3Cr_3O was measured by drop solution calorimetry as $\Delta_f^{\circ} H_{Zr_3Cr_3O} = -89.96 \pm 3.98\ kJ.mol^{-1}.atom^{-1}$. Its specific heat capacity Cp was measured over a wide temperature range of 1.8-1063K. The C_p data was fitted with a modified Einstein model allowing to determine the entropy of the formation. The reliability of the results was confirmed by comparison with the enthalpy increment.
5. DFT calculations were found in line with the experimental results for the atomic positions and enthalpy of formation considering that the simulations were performed at nearly 0 K.
6. A CALPHAD modeling gathering the newly assessed binary system Zr-Cr and Zr-O, Cr-O of the NUCLEA thermodynamic database and including these experimental and DFT results yield a consistent Zr-Cr-O model that well reproduces the isothermal section at 1200°C, 1500°C and 1700°C.

The CALPHAD optimization would benefit of:

- Additional experimental data of equilibria at high temperatures such as 1700°C and more interaction parameters to model the extension of binary phases in ternary systems.
- Measurement of the melting temperature of Zr_3Cr_3O.

Preliminary results of the U-Cr-O ternary system have been gathered with the final aim of performing a thermodynamic optimization. The phase relations within the U-Cr binary system along with the invariant reactions were confirmed and the available CALPHAD model of Berche *et al.* [1] was also confirmed to the NUCLEA Database format.

Promising results on the ternary systems are:

1. Observation of liquid demixing with a large gap extending from the Cr-O boundary system between metallic Cr and an oxide eutectic composition U3.9Cr37.8O58.3, supposed to be UO_2+Cr_2O_3 and for the U-O boundary system between a solidify liquid with an average composition of U59O40Cr1 and UO_2.

2. The specific heat of $UCrO_4$ at low temperatures (1.8K to 300K) was measured for the first time. It confirms the antiferromatic transition at about 43 K With the interpolation method, the entropy of $UCrO_4$ at 298K was calculated as 21.63kJ/(mol.atom)/K.

The U-Cr-O ternary system will benefit the future:

- Determination of the melting temperatures within the miscibility gap.
- Thermodynamic measurements of the ternary phase $UCrO_4$, which is the most stable ternary phase in the system. The heat capacity in the largest temperature interval possible and enthalpy of formation will help to model the Gibbs energy of the phase.
- Studies of other ternary compounds were reported in the literature, namely CrU_2O_6 and CrU_3O_{10-x}.
- CALPHAD modeling of the phase diagram. The modeling will be made based on phase relation data, thermodynamic properties of ternary phases and models of the 3 sub binary systems U-Cr, U-O and Cr-O.

All these works will be used for the development of the NUCLEA database of IRSN.

Reference

[1] A. Berche, N. Dupin, C. Guéneau, C. Rado, B. Sundman, and J. C. Dumas, 'Calphad thermodynamic description of some binary systems involving U', *Journal of Nuclear Materials*, vol. 411, no. 1–3, pp. 131–143, Apr. 2011, doi: 10.1016/j.jnucmat.2011.01.043.
[2] S. K. Rhee and M. Hoch, 'The system chromium-zirconium-oxygen at 1200, 1500, and 1700°C', *Trans. AIME*, vol. 230, no. 7, pp. 1687–1690, Dec. 1964.
[3] S. Yamanaka, J. Shimizu, and M. Miyake, 'Thermodynamic study of the compatibility of oxide fuel with metals', *Journal of Nuclear Materials*, vol. 201, pp. 27–34, May 1993, doi: 10.1016/0022-3115(93)90156-S.
[4] M. Bacmann, E. F. Lewy-Bertaut, and G. Bassi, 'Paramètres atomiques et structures magnétiques de $UCrO_4$', *Bulletin de la Société française de Minéralogie et de Cristallographie*, vol. 88, no. 2, pp. 214–218, 1965, doi: 10.3406/bulmi.1965.5838.

Abstract

The development of Accident Tolerant Fuel (ATF) nuclear systems is regarded as an interesting material answer to improve the light water reactors safety in case of loss of coolant scenario. Cr-coated zirconium alloy (M5®) and UO_2 pellets doped with Cr_2O_3 chromium oxide are among the most promising short-term solutions. This Ph.D. thesis aimed to improve the understanding of the in-core thermophysical behavior of these newly developed materials for severe accident conditions. To reach this objective, a combined experimental and modeling study of the thermodynamic properties of the Zr-Cr-O and U-Cr-O ternary systems was performed. The methodology based on the CALPHAD method firstly consisted of experimental re-investigation of doubtful or conflicting results of the open literature and secondary, in the thermodynamic computational optimization using selected experimental data from both an exhaustive bibliographic survey and our experimental outputs as well as DFT calculations. The experimental investigation comprised the re-assessment of the phase relations at elevated temperatures, the characterization of selected invariant transformations, and the measurement of some main thermodynamic properties of the intermediate phases. The CALPHAD thermodynamic optimizations were carried out using classical phase models to get a fully consistent agreement between all available thermodynamic parameters.

Foremost, the Zr-Cr binary system was carefully re-investigated by dedicated experiments aiming to determine accurate parameters of the eutectic and eutectoid invariant transformations. A rather complete analysis of the $ZrCr_2$ Laves compounds was performed to elucidate the thermochemical behavior and to measure the thermodynamic properties of the various polymorphic forms. Our investigation carried out with the help of spectroscopy, diffraction and calorimetry methods reveals that the C15 $MgCu_2$-type (low temperature) and C14 $MgZn_2$-type (high temperature) are stable and disregard the formation of the C36, $MgNi_2$-type form claimed as the intermediate product of the C14 to C15 transformation. The enthalpy of formation of both stable polymorphs was determined by coupling drop solution calorimetry and DFT calculations. Their specific heat capacity was measured in a wide temperature interval (1.8 - 1063K) affording reliable values of the entropy of formation. Secondly, the Zr-Cr CALPHAD modeling was performed using classical phase descriptions and based on selected experimental and DFT results yielding a consistent picture of the optimized thermodynamic parameters with the extensive available data for this binary system.

For the Zr-Cr-O ternary system, the isothermal sections at 1473K and 1773K were experimentally assessed with the help of powder diffraction, energy and wavelength dispersive spectroscopies and microscopic observations. Our study confirms that Zr_3Cr_3O is the unique intermediate phase of the ternary system. It is a line compound adopting a filled Ti_2Ni-type structure. Its enthalpy of formation was determined using drop calorimetry in Al-bath as well as its entropy of formation deduced from specific heat capacity measurements. The thermodynamic optimization of the ternary system was performed using the CALPHAD method, taking advantage of the newly re-assessed Zr-Cr system and the available Zr-O and Cr-O optimizations already present in the NUCLEA database. It yields a consistent thermodynamic description of the Zr-Cr-O ternary system with all the available data.

Regarding the ternary U-Cr-O ternary system, our investigation started with the CALPHAD modeling of the U-Cr binary system based on some new experiments in the vicinity of the eutectic reaction and for the U-rich region of the phase diagram. The new optimization of the U-Cr system is now implemented within the NUCLEA database. Some preliminary results were obtained for the U-Cr-O ternary system at 1273K as well as for the solidification paths revealing a significant miscibility gap at the liquid state presumably composed of metallic and ceramic components as observed for both U-O and Cr-O binary systems. The heat capacity at low temperatures of $UCrO_4$ was measured for the first time confirming its antiferromagnetic behavior below 44(1) K and allowing us to derive if entropy of formation.

All these results would benefit the thermodynamic NUCLEA database of IRSN developed for severe accident applications.

Résumé

Le développement de matériaux combustibles tolérants aux accidents (ATF) est un moyen d'améliorer la sûreté des réacteurs à eau légère. L'alliage de zirconium recouvert de Cr (M5) et le combustible UO_2 dopé à l'oxyde de chrome Cr_2O_3 figurent parmi les solutions à court terme les plus prometteuses. L'objectif de cette thèse était de réaliser une étude expérimentale des relations de phase, des propriétés thermodynamiques des systèmes ternaires Zr-Cr-O et U-Cr-O, et sur cette base expérimentale, de développer une modélisation thermodynamique de ces systèmes qui pourrait aider à évaluer le comportement de ces nouveaux concepts, en particulier à haute températures, conditions qui prévalent en situation d'accidents graves.

Pour le système binaire Zr-Cr, les expériences ont d'abord été consacrées à la détermination précise des transformations invariantes (eutectiques et eutectoïde) ; la phase $ZrCr_2$ Laves a été soigneusement étudiée. L'enthalpie de formation de cette phase a été mesurée par calorimétrie de dissolution. Sa capacité thermique spécifique a été mesurée sur un large intervalle de température (1.8K à 1063K). Une modélisation CALPHAD du système prenant en compte les données expérimentales obtenues et des simulations DFT a été réalisée.

Pour le système ternaire Zr-Cr-O, les sections isothermes à 1473K et 1773K ont été obtenues. Une méthode de préparation d'échantillons de Zr_3Cr_3O de haute pureté a été développée. La structure cristalline, l'enthalpie de formation et la capacité thermique spécifique de Zr_3Cr_3O ont été déterminées. Une modélisation CALPHAD a été faite en combinant ces nouveaux résultats et les modélisations des systèmes Zr-O et Cr-O déjà disponibles dans la base de données NUCLEA.

Une modélisation CALPHAD du système binaire U-Cr a été réalisée avec nos nouvelles mesures et les données publiées dans la littérature. Des résultats préliminaires ont été obtenus pour le système ternaire U-Cr-O à 1273K. Des échantillons d'$UCrO_4$ ont été préparés avec une grande pureté et leur capacité thermique à basse température a été mesurée ainsi que leur température de Néel.

Tous ces résultats bénéficieront à la base de données thermodynamiques NUCLEA de l'IRSN développée pour les applications liées aux accidents graves.